

Andreas Jörke

**Mechanisms and kinetics of
petro- and oleochemicals in
complex hydroformylation
reaction networks**





Mechanisms and kinetics of petro- and oleochemicals in complex hydroformylation reaction networks

Dissertation

zur Erlangung des akademischen Grades

Doktoringenieur (Dr.-Ing.)

von Dipl.-Ing. Andreas Jörke
geboren am 30. April 1986 in Magdeburg

genehmigt durch die Fakultät für Verfahrens- und Systemtechnik
der Otto-von-Guericke-Universität Magdeburg

Promotionskommission: apl. Prof. Dr. rer. nat. Heike Lorenz (Vorsitz)
Prof. Dr.-Ing. Andreas Seidel-Morgenstern (Gutachter)
Prof. Dr. rer. nat. Armin Börner (Gutachter)
Prof. Dr. rer. nat. Dieter Vogt (Gutachter)
Prof. Dr.-Ing. Christof Hamel (Mitglied)

eingereicht am 09. Januar 2018
Promotionskolloquium am 27. April 2018

Forschungsberichte aus dem Max-Planck-Institut
für Dynamik komplexer technischer Systeme

Band 50

Andreas Jörke

**Mechanisms and kinetics of petro-
and oleochemicals in complex
hydroformylation reaction networks**

Shaker Verlag
Aachen 2018

Bibliographic information published by the Deutsche Nationalbibliothek

The Deutsche Nationalbibliothek lists this publication in the Deutsche Nationalbibliografie; detailed bibliographic data are available in the Internet at <http://dnb.d-nb.de>.

Zugl.: Magdeburg, Univ., Diss., 2018

Copyright Shaker Verlag 2018

All rights reserved. No part of this publication may be reproduced, stored in a retrieval system, or transmitted, in any form or by any means, electronic, mechanical, photocopying, recording or otherwise, without the prior permission of the publishers.

Printed in Germany.

ISBN 978-3-8440-6059-1

ISSN 1439-4804

Shaker Verlag GmbH • P.O. BOX 101818 • D-52018 Aachen

Phone: 0049/2407/9596-0 • Telefax: 0049/2407/9596-9

Internet: www.shaker.de • e-mail: info@shaker.de

Vorwort

Die vorliegende Arbeit entstand während meiner Tätigkeit als wissenschaftlicher Mitarbeiter am Institut für Verfahrenstechnik der Otto-von-Guericke-Universität Magdeburg im Zeitraum zwischen 2012 und 2017 im Rahmen des durch die Deutsche Forschungsgemeinschaft geförderten Sonderforschungsbereiches Transregio-63 "Integrierte chemische Prozesse in flüssigen Mehrphasensystemen - InPROMPT". An dieser Stelle möchte ich mich für die finanzielle Unterstützung durch die DFG herzlich bedanken.

Mein besonderer und herzlicher Dank gilt Prof. Dr.-Ing. Andreas Seidel-Morgenstern und Prof. Dr.-Ing. Christof Hamel für die herausfordernde, spannende und interdisziplinäre Aufgabenstellung, die hervorragende Betreuung und die gewährten Freiräume zur selbstständigen Durchführung dieser Arbeit. Ebenso herzlich danke ich Prof. Dr. rer. nat. Armin Börner und Prof. Dr. rer. nat. Dieter Vogt für die anerkennende Begutachtung der vorliegenden Arbeit.

Für die hervorragende Zusammenarbeit innerhalb des SFB/TRR63 bedanke ich mich bei allen SFB-Kollegen aus Berlin, Dortmund und Magdeburg. Dabei möchte ich an dieser Stelle besonders Emilija Kohls für die Bereitstellung von Ergebnissen quantenchemischer Rechnungen erwähnen.

Weiterhin danke ich Dr. Marc Garland und Dr. Tung Dinh Nguyen vom Institute of Chemical and Engineering Sciences Singapur für die detaillierte Einführung in die Infrarot-Spektroskopie und Chemometrie, die experimentelle Unterstützung und die Gastfreundschaft während meines dortigen Forschungsaufenthaltes.

Anregungen entnahm ich den im Rahmen dieser Arbeit betreuten Bachelor-, Master- und Diplomarbeiten von Sven Gitte, Susann Triemer, Jorge Forasepci Marinas, Sabine Kirschtowski, Tanja Stuwe und Alpesh Mor.

Den Doktoranden und Mitarbeitern des Lehrstuhls für Chemische Verfahrenstechnik und der Arbeitsgruppe Physikalisch-Chemische Grundlagen der Prozesstechnik des Max-Planck-Institutes für Dynamik komplexer technischer Systeme Magdeburg, insbesondere Gregor Kiedorf, Martin Gerlach, Matthias Felischak, Thomas Munkelt,

Luise Blach, Erik Temmel, Peter Schulze und allen anderen, möchte ich an dieser Stelle herzlich für die tolle und spannende Zeit und Zusammenarbeit danken und hoffe, dass man sich wiedersieht. Ferner gilt mein Dank Marion Hesse, Nancy Ziebell, Sophia Pistorius und Stephanie Geyer für die herausragende und schnelle Hilfe in organisatorischen Angelegenheiten, sowie den Werkstätten der O-v-G-Universität und des MPI Magdeburg für die tatkräftige Unterstützung bei der technischen Realisierung der im Rahmen dieser Arbeit verwendeten experimentellen Aufbauten.

Zum Schluss gilt der größte Dank meiner Familie, insbesondere meinen Eltern. Ihr habt immer an mich geglaubt, mich unterstützt und ermutigt. Ohne euch wäre ich nicht so weit gekommen. Danke!

Mai 2018

Andreas Jörke

Abstract

The homogeneously rhodium-BiPhePhos catalyzed hydroformylation of renewable long-chain fatty acid methyl esters (FAME's) to polymer precursors is an important and promising example reaction for industrially relevant "Green Chemistry". A typical FAME of interest with internal double bond is methyl oleate, which can be produced from e.g. rapeseed oil. However, corresponding mechanistic kinetic models, needed for model-based process design and optimization, are still not available in the literature. Hence, it is intended to contribute to this field of research with this thesis, which is part of the collaborative research center SFB/TRR63 "Integrated Chemical Processes in Liquid Multiphase Systems".

Hydroformylation of substrates with internal double bond requires simultaneous double bond isomerization to produce linear aldehydes. If these substrates are esters, the ester group could in principle interact with the hydroformylation catalyst and affect its activity. These issues have to be understood in order to be quantified by mechanistic kinetic models. Hence, two model compounds were used in this thesis to study the kinetics of double bond isomerization, hydrogenation and (tandem isomerization-) hydroformylation reactions with and without ester-catalyst interactions: 1-decene as typical long-chain olefin and the structurally analogous and renewable FAME methyl 10-undecenoate. The reaction mechanisms of both substrates were investigated using *operando* ATR-FTIR spectroscopy to observe catalyst resting states and derive rate determining steps. Two catalyst species were detectable during isomerization, hydrogenation and hydroformylation of both substrates: Active hydrido-Rh^I-mono- and inactive dicarbonyl complexes. Substrate coordination to the Rh^I-monocarbonyl determined the reaction rates of both substrates and it was concluded that both substrates are converted by the same reaction mechanisms. Although no significant rate differences between both substrates were observable during hydroformylation, the catalyst activity was significantly reduced under CO free FAME isomerization or hydrogenation conditions. This catalyst deactivation depended on ester concentration and was assigned to the formation of inactive Rh^I-ester complexes. Oxidative addition of H₂ to Rh^I complexes formed isomerization and hydrogenation active Rh^{III}-trihydride complexes and restored partly the catalyst activity. The developed kinetic models quantify the respective mechanistic findings and are based on the specific reaction mechanisms for both model substrates.

Dynamic (semi-) batch experiments were conducted to estimate unknown kinetic model parameters of the developed mechanistic kinetic models. A model-based and universal "parameter subset selection" method, which was extended to a local analysis by exploiting dynamic parameter sensitivities, was used to systematically design the required experiments. Thus, parameter identifiability could be improved. The resulting experimental design divided the hydroformylation reaction network into double bond isomerization, hydrogenation and hydroformylation subnetworks, which were analyzed individually. After parameter estimation, the developed mechanistic kinetic models were able to reproduce all experimental observations for both substrates with high accuracy.

Conclusively, optimal process variable trajectories (reaction temperature and CO/H₂ partial pressures) for maximum linear aldehyde yield were calculated by dynamic optimization for both model substrates using the corresponding developed mechanistic kinetic models. The calculations showed that the hydroformylation of olefins and esters with terminal double bond should be conducted at low temperature and high synthesis gas pressure whereas the tandem isomerization-hydroformylation of internal olefins is most productive at high temperature and low synthesis gas pressure. The optimal synthesis gas composition and pressure for the tandem isomerization-hydroformylation of internal esters, however, differed significantly from internal olefin results due to interactions between the ester group, the catalyst and the gaseous reactants and was characterized by a high CO percentage. Transfer of these results to methyl oleate with internal double bond caused a significant increase in productivity and selectivity compared to published standard reaction conditions.

Kurzfassung

Die homogenen Rhodium-BiPhePhos katalysierte Hydroformylierung nachwachsender langkettiger Fettsäuremethylester (FAME) zu Polymervorstufen ist eine wichtige und vielversprechende Beispielreaktion für industriell relevante "Grüne Chemie". Ein typischer FAME mit interner Doppelbindung ist Ölsäuremethylester, der u.a. aus Rapsöl gewonnen werden kann. Entsprechende mechanistische kinetische Modelle für modellbasiertes Prozessdesign und Optimierung sind in der Literatur bisher jedoch noch nicht verfügbar. Es wird daher beabsichtigt mit der vorliegenden Arbeit, die Teil des Sonderforschungsbereiches SFB/TRR63 "Integrierte chemische Prozesse in flüssigen Mehrphasensystemen" ist, zu diesem Forschungsfeld beizutragen.

Die Hydroformylierung von Substraten mit interner Doppelbindung zu linearen Aldehyden setzt simultane Doppelbindungsisomerisierung voraus. Sollten diese Substrate Ester sein, ist es prinzipiell möglich, dass die Estergruppe mit dem Katalysator wechselwirkt und seine Aktivität beeinträchtigt. Diese Aspekte müssen verstanden werden, um durch mechanistische kinetische Modelle quantifiziert werden zu können. Daher wurden zwei Modellsubstanzen in dieser Arbeit verwendet, um die Kinetik der Doppelbindungsisomerisierungs-, Hydrierungs- und (isomerisierenden) Hydroformylierungsreaktionen mit und ohne Ester-Katalysator-Wechselwirkungen zu studieren: 1-Decen als typisches langkettiges Olefin und der strukturell analoge und nachwachsende FAME 10-Undecensäuremethylester. Die Reaktionsmechanismen beider Substrate wurden mittels *operando* ATR-FTIR Spektroskopie untersucht, um Katalysator-Ruhezustände zu beobachten und geschwindigkeitsbestimmende Schritte abzuleiten. Zwei Katalysatorspezies waren während der Isomerisierung, Hydrierung und Hydroformylierung beider Substrate beobachtbar: Aktive Hydrido-Rh^I-Mono- und inaktive Dicarbonyl-Komplexe. Die Koordinierung des Substrates am Rh^I-Monocarbonyl bestimmte die Reaktionsgeschwindigkeiten beider Substrate und es konnte geschlossen werden, dass beide Substrate nach dem gleichen Reaktionsmechanismus umgesetzt werden. Obwohl keine signifikanten Unterschiede zwischen den Reaktionsgeschwindigkeiten beider Substrate während der Hydroformylierung beobachtet werden konnten, war die Katalysatoraktivität unter CO freien FAME Isomerisierungs- und Hydrierungsbedingungen signifikant verringert. Diese Katalysatordeaktivierung zeigte eine deutliche Esterkonzentrationsabhängigkeit und wurde auf die Bildung inaktiver Rh^I-Ester-Komplexe

zurückgeführt. Oxidative Addition von H_2 an Rh^I -Komplexe bildete isomerisierungs- und hydrierungsaktive Rh^{III} -Trihydrid-Komplexe und stellte die Katalysatoraktivität teilweise wieder her. Die entwickelten kinetischen Modelle beinhalten die mechanistischen Erkenntnisse dieser Arbeit und basieren auf den spezifischen Reaktionsmechanismen für beide Modellsubstrate.

Dynamische (Semi-) Batch-Experimente wurden durchgeführt, um die unbekanntem Modellparameter der entwickelten mechanistischen kinetischen Modelle zu schätzen. Eine modellbasierte und universelle "parameter subset selection" Methode wurde zu einer lokalen Analyse durch das Ausnutzen dynamischer Parametersensitivitäten weiterentwickelt und für die systematische Planung der notwendigen Experimente genutzt. Dadurch konnte die Parameteridentifizierbarkeit verbessert werden. Der resultierende Versuchsplan teilt das Hydroformylierungsnetzwerk in Doppelbindungsisomerisierungs-, Hydrierungs- und Hydroformylierungs-Subnetzwerke auf, die individuell untersucht wurden. Die kinetischen Modelle beider Modellsubstrate waren nach erfolgter Parameterschätzung in der Lage, alle experimentellen Beobachtungen mit hoher Genauigkeit zu reproduzieren.

Abschließend wurden anhand der entwickelten mechanistischen kinetischen Modelle optimale Prozessvariablen-Trajektorien (Reaktionstemperatur und CO/H_2 Partialdrücke) für eine maximale Aldehydausbeute durch dynamische Optimierung für beide Modellsubstrate berechnet. Die Ergebnisse zeigten, dass die Hydroformylierung von Olefinen und Estern mit terminaler Doppelbindung bei niedriger Temperatur und hohem Synthesegasdruck durchgeführt werden sollte, während die tandem isomerisierende Hydroformylierung von internen Olefinen bei hoher Temperatur und niedrigem Synthesegasdruck am produktivsten ist. Die optimale Synthesegaszusammensetzung und -druck der tandem isomerisierenden Hydroformylierung von internen Estern unterschied sich jedoch signifikant von den Ergebnissen für interne Olefine aufgrund der Wechselwirkungen zwischen Estergruppe, Katalysator und den gelösten Gasen und war durch einen hohen CO -Anteil charakterisiert. Übertragung dieser Ergebnisse auf Ölsäuremethylester mit interner Doppelbindung führte zu signifikanten Produktivitäts- und Selektivitätssteigerungen im Vergleich zu publizierten Standardreaktionsbedingungen.

Contents

Nomenclature	1
1 Introduction	7
1.1 Industrial development and state of the art	7
1.1.1 Cobalt based processes	8
1.1.2 Rhodium based processes	8
1.2 Current research	9
1.2.1 Alternative catalyst metals	10
1.2.2 Ligands	10
1.2.3 Catalyst immobilization and recycling	14
1.2.4 Renewable substrates	15
1.3 Thesis goals	17
2 Theory and modeling	21
2.1 Thermodynamics	21
2.1.1 Non-stoichiometric Gibbs energy minimization	22
2.1.2 Benson's group contribution method	24
2.2 Kinetics	27
2.2.1 Reactor model and mass transfer	27
2.2.2 Kinetic modeling	30
2.3 Local parameter subset selection	33
2.3.1 Principle of local parameter subset selection	35
2.3.2 Illustration of the method using an example reaction	38
2.4 Summary	41
3 Hydroformylation of n-decene	43
3.1 Double bond isomerization equilibrium of n-decene	43
3.1.1 Calculation of thermodynamic state functions	46
3.1.2 Isomerization equilibrium composition and equilibrium constants	48
3.1.3 Experimental validation	51
3.2 Hydroformylation reaction mechanism for 1-decene	53
3.2.1 Mechanistic investigations using <i>operando</i> FTIR spectroscopy	56
3.2.2 Reduced hydroformylation reaction mechanism for n-decene	62

3.3	Kinetic modeling	63
3.3.1	Catalyst pre-equilibrium	65
3.3.2	Isomerization	65
3.3.3	Hydrogenation	66
3.3.4	Hydroformylation	67
3.4	Kinetic experiments and parameter estimation	69
3.4.1	Experimental design and subnetwork analysis	70
3.4.2	Isomerization subnetwork	72
3.4.3	Hydrogenation subnetwork	75
3.4.4	Hydroformylation network	76
3.4.5	Tandem isomerization-hydroformylation network	79
3.5	Optimal reaction control strategies	84
3.6	Summary	87
4	Hydroformylation of methyl 10-undecenoate	91
4.1	Comparison of UME to 1-decene	92
4.1.1	Isomerization subnetwork	93
4.1.2	Hydrogenation subnetwork	99
4.1.3	Hydroformylation network	101
4.2	Hydroformylation reaction mechanism for UME	103
4.2.1	Mechanistic investigations using <i>operando</i> FTIR spectroscopy	103
4.2.2	Extended hydroformylation reaction mechanism for UME	106
4.3	Kinetic modeling	108
4.4	Kinetic experiments and parameter estimation	110
4.4.1	Experimental design and subnetwork analysis	110
4.4.2	Isomerization subnetwork	111
4.4.3	Hydrogenation subnetwork	112
4.4.4	Hydroformylation network	114
4.5	Optimal reaction control strategies	118
4.6	Summary	121
5	Outlook	125
6	Summary and conclusions	127
	References	133
	Appendix A Experimental details	xiii
A.1	Setup	xiii
A.2	Procedures, solvents and materials	xvi
A.3	Gas chromatographic analysis	xvii

Appendix B Gas solubility and mass transfer coefficient	xix
Appendix C Characterization of gas-liquid mass transfer limitations	xxiii
Appendix D Local parameter subset selection results	xxvii
Appendix E Derivation of the non-stoichiometric equilibrium formulation	xxix
Appendix F Quantum chemical calculations	xxx
F.1 Comparison of BGCM to quantum chemical calculations	xxxi
F.2 Rh-BiPhePhos catalyst structures	xxxvi
Appendix G Additional experimental results	xxxvii

Nomenclature

Latin symbols

A	dimensionless rate constant at reference temperature	-
a	activity/absorbance	-
B	dimensionless activation energy	-
\bar{b}	vector of total amount of substance of chemical elements	mol
$\overline{\overline{C}}$	Christiansen Matrix	$s^{(1-M)}$
c	molar concentration	mol l^{-1}
c_p	molar heat capacity at const. pressure	$\text{J mol}^{-1} \text{K}^{-1}$
E	enhancement factor	-
E_A	activation energy	J mol^{-1}
f	right hand side of mass balance ODE	$\text{mol l}^{-1} \text{s}^{-1}$
$\overline{\overline{FIM}}$	Fisher-Information-Matrix	-
G	Gibbs energy	J
g	molar Gibbs energy	J mol^{-1}
H	Henry's constant	$\text{Pa m}^{-3} \text{mol}^{-1}$
h	molar enthalpy	J mol^{-1}
Ha	Hatta number	-
$\overline{\overline{I}}$	identity matrix	-
J	diffusion flux density	$\text{mol m}^{-2} \text{s}^{-1}$
K	(equilibrium/inhibition/...) constant	various
k	rate constant	s^{-1}
k_∞	collision factor	s^{-1}
k_{eff}	effective mass transfer coefficient	s^{-1}
M	number of catalytic steps per cycle	-
N	number/amount	-
n	amount of substance	mol
$\overline{\overline{P}}$	permutation matrix	-
p	pressure	bar
$\overline{\overline{Q}}$	orthogonal matrix	-
$\overline{\overline{R}}$	upper triangular matrix	-
R^2	linear correlation coefficient	-

\mathfrak{R}	sum of squares	$\text{mol}^2 \text{l}^{-2}$
r	reaction rate	$\text{mol l}^{-1} \text{s}^{-1}$
RF	response factor	-
$RMSE$	root mean squared error	-
$\overline{\overline{S}}$	Sensitivity Matrix	various
s	molar entropy	$\text{J mol}^{-1} \text{K}^{-1}$
STY	space time yield	$\text{kg m}^{-3} \text{s}^{-1}$
T	temperature	$\text{K} / ^\circ\text{C}$
t	time	s
TOF	turnover frequency	h^{-1}
$\overline{\overline{U}}$	unitary matrix	-
V	volume	m^3
$\overline{\overline{V}}$	unitary matrix	-
$\overline{\overline{V}}^T$	conjugate transpose matrix of $\overline{\overline{V}}$	-
X	conversion	-
x	molar fraction	-
Y	yield	-

Greek symbols

$\overline{\overline{\beta}}$	element-species-matrix	-
γ	activity coefficient	l mol^{-1}
Δ	difference/change	-
δ	film thickness/error	$\text{m}, -$
ϵ	tolerance	-
η_{mach}	machine precision	-
$\overline{\overline{\theta}}$	parameter vector	various
κ	condition number	-
λ	Lagrange multiplier	-
$\overline{\overline{\nu}}$	stoichiometric coefficient matrix	-
ν_i	stoichiometric coefficient of catalytic step i ($= 1 \forall i$ in this thesis)	-
ρ	residual/rank	$\text{mol l}^{-1}, -$
$\overline{\overline{\Sigma}}$	singular value matrix	-
σ	singular values	-
τ	normalized reaction time	-
$\overline{\overline{\phi}}$	Benson group matrix	-
Ω	product of ω 's	s^{1-M}
ω	pseudo first order rate coefficient	s^{-1}

Indices, sub- and superscripts

0	initial
abs	absolute
bg	Benson groups
CI	competitive inhibition
cal	calculated
cyc	cycle
d	double bond
e	element
el	chemical elements
eq	equilibrium
es	external symmetry
exp	experimental
f	formation
fix	fixed
gas	gas phase
<i>h, i, j, m</i>	counting indices
is	internal symmetry
liq	liquid phase
m	molecule
mod	model/modified
n	normalized
NCI	non-competitive inhibition
oi	optical isomers
p	parameters
ref	reference
rel	relative
rxn	reaction
s	species
sym	symmetry
t	time points
tot	total
°	at 1 bar _a
⊖	at 1 bar _a , 298 K
*	at phase boundary
^	reduced/lumped
·	flow/flux
~	approximated

Mathematic symbols and operators

$(\cdot)^T$	transpose
$(\cdot)^+$	Moore-Penrose pseudo-inverse
$\overline{(\cdot)}$	vector
$\overline{\overline{(\cdot)}}$	matrix
$(\cdot) \circ (\cdot)$	Hadarmad (entrywise) product
$\nabla(\cdot)$	gradient/Jacobian
$\nabla^2(\cdot)$	Hessian

Constants

R	gas constant	8.3145 J mol ⁻¹ K ⁻¹
---	--------------	--

Abbreviations

1D	1-decene
acac	acetylacetone
BGCM	Benson's group contribution method
BP	BiPhePhos
C10/dec	n-decene
CI	confidence interval
cat	catalyst
DC	dicarbonyl
DMF	n,n-dimethylformamide
div	divergence
EC	ester complex
FAME	fatty acid methyl ester
Hyd	hydrogenation
Hyf	hydroformylation
hOME	methyl stearate
hUME	methyl undecanoate
Inh	inhibitor
Iso	isomerization
ISTD	internal standard
iHyf	tandem isomerization-hydroformylation
ioxoUME	branched hydroformylation product of UME
iso-decene	internal n-decenes
iUME	internal UME isomers
LACS	least abundant catalys species
l:b	linear:branched
lig	ligand

MMS	micellar solvent system
MACS	most abundant catalyst species
MC	monocarbonyl
NLP	non-linear program
OME	methyl oleate + double bond isomers
oxoOME	linear + branched hydroformylation product of OME
oxoUME	linear hydroformylation product of UME
QM	quantum chemical
QRD	QR-decomposition
RDS	rate determining step
RS	resting state
SB	semi-batch (isobar)
SsS	subset selection
SVD	singular value decomposition
sub	substrate
TDTBPP	tris(2,4-di-tert-butylphenyl)phosphite
TH	trihydride
TMS	thermomorphic multicomponent solvent system
TPP	triphenylphosphine
TPPTS	tris(3-sulfophenyl)phosphine trisodium salt
UME	methyl 10-undecenoate
vacc	vacuum
ve	valence electron

1 Introduction

1.1 Industrial development and state of the art

The term hydroformylation refers to the catalytic conversion of a carbon-carbon double bond with synthesis gas (CO/H₂) to produce aldehydes, as shown in Figure 1.1 [Börner and Franke 2016]. This reaction, also known as "oxo-synthesis", was discovered coincidentally at the Ruhrchemie AG in Oberhausen, Germany by Otto Roelen in 1937/38 as he recycled undesired C₂ and C₃ olefin side products of the cobalt/iron/thorium catalyzed Fischer-Tropsch synthesis for oligomerization to higher hydrocarbons [Hibbel et al. 2013].

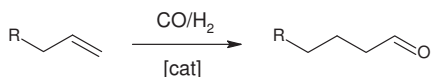


Figure 1.1: Catalyzed hydroformylation reaction converting olefins with terminal C-C double bond and synthesis gas (CO/H₂) to linear aldehydes.

Roelen found oxygenated products in the Fischer-Tropsch reactor outlet stream (propionaldehyde and diethylketone) and started systematic investigations to clarify the origin of these compounds. He concluded that the cobalt in the Fischer-Tropsch catalyst is responsible for the formation of these "oxo-products". His investigations lead to patents registration for the "oxo-synthesis" at the end of the 1930's with publication later on in the 1940's and 1950's [Roelen 1943, 1952; Falbe 1970]. Because of the industrial importance of "oxo-products" (aldehydes and alcohols from subsequent hydrogenation of the aldehyde) as intermediate platform chemicals, the hydroformylation reaction was utilized industrially soon after its discovery with the first production plant built in 1940 in Oberhausen, Germany. This plant used C₈-C₂₀ alkenes from cracking of Fischer-Tropsch waxes as substrates for the production of aliphatic alcohols [Hibbel et al. 2013]. Since then, the hydroformylation became the most important homogeneously catalyzed reaction for the industrial production of aldehydes, which are subsequently converted to detergents, plasticizers, fragrances and drugs. The annual worldwide production capacity in 2009 was 12 million tons (Germany: 2 million tons), of which n-butanal makes up the majority with ≈ 73 % [Bahrman et al. 2013].

1.1.1 Cobalt based processes

After the discovery of the catalytic hydroformylation activity of cobalt by Otto Roelen in the late 1930's, intensive investigations of this "first generation" catalyst were published in the early 1950's to 1960's. The homogeneous character of the Co-catalysis became clear [Wender et al. 1953; Orchin et al. 1956; Kirch and Orchin 1958] and fundamental work regarding the reaction mechanism revealed the catalytic nature of this important carbonylation reaction [Kirch and Orchin 1959; Heck and Breslow 1961]. The authors proved that a hydrido-Co-carbonyl complex $\text{HCo}(\text{CO})_4$ is the active catalyst. This catalyst requires harsh reaction conditions (temperature $\approx 110\text{-}180\text{ }^\circ\text{C}$, synthesis gas pressure $\approx 200\text{-}350\text{ bar}$) to counteract its relatively low activity [Bahrman et al. 2013]. The addition of phosphorus ligands (see section 1.2.2) to the Co-catalyst in the 1970's led to a significant catalyst activity increase [Bahrman et al. 2013; Hibbel et al. 2013]. Thus, monophosphine modified Co, the so-called "second generation" catalyst, allowed to operate the hydroformylation reaction under reduced synthesis gas pressure between 50 and 150 bar (Shell Process). Mainly, alcohols are produced using this catalyst due to fast subsequent aldehyde hydrogenation.

Over time, numerous patents and production processes were developed by the chemical industry based on Co-catalysis that are partly still under operation today because of the robustness and relatively low cost of cobalt [Bahrman et al. 2013].

1.1.2 Rhodium based processes

The discovery of Co as hydroformylation catalyst motivated investigations with the next group 9 element rhodium in the 1950's to develop new catalyst generations. It turned out that Rh is a (ten) thousandfold more active towards hydroformylation than Co but is also roughly a thousandfold more expensive [Jess and Wasserscheid 2013]. Nevertheless, the "third generation" hydrido-Rh-carbonyl catalyst $\text{HRh}(\text{CO})_4$ was patented 1956 by the Chemische Verwertungsgesellschaft mbH [Schiller 1956]. In the late 1960's, the superior catalytic hydroformylation performance of a triphenylphosphine (TPP) modified "fourth generation" rhodium-catalyst was proven experimentally and explained mechanistically [Evans et al. 1968]. The authors found that the rhodium reaction mechanism is analogous to cobalt catalysis. The ligand modification made the catalyst not only more active and stable but also more selective towards desired linear aldehydes compared to the "third generation" catalyst $\text{HRh}(\text{CO})_4$ [Garland and Pino 1991]. Accordingly, Rh-based processes started to replace, yet not completely, the established Co-based aldehyde production in the following decades.

In the mid 1970's, Union Carbide/Johnson Matthey/Davy McKee and Celanese (to-

day Oxea GmbH) started exploiting the high catalytic hydroformylation activity and regioselectivity of TPP modified Rh for industrial scale linear aldehydes production [Hibbel et al. 2013]. The high activity of Rh allowed to use mild reaction conditions in this Low Pressure Oxo (LPO) Process (temperature \approx 80-120 °C, synthesis gas pressure \approx 15-20 bar) for the conversion of propene to n-butanal. However, Rh is sensitive towards catalyst poisons and impurities. Hence, preprocessing of olefin and synthesis gas feed streams is mandatory as well as reprocessing of the recycled catalyst phase, consisting mainly of high boiling reaction byproducts [Beller 2006]. Nevertheless, Rh-based processes dominate nowadays due to increased selectivity towards preferred linear aldehydes, reduced undesired hydrogenation and mild reaction conditions, which is economically favorable [Beller et al. 1995; Börner and Franke 2016].

In the 1980's, Rhône-Poulenc and Ruhrchemie developed a very elegant hydroformylation process based on water soluble trisulfonated triphenylphosphine (TPPTS) modified Rh for the hydroformylation of propene [Hibbel et al. 2013]. The reactor contains an aqueous catalyst phase and an organic reactant phase. This multiphase concept drastically simplifies catalyst handling and recycling because the catalyst is insoluble in the organic product phase. Hence, process complexity and investment costs could be reduced drastically. In this manner, low Rh losses at ppb-levels and excellent regioselectivity towards linear aldehydes (\approx 97 %) were possible without accepting typical drawbacks of catalyst heterogenization (leaching and activity loss). Up to now, the Ruhrchemie/Rhône-Poulenc Process is the most important industrial process for C₄ aldehyde production. However, the process is limited to short-chain olefins because the low solubility of long-chain olefins in the aqueous catalyst phase leads to unacceptably low space-time-yields [Bahrman et al. 2013].

Union carbide started in the mid 1990's to convert olefins larger than C₄ in homogeneous liquid phase by using Rh-TPPTS dissolved in n-methylpyrrolidone to overcome the substrate solubility limitation of the Ruhrchemie/Rhône-Poulenc Process [Jess and Wasserscheid 2013]. This concept, however, requires complex and energy-intensive downstream separation, reprocessing and recycling of the precious catalyst, which is performed by extraction with water or other non-aqueous polar solvents.

1.2 Current research

Due to the economic importance of hydroformylation products, this industrially established reaction is still a topic of current research. The investigations are focused mostly on i) usage of alternative catalyst metals, ii) catalyst improvement by ligand modification, iii) technological measures for catalyst immobilization and recycling

and iv) renewable substrates for bio-based hydroformylation products. These topics were major driving factors for technology leaps in the past and still offer great potential for further improvement of hydroformylation processes.

1.2.1 Alternative catalyst metals

Besides Rh and Co, alternative transition metals like palladium [Drent and Budzelaar 2000; Konya et al. 2006; Jennerjahn et al. 2009], ruthenium [Kubis et al. 2016], iridium [Moreno 2003; Piras et al. 2011; Kubis et al. 2014], platinum [van Leeuwen et al. 1986, 1990; van der Vlugt et al. 2005] and even iron complexes [Breschi et al. 2000] were used as catalysts, partly with good to excellent product selectivity [Pospech et al. 2013]. However, it seems that these metals have generally lower catalytic hydroformylation activity compared to Rh and Co [Ternel et al. 2015]. For unmodified carbonyl complexes, the following activity trend was reported for several transition metals (from left: high activity to right: low activity) [van Leeuwen and Claver 2000; Behr and Neubert 2012; Börner and Franke 2016]:



Nevertheless, using alternative metals as catalysts could be attractive from an economic point of view due to their low cost compared to Rh. Thus, a hydroformylation company has the possibility to counteract the influence of metal price fluctuations on process profitability by choosing flexibly the catalyst with the best price-performance ratio.

Catalyst systems consisting of more than one metal were also investigated to improve overall catalyst activity and selectivity [Hsu and Orchin 1975; van Duren et al. 2007; Klähn and Garland 2015; Gaide et al. 2017a]. The following studies in this thesis will, however, focus on the most active and industrially most relevant rhodium exclusively.

1.2.2 Ligands

Ligand modification enables countless possibilities to change the steric and electronic properties of a homogeneous catalyst, resulting in altered activity and selectivity. The stability of a homogeneous catalyst is also greatly improved by ligand modification [Börner and Franke 2016]. The importance of ligands becomes even more clear when realizing that the modification of Rh with TPP or TPPTS resulted in the development of completely new hydroformylation processes on industrial scales with great economic importance.

It should be noted that ligands do not only influence the regioselectivity between linear and branched aldehydes but also the chemoselectivity of the hydroformylation

reaction, which is usually accompanied by undesired side reactions. Most dominantly, double bond isomerization forming n-olefin isomers with internal double bond (henceforth denoted as internal n-olefins) as well as hydrogenation of the double bond forming n-alkanes are occurring for straight chain n-olefins (see Figure 1.2) [Behr and Neubert 2012]. Thus, a reasonable ligand choice is important to tailor homogeneously catalyzed hydroformylation processes to substrate and desired product spectra.

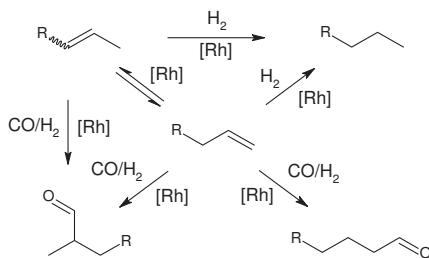


Figure 1.2: Hydroformylation reaction network catalyzed by Rh-complexes including double bond isomerization and hydrogenation side reactions as well as hydroformylation to branched aldehydes.

Generally, ligands are Lewis bases that form metal complexes by covalent or ionic bonding. They appear in countless designs and can be distinguished by their electron donor atom with phosphorus, nitrogen and oxygen being the most important. The following paragraph, however, will focus exclusively on the most important ligands used in hydroformylation¹: Phosphorus (P-) ligands [Behr and Neubert 2012].

Depending on the organic moieties attached to phosphorus, P-ligands can be categorized into the following substance classes [Behr and Neubert 2012]: phosphines PR₃, phosphinites R₂P(OR), phosphonites RP(OR)₂ and phosphites P(OR)₃ (R = aryl and/or alkyl moiety). From these classes, phosphines and phosphites are the most important [Beller 2006] with some prominent representatives that will be discussed briefly later on.

The electronic properties of a homogeneous catalyst are heavily influenced by the basicity of the attached ligand. As a consequence, ligands alter the bonding of substrates or other ligands and their transformations at the metal center and thus the activity of the catalyst [Behr and Neubert 2012]. Phosphines are generally stronger Lewis bases (σ -donors) since the electron donating alkyl/aryl groups increase electron density at the phosphorus atom, reinforcing the bonding of other ligands (e.g. CO) to the metal center. Phosphites are weaker Lewis bases (σ -donors) but stronger π -acceptors because of the electron withdrawing oxygen atoms next to phosphorus.

¹ Comprehensive reviews about various ligands in homogeneous catalysis in general can be found elsewhere [van Leeuwen and Claver 2000; Behr and Neubert 2012; Börner and Franke 2016].

Thus, phosphites compete with other ligands for π -electron back-bonding at the metal center, which weakens the bonding of other ligands (e.g. CO). This explains the increased acidity of phosphite modified hydrido-Co-complexes compared to phosphine modified hydrido-Co-complexes and the related hydroformylation activity differences reported in [Börner and Franke 2016].

The denticity of a ligand describes the amount of donor atoms² that can bind to a metal center. Mono- and sterically demanding bidentates (also called "chelates") are used frequently but also reports on tridentates are available [van Leeuwen and Claver 2000; Behr and Neubert 2012].

The discussion in the following will focus on mono- and bidentate phosphines and phosphites as they are most commonly applied [Beller 2006]. Some prominent representatives are shown in Figure 1.3. One of the most important and used monophosphines is TPP (see Figure 1.3a) [Dodonow and Medox 1928; Evans et al. 1968]. This relatively simple ligand was used in the LPO Process and enabled the utilization of active and selective Rh-catalysts for hydroformylation under mild conditions on industrial scales. Its trisulfonated and water soluble counterpart TPPTS is mainly used in the Ruhrchemie/Rhône-Poulenc Process, which is still the most important industrial scale hydroformylation process for short-chain olefins.

Using a monophosphite like tris(*o*-tert-butylphenyl) phosphite (see Figure 1.3b) as ligand resulted, compared to TPP, in a 10 to 30 times higher hydroformylation activity of Rh and good regioselectivity to linear aldehydes [van Leeuwen and Roobeek 1983; van Rooy et al. 1991, 1995].

The chelating diphosphine ligand Xantphos (see Figure 1.3c), developed by Piet van Leeuwen and co-workers, enabled excellent chemo- and regioselectivity as well as activity for Rh-catalyzed hydroformylation of mid-chain olefins (e.g. 1-octene) [Kranenburg et al. 1995]. Undesired side reactions (double bond isomerization and hydrogenation) were suppressed almost completely by using this ligand, even at elevated temperatures. The regioselectivity towards the linear aldehyde nonanal remained almost constant at $\approx 98\%$ between 40-80 °C, proving this ligand to be an excellent choice for Rh-catalyzed conversion of terminal alkenes to linear aldehydes. It was evident from their experimental comparison of numerous chelating diphosphines that the bite angle and sterics of the ligand strongly control the catalyst selectivity (wider bite angle = higher selectivity to linear aldehydes) [Kranenburg et al. 1995]. In the following years, the good performance of Rh-Xantphos catalysts motivated the development of a broad spectrum of Xantphos-type ligands, tunable by adjusting the bite angle [van Leeuwen and Claver 2000].

Union Carbide developed numerous phosphite ligands in the late 1980's of which the chelating diphosphite BiPhePhos (see Figure 1.3d) received some attention

² Synthesis of ligands with more than one donor atom is possible by using organic backbone bridges.

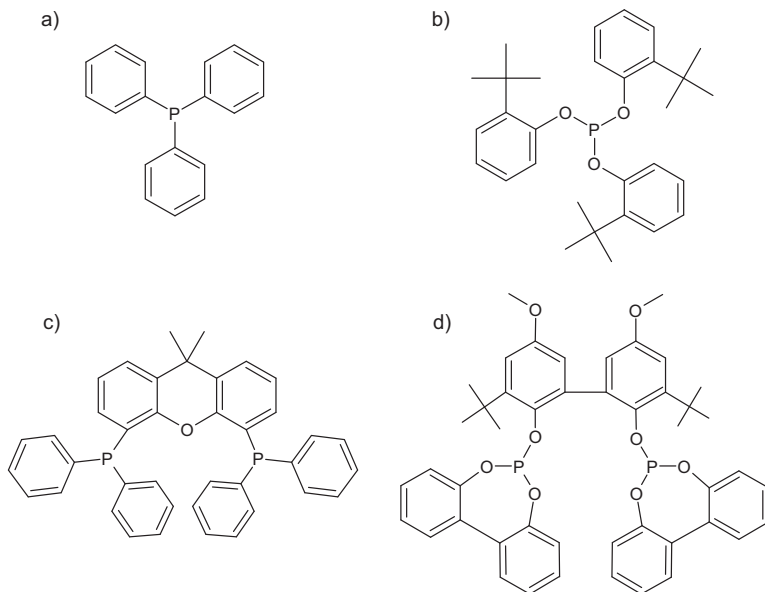


Figure 1.3: Representative mono- and diphosphorus ligands: a) triphenylphosphine [Dodonow and Medox 1928; Evans et al. 1968], b) tris(*o*-tert-butylphenyl) phosphite [van Leeuwen and Roobeek 1983], c) Xantphos [Kranenburg et al. 1995] and d) BiPhePhos [Billig et al. 1987, 1988].

recently [Billig et al. 1987, 1988]. Rh-BiPhePhos catalysts are characterized by an excellent hydroformylation activity, high aldehyde regioselectivity of $\approx 99\%$ and low hydrogenation activity, comparable to Xantphos [Moasser et al. 1995; van Rooy et al. 1996a]. The most striking difference to Xantphos, however, is the high double bond isomerization activity of BiPhePhos. Hence, conversion of straight-chain 1-olefins is always accompanied by double bond isomerization, leading to significant yields of less reactive internal olefins. This side reaction lowers the overall aldehyde yield and leads to the formation of undesired branched aldehydes from hydroformylation of internal olefins [Behr and Neubert 2012; Franke et al. 2012]. Although the isomerization feature of Rh-BiPhePhos catalysts seems to be a drawback compared to using Xantphos, it opens up new possibilities in terms of converting internal *n*-olefins to linear aldehydes, known as tandem³ isomerization-hydroformylation [Beller et al. 1999; van der Veen et al. 1999; Börner et al. 2001; Klein et al. 2001; Behr et al. 2003; Vogl et al. 2005; Vilches-Herrera

³ In this thesis, the term tandem reaction refers to auto-tandem reactions, using one catalyst for various tasks, and has to be differentiated from e.g. orthogonal tandem reactions, using various different catalysts for one task each [Behr and Neubert 2012].

et al. 2014]. Using mixtures of internal n-olefins as hydroformylation substrates is interesting from an industrial point of view because those mixtures are easily available from cracking and refining processes (raffinate I-III containing internal n-butenes) and subsequent oligomerization (internal n-octenes or n-dodecenes) [Jess and Wasserscheid 2013; Börner and Franke 2016]. Rh-BiPhePhos was proven to be an excellent catalyst with outstanding regioselectivity for this tandem reaction, e.g. for the conversion of internal n-octenes (< 4 % 1-octene) to linear nonanal (yield \approx 92 %) at 140 °C and 20 bar synthesis gas [Börner et al. 2001; Behr et al. 2003; Vogl et al. 2005].

1.2.3 Catalyst immobilization and recycling

The catalyst material (metal precursors and ligands) used for hydroformylation is usually associated with high investment cost [Behr and Neubert 2012]. Hence, it is of great importance for the profitability of hydroformylation processes to minimize catalyst losses. Established industrial processes utilize downstream extraction and distillation processes for catalyst recycling (e.g. LPO Process) or immobilization by introduction of an additional phase (e.g. Ruhrchemie/Rhône-Poulenc Process). These measures are characterized by certain drawbacks: i) Downstream extraction processes require additional extraction agents and lead to complicated and energy intensive process structures with many recycle streams, ii) distillation induces thermal stress that may cause ligand and catalyst degradation and iii) using aqueous phases for heterogenization is limited to short-chain olefins due to low solubility of long-chain olefins in water [Behr 1998; Jess and Wasserscheid 2013].

Besides other concepts for catalyst immobilization (e.g. supported ionic liquid phase (SILP) catalysts [Walter et al. 2015]) or catalyst retention by membranes [Behr 1998; Janssen et al. 2010], current research focuses e.g. on developing complex hydroformylation solvent mixtures with switchable phase behavior to overcome the mentioned drawbacks. Research activities in this direction are pooled, inter alia, in the collaborative research center SFB/TRR63 "Integrated Chemical Processes in Liquid Multiphase Systems (InPROMPT)", funded by the German Science Foundation. This project is dedicated, amongst others, to investigate and develop two switchable solvent systems for homogeneously catalyzed carbonylation reactions: Thermomorphic multicomponent solvent systems (TMS) [Behr and Fängewisch 2001; Dreimann et al. 2017b] and micellar solvent systems (MSS) [Platone and Tinucci 1991; van Vyve and Renken 1999; Haumann et al. 2002; Pogrzeba et al. 2016]. Both concepts aim for overcoming the short-chain olefin limitation of the Ruhrchemie/Rhône-Poulenc Process without using cumbersome downstream extraction or distillation processes for catalyst recycling.

The MSS are complex heterogeneous liquid multiphase systems consisting of an

aqueous catalyst phase and an organic reactant phase, exploiting surfactants to overcome the low solubility of olefins in the aqueous catalyst phase. Besides the aqueous catalyst phase and the organic reactant phase, a third micellar phase is formed in this way, depending on temperature and surfactant concentration. It was possible to convert long-chain olefins (1-dodecene) selectively to tridecanal using a water soluble Rh-SulfoXantphos catalyst in a MSS with minimal catalyst leaching in the organic phase (< 0.1 ppm rhodium, < 0.8 ppm phosphorus) [Nowothnick et al. 2013]. However, the MSS is a complex micro-structured system [Hohl et al. 2016] that suffers from inter-phase mass transfer limitations, which leads to low reaction rates. Nevertheless, it was possible to operate a mini-plant continuously over 150 h, using the MSS concept, which proved its applicability [Illner et al. 2016].

The TMS concept is related to the MSS since it also consists of a liquid polar catalyst phase and a liquid organic non-polar reactant phase but without an additional surfactant. Instead, the reactants itself act as phase mediator. At low temperatures, the system is heterogeneous with catalyst and reactants separated. At elevated reaction temperatures, the system becomes completely homogeneous due to temperature dependence of the miscibility gap caused by the phase mediator. Therefore, the hydroformylation can be conducted very efficiently and fast without mass transfer limitations and with elegant catalyst recycling after phase split caused by temperature reduction. It was also possible to demonstrate the applicability of the TMS system in continuous mini-plant operation for the hydroformylation of 1-dodecene using DMF and n-decane as polar and non-polar solvents, respectively [Dreimann et al. 2016]. However, the catalyst leaching was low but not satisfactory (leaching of ≈ 7 ppm rhodium and phosphorus) [Schäfer et al. 2012]. Additional organic solvent nanofiltration allowed to reduce catalyst leaching below 1 ppm under continuous mini-plant operation [Dreimann et al. 2017a].

1.2.4 Renewable substrates

Olefins are the most important hydroformylation substrate substance class to be converted to valuable aldehydes, as already discussed above. However, everyone ought to be aware that olefins are produced from mineral oil⁴, which is evidently a finite resource. Hence, steadily increasing world population and thereto relating energy demand and oil consumption will change the availability and prices of fossil raw materials in the future. This development will affect the economics of hydroformylation and industrial chemicals production in general. It is therefore attractive from an industrial perspective to find renewable and sustainable substrates

⁴ So is synthesis gas. However, biomass gasification could be used alternatively for sustainable generation of synthesis gas [Saxena et al. 2008].

for hydroformylation processes utilizing established technology.

One possibility is the direct utilization of unsaturated plant oils [Kandanarachchi et al. 2002] or their derivatives, such as fatty acid methyl esters [Frankel 1973; Muilwijk et al. 1997; Behr et al. 2005, 2008; Behr and Vorholt 2012]. Unsaturated fatty acids or their methyl esters are attractive because they are i) usually long-chain molecules, ii) already functionalized with a carbonyl group, iii) renewable and iv) available from trans-esterification processes (biodiesel production) [Vanbésien et al. 2016].

One important fatty acid is the C₁₈ unsaturated oleic acid, which makes up $\approx 80\%$ of the fatty acids in high oleic (HO) sunflower and high oleic/low linolenic (HOLL) rapeseed oil [Dubois et al. 2008], or rather its trans-esterification product: methyl oleate (OME). One possibility of utilizing OME is metathesis with ethylene to produce 1-decene, which can be hydroformylated to undecanal directly using conventional technology, and methyl 9-decenoate, which can be used in follow up chemistry to produce polyesters, nylon-10 or epoxy resins [Behr et al. 2008]. Even more attractive is the direct hydroformylation of OME to exploit its long carbon chain for the production of long-chain bifunctional oxo-esters, which can be converted subsequently by hydrogenation to hydroxy-esters and finally by polycondensation to renewable polyesters (see Figure 1.4) [Muilwijk et al. 1997; Behr and Vorholt 2012].

Another renewable substrate of interest is soy bean oil or its derivatives. Full conversion of soy bean oil biodiesel (mono- and polyunsaturated methyl esters) to the corresponding branched oxo-esters was demonstrated in [Ramalho et al. 2014] using a Rh-TPP catalyst in an ionic liquid.

Another example on using renewable feedstocks is the hydroformylation of methyl 10-undecenoate with terminal double bond, which is produced from castor oil. This reaction was demonstrated successfully with almost complete conversion and high selectivity to the linear oxo-ester using a Rh-TPPTS catalyst in aqueous phase supported by surfactants to increase the solubility of the methyl ester in water [Fell et al. 1995].

All these studies proved the feasibility of renewables conversion by established hydroformylation technology, which paved the way for industrial large scale application. Two processes, operated by Dow Chemical and BASF, are currently utilizing hydroformylation of plant oil derivatives for the production of soy bean oil based polyols for soft polyurethane foams ("RENUVA", Dow) and castor oil based polyether polyols for rigid foams and mattresses ("Lupranol Balance 35", BASF) [Vanbésien et al. 2016].

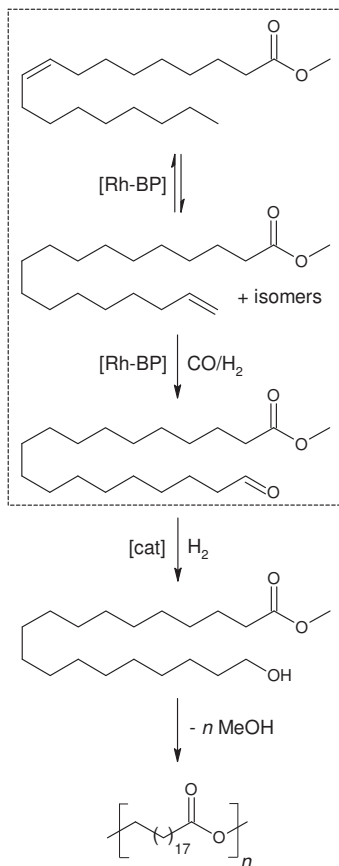


Figure 1.4: Value chain of polyester production from plant oil derived methyl oleate by Rh-BiPhePhos catalyzed tandem isomerization-hydroformylation (highlighted in dashed box) to oxo-esters followed by hydrogenation to hydroxy-esters and subsequent polycondensation to polyesters.

1.3 Thesis goals

The aforementioned synthesis of renewable polyesters from OME requires initially a tandem isomerization-hydroformylation step (see dashed box in Figure 1.4). This step should be conducted using a double bond isomerization-active hydroformylation catalyst, like Rh-BiPhePhos. However, the reported yield of linear oxo-ester using this catalyst was low ($\approx 20\%$), even after 17 h reaction time ($TOF \approx 10\text{ h}^{-1}$) under typical

hydroformylation conditions⁵ [Behr et al. 2005]. Moreover, significant hydrogenation to undesired methyl stearate ($\approx 25\%$ yield) occurred, which should be prevented. Obviously, it is necessary to adjust reactor design and reaction conditions to achieve high yields of desired linear oxo-esters, if the catalyst system is not a degree of freedom. A sound and rigorous reactor design and reaction conditions optimization, however, requires detailed kinetic models, preferably based on reaction mechanisms. Unfortunately, such kinetic models for tandem isomerization-hydroformylation systems are not available in the literature so far, especially not for unsaturated esters. It is thus intended by the already mentioned collaborative research center SFB/TRR63 to contribute significantly to this field of research as well.

The development of a desired mechanistic kinetic model for the hydroformylation of OME requires to understand the following issues: i) Thermodynamics, reaction mechanism and kinetics of the double bond isomerization and its interplay with hydroformylation and ii) interactions between the ester group and the Rh-catalyst. However, OME is not a well suited substrate for clarification of these issues because it contains both, an internal double bond and an ester group. Consequently, correct assignment of observations to causes is difficult. Hence, it is intended with this thesis as part of the SFB/TRR63 to study the mentioned challenges separately by using relevant model compounds (1-decene as representative long-chain olefin and methyl 10-undecenoate (UME) as interesting renewable oleo-ester derived from castor oil, see Figure 1.5).

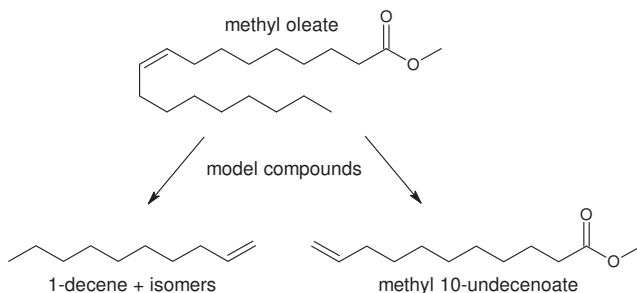


Figure 1.5: Model compounds for the separate study of tandem isomerization-hydroformylation (left: 1-decene + double bond isomer mixtures) and substrate effects caused by interactions between the catalyst and the ester group (right: methyl 10-undecenoate).

These model compounds were chosen because 1-decene and its double bond isomers can be resolved completely using gas chromatography, which allows to investigate the thermodynamics and kinetics of double bond isomerization as well as the

⁵ 115 °C, 20 bar synthesis gas, $c_{\text{sub}}^0 = 0.6 \text{ mol l}^{-1}$, Rh:sub (molar) = 1:320 and Rh:lig (molar) = 1:3

hydroformylation reaction. Comparison with the structurally analogous UME will reveal differences and similarities in reactivity of both substrates, which can be traced to interactions between the ester group and the catalyst.

As main outcome of the thesis, mechanistic kinetic models will be developed for both model substrates using a Rh-BiPhePhos catalyst. These models will cover the hydroformylation case as well as all relevant borderline cases like double bond isomerization, hydrogenation and tandem isomerization-hydroformylation. Subsequently, conclusions regarding improved reaction conditions for the tandem isomerization-hydroformylation of OME will be drawn. The following enumeration summarizes the goals and proceedings of this thesis.

1. Mechanistic kinetic modeling of the Rh-BiPhePhos catalyzed double bond isomerization, hydrogenation, hydroformylation and tandem isomerization-hydroformylation of 1-decene and internal n-decenes:
 - a) Calculation of the thermodynamic double bond isomerization reaction equilibrium and related equilibrium constants
 - b) Detection of relevant catalyst species and rate determining steps using *operando* FTIR spectroscopy to reduce a general reaction mechanism
 - c) Development of a mechanistic kinetic model for the (tandem isomerization-) hydroformylation including double bond isomerization and hydrogenation
 - d) Regression of the developed kinetic model to isomerization, hydrogenation and (tandem isomerization-) hydroformylation (semi-) batch experiments
 - e) Development of optimal reaction control strategies for the (tandem isomerization-) hydroformylation of n-decenes
2. Mechanistic kinetic modeling of the Rh-BiPhePhos catalyzed double bond isomerization, hydrogenation and hydroformylation of UME:
 - a) Comparison of 1-decene key experiments to UME data to reveal interactions between the ester group and the Rh-BiPhePhos catalyst
 - b) Detection of relevant catalyst complexes, rate determining steps using *operando* FTIR spectroscopy
 - c) Enhancement of the reaction mechanism and adjustment of the developed kinetic model accordingly with subsequent regression to (semi-) batch experiments
 - d) Development of optimal reaction control strategies for the (tandem isomerization-) hydroformylation of UME
3. Development of improved reaction conditions for the tandem isomerization-hydroformylation of OME and their validation by preliminary experiments

The thesis is organized as described in the following. First, the chapter "Theory and modeling" summarizes all calculation methods and modeling approaches used in this thesis. These include thermodynamic calculations, reactor and mass transfer modeling and the derivation of mechanistic kinetic rate equations. Since rate equations based on reaction mechanisms usually contain a high number of unknown kinetic parameters, it is crucial to determine the identifiability of these parameters, depending on the experimental design, if subsequent parameter estimation is of interest. Hence, a method based on local parameter sensitivities, local parameter subset selection, was developed for dynamic batch-reaction systems and will be presented in this chapter. This method will be illustrated by application to an example batch-reaction with a typical and relevant structure for homogeneously catalyzed reactions but is generally applicable to other dynamic systems. The next two chapters "Hydroformylation of 1-decene" and "Hydroformylation of methyl 10-undecenoate" contain results with respect to the first and second point of the list above. An outlook will be given in terms of application of the findings of this thesis to the tandem isomerization-hydroformylation of OME to demonstrate the remaining optimization potential of this reaction.

2 Theory and modeling

A significant part of the goals of this thesis is not achievable without mathematical methods, modeling and parameter estimation. Therefore, this chapter summarizes all models, modeling approaches and mathematical tools that were used or developed in this thesis. The first part of this chapter covers all thermodynamic models and calculation approaches that were used to understand the isomerization equilibrium of n-decenes. The second part of this chapter explains how mechanistic kinetic rate equations were derived from reaction mechanisms and how the necessary multiphase (semi-) batch reactor model was set up. The third and last part of this chapter introduces the parameter subset selection method, which was extended in this thesis to a local analysis for dynamic parameter estimation problems to determine parameter identifiability depending on the experimental design.

It should be noted that the author of this thesis published significant parts of the following chapter as first author in [Jörke et al. 2015a,b, 2016, 2017a]. Further details and results can be found in the cited articles.

2.1 Thermodynamics

The double bond isomerization plays a crucial role in hydroformylation systems, as already discussed in chapter 1. Since internal n-olefins are molecules with similar structure and thus Gibbs energy, the isomerization reaction is equilibrium limited. It is of high interest to understand the double bond isomerization equilibrium in order to understand the isomerization side reaction and the tandem isomerization-hydroformylation reaction.

This section is dedicated to an elegant method for the calculation of chemical reaction equilibria without assuming a specific stoichiometry. This method is based on Gibbs energy minimization [White et al. 1958] and known as non-stoichiometric equilibrium formulation. From the calculated equilibrium composition, equilibrium constants can be derived and used in further kinetic modeling to reduce the amount of unknown parameters. A major advantage of the method is that no specific stoichiometry has to be provided, which is beneficial for systems with a high number of species or unknown reaction networks. Instead, only thermodynamic state functions of

formation of the considered species at equilibrium are required. The method will be derived and explained in the first part of this section.

Unfortunately, the availability of thermodynamic data for long-chain n-olefin isomers is limited in the literature. One possibility to obtain missing state functions would be experimental measurements, which require availability of all n-olefin isomers as pure samples in substantial amounts. If the required samples cannot be purchased or synthesized, predictive methods can be used to calculate missing thermodynamic state functions. In this thesis, Benson's group contribution method (BGCM) [Benson et al. 1969] was chosen for this task, which will be explained in detail in the second part of this section. Although more modern and sophisticated methods for the calculation of thermodynamic state functions are available (e.g. quantum chemical calculations), Benson's method was preferred because it was closer to experimental data (see appendix F for a detailed discussion). Other, more modern incremental methods, such as the methods of Joback or Constantinou and Gani [Pohling et al. 2000], are not well suited for internal n-olefins because they cannot distinguish between trans and cis isomers. A detailed discussion of these methods is beyond the scope of this thesis and can be found elsewhere [Pohling et al. 2000].

2.1.1 Non-stoichiometric Gibbs energy minimization

The stoichiometric formulation and numerical solution of complex reaction equilibrium networks is tedious, if the number of equilibrium reactions and components is large. Also, all significant reactions that contribute to the network have to be known. In the case of n-decene isomerization, 18 possible equilibrium reactions for nine n-decene isomers, under the assumption that next neighbor isomers are at equilibrium with each other, can be considered (see figure Figure 3.1). According to a closed thermodynamic cycle, $N_s - 1$ equilibria have to be solved for N_s considered species at equilibrium containing N_{el} different chemical elements (e.g. n-decene: $N_{el} = 2, C$ and H). Hence, the simultaneous solution of eight non-linear equations with eight unknown extents of reaction is necessary to calculate the n-decene isomerization reaction equilibrium using a stoichiometric formulation. However, the stoichiometry of the reaction network has to be known, which may not always be the case.

Alternatively, calculation of reaction equilibria can be performed by minimizing the Gibbs energy G of the considered system (2.1) subject to atom balances for chemical elements (2.2) under variation of the amount of substances at equilibrium $\bar{n} \in \mathbb{R}^{N_s \times 1}$ [White et al. 1958]. This approach requires provision of thermodynamic state functions in terms of molar standard potentials $\Delta \bar{g} \in \mathbb{R}^{N_s \times 1}$, the total amount of substance of all chemical elements in the system $\bar{b} \in \mathbb{N}_0^{N_{el} \times 1}$ and the element-species-matrix $\bar{\beta} \in \mathbb{N}_0^{N_s \times N_{el}}$. This method reduces computational efforts drastically because only

$N_{\text{el}} + 1$ equations have to be solved for species containing N_{el} different chemical elements. The benefit of using this method becomes obvious, if the considered system contains a high number of species consisting of a low number of chemical elements, which is usually the case in organic chemistry.

$$G_{\text{eq}} = \min_{\bar{n}} G = \Delta_f \bar{g}^T \bar{n} \quad (2.1)$$

s.t.

$$\bar{0} = \bar{b} - \bar{\beta}^T \bar{n} \quad (2.2)$$

The optimization problem (2.1)-(2.2) can be transformed into a non-linear algebraic equation system (2.3)-(2.4) (see appendix E), which has to be solved numerically. The degrees of freedom are Lagrange multipliers $\bar{\lambda} \in \mathbb{R}^{N_{\text{el}} \times 1}$, originating from the transformation of (2.1)-(2.2) into (2.3)-(2.4), and the total amount of substance n_{tot} at equilibrium.

$$\bar{0} = \frac{\bar{b}}{n_{\text{tot}}} - \bar{\beta} \bar{x} \quad (2.3)$$

$$0 = \|\bar{x}\|_1 - 1 \quad (2.4)$$

with

$$\bar{x} = \exp\left(\frac{1}{RT} \left(\bar{\beta} \bar{\lambda} - \Delta_f \bar{g}^\circ(T)\right) - \bar{1}\right)$$

The necessary standard molar potentials of formation $\Delta_f \bar{g}^\circ(T)$ can be calculated from enthalpies and entropies of formation of the considered compounds (see next section). Solving (2.3)-(2.4) is possible by e.g. using a Levenberg-Marquardt-algorithm implemented as "fsolve" in Matlab. However, the numerical solution requires initial values for the degrees of freedom $\bar{\lambda}$ and n_{tot} .

Finding "good" initial values for Lagrange multipliers $\bar{\lambda}$ is not intuitive since they lack physical interpretation but is crucial for the numerical solver to converge. Thus, a strategy for calculation of "good" initial values for $\bar{\lambda}$ was developed and will be explained in the following paragraphs.

Starting point for the calculation of "good" initial values for $\bar{\lambda}$ is the necessary first order optimality condition (E.8) for the solution of the optimization problem (2.1).

This equation is rewritten in (2.5).

$$\begin{pmatrix} \beta_{1,1} & \cdots & \beta_{1,N_{\text{el}}} \\ \vdots & \ddots & \vdots \\ \beta_{N_s,1} & \cdots & \beta_{N_s,N_{\text{el}}} \end{pmatrix} \cdot \begin{pmatrix} \lambda_1 \\ \vdots \\ \lambda_{N_{\text{el}}} \end{pmatrix} = \begin{pmatrix} \Delta_f g_1^\circ(T) + RT(\ln(x_1) + 1) \\ \vdots \\ \Delta_f g_{N_s}^\circ(T) + RT(\ln(x_{N_s}) + 1) \end{pmatrix} \quad (2.5)$$

Obviously, the rank of $\bar{\bar{\beta}} (= \rho)$ represents the number of linearly independent Lagrange multipliers.. If $\rho = N_{\text{el}}$, an explicit expression for initial Lagrange multipliers $\bar{\lambda}^0$ (2.6) follows from rearranging (2.5) using the Moore-Penrose pseudo-inverse of the usually non-square element-species-matrix $\bar{\bar{\beta}}^+$. The initial values can be calculated by setting the unknown molar fractions \bar{x} to meaningful positive values < 1 (e.g. $x_i = 1/N_s$).

$$\begin{pmatrix} \lambda_1^0 \\ \vdots \\ \lambda_{N_{\text{el}}}^0 \end{pmatrix} = \begin{pmatrix} \beta_{1,1} & \cdots & \beta_{1,N_{\text{el}}} \\ \vdots & \ddots & \vdots \\ \beta_{N_s,1} & \cdots & \beta_{N_s,N_{\text{el}}} \end{pmatrix}^+ \cdot \begin{pmatrix} \Delta_f g_1^\circ(T) + RT(\ln(x_1) + 1) \\ \vdots \\ \Delta_f g_{N_s}^\circ(T) + RT(\ln(x_{N_s}) + 1) \end{pmatrix} \quad (2.6)$$

The resulting Lagrange multipliers from assuming $x_i = 1/N_s$ represent a "wrong" equilibrium composition but fulfill the atom balances and are thus considered "good" initial values for the numerical solution of (2.3)-(2.4).

If $N_{\text{el}} > \rho$, $N_{\text{el}} - \rho$ Lagrange multipliers are linearly dependent and (2.5) is

$$\begin{pmatrix} \beta_{1,1} & \cdots & \beta_{1,\rho} & \cdots & \beta_{1,N_{\text{el}}} \\ \vdots & \ddots & \vdots & \ddots & \vdots \\ \beta_{\rho,1} & \cdots & \beta_{\rho,\rho} & \cdots & \beta_{\rho,N_{\text{el}}} \\ \vdots & \ddots & \vdots & \ddots & \vdots \\ \beta_{N_s,1} & \cdots & \beta_{N_s,\rho} & \cdots & \beta_{N_s,N_{\text{el}}} \end{pmatrix} \cdot \begin{pmatrix} \lambda_1 \\ \vdots \\ \lambda_\rho \\ \vdots \\ \lambda_{N_{\text{el}}} \end{pmatrix} = \begin{pmatrix} \Delta_f g_1^\circ(T) + RT(\ln(x_1) + 1) \\ \vdots \\ \Delta_f g_{N_s}^\circ(T) + RT(\ln(x_{N_s}) + 1) \end{pmatrix}. \quad (2.7)$$

Generation of initial values for the remaining linearly independent Lagrange multipliers $\bar{\lambda}_{1:\rho}^0$ is possible by reformulation of (2.7), using an element-species-submatrix $\bar{\bar{\beta}}_{1:N_s,1:\rho}$ (2.8) and non-zero values for the remaining linearly dependent $\bar{\lambda}_{\rho+1:N_{\text{el}}}^{\text{fix}}$.

$$\bar{\bar{\beta}}_{1:N_s,1:\rho} \cdot \begin{pmatrix} \lambda_1^0 \\ \vdots \\ \lambda_\rho^0 \end{pmatrix} + \bar{\bar{\beta}}_{1:N_s,\rho+1:N_{\text{el}}} \cdot \begin{pmatrix} \lambda_{\rho+1}^{\text{fix}} \\ \vdots \\ \lambda_{N_{\text{el}}}^{\text{fix}} \end{pmatrix} = \begin{pmatrix} \Delta_f g_1^\circ(T) + RT(\ln(x_1) + 1) \\ \vdots \\ \Delta_f g_{N_s}^\circ(T) + RT(\ln(x_{N_s}) + 1) \end{pmatrix} \quad (2.8)$$

From rearranging (2.8) follows an explicit expression for the remaining linearly independent Lagrange multipliers $\bar{\lambda}_{1:\rho}^0$ (2.9).

$$\begin{pmatrix} \lambda_1^0 \\ \vdots \\ \lambda_\rho^0 \end{pmatrix} = \bar{\bar{\beta}}_{1:N_s,1:\rho}^+ \cdot \left(\begin{pmatrix} \Delta_f g_1^\circ(T) + RT(\ln(x_1) + 1) \\ \vdots \\ \Delta_f g_{N_s}^\circ(T) + RT(\ln(x_{N_s}) + 1) \end{pmatrix} - \bar{\bar{\beta}}_{1:N_s,\rho+1:N_{\text{el}}} \cdot \begin{pmatrix} \lambda_{\rho+1}^{\text{fix}} \\ \vdots \\ \lambda_{N_{\text{el}}}^{\text{fix}} \end{pmatrix} \right) \quad (2.9)$$

2.1.2 Benson's group contribution method

Benson's group contribution method is an incremental method that is able to calculate thermodynamic state functions of formation (enthalpy, entropy, heat capacity) from

isomers of one molecule. The internal symmetry numbers \overline{N}_{is} are obtained by multiplying the amounts of identical arrangements that occur while rotating the end groups of the molecule by 360 degrees. The external symmetry numbers \overline{N}_{es} represent the amount of appearing identical geometric projections while rotating the whole molecule around a symmetry axis by 360 degrees.

Calculation of temperature dependent thermodynamic state functions of formation for all n-decene isomers is possible using (2.10)-(2.19) [Benson et al. 1969; Pohling et al. 2000]. All necessary increment values associated with Benson groups that appear in all n-decenes are summarized in Table 3.1, see section 3.1.1. The temperature dependence of thermodynamic state functions was expressed by linearly interpolated heat capacities and Kirchhoff's law [Pohling et al. 2000].

The calculated thermodynamic state functions will be presented in section 3.1.1 and serve for the calculation equilibrium compositions using (2.3)-(2.4) and equilibrium constants to reduce the amount of unknown model parameters.

$$\Delta_f \overline{g}^\circ(T) = \Delta_f \overline{h}^\circ(T) - T \Delta_f \overline{s}^\circ(T) \quad (2.10)$$

with

$$\Delta_f \overline{h}^\circ(T) = \Delta_f \overline{h}^\circ + \int_{T^\circ}^T \Delta_f \overline{c}_p(T) dT \quad (2.11)$$

$$\overline{s}^\circ(T) = \overline{s}^\circ + \int_{T^\circ}^T \frac{\overline{c}_p(T)}{T} dT \quad (2.12)$$

$$\Delta_f \overline{s}^\circ(T) = \Delta_f \overline{s}^\circ + \int_{T^\circ}^T \frac{\Delta_f \overline{c}_p(T)}{T} dT \quad (2.13)$$

$$\Delta_f \overline{h}^\circ = \overline{\phi}^T \overline{h}_m^\circ \quad (2.14)$$

$$\Delta_f \overline{s}^\circ = \overline{s}^\circ - \overline{\beta} \overline{s}_e^\circ \quad (2.15)$$

$$\overline{s}^\circ = \overline{\phi}^T \overline{s}_m^\circ + \overline{s}_{sym}^\circ \quad (2.16)$$

$$\overline{s}_{sym}^\circ = R \cdot [\ln(\overline{N}_{oi}) - \ln(\overline{N}_{is} \circ \overline{N}_{es})] \quad (2.17)$$

$$\Delta_f \overline{c}_p(T) = \overline{c}_p(T) - \overline{\beta} \overline{c}_{pe}(T) \quad (2.18)$$

$$\overline{c}_p(T) = \overline{\phi}^T \overline{c}_{pm}(T) \quad (2.19)$$

2.2 Kinetics

The following section focuses on the derivation of kinetic rate equations from reaction mechanisms based on a general method first described in the 1930's [Christiansen 1953]. The method is explained in detail in the second part of this section and will be applied to an example reaction $A \rightleftharpoons B$ with typical structure for homogeneously catalyzed reactions.

The unknown kinetic parameters of the derived kinetic models for the real hydroformylation systems in this thesis were estimated using (semi-) batch experimental data (see section 3.4 and 4.4). Thus, a (semi-) batch reactor model is required to map experimentally determined and time-resolved concentration profiles to reaction rates. Since the hydroformylation is a gas-liquid reaction, the mass transfer of gaseous reactants from the gas phase to the liquid phase has to be included in the model and characterized as well. This multiphase reactor model will be derived in the first part of this section.

2.2.1 Reactor model and mass transfer

The general mass balance of a constant volume reaction (2.20) can be simplified since the kinetic experiments were carried out in ideally mixed (semi-) batch reactors without inlet or outlet flows (see Figure A.1). Thus, the liquid reactant phase is described sufficiently by (2.21). The reactor was assumed to be isothermal because a significant temperature increase due to the exothermicity of the reactions conducted was not detectable during experiments. The liquid phase mass balances (2.21) contain only the stoichiometric coefficient matrix of the reaction network \bar{v} and the vector of reaction rates \bar{r} as molar sources and sinks on the right hand side. The derivation of these reaction rate equations from catalytic reaction mechanisms is explained later on in section 2.2.2.

$$\frac{\partial c_i}{\partial t} = -\text{div} J_i = 0 + \sum_j v_{ij} r_j \quad (2.20)$$

$$\frac{dc_i}{dt} = \sum_j v_{ij} r_j \quad i = \text{liquid reactants} \quad (2.21)$$

The hydroformylation is a typical gas-liquid reaction. Therefore, the mass transfer of the gaseous reactants into the liquid phase has to be considered in the reactor model. A linear driving force approach was used to describe the transport of CO and H₂ through the phase boundary with film thickness δ (see Figure 2.2). The phase boundary was assumed to be free of mass accumulation. In terms of mass transfer resistance, it is reasonable to assume a dominating resistance in the liquid phase

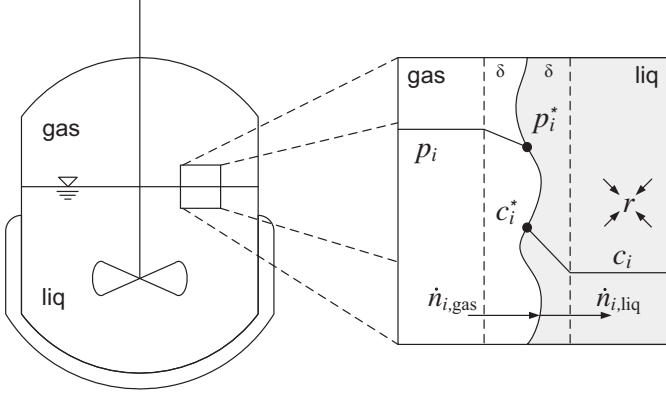


Figure 2.2: General scheme of the linear driving force approach for mass transfer of gaseous reactants from the gas phase into the liquid phase.

compared to the gas phase for sparingly soluble gases like H_2 and CO [Baerns 2012]. Combining these assumptions with a linear driving force approach results in the following expression (2.22) for the molar flux \dot{n}_i of CO and H_2 from the gas into the liquid phase (see Figure 2.2).

$$-\dot{n}_{i,\text{gas}} = \dot{n}_{i,\text{liq}} = \dot{n}_i = k_1 a (c_i^* - c_i) V_{\text{liq}} = k_{\text{eff}} (c_i^* - c_i) V_{\text{liq}} \quad (2.22)$$

The extent of mass transfer resistance is represented by the dominating liquid phase mass transfer coefficient k_1 . Since the interfacial area a cannot be determined easily, the product $k_1 a$ was considered an effective mass transfer coefficient k_{eff} . This effective mass transfer coefficient was determined in preliminary gas solubility experiments (see appendix B).

The mass balance of gaseous reactants dissolved in the liquid phase (2.23) follows from including their molar flux from the gas phase (2.22) into the batch mass balance (2.21).

$$\frac{dc_i}{dt} = \frac{\dot{n}_i}{V_{\text{liq}}} + \sum_j v_{ij} r_j = k_{\text{eff}} (c_i^* - c_i) + \sum_j v_{ij} r_j \quad i = CO, H_2 \quad (2.23)$$

Henry's law (2.24) was used in this thesis to describe the equilibrium between partial pressure p_i^* and concentration c_i^* of a dissolved gaseous reactant directly at the gas-liquid phase interface. Although there are highly sophisticated gas solubility models based on equations of state (e.g. PC-SAFT [Lemberg et al. 2017]), the usage of Henry's law is justified because the relation between gas pressure and liquid concentration in the pressure range of interest is almost perfectly linear in the used hydroformylation reactant-solvent system (see appendix A) [Vogelpohl et al. 2013,

2014]. The temperature dependence of the Henry constant was included using a reparameterized reference-temperature centered Arrhenius approach [Schwaab and Pinto 2007; Schwaab et al. 2008].

$$p_i^* = H_i(T) c_i^* = H_{i,\text{ref}} \exp\left[B_i \left(\frac{T_{\text{ref}}}{T} - 1\right)\right] c_i^* \quad (2.24)$$

From using Henry's law and the assumption of a negligible gas phase mass transfer resistance follows (2.25). This equation inserted into (2.23) results in the final mass balance for dissolved CO and H₂ in the liquid phase (2.26).

$$p_i^* = H_i c_i^* \cong p_i \quad i = \text{CO, H}_2 \quad (2.25)$$

$$\frac{dc_i}{dt} = k_{\text{eff}} \left(\frac{p_i}{H_i} - c_i \right) + \sum_j v_{ij} r_j \quad i = \text{CO, H}_2 \quad (2.26)$$

The only sink in the gas phase is the molar flux of the gaseous reactants into the liquid phase \dot{n} . The gas phase mass balances in terms of partial pressures p of the gaseous reactants CO and H₂ (2.27) follows in this case from using (2.22) and (2.25).

$$\begin{aligned} \frac{dp_i}{dt} &= -\frac{\dot{n}_i RT}{V_{\text{gas}}} = -k_{\text{eff}} \left(\frac{p_i V_{\text{liq}}}{H_i} - c_i V_{\text{liq}} \right) \frac{RT}{V_{\text{gas}}} \\ &= -k_{\text{eff}} \left(\frac{p_i}{H_i} - c_i \right) \frac{V_{\text{liq}}}{V_{\text{gas}}} RT \quad i = \text{CO, H}_2 \end{aligned} \quad (2.27)$$

It should be noted that gas and liquid volumes are constant because the molar density in the liquid phase remains constant.

The influence of mass transfer limitations in fluid-fluid reactions can be characterized by the Hatta number Ha [Baerns 2012]. This dimensionless number relates the reaction rate to the interfacial mass transfer rate. It is analogous to the Thiele-modulus known in heterogeneous catalysis. Four typical Hatta regimes can be distinguished:

I: Slow reaction ($\text{Ha} < 0.3$): Bulk reaction

II: Transition regime ($0.3 \leq \text{Ha} \leq 3$): Bulk reaction

III: Fast reaction ($\text{Ha} > 3$): Film reaction

IV: Instantaneous reaction ($\text{Ha} \gg 3$): Reaction in the phase boundary

The mass transfer situation of the studied hydroformylation system is characterized by a maximum Hatta number of ≈ 2 in the worst case of low synthesis gas pressure or less (for more details, see appendix C). This corresponds to the transition regime where mass transfer and reaction rate are in a similar order of magnitude with the reaction taking place in the bulk. This justifies to use the linear driving force approach

(see Figure 2.2) and using the value for the effective mass transfer coefficient k_{eff} determined from preliminary gas solubility experiments without reaction [Baerns 2012].

2.2.2 Kinetic modeling

The mechanistic kinetic modeling followed Christiansen's method in this thesis [Christiansen 1953]. This method applies Bodenstein's principle [Levenspiel 1999] to a steady state catalytic cycle or sequence with M steps. It is assumed that the concentration of catalytic intermediates remains at trace level and that all steps involve maximum one catalytic intermediate as reactant to make use of linear algebra. Details about the cumbersome derivation of the method's equations can be found in the literature [Christiansen 1953; Helfferich 2004; Murzin and Salmi 2005].

The central quantities of this method are pseudo first-order rate coefficients ω_{ij} for a reaction of a catalytic intermediate i to intermediate j . These pseudo first-order rate coefficients are the product of a pseudo rate constant and the concentrations of reactants that enter the catalytic cycle or sequence. If no reactant is entering in a step, the corresponding first-order rate coefficient is equal to the pseudo rate constant. The pseudo rate constant is the product of the rate constant of an elementary step and the constant concentration of the catalyst intermediate that drives the elementary reaction (Bodenstein approximation). Per convention, the starting intermediate of the catalytic cycle or sequence is denoted with index = 1. All following intermediates are numbered continuously.

The general expression of the reaction rate r for a given catalytic reaction cycle (2.28) is given [Christiansen 1953; Helfferich 2004; Murzin and Salmi 2005]:

$$r = \frac{\left(\prod_{i=1}^{M-1} \omega_{i(i+1)} \omega_{M1} - \prod_{i=1}^{M-1} \omega_{(i+1)i} \omega_{1M} \right) c_{\text{cat,cyc}}}{\sum_i \sum_j C_{ij} + \sum_j C_{mj} K_{\text{NCl}} c_{\text{Inh}}} \quad (2.28)$$

with

$$\bar{C} = \begin{pmatrix} v_1 \omega_{23} \omega_{34} \dots \omega_{M1} & \omega_{21} v_2 \omega_{34} \dots \omega_{M1} & \dots & \omega_{21} \omega_{32} \omega_{43} \dots v_M \\ \omega_{12} v_2 \omega_{34} \dots \omega_{M1} & \omega_{12} \omega_{32} v_3 \dots \omega_{M1} & \dots & v_1 \omega_{32} \omega_{43} \dots \omega_{1M} \\ \vdots & \vdots & \ddots & \vdots \\ \omega_{12} \omega_{23} \omega_{34} \dots v_M & v_1 \omega_{23} \omega_{34} \dots \omega_{1M} & \dots & \omega_{21} \omega_{32} \dots v_{M-1} \omega_{1M} \end{pmatrix}. \quad (2.29)$$

In this equation, $c_{\text{cat,cyc}}$ represents the catalyst concentration available for the catalytic cycle. It can be less than the total amount of catalyst present in the system due to competitive inhibition reactions and catalyst pre-equilibria. How this inhibition is taken into account will be explained later with an example reaction (see Figure 2.3).

The square Christiansen Matrix $\overline{\overline{C}}$ in (2.28) contains permutations of the pseudo-first order rate coefficients ω_{ij} of all forward and backward elementary reactions and the stoichiometric coefficient ν_i of each i th step (always = 1 in all cases relevant for this thesis). Generally, $\overline{\overline{C}}$ for a catalytic cycle with M intermediates and steps is given by (2.29). The sum of j th row of the Christiansen Matrix $\overline{\overline{C}}$ can physically be interpreted as the concentration of the corresponding j th catalytic intermediate of a catalytic cycle [Helferich 2004]. Thus, rows can be neglected, if corresponding intermediates are present in negligible amounts (least abundant catalytic species = LACS). On the other hand, all but one row can be neglected, if it is known that the corresponding intermediate is the most abundant catalytic species (MACS). Preliminary spectroscopic investigations (e.g. FTIR, NMR,...) can be used to determine, if MACS or LACS are present, which directly leads to reasonable model reduction. Furthermore, entries in $\overline{\overline{C}}$ can be neglected, if one of the pseudo-first order rate coefficient is zero (step is irreversible) or extremely small compared to the other rate coefficients (rate determining step (RDS)).

The second term in the denominator of (2.28) represents inhibition by formation of stable intermediates outside the catalytic cycle (non-competitive inhibition, see Figure 2.3). The index m refers to the m th intermediate in the catalytic cycle that is at equilibrium with the stable intermediate.

To illustrate the method, it will be applied to a relevant example reaction (2.30), which represents a typical homogeneously catalyzed reversible reaction .



The mechanism of the reversible reaction is shown in Figure 2.3. It contains two typical inhibition reactions occurring in homogeneous catalysis, which form stable and inactive resting states (RS) or catalyst intermediates: A competitive inhibition ($X_1 + \text{Inh} \rightleftharpoons \text{RS}$) and a non-competitive inhibition reaction ($X_3 + \text{Inh} \rightleftharpoons X_{\text{inactive}}$)

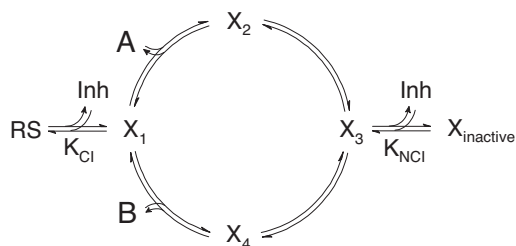


Figure 2.3: Reversible reaction mechanism of the synthetic example reaction $A \rightleftharpoons B$ with competitive (left) and non-competitive (right) inhibition reactions.

[Helffferich 2004]. Competitive inhibition is typical for ligand-deficient catalysis, e.g. the loss of a CO ligand prior to olefin coordination in hydroformylation [Kranenburg et al. 1995]. An example for the non-competitive inhibition is the formation of coordinatively saturated acyl-complexes during hydroformylation at high CO concentrations [Garland and Pino 1991].

A catalyst mass balance (3.11) and a mass action law formulation (2.32) of the pre-equilibrium between the resting state and the catalyst material in the cycle are used to describe the competitive inhibition.

$$c_{\text{cat,tot}} = c_{\text{RS}} + c_{\text{cat,cyc}} \quad (2.31)$$

$$K_{\text{CI}} = \frac{c_{\text{RS}}}{c_{\text{cat,cyc}}c_{\text{Inh}}} \quad (2.32)$$

From combining (3.11) and (2.32) follows an explicit expression for the available catalyst concentration $c_{\text{cat,cyc}}$ (2.33), required in (2.28).

$$c_{\text{cat,cyc}} = \frac{c_{\text{cat,tot}}}{(1 + K_{\text{CI}}c_{\text{Inh}})} \quad (2.33)$$

Furthermore, pseudo-first order rate coefficients ω_{ij} are required to be inserted into (2.28) and (2.29). This pseudo-first order rate coefficients for the example reaction are summarized in (2.34).

$$\begin{aligned} \omega_{12} &= k_{12}c_A & \omega_{21} &= k_{21} \\ \omega_{23} &= k_{23} & \omega_{32} &= k_{32} \\ \omega_{34} &= k_{34} & \omega_{43} &= k_{43} \\ \omega_{41} &= k_{41} & \omega_{14} &= k_{14}c_B. \end{aligned} \quad (2.34)$$

For the most general kinetic model that includes no assumptions regarding LACS, MACS, irreversibility or rate determining steps, the Christiansen Matrix of the example reaction (2.35) includes only non-zero terms. The terms in (2.35) are constants (first row) or depend on the concentrations of A or B. For improved clarity, the products in the Christiansen Matrix (2.35) are represented by Ω 's.

$$\bar{\bar{C}} = \begin{pmatrix} \Omega_{11} & \Omega_{12} & \Omega_{13} & \Omega_{14} \\ \Omega_{21}(c_A) & \Omega_{22}(c_A) & \Omega_{23}(c_A) & \Omega_{24}(c_B) \\ \Omega_{31}(c_A) & \Omega_{32}(c_A) & \Omega_{33}(c_B) & \Omega_{34}(c_B) \\ \Omega_{41}(c_A) & \Omega_{42}(c_B) & \Omega_{43}(c_B) & \Omega_{44}(c_B) \end{pmatrix} \quad (2.35)$$

with e.g.

$$\Omega_{11} = \omega_{23}\omega_{34}\omega_{41} = \text{const. (see eq. (2.29))}$$

The sum over all elements of the Christiansen Matrix can be simplified to (2.36) after lumping all constants to inhibition constants K .

$$\sum_i \sum_j C_{ij} = K_1 + K_2 c_A + K_3 c_B \quad (2.36)$$

The reaction rate r_{rxn} (2.37) follows from inserting (2.36) and (2.33) into (2.28).

$$r_{\text{rxn}} = \frac{k_{\text{rxn}}(T) (c_A - c_B / K_{\text{eq}}) c_{\text{cat,tot}}}{(1 + K_{\text{I}} c_A + K_{\text{II}} c_B + (K_{\text{III}} c_A + K_{\text{IV}} c_B) K_{\text{NCl}} c_{\text{Inh}}) (1 + K_{\text{Cl}} c_{\text{Inh}})} \quad (2.37)$$

The temperature dependence of the reaction rate is a result of the temperature dependence of all involved rate constants. However, considering all elementary step rate constants and their temperature dependence would make the final model complicated. Therefore, the temperature dependence of the reaction rate is expressed using a standard Arrhenius approach for the apparent rate constant $k_{\text{rxn}}(T)$. Re-parameterization of the Arrhenius approach (2.38) reduces correlations between apparent collision factor and activation energy [Schwaab and Pinto 2007; Schwaab et al. 2008]. Including the temperature dependence, the final reaction rate model contains eight unknown kinetic parameters and one equilibrium constant. Determination of parameter identifiability will be explained with the presented example reaction rate r_{rxn} in the next section.

$$k(T) = \exp\left(A + B \left(1 - \frac{T_{\text{ref}}}{T}\right)\right) \quad (2.38)$$

$$k_{\infty} = \exp(A + B) \quad (2.39)$$

$$E_A = B \cdot R T_{\text{ref}} \quad (2.40)$$

The kinetic modeling of real hydroformylation systems in this thesis followed the same methods presented above. Specific details about the derivation of mechanistic kinetic models for the individual hydroformylation (sub)networks (assumptions, rate determining steps,...) will be discussed in the corresponding sections.

2.3 Local parameter subset selection

Constitutive equations, such as reaction rate laws, contain usually parameters with unknown values (see equation (2.37)). Estimation of these parameters and model regression to experimental data is an important task in chemical engineering. It forms the basis for the usage of constitutive models in computer simulations for process design and optimization. Since these models may include a high number of unknown parameters, it is likely that statistically significant estimation of some of

these parameters is not possible with a given experimental design. Thus, ill-posed inverse problems arise with respect to parameter estimation. The solution of these problems, if not treated to improve the ill-posedness, is not unique and shows strong parameter correlations and physically non-interpretable parameter values [McLean and McAuley 2012].

To overcome this problem, methods based on parameter sensitivity analysis were developed [Reid 1976; Cobelli and DiStefano 1980; Caracotsios and Stewart 1985; McLean et al. 2012; Zhang et al. 2014]. These methods aim for the improvement of the experimental design or model reduction with the purpose of transforming the ill-posed problem into a well-posed problem with a unique solution. It is also intended to maximize the number of identifiable parameters.

One of these methods is known as parameter subset selection (SsS) [Burth et al. 1999; Fink et al. 2007]. This method utilizes the Fisher Information Matrix \overline{FIM} [Cobelli and DiStefano 1980] to divide the vector of unknown model parameters $\bar{\theta}$ into an identifiable sensitive and a non-sensitive subset. It should be noted that experimental designs often are chosen "arbitrarily" meaning that the experimentalist designs the experiments based on experience. In this case, parameter subset selection is suitable to check how much and which of the unknown parameters can be estimated with a given experimental design. If the result is not satisfactory, the experimental design has to be adjusted in order to meet the desired requirements. However, it is also possible to use parameter subset selection in an inverse, iterative or sequential manner. This strategy aims for designing the $(i + 1)$ th experiment via optimization of a scalar measure of the \overline{FIM} , containing the information from all previous i experiments, by adjusting the experimental design variables of the next experiment to achieve a maximum increase in information [Ford and Silvey 1980; Doví et al. 1993; Barz et al. 2013; Barz and Wozny 2014; López C. et al. 2015]. In this case, the final number of experiments is unknown in the beginning. It is, however, beyond the scope of this thesis to deepen the subject of rigorous experimental design and it was decided to use parameter subset selection to identify sensitive parameter subsets from given experience based experimental designs.

The global form of the SsS technique was applied successfully to several problems [Čapek and Seidel-Morgenstern 2001; Fink et al. 2007; Cintrón-Arias et al. 2009; Rao et al. 2009; Barz et al. 2013; López C. et al. 2013; Kiedorf et al. 2014] to determine which parameters are identifiable and belong to the sensitive parameter subset. It was not possible to study a possible time dependence of the sensitive parameter subset because of the global nature of the analysis. However, knowing this time dependence is crucial, if dynamic (semi-) batch experiments are used to generate data, as it is the case in this thesis, because the subset of sensitive parameters is then not only a function of the experimental design but also a function of time. Furthermore, it tells

the experimentalist at which time of the experiment a measurement is generating more information and thus guides sampling. Hence, the global form presented in the literature was extended to a local analysis in this thesis to study time dependent parameter subsets. The local analysis will be explained in the following sections and applied to the synthetic example reaction (2.30) below and to real hydroformylation (sub)networks in their corresponding sections.

2.3.1 Principle of local parameter subset selection

The main idea behind parameter subset selection is exploiting the fact that parameter estimation is an unconstrained non-linear optimization problem (2.41). The N_p parameter values $\bar{\theta} \in \mathbb{R}^{N_p \times 1}$ are calculated by minimizing a scalar sum of squares $\mathfrak{R}(\bar{\theta})$ that is calculated from residuals $\bar{\rho} \in \mathbb{R}^{(N_s \cdot N_t) \times 1}$, describing deviations between N_s model states and their measurements at N_t time points. Often in chemistry (and in this thesis), the measured states are reactant concentrations \bar{c} , which depend via reaction rates indirectly on each other, process variables (temperature T , partial pressures \bar{p}) and model parameters $\bar{\theta}$.

$$\text{Obj} = \min_{\bar{\theta}} \mathfrak{R}(\bar{\theta}) = \bar{\rho}^T \bar{\rho} \quad \text{with} \quad \bar{\rho} = \bar{c}_{\text{mod}}(\bar{c}_{\text{mod}}, T, \bar{p}, \bar{\theta}) - \bar{c}_{\text{exp}} \quad (2.41)$$

Standard Newton algorithms solve this type of problems iteratively with a quadratic approximation of the objective function $\tilde{\mathfrak{R}}$ (2.42).

$$\mathfrak{R}(\bar{\theta}) \approx \tilde{\mathfrak{R}}(\bar{\theta}_h + \Delta\bar{\theta}) = \mathfrak{R}(\bar{\theta}_h) + \nabla \mathfrak{R}(\bar{\theta}_h)^T \Delta\bar{\theta} + \frac{1}{2} \Delta\bar{\theta}^T \nabla^2 \mathfrak{R}(\bar{\theta}_h) \Delta\bar{\theta} \quad (2.42)$$

The minimum of the quadratic approximation at iteration h is given by (2.43). From the minimum follows the Newton step in the parameter space (2.44). From (2.44) can be seen that the Hessian $\nabla^2 \mathfrak{R}(\bar{\theta}_h) \in \mathbb{R}^{N_p \times N_p}$ has to be a regular matrix. Otherwise, the inverse does not exist and the Newton step in the parameter space is not unique since the numerical inverse of a non-regular matrix introduces huge errors. Thus, the rank of the Hessian can also be interpreted as the number of linearly independent and identifiable parameters.

$$\frac{d\tilde{\mathfrak{R}}}{d\Delta\bar{\theta}} = 0 = \nabla \mathfrak{R}(\bar{\theta}_h) + \nabla^2 \mathfrak{R}(\bar{\theta}_h) \Delta\bar{\theta} \quad (2.43)$$

$$\bar{\theta}_{h+1} = \bar{\theta}_h - \nabla^2 \mathfrak{R}(\bar{\theta}_h)^{-1} \nabla \mathfrak{R}(\bar{\theta}_h) \quad (2.44)$$

The Hessian is the second derivative of the objective function with respect to the degrees of freedom: The unknown model parameters (2.46). Since the residual should be small and hardly non-linear near the optimum, the second term in (2.46) is

negligible. The partial derivative of the residual vector with respect to the parameter vector in (2.46) is called Sensitivity Matrix $\bar{\bar{S}} \in \mathbb{R}^{N_s \times N_p}$ [Caracotsios and Stewart 1985]. Since the experimentally observed states do not depend on the model parameters, the Sensitivity Matrix is equal to the derivative of the model states with respect to the model parameters. The product of the Sensitivity Matrix with itself in (2.47) is known as Fischer Information Matrix $\bar{\bar{FIM}} \in \mathbb{R}^{N_p \times N_p}$ [McLean and McAuley 2012].

$$\nabla^2 \mathfrak{R} = 2\bar{\rho} \frac{\partial \bar{\rho}}{\partial \theta} \quad (2.45)$$

$$\nabla^2 \mathfrak{R} = 2 \frac{\partial \bar{\rho}}{\partial \theta} \frac{\partial \bar{\rho}}{\partial \theta} + \bar{\rho} \frac{\partial^2 \bar{\rho}}{\partial \theta^2} \approx 2 \frac{\partial \bar{\rho}}{\partial \theta} \frac{\partial \bar{\rho}}{\partial \theta} \quad (2.46)$$

$$= 2 \frac{\partial \bar{c}_{\text{mod}}}{\partial \theta} \frac{\partial \bar{c}_{\text{mod}}}{\partial \theta} = 2\bar{\bar{S}}^T \bar{\bar{S}} = \bar{\bar{FIM}} \in \mathbb{R}^{(N_p \times N_p) \times N_t} \quad (2.47)$$

It should be noted that the residual $\bar{\rho}$ is a function of time for dynamic (semi-) batch processes because the model states are a function of time and therefore $\bar{\bar{S}}$ as well as $\bar{\bar{FIM}}$ are time dependent matrices.

Taking the first derivative of the mass balances of the model states with respect to model parameters generates a differential equation for the dynamic Sensitivity Matrix (2.48).

$$\frac{\partial}{\partial \theta} \frac{d\bar{c}_{\text{mod}}}{dt} = \frac{d}{dt} \frac{\partial \bar{c}_{\text{mod}}}{\partial \theta} = \frac{d\bar{\bar{S}}}{dt} = \frac{\partial}{\partial \theta} \bar{f}(\bar{c}_{\text{mod}}, T, \bar{p}, \bar{\theta}) \quad (2.48)$$

Applying the chain rule to (2.48) generates the differential equation for the Sensitivity Matrix (2.49). This equation contains two Jacobi matrices, $\partial \bar{f} / \partial \bar{c}_{\text{mod}}$ and $\partial \bar{f} / \partial \bar{\theta}$, which are known because the right hand sides of the ODE system are known. They can be provided numerically or analytically. The enhanced ODE system, consisting of (2.26) and (2.49), is solved numerically to obtain the dynamic Sensitivity Matrix $\bar{\bar{S}}(t)$. Since the states at $t = 0$ do not depend on model parameters (adjusted by the experimental design), the initial condition for (2.49) is always $\bar{\bar{S}}(t = 0) = \bar{\bar{0}}$.

$$\frac{d\bar{\bar{S}}}{dt} = \frac{\partial \bar{f}}{\partial \bar{c}_{\text{mod}}} \bar{\bar{S}} + \frac{\partial \bar{f}}{\partial \bar{\theta}} \quad (2.49)$$

It is necessary to normalize the Sensitivity Matrix because the entries have otherwise various dimensions, which complicates their comparison. The normalized Sensitivity Matrix $\bar{\bar{S}}_n$ is calculated by multiplying the Sensitivity Matrix entries S_{ij} with the corresponding parameter j and dividing it by the corresponding state i (2.50). The matrix $\bar{\bar{S}}_n$

in (2.50) is the Identity Matrix with the dimension $N_p \times N_p$ (left) or $N_s \times N_s$ (right).

$$\bar{\bar{S}}_n = \left((\bar{\bar{S}} \cdot (\bar{\theta} \cdot \bar{I}))^T \cdot (\bar{c}_{\text{mod}} \cdot \bar{I})^{-1} \right)^T \quad (2.50)$$

The information from several experiments of a complex experimental design is included into the $\bar{\bar{FIM}}$ by "stacking" normalized Sensitivity Matrices of the single experiments of the design.

$$\bar{\bar{FIM}} = 2\bar{\bar{S}}_{n,\text{tot}}^T \cdot \bar{\bar{S}}_{n,\text{tot}} = 2 \begin{pmatrix} \bar{\bar{S}}_{n,1} \\ \vdots \\ \bar{\bar{S}}_{n,N_{\text{exp}}} \end{pmatrix}^T \cdot \begin{pmatrix} \bar{\bar{S}}_{n,1} \\ \vdots \\ \bar{\bar{S}}_{n,N_{\text{exp}}} \end{pmatrix} \quad (2.51)$$

Once the $\bar{\bar{FIM}}$ is calculated, it is treated with singular value decomposition (SVD) (2.52) [Golub 1965] to determine its rank. This rank corresponds obviously to the number of independent and identifiable model parameters, as mentioned above. The SVD decomposes the $\bar{\bar{FIM}}$ into the matrices, $\bar{\bar{U}}$, $\bar{\bar{\Sigma}}$ and $\bar{\bar{V}}$. The diagonal matrix $\bar{\bar{\Sigma}}$ contains the singular values $\bar{\sigma}$ of the $\bar{\bar{FIM}}$. Per definition, the rank of a matrix is equal to the number of singular values $\bar{\sigma} \neq 0$.

$$\bar{\bar{FIM}} \stackrel{\text{SVD}}{=} \bar{\bar{U}} \bar{\bar{\Sigma}} \bar{\bar{V}}^T \quad (2.52)$$

For numerical matrices, it is beneficial to introduce the condition number κ_i which is the ratio of the largest singular value σ_1 to the i th singular value σ_i (2.53). The numerical rank is then the number of condition numbers κ_i with a value less than a "numerical tolerance" ϵ . This tolerance value depends on the machine precision η_{mach} and the largest dimension of the evaluated matrix, which is the number of unknown parameters N_p (2.53) [Fink et al. 2007; Matlab R2014a].

$$\kappa_i = \frac{\sigma_1}{\sigma_i} \leq \epsilon = \frac{1}{N_p \sqrt{\eta_{\text{mach}}}} \quad (2.53)$$

Applying QR decomposition (QRD) with column pivoting (2.54) [Golub 1965] to the $\bar{\bar{FIM}}$ generates a lower triangle matrix $\bar{\bar{Q}}$, an upper triangle matrix $\bar{\bar{R}}$ and a permutation matrix $\bar{\bar{P}}$. This matrix rearranges the columns of the $\bar{\bar{FIM}}$ in a way that the absolute values of the diagonal elements of $\bar{\bar{R}}$ decrease from left to right ($|R_{ii}| > |R_{jj}|$ with $i > j$). This permutation can be interpreted as sorting the parameters with decreasing impact on the model states and increasing linear

dependence from left to right.

$$\overline{FIM} \stackrel{\text{QRD}}{=} \overline{Q} \overline{R} \cdot \overline{P} \quad (2.54)$$

The two techniques (SVD and QRD) reveal the sensitive parameter subset. It corresponds to the associated parameters of the first rank(\overline{FIM}) elements of the parameter vector after permutation with \overline{P} .

2.3.2 Illustration of the method using an example reaction

The mechanistic kinetic model of the example reaction $A \rightleftharpoons B$ (2.37) contains eight unknown kinetic parameters assuming a known equilibrium constant K_{eq} . The kinetic parameter vector $\overline{\theta}$ is:

$$\overline{\theta} = (A_{\text{rxn}} B_{\text{rxn}} K_I K_{II} K_{III} K_{IV} K_{Cl} K_{NCl})^T \quad (2.55)$$

Since the concentrations of A and B are linear dependent, the Sensitivity Matrix of one numerical experiment has always the rank 1. Therefore, minimum eight numerical batch experiments are necessary to possibly achieve a full rank \overline{FIM} . The numerical experimental design was chosen arbitrarily for the demonstration and is summarized in Table 2.2.

Table 2.2: Numerical experimental design for the test reaction $A \rightleftharpoons B$.

Experiment	I	II	III	IV	V	VI	VII	VIII
$c_A^0 / \text{mol l}^{-1}$	0.5	0.25	1	0	0	1	1	1
$c_B^0 / \text{mol l}^{-1}$	0	0.75	0	1	0.5	0	0	0
$c_{\text{Inh}} / \text{mmol l}^{-1}$	0	0	0.1	0	1	2	0	0
$T / ^\circ\text{C}$	100	100	100	100	100	100	90	110

After solving a dynamic batch mass balance (2.56) along the normalized reaction time τ together with (2.49), the dynamic normalized parameter sensitivities resulting from the numerical experimental design, shown in Figure 2.4, can be studied. The dynamic concentration profiles are omitted in the discussion for they do not contain any specific or interesting features.

It should be noted at this point that the result of the sensitivity analysis depends on initial parameter values. Hence, good initial parameter value estimates have to be provided from prior knowledge or literature.

$$\frac{dc_A}{d\tau} = -r_{\text{rxn}}(\overline{\theta}, c_A, c_B, c_{\text{Inh}}, T) = -\frac{dc_B}{d\tau} \quad (2.56)$$

It can clearly be seen in Figure 2.4 that the parameter sensitivities with respect to component A are strongly time dependent with maxima in some numerical experiments. This behavior is meaningful because kinetic parameters have only an influence on the changes of states far away from equilibrium. Once the conversion approaches the equilibrium state, the rate constants do not have any influence anymore. These results clearly prove that the experimental design strongly influences the parameter sensitivities and help to quantify and evaluate this influence.

The results of processing the \overline{FIM} with SVD and QRD are summarized in Figure 2.5. The figure contains three parts: a) dynamic condition numbers $\bar{\kappa}$, b) dynamic rank of the \overline{FIM} and c) a plot that shows the dynamics of the sensitive parameter subset. It

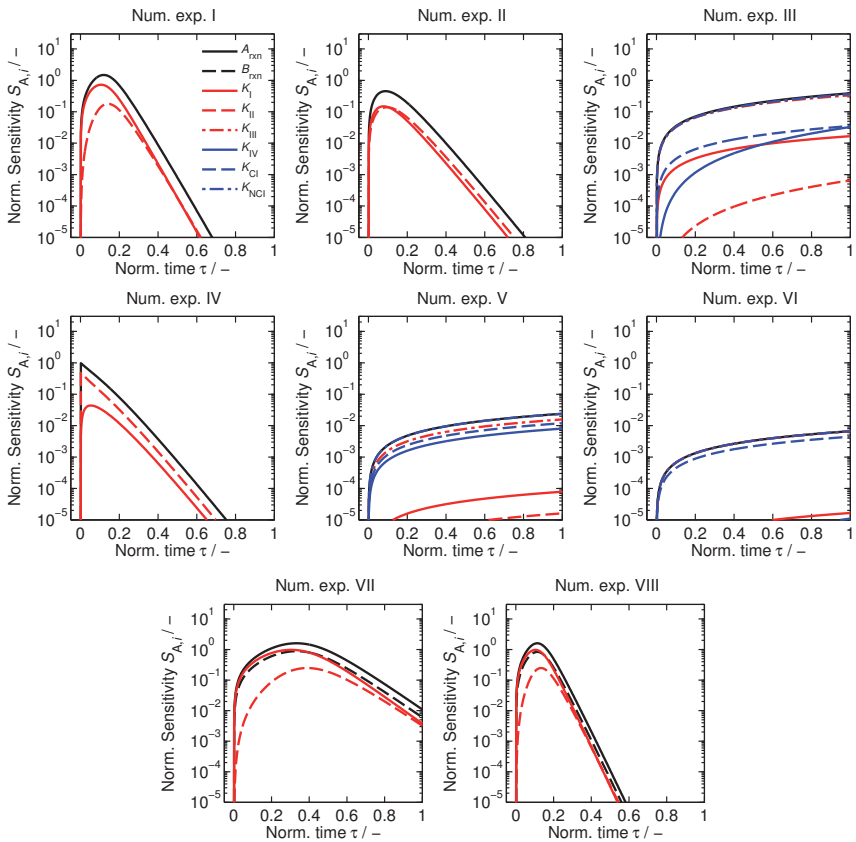


Figure 2.4: Normalized dynamic parameter sensitivities with respect to component A of the example reaction according to the numerical experimental design summarized in Table 2.2.

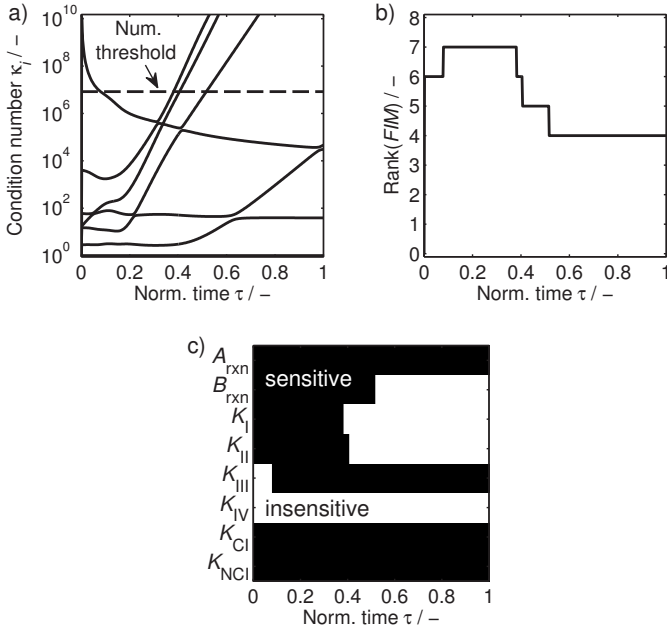


Figure 2.5: Dynamic analysis of the $\overline{\overline{FIM}}$: a) dynamic condition numbers $\bar{\kappa}$, b) dynamic rank of the $\overline{\overline{FIM}}$ and c) dynamic sensitive parameter subset (black = parameter is sensitive/identifiable, white = parameter is insensitive/non-identifiable).

can clearly be seen in Figure 2.5a that the condition numbers $\bar{\kappa}$ of the $\overline{\overline{FIM}}$ are time functions. The rank of the FIM in Figure 2.5b is also a time function since some condition numbers exceed the numerical tolerance at certain times. This indicates that time domains exist within the experiments with higher or lower information content. As a consequence, the sensitive parameter subset in Figure 2.5c is time dependent because the rank of the $\overline{\overline{FIM}}$ is equal to the number of sensitive parameters.

Some parameters are sensitive all over the normalized reaction time τ (A_{rxn}, K_{Cl}, K_{NCl}) whereas others lose their sensitivity (B_{rxn}, K_{I-III}) or do not have sensitivity at all (K_{IV}). It is perfectly reasonable that K_{IV} has no sensitivity at all because K_{III} and K_{IV} are multiplied in the corresponding term with K_{NCl} . Because of this multiplication, only two of the three parameters are linearly independent. Thus, reduction of the model is necessary by replacing K_{III} and K_{IV} with $\hat{K}_{III,IV} = K_{III,IV} \cdot K_{NCl}$, if a value for K_{NCl} cannot be estimated otherwise. The final reduced kinetic model for the test reaction \hat{r}_{rxn} as well as the reduced parameter vector $\hat{\theta}$ are summarized in (2.57),

respectively. In principle, the reduced model could be fitted to experimental data according to the experimental design and the remaining seven sensitive parameters could be estimated with low uncertainty. Additionally, the numerical study reveals a time information that influences the sampling strategy for a possible realization of the numerical experiments. It is obviously beneficial to have a high sampling rate in the first 10-40 % of the normalized reaction time because in this domain most of the parameters are sensitive. Afterwards, a lower sampling rate would be sufficient.

$$\hat{r}_{\text{rxn}} = \frac{k_{\text{rxn}}(T) (c_A - c_B/K_{\text{eq}}) c_{\text{cat,tot}}}{(1 + K_{\text{I}}c_A + K_{\text{II}}c_B + (\hat{K}_{\text{III}}c_A + \hat{K}_{\text{IV}}c_B) c_{\text{Inh}}) (1 + K_{\text{CI}}c_{\text{Inh}})} \quad (2.57)$$

with

$$\bar{\theta} = (A_{\text{rxn}} B_{\text{rxn}} K_{\text{I}} K_{\text{II}} \hat{K}_{\text{III}} \hat{K}_{\text{IV}} K_{\text{CI}})^{\text{T}}$$

2.4 Summary

This chapter was dedicated to calculation methods and modeling approaches used in the thesis. The presented methods comprise thermodynamic calculations, reactor and mass transfer modeling, derivation of mechanistic kinetic rate equations and parameter identifiability analysis.

Regarding thermodynamics, Benson's group contribution method (BGCM) for the calculation of thermodynamic state functions of formation of organic molecules was presented [Benson et al. 1969]. These state functions are required for the presented Gibbs energy minimization method for non-stoichiometric equilibrium calculations [White et al. 1958].

In order to estimate kinetic parameters from (semi-) batch experiments, a corresponding standard (semi-) batch reactor model including gas-liquid mass transfer was derived. Mass transfer limitations are of minor importance for the used equipment in this thesis.

The derivation of kinetic models followed the method presented first in [Christiansen 1953] and is based on catalytic reaction mechanisms. Thus, it is possible to derive mechanistic kinetic rate equations, which include changing partial reaction orders of reactants due to changing concentration regimes, rate determining step assumptions, catalyst pre-equilibria and competitive catalyst inhibition as well as catalyst deactivation due to non-competitive inhibition reactions. Furthermore, knowledge from preliminary spectroscopic investigations can directly be used to reduce the complexity of the kinetic model [Helfferich 2004].

Conclusively, a method for the analysis of parameter identifiability, parameter subset selection, was presented and extended to a local analysis. The method divides a set of unknown parameters into a sensitive (identifiable) and insensitive (non-identifiable)

subset, depending on the experimental design. Illustration of the method was done by applying it to a synthetic example reaction with a typical structure for homogeneously catalyzed systems.

It can be concluded that proper kinetic analysis and modeling should be supported systematically by mathematical methods and tools for e.g. parameter identifiability analysis to avoid pitfalls in parameter estimation, such as strong parameter correlations. All presented methods and models will be used and applied in the following two chapters to increase the reliability of the developed mechanistic kinetic models.

3 Hydroformylation of n-decene

This chapter is dedicated to the Rh-BiPhePhos catalyzed hydroformylation of 1-decene as representative long chain olefin. Special emphasis is given to relevant side reactions, namely hydrogenation and most importantly double bond isomerization, to be able to understand the tandem isomerization-hydroformylation of internal n-decenes to undecanal. The presented results were achieved using the methods and models presented in chapter 2.

In the first part of this chapter, calculation results regarding thermodynamic state functions of n-decene double bond isomers as well as the double bond isomerization reaction equilibrium and their experimental validation are discussed. The second part of this chapter addresses the reaction mechanism and its simplification based on *operando* FTIR spectroscopic measurements. Subsequently, kinetic models based on the simplified reaction mechanism are presented and fitted to carefully designed (semi-) batch experiments. The last part of this chapter uses the parameterized mechanistic kinetic model to calculate optimal dynamic reaction control profiles in terms of reaction temperature and synthesis gas pressure to compare and discuss ideal reaction conditions for the hydroformylation of 1-decene as well as the tandem isomerization-hydroformylation.

It should be noted that the author of this thesis published significant parts of the following chapter as first author in [Jörke et al. 2015a, 2016, 2017a,b]. Further details and results can be found in the respective cited articles.

3.1 Double bond isomerization equilibrium of n-decene

The double bond isomerization occurring during Rh-BiPhePhos catalyzed hydroformylation is the most dominant side reaction or can even be essential for tandem isomerization-hydroformylation reactions as already mentioned in chapter 1. Since the double bond isomerization reaction is equilibrium limited, thermodynamic state functions as well as equilibrium constants are required for further kinetic analysis and subsequent optimal reaction control. Figure 3.1 shows a possible equilibrium reaction network representing the double bond isomerization of n-decenes. In principle 18 equilibrium reactions for nine n-decene isomers are possible under the assumption

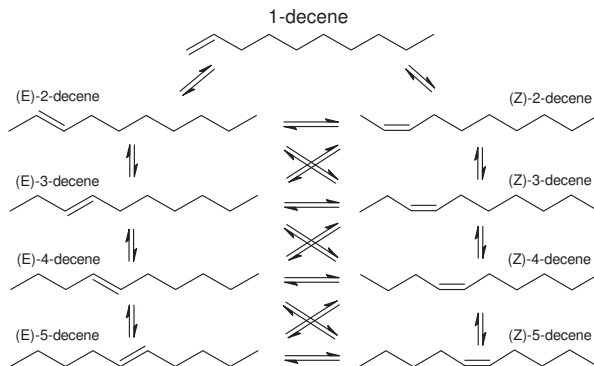


Figure 3.1: Possible n-decene double bond isomerization equilibrium network.

that next neighbor isomers are at equilibrium with each other. It should be noted that the double bond isomerization reaction is catalyzed by Rh-BiPhePhos complexes used in this thesis. However, the catalyst was omitted in Figure 3.1 because a catalyst does not change the reaction equilibrium which is the focus of this section.

Only few publications addressed the topic of long-chain olefin double bond isomerization, although this side reaction is significantly important as already discussed. Therefore, relevant publications dedicated to n-olefin double bond isomerization are summarized in the following paragraphs to compare their findings with results from this thesis.

An equilibrium composition of n-hexene isomers was generated using a PdCl₂-CuCl₂ catalyst at 30 °C in methanol [Dahl et al. 1997]. The authors reported the following double bond isomer composition: 1-hexene (1.2 %), trans-2-hexene (61.4 %), cis-2-hexene (16.6 %), trans-3-hexene (19.8 %) and cis-3-hexene (1.0 %). It was concluded that, thermodynamically, trans isomers are favored over cis isomers. Additionally, the presented data indicates that 2-hexenes are favored at equilibrium over the symmetrical 3-hexenes with most internal double bond position.

The double bond isomerization of n-octenes was studied in [Morrill and D'Souza 2003] using a RhCl₃·nH₂O/BH₃·THF catalyst system in THF as solvent at room temperature. At equilibrium, the composition of double bond isomers was determined by the authors to be 0.6, 39.3, 33.4 and 26.7 % for 1-, 2-, 3- and 4-octene, respectively. These findings are in agreement with measurements presented in [Selent et al. 2011]. From kinetic experiments, the authors concluded that isomerization of the double bond to more internal positions follows a series reaction scheme.

The tandem isomerization-hydroformylation of a internal n-octenes using a Rh-BiPhePhos catalyst in toluene or propylene carbonate was studied in [Behr et al. 2004]. The double bond isomer composition of 1-, 2-, 3- and 4-octenes at equilibrium

was found to be 2, 11, 28, 59 %, respectively. This isomer distribution pattern differs significantly from findings in the literature [Dahl et al. 1997; Morrill and D'Souza 2003; Selent et al. 2011]. The presented experimental data indicates that the double bond isomerization from terminal to internal positions is faster by a factor of ≈ 3.5 compared to back-isomerization.

The isomerization of n-decenes in the presence of a Ni-stearate-ethylaluminium-chloride catalyst in n-heptane as solvent was investigated in [Startseva et al. 2004]. At equilibrium, the ratio of 2 : 3 : 4 : 5-decene was found to be 1 : 1 : 1.4 : 0.7, respectively. The corresponding trans/cis ratios were determined to be 2.93, 5.71, 4.61 and 3.75. Interestingly, the presented double bond isomer distribution pattern at equilibrium is again different from the aforementioned publications.

The studies presented in [Jennerjahn et al. 2009] focused on hydroformylation issues using a $[\text{Pd}(\text{acac})_2]/\text{ligand}/p\text{-toluenesulfonic acid}$ catalyst system, using several different ligands and substrates. However, they studied isomerization of n-octenes as well since it appeared as side reaction. The presented data indicated a kinetic favorization of cis-2-olefins as well as a thermodynamic favorization of 2-olefins over other internal n-olefins. At equilibrium, the most internal n-olefin, 4-octene, was found experimentally to be the least favored internal n-olefin. This pattern is in agreement with several other publications [Dahl et al. 1997; Morrill and D'Souza 2003; Startseva et al. 2004; Selent et al. 2011].

Summarizing, the double bond isomerization of long-chain n-olefins is characterized by the following features:

- Thermodynamically, internal olefins are favored over terminal olefins and trans olefins are favored over cis olefins.
- Kinetically, cis isomers are favored over trans isomers.
- The 2-olefin is the most abundant isomer at equilibrium.
- Double bond isomerization follows a series reaction pattern from terminal to internal positions.
- Isomerization from terminal to internal positions is significantly faster than the back-isomerization from internal to terminal positions.

However, the literature is partly inconsistent with respect to e.g. the distribution pattern of internal n-olefins at equilibrium. Therefore, it is questionable, if isomers were assigned correctly in terms of analytics or if the equilibrium state was really reached in those contributions because the thermodynamic reaction equilibrium should be independent of the used catalyst. Thus, it would be attractive to calculate the thermodynamic isomerization reaction equilibrium using only thermodynamic data to generate

reliable equilibrium constants. Hence, this section is dedicated to the following issues connected with double bond isomerization of n-decenes:

- Calculation of thermodynamic state functions of n-decenes using Benson's group contribution method presented in section 2.1.2
- Calculation of the double bond isomerization equilibrium composition and corresponding equilibrium constants using non-stoichiometric Gibbs energy minimization presented in section 2.1.1.
- Experimental validation of the calculated equilibrium composition

3.1.1 Calculation of thermodynamic state functions

This section summarizes calculation results of thermodynamic state functions of all n-decene isomers using Benson's group contribution method (BGCM) (see equations (2.10)-(2.19) discussed in section 2.1.2). Table 3.1 summarizes the used group contribution increment values taken from the literature. It should be noted that all increment values in Table 3.1 refer to the gas phase, although the equilibrium reaction occurs in liquid phase. Considering n-decene isomers in the condensed state is not necessary since similar enthalpies and entropies of vaporization for all n-decene isomers are likely. Thus, the phase change contribution will cancel out and the usage of gas phase data is justified for subsequent calculation of the isomerization reaction equilibrium using the non-stoichiometric approach based on Gibbs energy minimization (see section 2.1.1).

Table 3.1: Benson group increments for n-decene isomers. Superscripts indicate literature references (1: [Domalski and Hearing 1988], 2: [Pohling et al. 2000]).

Benson group	$\bar{h}_m^\ominus / \text{J mol}^{-1}$	$\bar{s}_m^\ominus / \text{J mol}^{-1} \text{K}^{-1}$	$\bar{c}_{\text{Pm}}(T) / \text{J mol}^{-1} \text{K}^{-1}$		
			289 K	400 K	500 K
$\text{C}_d\text{-}(2\text{H})$	26.32 ¹	115.52 ¹	21.38 ¹	26.62 ²	31.44 ²
$\text{C}_d\text{-}(\text{C},\text{H})$	36.32 ¹	33.05 ¹	18.74 ¹	21.05 ²	24.32 ²
$\text{C}\text{-}(\text{C}_d, \text{C}, 2\text{H})$	-20.88 ¹	38.20 ¹	20.63 ¹	28.71 ²	34.83 ²
$\text{C}\text{-}(2\text{C}, 2\text{H})$	-20.63 ¹	39.16 ¹	22.89 ¹	29.09 ²	34.53 ²
$\text{C}\text{-}(\text{C}, 3\text{H})$	-42.26 ¹	127.32 ¹	25.73 ¹	32.82 ²	39.35 ²
$\text{C}\text{-}(\text{C}_d, 3\text{H})$	-42.26 ¹	127.32 ¹	25.73 ¹	32.82 ²	39.35 ²
cis-interaction	4.85 ¹	5.06 ¹	-8.03 ¹	-8.03 ¹	-8.03 ¹
Chemical element		$\bar{s}_e^\ominus / \text{J mol}^{-1} \text{K}^{-1}$	$\bar{c}_{\text{Pe}}(T) / \text{J mol}^{-1} \text{K}^{-1}$		
			289 K	400 K	500 K
C		6 ²	9.0 ²	12.0 ²	15.0 ²
H		130 ²	29.0 ²	29.0 ²	29.0 ²

Figure 3.2 illustrates the temperature dependence of these state functions, namely heat of formation, entropy, entropy change of formation and Gibbs energy of formation in a temperature interval between 25 °C and 200 °C for all possible n-decene double bond isomers. Table 3.2 summarizes these state functions at standard temperature (gas phase). The calculated heat of formation and Gibbs enthalpy of formation of 1-decene at standard temperature are $-124.28 \text{ kJ mol}^{-1}$ and $120.23 \text{ kJ mol}^{-1}$, respectively. The corresponding literature values presented in [Pohling et al. 2000] are in good agreement with these results ($-124.2 \text{ kJ mol}^{-1}$ and $121.1 \text{ kJ mol}^{-1}$, respectively). However, the absolute values of the calculated thermodynamic state functions, especially the Gibbs energies of formation, are within a narrow range (see Table 3.2), making the reaction equilibrium calculation prone to errors in state function calculations. The small differences in the thermodynamic state functions result from the fact that all considered molecules are positional double bond isomers with a very similar molecular structure. No difference can be made between 3- and 4-decene because only next neighbor interactions are included in BGCM resulting

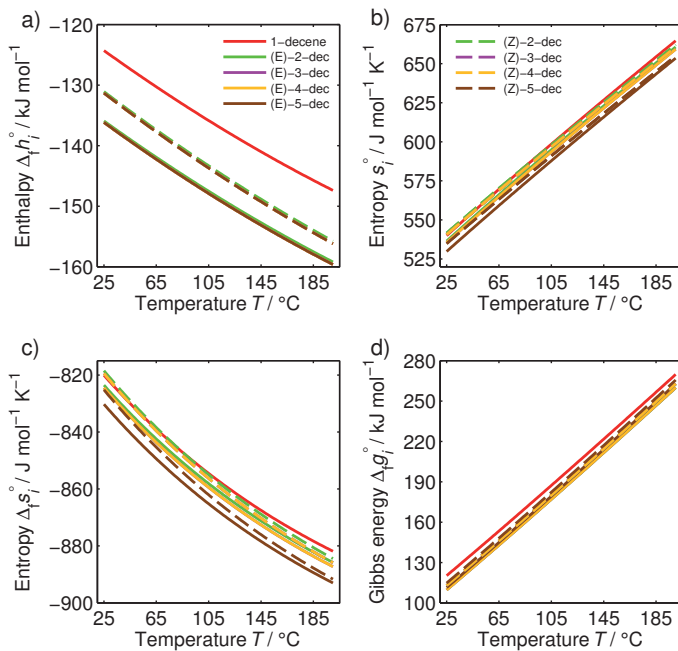


Figure 3.2: Temperature dependent thermodynamic state functions of all n-decene double bond isomers calculated using BGCM: a) Enthalpy of formation, b) Entropy, c) Entropy change of formation, d) Gibbs energy of formation.

Table 3.2: Thermodynamic state functions of n-decene isomers at standard temperature (298 K) calculated with (2.10)-(2.19) (gas phase).

	$\Delta_f \bar{h}^\ominus$	\bar{s}^\ominus	$\Delta_f \bar{s}^\ominus$	$\Delta_f \bar{g}^\ominus$	$\bar{c}_p(298\text{ K})$
	kJ mol^{-1}	$\text{J mol}^{-1} \text{K}^{-1}$	$\text{J mol}^{-1} \text{K}^{-1}$	kJ mol^{-1}	$\text{J mol}^{-1} \text{K}^{-1}$
1-decene	-124.28	539.92	-820.08	120.23	223.82
(E)-2-dec	-135.91	536.47	-823.53	109.63	224.02
(E)-3-dec	-136.16	535.51	-824.49	109.66	221.76
(E)-4-dec	-136.16	535.51	-824.49	109.66	221.76
(E)-5-dec	-136.16	529.75	-830.25	111.38	221.76
(Z)-2-dec	-131.06	541.53	-818.47	112.97	215.99
(Z)-3-dec	-131.31	540.57	-819.43	113.00	213.73
(Z)-4-dec	-131.31	540.57	-819.43	113.00	213.73
(Z)-5-dec	-131.31	534.81	-825.19	114.72	213.73

in identical group contributions and consequently identical thermodynamic state functions for these isomers.

It can be seen from Figure 3.2d and Table 3.2 that 1-decene is the thermodynamically most unfavored isomer since the terminal double bond is energetically disfavored compared to an internal double bond. Furthermore, the presented results prove cis isomers thermodynamically always less stable than the corresponding trans isomers because of intramolecular repulsive interactions arising from the cis-structure [Jörke et al. 2016]. The values of Gibbs energy of formation of the symmetric 5-decenes are higher compared to the other internal n-decenes which is equivalent to less thermodynamic stability. The lower thermodynamic stability of the symmetrical double bond isomer can be explained by an additional entropic contribution punishing the symmetry of the molecules because symmetry can be interpreted as an expression of order. Therefore, it can be expected that symmetrical double bond isomers appear at a lower concentration at equilibrium compared to non-symmetrical ones, which is in accordance to several experimental findings in the literature [Dahl et al. 1997; Morrill and D'Souza 2003; Startseva et al. 2004; Selent et al. 2011].

In the following section, the presented thermodynamic state functions were used to calculate the thermodynamic reaction equilibrium of the double bond isomerization of n-decenes using a non-stoichiometric approach based on Gibbs energy minimization (see section 2.1.1).

3.1.2 Isomerization equilibrium composition and equilibrium constants

Since $N_s - 1$ equilibrium reactions are necessary to describe N_s species at equilibrium using a stoichiometric approach, the simultaneous solution of eight non-linear

equations would be necessary to calculate the reaction equilibrium of n-decene isomerization. Additionally, it would be necessary to provide a distinct stoichiometry for setting up classical mass action law formulations which may not be known *a priori*. Using a non-stoichiometric equilibrium formulation based on Gibbs energy minimization, explained in 2.1.1, is advantageous in this case because the number of equations to be solved is reduced and no distinct stoichiometry has to be provided. On the example of n-decene double bond isomerization, the non-stoichiometric method reduces the complexity of the problem to $N_{el} + 1 = 3$ non-linear equations (N_{el} = number of different chemical elements present in n-decene double bond isomers: C and H) with three degrees of freedom (total amount of substance n_{tot} and two Lagrange multipliers for every chemical element, see section 2.1.1). The complexity can be reduced even further because the total amount of substance n_{tot} in case of n-decene isomerization remains constant and is known. Therefore, the dimension of the solution reduces to two Lagrange multipliers in this case. Since only two chemical elements are present in n-decene isomers and all isomers, obviously, contain the same amount of elements, the rank of the corresponding element-species-matrix $\bar{\beta}$ is equal to 1. Hence, the solution of the n-decene isomerization equilibrium problem requires only one Lagrange multiplier as degree of freedom to fulfill (2.3) and (2.4), whereas the other Lagrange multiplier can be fixed to any non-zero value because it is linearly dependent (see section 2.1.1).

The numerical solution of (2.3) and (2.4) was carried out using the "fsolve" solver in Matlab 2012a. Figure 3.3 summarizes the results in terms of n-decene isomer distribution at equilibrium as a function of temperature. The calculated isomer distribution is presented as all possible internal cis and trans n-decenes in Figure 3.3a and double bond positions along the carbon chain in Figure 3.3b. At equilibrium,

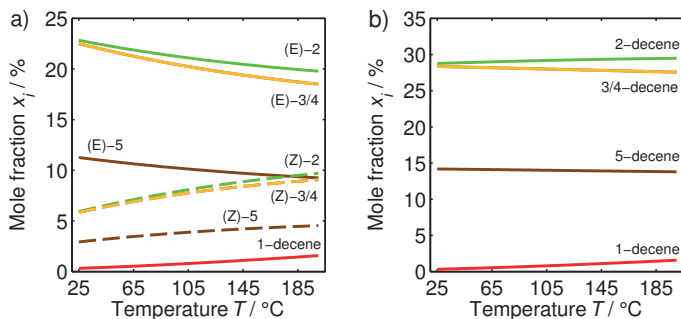


Figure 3.3: Calculated distribution of internal n-decenes at thermodynamic equilibrium as a function of temperature. a) All possible cis and trans isomers. b) Double bond positions along the carbon chain.

the calculations reveal that the least abundant n-decene is 1-decene with a mole fraction of about 1% relative to all n-decene isomers. Regarding internal n-decenes, the trans isomers are clearly dominating the cis isomers. Within internal cis and trans isomers, the double bond at second position is always the most stable one. Also, the symmetrical double bond isomers are always present in lower concentrations compared to their non-symmetrical counterparts.

The calculated double bond isomer distribution pattern is in accordance to several experimental findings presented in [Dahl et al. 1997; Morrill and D'Souza 2003; Startseva et al. 2004; Selent et al. 2011] but remains contradictory to findings presented in [Behr et al. 2004]. However, it corresponds to trends in Gibbs energy being discussed in the previous section. Hence, it is concluded that the calculated thermodynamic state functions as well as the equilibrium composition are reliable and can be used to calculate equilibrium constants to be used later on in kinetic models.

With increasing temperature from 25 to 200 °C, the double bond isomer equilibrium distribution changes slightly with a concentration increase of 1-decene and cis-decenes while the concentrations of trans-decenes decrease. Hence, temperature dependent equilibrium constants $K_{ij}^{\text{eq}}(T)$ can be calculated from the presented double bond isomer distribution, which are the concentration ratios of isomer i to isomer j at every temperature. They can be calculated by a classical mass action law formulation (3.1). The activity coefficients γ_i in (3.1) describe non-ideal molecule-molecule interactions as well as molecule-solvent interactions [Lemberg et al. 2017]. They can be canceled out in (3.1) because the internal n-decenes differ only in double bond position, leading to very similar activity coefficients for all internal n-decenes. Thus, the introduced error should be small.

$$K_{ij}^{\text{eq}}(T) = \frac{a_i(T)}{a_j(T)} = \frac{\gamma_i x_i(T)}{\gamma_j x_j(T)} \approx \frac{x_i(T)}{x_j(T)} \quad (3.1)$$

The calculated equilibrium constants are presented in Figure 3.4. It can be seen in Figure 3.4 that only K_{21}^{eq} is temperature dependent to a significant extend. A polynomial fit of $K_{21}^{\text{eq}}(T)$ is presented in (3.2) covering the studied temperature interval. It becomes obvious from the comparably high value of K_{21}^{eq} (33.77 at a typical reaction temperature of 115 °C) that in equilibrium only small amounts of 1-decene will be present which was confirmed experimentally in the literature [Dahl et al. 1997; Morrill and D'Souza 2003; Behr et al. 2004; Startseva et al. 2004; Selent et al. 2011].

$$K_{21}^{\text{eq}}(T) = 6.5744 \cdot 10^{-8} \text{ } ^\circ\text{C}^{-4} T^4 - 4.5487 \cdot 10^{-5} \text{ } ^\circ\text{C}^{-3} T^3 + 1.2448 \cdot 10^{-2} \text{ } ^\circ\text{C}^{-2} T^2 - 1.7344 \text{ } ^\circ\text{C}^{-1} T + 1.2628 \cdot 10^2 \quad (3.2)$$

The other equilibrium constants are almost temperature independent and therefore assumed to be constant in this thesis for all further calculations. Their values at typical reaction temperature of 115 °C are summarized in (3.3)-(3.6).

$$K_{21}^{\text{eq}}(115 \text{ }^\circ\text{C}) = 33.77 \quad (3.3)$$

$$K_{32}^{\text{eq}} = 0.96 \quad (3.4)$$

$$K_{43}^{\text{eq}} = 1.00 \quad (3.5)$$

$$K_{54}^{\text{eq}} = 0.50 \quad (3.6)$$

Regarding the trans-cis ratio presented in Figure 3.4b, it can be seen that it is equal for all internal n-decenes because the same cis-contribution is added to all thermodynamic state functions in BGCM. However, the values correspond well to reported trans-cis ratios in the literature [Startseva et al. 2004].

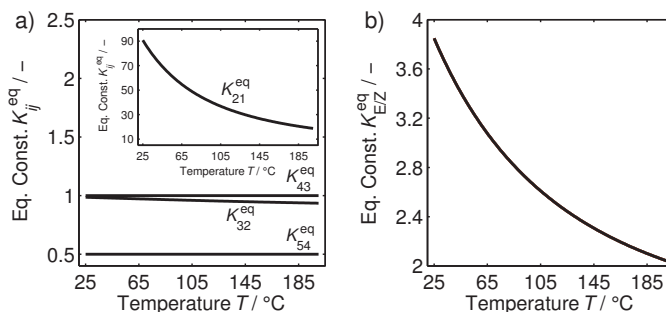


Figure 3.4: Temperature dependent isomerization equilibrium constants for n-decenes with respect to double bond positions.

3.1.3 Experimental validation

In this section, the calculated n-decene double bond isomerization equilibria are validated with experimental data. Hence, an isomerization batch experiment with initially pure 1-decene ($c_{1D}^0 = 0.9 \text{ mol l}^{-1}$) was performed until the equilibrium state was reached at 105 °C. The experimental procedure included activation of the Rh-BiPhePhos catalyst with 10 bar synthesis gas in a thermomorphic solvent (TMS). Subsequently, the gas phase was exchanged to 1 bar nitrogen to prevent hydroformylation and hydrogenation. Injecting the substrate 1-decene started the isomerization reaction. More experimental details about procedures, substances, solvents, apparatuses and analytics are summarized in appendix A and section 3.4.

The experimental data in Figure 3.5 proves fast isomerization of 1-decene and high catalyst activity with an initial turn over frequency (TOF) (3.7) of $\approx 3 \cdot 10^5 \text{ h}^{-1}$.

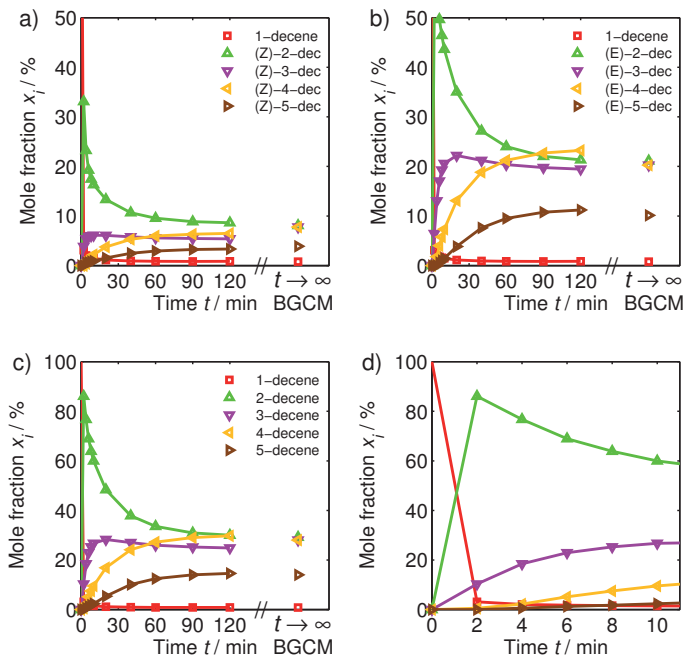


Figure 3.5: Experimentally observed n-decene double bond isomer composition: a) 1-decene and cis isomers, b) 1-decene and trans isomers, c) and d) 1-decene and double bond position isomers. (TMS, 105 °C, 3 bar N₂, $c_{\text{sub}}^0 = 0.9 \text{ mol l}^{-1}$, Rh:sub (molar) = 1:10000, Rh:lig (molar) = 1:3)

Compared to the isomerization rate of 1-decene, the isomerization rates of internal n-decenes were found to become significantly lower with more internal double bond position. This is reasonable because steric hindrances due to the complex ligand structure (see appendix F.2) will increase for more internal double bond positions [Behr and Neubert 2012].

The reaction equilibrium between all n-decene double bond isomers was reached after ≈ 120 minutes (Figure 3.5c) with almost quantitative conversion of 1-decene to internal n-decenes after 2 minutes (Figure 3.5d). The composition of internal n-decenes (after 24h of isomerization) is summarized in Table 3.3. It can be seen that the concentrations converged to the calculated equilibrium composition using BGCM (denoted with $t \rightarrow \infty$) presented in the previous section. Only minor deviations exist between the calculated and experimentally determined equilibrium composition, confirming the calculations. At equilibrium, only small amounts of 1-decene were detected ($< 1\%$). Regarding internal n-decenes, the symmetric 5-decenes were found to be present at concentrations half as much as the other internal n-decenes,

confirming the thermodynamic calculations and double bond isomer distribution patterns in the literature [Dahl et al. 1997; Morrill and D'Souza 2003; Startseva et al. 2004; Selent et al. 2011]. The mean ratio between trans/cis internal n-decenes was experimentally determined to be between 3.0-3.5, which is in accordance to results presented in Figure 3.4b and the literature [Startseva et al. 2004].

The results prove successful calculations of the n-decene double bond isomerization equilibrium using Gibbs energy minimization and Benson's group contribution method. Hence, the calculated equilibrium constants can be regarded as reliable and will be used in further kinetic modeling. Furthermore, the presented methods are generally applicable to other substrates, which cannot be resolved experimentally in its entirety.

Table 3.3: Experimentally observed n-decene isomerization equilibrium composition in mole fractions after 24 h at 378 K and 3 bar N₂ and calculated equilibrium composition using thermodynamic state functions obtained with BCGM.

	1-decene	(E)-2	(E)-3	(E)-4	(E)-5	(Z)-2	(Z)-3	(Z)-4	(Z)-5
$x_{i,\text{exp}}^{\text{eq}} / \%$	0.81	19.47	19.06	24.45	12.23	7.92	5.34	7.05	3.66
$x_{i,\text{cal}}^{\text{eq}} / \%$	0.79	21.11	20.25	20.25	10.13	8.08	7.76	7.76	3.88
$\Delta x_{i,\text{abs}}^{\text{eq}} / \%$	0.02	1.64	1.19	4.20	2.10	0.16	2.42	0.71	0.22
$\Delta x_{i,\text{rel}}^{\text{eq}} / \%$	2.47	8.42	6.24	17.18	17.17	2.02	45.32	10.07	6.01

3.2 Hydroformylation reaction mechanism for 1-decene

It is one of the major goals of this thesis to create a mechanistic kinetic model that describes the Rh-BiPhePhos catalyzed hydroformylation of 1-decene including all relevant side reactions, such as double bond isomerization and hydrogenation. Since the model derivation is based on reaction mechanisms, it should be able to describe all borderline cases in terms of reactions conditions and therefore also the tandem isomerization-hydroformylation with one set of kinetic parameters. However, mechanistic kinetic models derived from complex catalytic reaction mechanisms often contain a large number of unknown kinetic parameters which are difficult to estimate [Helfferich 2004]. Therefore, it is necessary to reasonably simplify reaction mechanisms to reduce these models for an efficient and effective parameter estimation. Reasonable simplification in this context means to find relevant Rh-species and reaction steps that contribute to the overall catalyst material mass balance and reactions rates, respectively, which are the issues of the following sections.

One generally accepted hydroformylation mechanism for cobalt and rhodium catalysts is the "Wilkinson" cycle (see Figure 3.6) [Evans et al. 1968]. This mechanism

was extended to take the most dominant side reactions (double bond isomerization, hydrogenation and iso-aldehyde production) into account [Markert et al. 2013; Kiedorf et al. 2014]. The mechanism can be divided into two parts: (1) the catalyst formation and pre-equilibrium and (2) the coupled reaction cycles consisting of double bond isomerization (branch **I**), double bond hydrogenation (branch **IIa-b**) and hydroformylation (branch **IIIa** for the production of linear aldehydes and **IIIb** for the production of branched aldehydes).

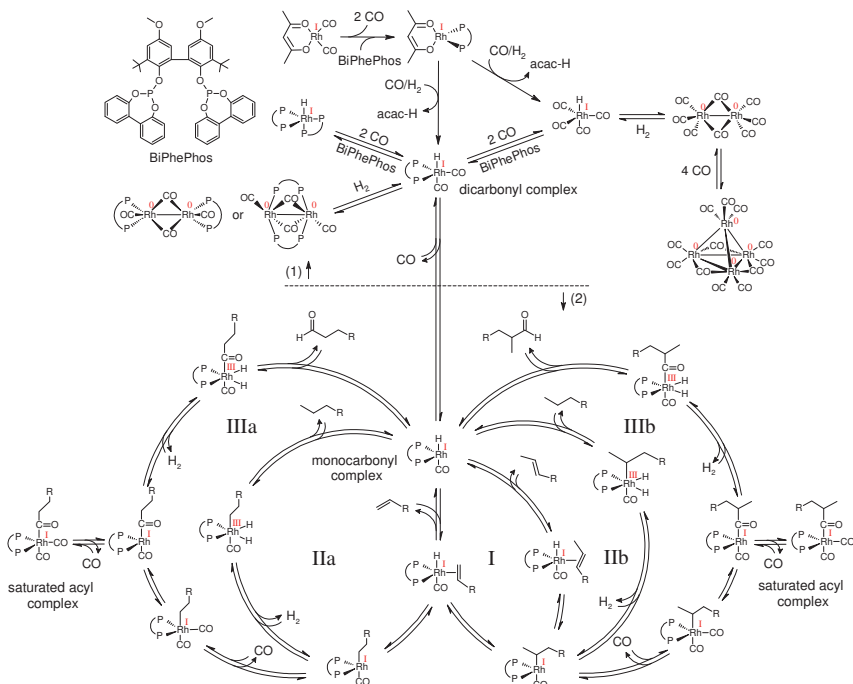


Figure 3.6: Extended most general Rh-BiPhePhos catalyzed hydroformylation reaction mechanism including catalyst pre-equilibria as well as main and side reactions: **I** double bond isomerization, **IIa-b** hydrogenation, **IIIa** hydroformylation producing linear aldehydes and **IIIb** hydroformylation producing branched aldehydes.

Regarding the catalyst pre-equilibrium depicted in part (1) of Figure 3.6, it is crucial to accurately balance the active, inactive or non-selective catalyst material present under reaction conditions. It is reasonable to assume equilibrium between these catalyst complexes since it was found experimentally with *operando* FTIR spectroscopy that transformation of Rh-complexes into each other is very fast compared to substrate conversion, even at room temperature [Kubis 2012; Kubis et al. 2012; Jörke et al.

2017b]. Several catalyst species were reported in the literature: Rh-dimers [Moasser et al. 1995; Bronger et al. 2004; Deshpande et al. 2011], hydrido-Rh-dicarbonyl complexes [Evans et al. 1968; Deshpande et al. 2011; Selent et al. 2011; Kubis 2012], Rh-bischelate complexes [Hamerla et al. 2013], Rh-tetracarbonyl complexes and higher clusters [Chew et al. 2002; Li et al. 2002; Hamerla et al. 2013] and the hydrido-Rh-monocarbonyl complex as active catalyst [Evans et al. 1968; Carvajal et al. 2009]. However, it depends strongly on the electronic and steric interactions between ligand and metal, if a specific catalyst complex is present to a significant extend or not. Hence, experimental investigations supported by computational chemistry are essential to identify relevant (non-) reactive and (non-) selective catalyst complexes. Regarding the Rh-BiPhePhos catalyst system used in this thesis, FTIR spectroscopic investigations in combination with DFT calculations proved the existence of hydrido-Rh-dicarbonyl complexes under hydroformylation conditions with *e,e*-coordination of the ligand [Kubis 2012].

The coupled reaction cycles are depicted in part (2) of Figure 3.6. In the case of hydroformylation, the olefin coordinates at the unsaturated and active 16 valence electron (ve) hydrido-Rh-carbonyl complex HRh(BP)(CO). Which carbon of the double bond is inserted into the Rh-hydride bond decides whether a linear or a branched aldehyde is formed (branch **IIIa** or **IIIb**). After addition and migratory insertion of CO into the alkyl substituent, an unsaturated acyl complex is formed. Subsequently, oxidative H₂ addition to the unsaturated acyl complex changes the oxidation state of Rh from I to III. Finally, reductive elimination releases the aldehyde, reduces the oxidation state of Rh back to I and the active 16ve hydrido-Rh-monocarbonyl is formed back again to close the catalytic cycle. Hydrogenation occurs, if oxidative H₂ addition happens before CO addition (branch **IIa-b**). If β -H elimination follows the double bond insertion, internal n-olefins are produced until thermodynamic equilibrium is reached (branch **I**).

The mechanism of the tandem isomerization-hydroformylation of internal n-olefins consists of two cycles running simultaneously. First, the hydroformylation reaction consumes terminal 1-olefins from the n-olefin double bond isomer mixture and disturbs the isomerization equilibrium. At the same time, the isomerization reaction counteracts this disturbance to restore the thermodynamic equilibrium. In this manner, new terminal 1-olefins are produced from internal n-olefins, which are then available for hydroformylation again [Vilches-Herrera et al. 2014].

Taking all these steps into account would lead to a very general kinetic model. However, it is unlikely that all steps are equally fast and contribute to the overall reaction rate. Hence, the most general kinetic model is overparameterized and needs to be reduced. Significant model reduction can be achieved by assuming one step in the catalytic reaction mechanisms as rate determining step (RDS) [Helfferich 2004].

In the literature, mainly two possible RDS are discussed for the hydroformylation of cyclic, branched and straight-chain olefins: i) the oxidative addition of hydrogen to the unsaturated acyl complex, which was observed for unmodified Rh-carbonyl complexes [Garland and Pino 1991; Fyhr and Garland 1993; Zhang et al. 2003], monophosphine modified Rh [Bhanage et al. 1997; Nair et al. 1999; Caporali et al. 2004; Shaharun et al. 2009] and also monophosphite modified Rh [van Rooy et al. 1995; Kubis et al. 2012] and ii) the coordination of the olefin double bond to the 16ve hydrido-Rh-monocarbonyl complex which was also observed for monophosphine modified Rh [van Rooy et al. 1996b], diphosphine modified Rh [Bronger et al. 2004; Zuidema et al. 2008], monophosphite modified Rh [Dabbawala et al. 2009; Shaharun et al. 2010; Güven et al. 2014] and diphosphite modified Rh [van Rooy et al. 1996a; van Leeuwen et al. 2000; Rush et al. 2009].

Two effects are responsible for observing different rate determining steps: i) the ligand type (phosphines: σ -donor, phosphites: π -acceptor) influences the π -backbonding ability of the metal with respect to substrates or CO ligands and ii) steric hindrances between substrate and ligand can affect coordination and transformation of substrates at the metal center, if bulky ligands are used [van Leeuwen et al. 2000; Behr and Neubert 2012; Franke et al. 2012]. The coupling of both effects explains why the same catalyst shows different RDS with different substrates [van Rooy et al. 1995; Caporali et al. 2004]. Thus, no general statement regarding rate determining steps for a specific hydroformylation catalyst system can be made.

Operando FTIR spectroscopy is a very useful tool to investigate homogeneously catalyzed reactions regarding the detection of reactants, catalytic intermediates and products [Behr and Neubert 2012; Diebolt et al. 2012] It is especially well suited for the detection and distinction of metal-carbonyls [Braterman 1975]. Hence, this technique was applied in this thesis to the Rh-BiPhePhos catalyzed isomerization, hydrogenation and hydroformylation of 1-decene (see section 3.2.1) and UME (see section 4.2.1) to clarify which relevant catalyst species are observable. Conclusions regarding relevant catalyst complexes contributing to the Rh mass balance can be drawn in terms of catalyst pre-equilibria. Rate determining steps can also be identified because the intermediate before a slow step would accumulate as a consequence of Bodenstein's principle and thus become visible in the IR spectrum.

3.2.1 Mechanistic investigations using *operando* FTIR spectroscopy

This section presents experimental results of *operando* FTIR spectroscopic investigations of the Rh-BiPhePhos catalyzed isomerization, hydrogenation and hydroformylation of 1-decene. It is the goal to find relevant Rh-complexes that contribute to the overall catalyst material mass balance and to identify rate determining steps.

The pre-formation of the hydroformylation catalyst is done by stirring (800 rpm) a toluene solution (15 ml) of catalyst precursor $\text{Rh}(\text{acac})(\text{CO})_2$ (12 mg) and ligand BiPhePhos (60 mg) at 40 °C under 10 bar synthesis gas in a 75 ml sealed batch autoclave equipped with a Si-ATR probe attached to a FTIR spectrometer (Fa. Mettler Toledo, ReactIR10, resolution = 4 cm^{-1}). Injecting the substrate 1-decene (4.5 ml in 5.5 ml toluene) after catalyst activation starts the hydroformylation including side reactions. Studying subnetworks (isomerization or hydrogenation) individually is possible by changing the gas phase composition after catalyst activation. Exchanging synthesis gas with inert nitrogen or CO allows the double bond isomerization only after substrate injection whereas exchanging synthesis gas with pure hydrogen leads to hydrogenation and isomerization. This subnetwork analysis strategy will be explained in more detail in section 3.4.1. More experimental details about equipment and materials are summarized in appendix A.

Figure 3.7 summarizes series of *operando* FTIR spectra recorded during a) isomerization, b) hydrogenation and c) hydroformylation of 1-decene focusing on reactants and reaction products. Most interesting in this context are the $=\text{C}-\text{H}$ bending vibration region between 850 - 1050 cm^{-1} to observe conversion of the double bond as well as isomerization from terminal to internal positions and the $\text{C}=\text{O}$ stretching vibration region between 1650 - 1800 cm^{-1} to observe aldehyde production. Even at 40 °C, the catalyst is active, the reactions are fast and high conversions and yields can be achieved. Thus, a wide conversion range could be studied. Under isomerization conditions, fast isomerization occurs until complete conversion of 1-decene ($=\text{C}-\text{H}$ bending bands at 911 and 994 cm^{-1}) after 12 minutes to internal n-decenes ($=\text{C}-\text{H}$ bending band at 967 cm^{-1}). The same holds for the hydrogenation experiment where isomerization and hydrogenation are running simultaneously. It is not possible to observe the alkane product directly because it has the same bands as the olefin, apart from bands belonging to the double bond. Thus, decreasing signal intensity of the band belonging to the internal double bond at 967 cm^{-1} proves alkane production indirectly. Under hydroformylation conditions, almost no double bond isomerization and hydrogenation occurs whereas high conversion of 1-decene to undecanal ($\text{C}=\text{O}$ carbonyl stretching band at 1729 cm^{-1}) is achieved. The selectivity to the linear aldehyde, expressed as linear-to-branched aldehyde ratio, was confirmed using gas chromatography to be $\approx 99:1$.

Figure 3.8 summarizes series of *operando* FTIR spectra recorded during a) isomerization, b) hydrogenation and c) hydroformylation of 1-decene focusing on the metal carbonyl region to detect catalyst complexes or intermediates. The pre-formation of the Rh-BiPhePhos catalyst starts with dissolving the precursor $\text{Rh}(\text{acac})(\text{CO})_2$ in toluene and bringing it into contact with the ligand BiPhePhos (BP). The resulting $\text{Rh}(\text{acac})(\text{BP})$ complex is formed instantly under release of two equivalents gaseous

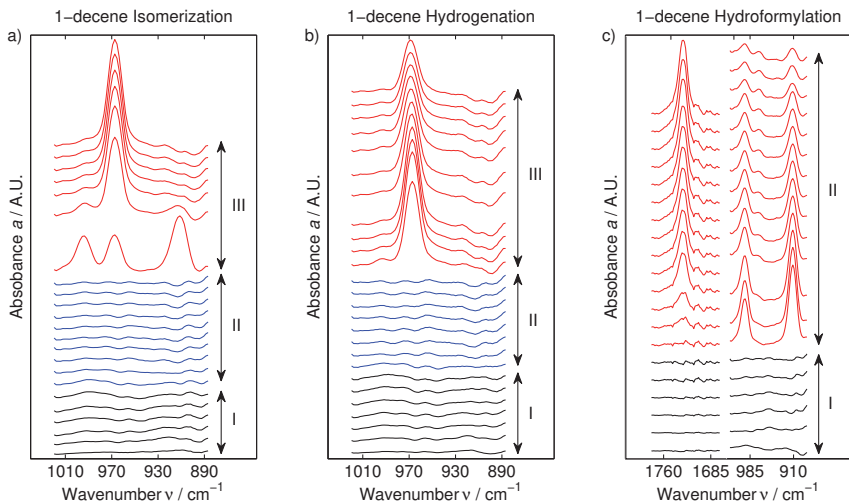


Figure 3.7: *Operando* FTIR spectra (=C–H bending vibration and C=O stretching vibration region) recorded during isomerization, hydrogenation and hydroformylation of 1-decene after solvent background subtraction. a) I: catalyst activation at 10 bar synthesis gas, II: gas phase exchange to 1 bar N₂, III: substrate injection, b) I: catalyst activation at 10 bar synthesis gas, II: gas phase exchange to 10 bar H₂, III: substrate injection and c) I: catalyst activation at 10 bar synthesis gas, II: substrate injection at 20 bar synthesis gas. (toluene, 40 °C, $c_{\text{sub}}^0 = 1 \text{ mol l}^{-1}$, Rh:sub (molar) = 1:500, Rh:lig (molar) = 1:1.5, time interval between spectra = 6 min)

CO [Jörke et al. 2017b]. Since the mixing of both substances took place beforehand, the starting signal belongs to the Rh(acac)(BP) complex in toluene that, of course, does not include carbonyl signals and thus appears as flat baseline (see first spectra in Figure 3.8a-c). Adding 10 bar synthesis gas under stirring initiated catalyst activation to form the hydrido-Rh-dicarbonyl complex HRh(BP)(CO)₂ with typical carbonyl bands at 2017 and 2075 cm⁻¹. These wavenumbers correspond to an *η,η*-coordinated ligand and were reported for this type of catalyst in the literature [Moasser et al. 1995; van Leeuwen et al. 2000; Kubis 2012]. Interestingly, no other carbonyl signals were detectable giving rise to the conclusion that using BiPhePhos as ligand allows the formation of hydrido-Rh-dicarbonyl complexes under synthesis gas atmosphere exclusively (see Figure 3.8a-c section I). Addition of 1-decene into the synthesis gas atmosphere does not change the detected spectra despite a reduction of signal intensity caused by dilution (see Figure 3.8c section II). The observed Rh-carbonyl bands belonging to the hydrido-Rh-dicarbonyl complex remain stable over the whole conversion range (> 90 %) and saturated acyl complexes were not observed.

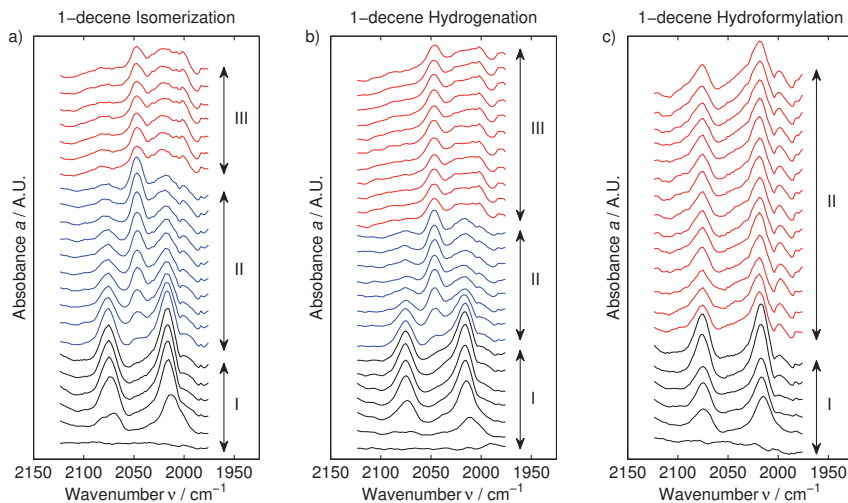


Figure 3.8: *Operando* FTIR spectra (metal carbonyl vibration region) recorded during isomerization, hydrogenation and hydroformylation of 1-decene after solvent background subtraction. a) I: catalyst activation at 10 bar synthesis gas, II: gas phase exchange to 1 bar N_2 , III: substrate injection, b) I: catalyst activation at 10 bar synthesis gas, II: gas phase exchange to 10 bar H_2 , III: substrate injection and c) I: catalyst activation at 10 bar synthesis gas, II: substrate injection at 20 bar synthesis gas. (toluene, $40\text{ }^\circ\text{C}$, $c_{\text{sub}}^0 = 1\text{ mol l}^{-1}$, Rh:sub (molar) = 1:500, Rh:lig (molar) = 1:1.5, time interval between spectra = 6 min)

If the synthesis gas atmosphere is exchanged after catalyst activation with inert nitrogen or hydrogen (see Figure 3.8a-b section II) significant changes were observed in the Rh-carbonyl region. The bands belonging to the hydrido-Rh-dicarbonyl complex disappear almost completely and a new band rises at 2047 cm^{-1} . This band remains stable under isomerization and hydrogenation conditions over the full conversion range. Other bands, however, were not detectable (see Figure 3.8a-b) section III). Whereas it is pretty obvious that the bands at 2017 and 2075 cm^{-1} belong to the hydrido-Rh-dicarbonyl complex $\text{HRh}(\text{BP})(\text{CO})_2$ [Moasser et al. 1995; van Leeuwen et al. 2000; Kubis 2012], the new band at 2047 cm^{-1} was not described in the literature yet. Since the conditions under which this band appears are almost CO free, it is likely that a hydrido-Rh-monocarbonyl complex $\text{HRh}(\text{BP})(\text{CO})$ was formed, confirming the catalyst pre-equilibrium shown in Figure 3.6. Such a complex would be an extremely reactive unsaturated 16ve complex. Hence, a free ligand or the sterically less demanding H-acac might take the free coordination site, stabilizing the monocarbonyl complex without deactivating it. An approaching substrate molecule

would replace such a “placeholder” molecule easily, so it was omitted in Figure 3.6 for better clarity.

Detailed DFT calculations were performed in [Kohls 2018 - in preparation] to identify the catalyst complexes being responsible for the experimentally observed FTIR spectra. In total, four potentially relevant Rh-BiPhePhos catalyst structures were calculated using the BP86 functional/def2-TZVP basis set for comparison to experimental data: i) a hydrido-Rh-dicarbonyl complex $\text{HRh}(\text{BP})(\text{CO})_2$ with *e,e*-coordination of the ligand ii) a Rh-dimer with simultaneously bridging μ -CO and ligand, iii) a hydrido-Rh-monocarbonyl complex with trans coordination of hydride and CO in the same vertical axis and iv) a hydrido-Rh-monocarbonyl complex with cis coordination of hydride and CO [Kohls 2017, 2018 - in preparation]. The corresponding structures are shown in Figure F.3 in appendix F.2. In Figure 3.9, the corresponding calculated IR spectra are compared to experimentally observed FTIR spectra. The presence of the hydrido-Rh-dicarbonyl complex $\text{HRh}(\text{BP})(\text{CO})_2$ with

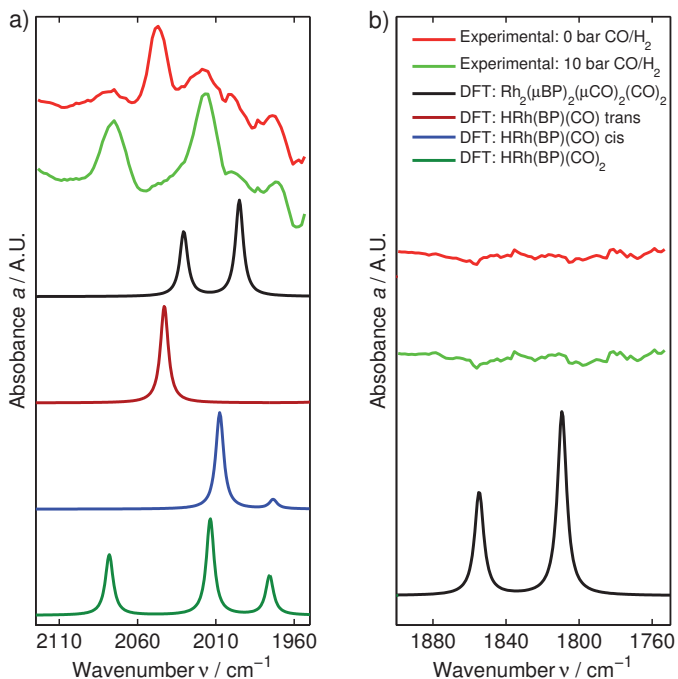


Figure 3.9: Comparison of experimentally observed FTIR spectra with DFT calculations (shifted by 15 cm^{-1} to higher wavenumbers) taken from [Kohls 2017, 2018 - in preparation]: a) Rh-carbonyl region, b) bridging carbonyl region.

e,e -coordination of the ligand was clearly confirmed by DFT calculations. The band at 2047 cm^{-1} appearing in absence of CO was assigned to a hydrido-Rh-monocarbonyl complex $\text{HRh}(\text{BP})(\text{CO})$ with the hydride and the carbonyl ligand in the same vertical axis¹. The *cis* isomer of this complex was not observable. A Rh-dimer could not be confirmed neither, even under extreme CO or H_2 lean conditions, because of the absence of typical bridging $\mu\text{-CO}$ signals between 1800 and 1900 cm^{-1} and the non-matching carbonyl bands around 2000 cm^{-1} .

The hydroformylation experiment shown in Figure 3.7c was used to analyze the kinetics of the hydroformylation reaction until high substrate conversion of $\approx 80\%$ (see Figure 3.10). Normalizing the observed $\text{C}=\text{O}$ stretching band of undecanal at 1729 cm^{-1} band as well as the $=\text{C}-\text{H}$ bending band at 911 cm^{-1} of 1-decene in accordance to the stoichiometry of the hydroformylation reaction (see Figure 3.10a) allowed to use them for the calculation of time dependent 1-decene conversion X (3.9) and subsequently the turnover frequency TOF (3.7).

$$TOF = \frac{r_{\text{hyf}}(t)}{c_{\text{Rh,tot}}} \quad (3.7)$$

$$r_{\text{hyf}} = -\frac{dc_{1\text{D}}}{dt} \approx -\frac{\Delta c_{1\text{D}}}{\Delta t} \quad (3.8)$$

$$X = \frac{c_{1\text{D}}^0 - c_{1\text{D}}}{c_{1\text{D}}^0} = 1 - \frac{a_{911\text{ cm}^{-1}}}{a_{911\text{ cm}^{-1}}^0} \quad (3.9)$$

$$c_{1\text{D}}^n = \frac{c_{1\text{D}}}{c_{1\text{D}}^0} = \frac{a_{911\text{ cm}^{-1}}}{a_{911\text{ cm}^{-1}}^0} \quad (3.10)$$

The TOF corresponds to the reaction rate and was plotted vs. the normalized concentration 1-decene (3.10) in Figure 3.10b. The linear regression in Figure 3.10b shows an excellent linear correlation coefficient ($R^2 = 0.9520$). The same result was obtained using a higher initial concentration of 1-decene (1.63 mol l^{-1}) and lower Rh:substrate ratio (1:1000) [Jörke et al. 2017b]. Hence, the hydroformylation of long-chain *n*-olefins is evidently a first-order reaction with respect to the substrate concentration, if a Rh-BiPhePhos catalyst is used. Combining this finding with the aforementioned IR results (no detectable Rh-intermediate from "inside" the catalytic cycles) leads to the conclusion that the olefin coordination to the Rh-catalyst is rate determining.

¹ As already discussed, an attached ligand, solvent or H-acac molecule is probably stabilizing the hydrido-Rh-monocarbonyl. DFT calculations proved no significant shift of the CO band, if a solvent molecule (DMF) is taking the free coordination site [Kohls 2017, 2018 - in preparation].

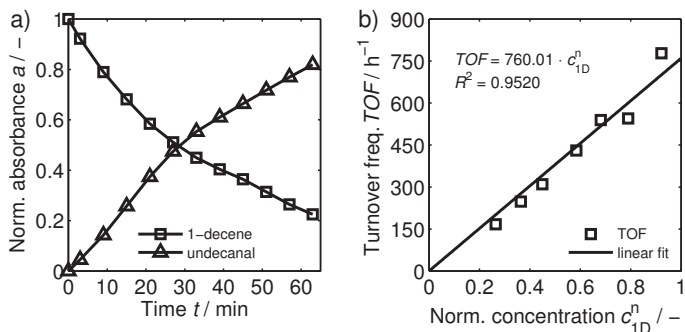


Figure 3.10: Hydroformylation kinetics studied with *operando* FTIR spectroscopy: a) concentration profiles of 1-decene and undecanal and b) linear regression of the *TOF* vs. substrate concentration. (toluene, 40 °C, 20 bar synthesis gas, $c_{\text{sub}}^0 = 1 \text{ mol l}^{-1}$, Rh:sub (molar) = 1:500, Rh:lig (molar) = 1:1.5)

3.2.2 Reduced hydroformylation reaction mechanism for n-decene

The IR-spectroscopic findings presented in the previous section allow to derive a reduced hydroformylation reaction mechanism for n-decenes presented in Figure 3.11. The following assumptions were made to reduce the reaction mechanism:

1. All inactive or non selective species are neglected except for the hydrido-Rh-dicarbonyl complex $\text{HRh}(\text{BP})(\text{CO})_2$.
2. All oxidative additions of hydrogen are irreversible as well as all reductive elimination steps [Garland and Pino 1991; van Rooy et al. 1995; Bhanage et al. 1997].
3. The coordination of the olefin double bond to the catalyst is rate determining for isomerization, hydrogenation and hydroformylation.

The well-founded complexity reduction, especially in the catalyst pre-equilibrium, allows the derivation of handy mechanistic kinetic models with a low number of unknown parameters without accepting accuracy losses. In the following section, a corresponding mechanistic kinetic model will be derived using the reduced reaction mechanism and including all relevant side reactions (isomerization and hydrogenation) as well as the main hydroformylation reaction.

than internal n-decenes due to less steric hindrances (see [Behr and Neubert 2012] and section 3.4.2 in this work). Therefore, the branch **IIb** in figure Figure 3.11 was neglected and only one reaction rate equation is needed for the hydrogenation of 1-decene to decane (r_{hyd}). In case of hydroformylation, it is assumed that 1-decene is converted to the desired linear aldehyde undecanal (r_{hyf1}) but also to the undesired branched aldehyde 2-methyl-decanal (r_{hyf2}). Additionally, internal n-decenes can also be converted to branched aldehydes. However, it was not possible in this thesis to distinguish which internal olefin is converted to which branched aldehyde. Thus, a third rate law was set up, which represents the transformation of the sum of all internal n-decenes to the pseudo-component "iso-aldehyde" (r_{hyf3}).

If several catalytic cycles are running in parallel, as it is the case for Rh-BiPhePhos, it is possible that they have an influence on each other making the kinetic modeling very complicated. However, considering the reaction cycles as independent from each other, justifying the usage of equation (2.28) without taking interaction between cycles into account, is possible, if the majority of the catalyst material is located at the starting point of the cycles and not within a cycle [Helferich 2004]. This situation is equivalent with the substrate coordination to the catalyst being the rate determining step which is the case for the Rh-BiPhePhos catalyst used (see section 3.2.1). The following subsections will illustrate the derivation of all rate equations using Christiansen's approach presented in detail in section 2.2.2 as well as the derivation of an equation representing the catalyst pre-equilibrium.

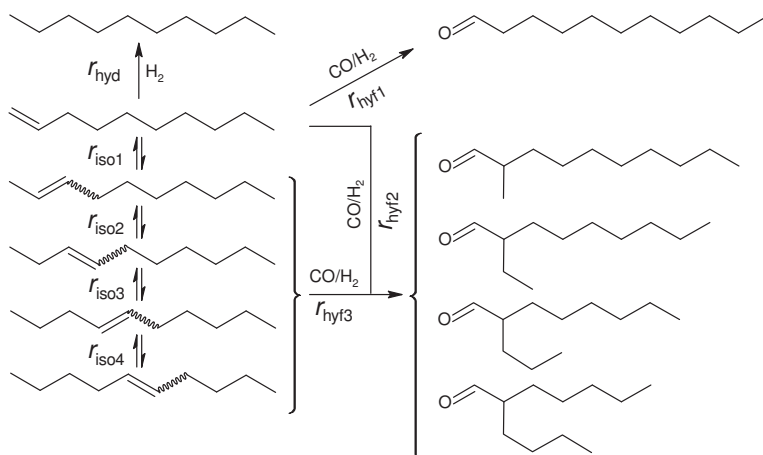


Figure 3.12: Hydroformylation reaction network of 1-decene including main (r_{hyf1}) and side reactions.

3.3.1 Catalyst pre-equilibrium

The catalyst pre-equilibrium is an important part of the kinetic model because it controls the amount of available active catalyst. The equilibrium assumption between saturated 18ve hydrido-Rh-dicarbonyl (DC) complexes $\text{HRh}(\text{BP})(\text{CO})_2$ and active 16ve hydrido-Rh-monocarbonyl (MC) complexes $\text{HRh}(\text{BP})(\text{CO})$ is equivalent with a fast dissociation of CO. Assuming a fast dissociation of CO is reasonable for phosphite ligands, because CO and the phosphite compete with each other for π -backbonding at the Rh-center, which weakens the Rh-CO bond [Kamer et al. 2004; Shaharun et al. 2010; Behr and Neubert 2012; Franke et al. 2012]. The reversibility of this reaction was proven experimentally in this thesis using *operando* FTIR spectroscopy in section 4.2.1 (see Figure 4.11b). Hence, the concentration of $\text{HRh}(\text{BP})(\text{CO})$ can be calculated from a Rh mass balance (3.11) and a mass action law formulation of the equilibrium between those complexes (3.12). The total amount of Rh is equal to the amount of catalyst precursor $\text{Rh}(\text{acac})(\text{CO})_2$.

$$c_{\text{Rh,tot}} = c_{\text{DC}} + c_{\text{MC}} \quad (3.11)$$

$$K_{\text{cat}}^I = \frac{c_{\text{DC}}}{c_{\text{MC}}c_{\text{CO}}} \quad (3.12)$$

Combining equations (3.11) and (3.12) leads to an explicit expression for the concentration of active $\text{HRh}(\text{BP})(\text{CO})$ as function of the catalyst precursor and dissolved CO concentrations (3.13).

$$c_{\text{MC}} = \frac{c_{\text{Rh,tot}}}{(1 + K_{\text{cat}}^I c_{\text{CO}})} \quad (3.13)$$

3.3.2 Isomerization

The double bond isomerization of n-decenes is a reversible equilibrium limited reaction. Therefore, all four steps in the corresponding reaction cycle are reversible and no step can be neglected. The set of pseudo first-order rate coefficients ω_{ij} (3.14) (see section 2.2.2) holds for all four isomerization rate equations that are necessary to describe the isomerization equilibrium of n-decenes.

$$\begin{aligned} \omega_{12} &= k_{12}c_{iD} & \omega_{21} &= k_{21} \\ \omega_{23} &= k_{23} & \omega_{32} &= k_{32} \\ \omega_{34} &= k_{34} & \omega_{43} &= k_{43} \\ \omega_{41} &= k_{41} & \omega_{14} &= k_{14}c_{(i+1)D} \end{aligned} \quad i = 1 \dots 4 \quad (3.14)$$

The resulting Christiansen Matrix $\bar{\bar{C}}_{\text{iso}}$ (3.15) (cf. equation (2.29)) depends on a constant term (first row), substrate concentration c_{iD} and product isomer concentration $c_{(i+1)D}$.

$$\bar{\bar{C}}_{\text{iso}} = \begin{pmatrix} \Omega_{11} & \Omega_{12} & \Omega_{13} & \Omega_{14} \\ \Omega_{21}(c_{iD}) & \Omega_{22}(c_{iD}) & \Omega_{23}(c_{iD}) & \Omega_{24}(c_{(i+1)D}) \\ \Omega_{31}(c_{iD}) & \Omega_{32}(c_{iD}) & \Omega_{23}(c_{(i+1)D}) & \Omega_{34}(c_{(i+1)D}) \\ \Omega_{41}(c_{iD}) & \Omega_{42}(c_{(i+1)D}) & \Omega_{23}(c_{(i+1)D}) & \Omega_{44}(c_{(i+1)D}) \end{pmatrix} \quad i = 1 \dots 4 \quad (3.15)$$

From assuming the substrate coordination to be rate determining (holds also for the coordination of the product isomer) follows a simplified Christiansen Matrix. Only constant terms of the first row remain in the simplified Christiansen Matrix (3.16) because all terms containing the elementary step rate constant k_{12} and k_{14} , representing coordination of n-decenes, are negligibly small.

$$\bar{\bar{C}}_{\text{iso}} = \begin{pmatrix} \Omega_{11} & \Omega_{12} & \Omega_{13} & \Omega_{14} \\ 0 & 0 & 0 & 0 \\ 0 & 0 & 0 & 0 \\ 0 & 0 & 0 & 0 \end{pmatrix} \quad (3.16)$$

Applying (2.28) using (3.16) leads to the final explicit n-decene double bond isomerization rate expressions (3.18) after lumping all elementary step rate constant products in (3.17).

$$r_{\text{iso}i} = \frac{k_{12}k_{23}k_{34}k_{41}c_{iD} - k_{21}k_{32}k_{43}k_{14}c_{jD}}{\begin{pmatrix} k_{23}k_{34}k_{41} + k_{21}k_{34}k_{41} + \\ k_{21}k_{32}k_{41} + k_{21}k_{32}k_{43} \end{pmatrix}} \cdot \frac{c_{\text{Rh,tot}}}{(1 + K_{\text{cat}}^I c_{\text{CO}})} \quad (3.17)$$

$$r_{\text{iso}i} = k_{\text{iso}i}(T) \left(c_{iD} - \frac{c_{jD}}{K_{ji}^{\text{eq}}} \right) \cdot \frac{c_{\text{Rh,tot}}}{(1 + K_{\text{cat}}^I c_{\text{CO}})} \quad i = 1 \dots 4, j = i + 1 \quad (3.18)$$

3.3.3 Hydrogenation

The hydrogenation of 1-decene to n-decane is not reversible because the reductive product elimination step as well as the oxidative hydrogen addition step are considered to be irreversible. Thus, the corresponding pseudo first-order rate coefficients of the backward reactions ω_{43} and ω_{14} are zero. The resulting set of pseudo first-order

rate coefficients is summarized in (3.19).

$$\begin{aligned}
 \omega_{12} &= k_{12}c_{1D} & \omega_{21} &= k_{21} \\
 \omega_{23} &= k_{23} & \omega_{32} &= k_{32} \\
 \omega_{34} &= k_{34}c_{H2} & \omega_{43} &= 0 \\
 \omega_{41} &= k_{41} & \omega_{14} &= 0
 \end{aligned} \tag{3.19}$$

The resulting Christiansen Matrix $\bar{\bar{C}}_{\text{hyd}}$ (3.20) (cf. equation (2.29)) depends on a constant term, substrate concentration c_{1D} and dissolved hydrogen concentration c_{H2} .

$$\bar{\bar{C}}_{\text{hyd}} = \begin{pmatrix} \Omega_{11}(c_{H2}) & \Omega_{12}(c_{H2}) & \Omega_{13} & 0 \\ \Omega_{21}(c_{1D}, c_{H2}) & \Omega_{22}(c_{1D}) & 0 & 0 \\ \Omega_{31}(c_{1D}) & 0 & 0 & 0 \\ \Omega_{41}(c_{1D}, c_{H2}) & 0 & 0 & 0 \end{pmatrix} \tag{3.20}$$

From assuming the substrate coordination to be rate determining follows a simplified Christiansen Matrix depending only on a constant term and the concentration of dissolved hydrogen (3.21) because all terms containing the corresponding elementary step rate constant k_{12} are negligibly small.

$$\bar{\bar{C}}_{\text{hyd}} = \begin{pmatrix} \Omega_{11}(c_{H2}) & \Omega_{12}(c_{H2}) & \Omega_{13} & 0 \\ 0 & 0 & 0 & 0 \\ 0 & 0 & 0 & 0 \\ 0 & 0 & 0 & 0 \end{pmatrix} \tag{3.21}$$

Applying (2.28) using (3.21) leads to the final explicit 1-decene hydrogenation rate expression (3.22) after lumping all elementary step rate constant products in (3.22).

$$r_{\text{hyd}} = \frac{k_{12}k_{23}k_{34}k_{41} c_{1D} c_{H2}}{\left(\frac{k_{21}k_{32}k_{41} + (k_{23}k_{34}k_{41} + k_{21}k_{34}k_{41}) c_{H2}}{1 + K_{\text{cat}}^1 c_{\text{CO}}} \right)} \cdot \frac{c_{\text{Rh,tot}}}{(1 + K_{\text{cat}}^1 c_{\text{CO}})} \tag{3.22}$$

$$r_{\text{hyd}} = \frac{k_{\text{hyd}}(T) c_{1D} c_{H2}}{(1 + K_{\text{hyd}} c_{H2})} \cdot \frac{c_{\text{Rh,tot}}}{(1 + K_{\text{cat}}^1 c_{\text{CO}})} \tag{3.23}$$

3.3.4 Hydroformylation

The hydroformylation of 1-decene to undecanal is not reversible because the reductive product elimination step as well as the oxidative hydrogen addition step are considered to be irreversible. Thus, the corresponding pseudo first-order rate coefficients of the backward reactions ω_{65} and ω_{16} are zero. The resulting set of pseudo first-order

rate coefficients is summarized in (3.24).

$$\begin{aligned}
 \omega_{12} &= k_{12}c_{1D} & \omega_{21} &= k_{21} \\
 \omega_{23} &= k_{23} & \omega_{32} &= k_{32} \\
 \omega_{34} &= k_{34}c_{CO} & \omega_{43} &= k_{43} \\
 \omega_{45} &= k_{45} & \omega_{54} &= k_{54} \\
 \omega_{56} &= k_{56}c_{H2} & \omega_{65} &= 0 \\
 \omega_{61} &= k_{61} & \omega_{16} &= 0
 \end{aligned} \tag{3.24}$$

The corresponding Christiansen Matrix $\bar{\bar{C}}_{\text{hyf}}$ (3.25) (cf. equation (2.29)) depends on a constant term, substrate concentration c_{1D} and dissolved H_2 and CO concentrations c_{H2} and c_{CO} , respectively.

$$\bar{\bar{C}}_{\text{hyf}} = \begin{pmatrix} \Omega_{11}(c_{CO}, c_{H2}) & \Omega_{12}(c_{CO}, c_{H2}) & \Omega_{13}(c_{H2}) & \Omega_{14}(c_{H2}) & \Omega_{15} & 0 \\ \Omega_{21}(c_{1D}, c_{CO}, c_{H2}) & \Omega_{22}(c_{1D}, c_{H2}) & \Omega_{23}(c_{1D}, c_{H2}) & \Omega_{24}(c_{1D}) & 0 & 0 \\ \Omega_{31}(c_{1D}, c_{H2}) & \Omega_{32}(c_{1D}, c_{H2}) & \Omega_{33}(c_{1D}) & 0 & 0 & 0 \\ \Omega_{41}(c_{1D}, c_{CO}, c_{H2}) & \Omega_{42}(c_{1D}, c_{CO}) & 0 & 0 & 0 & 0 \\ \Omega_{51}(c_{1D}, c_{CO}) & 0 & 0 & 0 & 0 & 0 \\ \Omega_{61}(c_{1D}, c_{CO}, c_{H2}) & 0 & 0 & 0 & 0 & 0 \end{pmatrix} \tag{3.25}$$

From assuming the substrate coordination to be rate determining follows a simplified Christiansen Matrix depending only on a constant term and the concentrations of dissolved H_2 and CO (3.21) because all terms containing the corresponding elementary step rate constant k_{12} are negligibly small.

$$\bar{\bar{C}}_{\text{hyf}} = \begin{pmatrix} \Omega_{11}(c_{CO}, c_{H2}) & \Omega_{12}(c_{CO}, c_{H2}) & \Omega_{13}(c_{H2}) & \Omega_{14}(c_{H2}) & \Omega_{15} & 0 \\ 0 & 0 & 0 & 0 & 0 & 0 \\ 0 & 0 & 0 & 0 & 0 & 0 \\ 0 & 0 & 0 & 0 & 0 & 0 \\ 0 & 0 & 0 & 0 & 0 & 0 \\ 0 & 0 & 0 & 0 & 0 & 0 \end{pmatrix} \tag{3.26}$$

Applying (2.28) using (3.26) leads to the final explicit 1-decene hydroformylation rate expression (3.28) after lumping all elementary step rate constant products in (3.27).

$$r_{\text{hyf1}} = \frac{k_{12}k_{23}k_{34}k_{45}k_{56}k_{61} c_{1D} c_{CO} c_{H2}}{\left(\begin{aligned} &k_{21}k_{32}k_{43}k_{54}k_{61} + \\ &(k_{21}k_{32}k_{45}k_{56}k_{61} + k_{21}k_{32}k_{43}k_{56}k_{61}) c_{H2} + \\ &(k_{23}k_{34}k_{45}k_{56}k_{61} + k_{21}k_{34}k_{45}k_{56}k_{61}) c_{H2}c_{CO} \end{aligned} \right)} \cdot \frac{c_{\text{Rh,tot}}}{(1 + K_{\text{cat}}^I c_{CO})} \tag{3.27}$$

$$r_{\text{hyf1}} = \frac{k_{\text{hyf1}}(T) c_{1D} c_{\text{CO}} c_{\text{H2}}}{\left(1 + K_{\text{hyf}}^{\text{I}} c_{\text{H2}} + K_{\text{hyf}}^{\text{II}} c_{\text{H2}} c_{\text{CO}}\right)} \cdot \frac{c_{\text{Rh,tot}}}{\left(1 + K_{\text{cat}}^{\text{I}} c_{\text{CO}}\right)} \quad (3.28)$$

In principle, the rate equations describing the production of branched aldehydes from 1-decene as well as from internal n-decenes (3.29)-(3.30) have the same structure as the rate equation for the production of undecanal (3.28) but with different kinetic parameter values.

$$r_{\text{hyf2}} = \frac{k_{\text{hyf2}}(T) c_{1D} c_{\text{CO}} c_{\text{H2}}}{\left(1 + K_{\text{hyf}}^{\text{III}} c_{\text{H2}} + K_{\text{hyf}}^{\text{IV}} c_{\text{H2}} c_{\text{CO}}\right)} \cdot \frac{c_{\text{Rh,tot}}}{\left(1 + K_{\text{cat}}^{\text{I}} c_{\text{CO}}\right)} \quad (3.29)$$

$$r_{\text{hyf3}} = \frac{k_{\text{hyf3}}(T) \sum_{i=2}^5 c_{iD} c_{\text{CO}} c_{\text{H2}}}{\left(1 + K_{\text{hyf}}^{\text{III}} c_{\text{H2}} + K_{\text{hyf}}^{\text{IV}} c_{\text{H2}} c_{\text{CO}}\right)} \cdot \frac{c_{\text{Rh,tot}}}{\left(1 + K_{\text{cat}}^{\text{I}} c_{\text{CO}}\right)} \quad (3.30)$$

The temperature dependence of the rate constants is expressed by a reparameterized Arrhenius approach (2.38) described in more detail in section 2.2.2. Summarizing, eight rate equations were derived containing 22 unknown parameters including kinetic rate constants, apparent activation energies, inhibition constants and equilibrium constants. Values for the four double bond isomerization equilibrium constants K_{ij}^{eq} were calculated in section 3.1.2.

The next section is dedicated to carefully designed kinetic (semi-) batch experiments to generate experimental data for the estimation of the unknown kinetic parameters.

3.4 Kinetic experiments and parameter estimation

In this section, the design of kinetic (semi-) batch experiments using the equipment described in detail in appendix A is explained in terms of a subnetwork analysis strategy. The estimation of unknown kinetic parameter values belonging to the kinetic model developed in the previous section follows subsequently. The parameter estimation was performed by minimizing a least-squares objective function using experimental data from (semi-) batch experiments, the developed kinetic model and the reactor model presented in section 2.2.1. Matlab 2012a was used with a standard non-linear least-squares solver (lsqnonlin) and central differences for gradient approximation. All experiments were evaluated simultaneously to estimate the kinetic parameter vector as a whole without using sequential fitting procedures. Therefore, all estimated kinetic parameter values are valid for all studied reaction conditions, although the subnetworks will be discussed individually in the corresponding sections.

3.4.1 Experimental design and subnetwork analysis

Since all branches in the extended mechanism discussed above run in parallel, it is difficult to study them individually. Therefore, the complex system was divided into three major subnetworks (isomerization, hydrogenation and hydroformylation). Controlling which reaction takes place is possible by manipulating the gas phase composition which is possible by gas phase exchange after activation of the catalyst with synthesis gas. Subsequently, it was possible to study the individual subnetworks with increasing complexity (isomerization < hydrogenation < hydroformylation).

3.4.1.1 Catalyst activation

To activate the catalyst, the Rh-precursor $\text{Rh}(\text{acac})(\text{CO})_2$ and the ligand BiPhePhos were dissolved in DMF and n-dodecane at room temperature. Details about the used thermomorphic multicomponent solvent system (TMS) are summarized in appendix A. The mixture was added to the reactor and inertized under stirring with Schlenk technique using nitrogen. Pressurizing the reactor with synthesis gas ($\text{CO}:\text{H}_2 = 1:1$, isomerization/hydrogenation: 15 bar, hydroformylation: ≈ 2 bar less than reaction pressure) while heating up the mixture to reaction temperature (95 - 135 °C, ca. 30 min) under constant stirring (1200 rpm) initiated the formation of saturated 18ve hydrido-Rh-dicarbonyl complexes $\text{HRh}(\text{BP})(\text{CO})_2$ (see Figure 3.8 in section 3.2.1).

3.4.1.2 Isomerization subnetwork

Studying the isomerization subnetwork aims for generation of experimental data to estimate kinetic parameters that belong to the derived isomerization reaction rate laws $r_{\text{iso}1-4}$ (3.18) (cf. Figure 3.12). The procedure is explained in the following.

The synthesis gas atmosphere was removed completely after catalyst activation to perform double bond isomerization reactions without hydrogenation or hydroformylation. Cooling down the reactor to room temperature before removing the gas phase using a vacuum pump and inert nitrogen for flushing was necessary to avoid evaporation of the solvents. Subsequent n-olefin injection into the reaction mixture containing the activated catalyst via a pressure lock with inert pressurized nitrogen or CO starts the isomerization reaction (see appendix A for more details about the used equipment).

Using CO as injection gas allows to study the CO dependence of the equilibrium between the saturated and inactive 18ve hydrido-Rh-dicarbonyl complex $\text{HRh}(\text{BP})(\text{CO})_2$ and the unsaturated and active 16ve hydrido-Rh-monocarbonyl complex $\text{HRh}(\text{BP})(\text{CO})$ indirectly. This is possible, because the isomerization reaction itself is not influenced by CO (see Figure 3.11). Hence, a CO induced change in isomerization rate has to originate from the formation of inactive $\text{HRh}(\text{BP})(\text{CO})_2$

reducing the overall available amount of active catalyst material. In total, six isomerization experiments were performed. The experimental conditions, initial pressures and initial molar ratios are summarized in Table 3.4. At CO pressures below 2 bar, additional 2 bar of inert nitrogen was added to allow sampling of the liquid reaction mixture. In all other cases, the partial pressure of CO is identical to the total pressure.

3.4.1.3 Hydrogenation subnetwork

Investigating the hydrogenation subnetwork aims for generation of experimental data to estimate kinetic parameters that belong to the derived hydrogenation reaction rate law r_{hyd} (3.23). Additionally, the isomerization reaction rates $r_{\text{iso}1-4}$ (3.18) are included in the hydrogenation subnetwork (cf. Figure 3.12). In the following, the procedure is explained.

The synthesis gas atmosphere was removed completely after catalyst activation and replaced with pure H_2 . The applied H_2 pressure before substrate injection was set to 1-2 bar below the initial hydrogenation pressure to keep the catalyst close to the desired reaction conditions. Different feed mixtures were hydrogenated to study, if the components are influencing each other. In total, four hydrogenation experiments were performed. The experimental conditions, initial H_2 pressures and initial molar ratios are summarized in table Table 3.4. It should be noted that the hydrogenation subnetwork includes the isomerization subnetwork.

3.4.1.4 Hydroformylation network

Investigating the hydroformylation network aims for generation of experimental data to estimate kinetic parameters that belong to the derived hydroformylation reaction rate laws $r_{\text{hyf}1-3}$ (3.28)-(3.30). Additionally, the isomerization $r_{\text{iso}1-4}$ (3.18) and hydrogenation reaction rates r_{hyd} (3.23) are included in the hydroformylation network (cf. Figure 3.12). In the following, the procedure is explained.

Performing hydroformylation reactions does not require to exchange the gas phase after catalyst activation. Using 1-decene and a technical equilibrium mixture of internal n-decenes in different feed ratios allowed to study the coupling between isomerization and hydroformylation. Since the tandem isomerization-hydroformylation reaction is slow, reaction temperature and catalyst loading were increased up to 135 °C to preserve the catalyst from thermal stress induced degradation [Gaide et al. 2017b] and a Rh:substrate ratio of 1:500, respectively. In total, eight hydroformylation experiments using 1-decene as initial substrate and five tandem isomerization-hydroformylation experiments using an equilibrated n-decene mixture as initial substrate were performed. The experimental conditions, initial synthesis gas

pressures and initial molar ratios are summarized in Table 3.4. It should be noted that the hydroformylation network is the most general case including the isomerization and hydrogenation subnetworks.

Table 3.4: Experimental design for subnetwork analysis: Isomerization, hydrogenation, hydroformylation and tandem isomerization-hydroformylation. Solvent: TMS. Rh:lig (molar) = 1:3 (except iHyf4 and 5: 1:5). Initial concentration of n-decene: 0.9 mol l^{-1} (except iHyf5: 1.2 mol l^{-1}).

Exp. ID	p / bar	T / °C	1D:iD	Rh:substrate	Gas supply
Iso1	0	105	1:0	1:10000	No consumption
Iso2	1	105	1:1	1:10000	No consumption
Iso3	5	105	1:0	1:10000	No consumption
Iso4	10	105	1:0	1:10000	No consumption
Iso5	5	95	1:0	1:10000	No consumption
Iso6	5	115	1:0	1:10000	No consumption
Hyd1	20	105	3:1	1:10000	batch
Hyd2	21	105	0:1	1:10000	batch
Hyd3	10	95	0:1	1:10000	batch
Hyd4	10	115	0:1	1:10000	batch
Hyf1	5	105	1:0	1:10000	batch
Hyf2	10	105	1:0	1:10000	batch
Hyf3	20	105	1:0	1:10000	batch
Hyf4	20	105	1:1	1:10000	batch
Hyf5	5	105	7:4	1:10000	batch
Hyf6	5	105	2:9	1:10000	batch
Hyf7	20	115	1:0	1:10000	batch
Hyf8	20	95	1:0	1:10000	batch
iHyf1	5	105	0:1	1:1000	semi-batch
iHyf2	10	105	0:1	1:1000	semi-batch
iHyf3	20	105	0:1	1:1000	semi-batch
iHyf4	5	135	0:1	1:1000	semi-batch
iHyf5	5	135	0:1	1:500	semi-batch

3.4.2 Isomerization subnetwork

Six isomerization batch experiments were performed (see Table 3.4) to estimate kinetic parameter values using the generated experimental data. Time resolved concentration profiles of the isomerization of 1-decene to internal n-decenes are presented in Figure 3.13 as well as the corresponding modeling results. The estimated kinetic parameters for catalyst pre-equilibrium and double bond isomerization are summarized in Table 3.5.

According to experimental results, the n-decene double bond isomerization is strongly dependent on the applied partial pressure of CO. Without CO (Iso1),

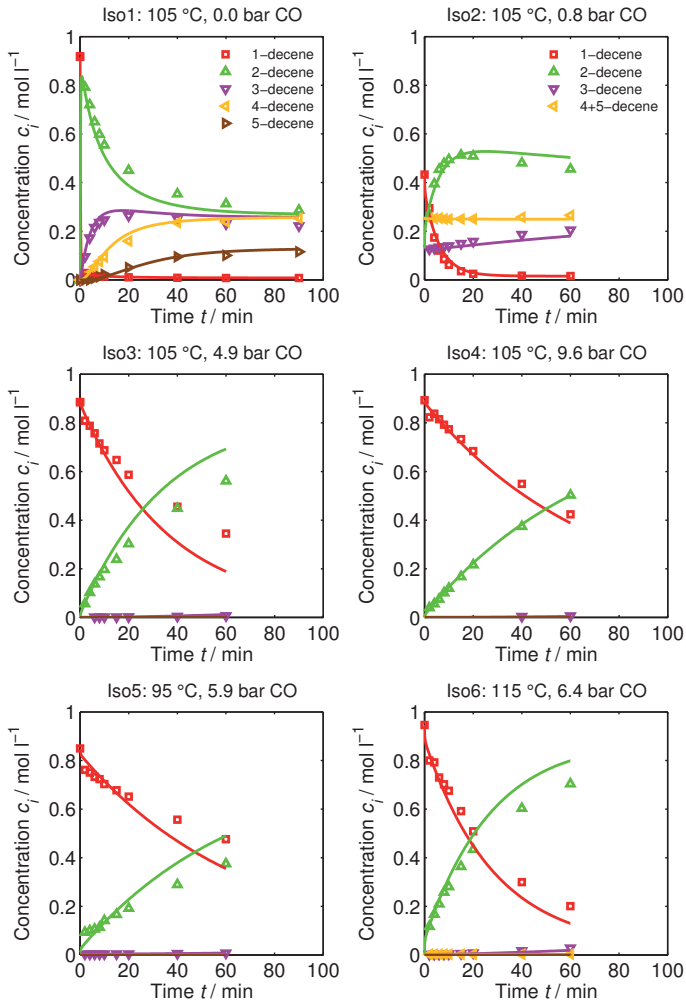


Figure 3.13: Experimental and modeling results of the isomerization subnetwork analysis for 1-decene. Symbols: Experimental data, Solid lines: Corresponding simulation using the developed mechanistic kinetic model with estimated parameter values. Legend in Iso1 holds for all plots except for Iso2. Experimental conditions: See Table 3.4.

the catalyst activity was extremely high (initial $TOF \approx 3 \cdot 10^5 \text{ h}^{-1}$). The reaction equilibrium between all possible n-decene isomers was reached in a series reaction sequence (see Figure 3.12) after 90 minutes. However, already low CO partial pressures (Iso2) inhibit the isomerization reaction rate significantly. At higher partial

pressures of CO (>5 bar, Iso3-6), no significant detection of double bond isomers beyond 2-decene was possible, indicating a strong reduction of catalyst activity. The observed reaction rate reduction is assigned to the formation of saturated and inactive hydrido-Rh-dicarbonyl complexes $\text{HRh}(\text{BP})(\text{CO})_2$ by the presence of strongly binding CO. Figure 3.14 shows the percentage of active catalyst material as a function of dissolved CO (3.13). It can be seen that already low CO partial pressures of 2 bar reduce the relative amount of active catalyst material below 1 % proving the catalyst pre-equilibrium being strongly on the side of the saturated Rh-dicarbonyl complex $\text{HRh}(\text{BP})(\text{CO})_2$. A very similar trend was found using a TDTBPP ligand in twenty-fold excess [Kubis et al. 2012].

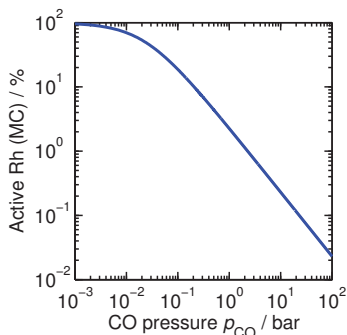


Figure 3.14: Relative amount of active catalyst in % as a function of CO partial pressure at 115 °C (equation (3.13)). The gas solubility of CO was determined experimentally for the used TMS (see appendix B).

It is evident from experimental data (Iso1) that isomerization rates slowed down with more internal double bond position. The corresponding relative isomerization rate constants at reference temperature are $k_{\text{iso1}} : k_{\text{iso2}} : k_{\text{iso3}} : k_{\text{iso4}} = 161.2 : 2.7 : 2.7 : 1$ (see table Table 3.5). One possible interpretation of decreasing rate constant values is an increase of steric hindrances for the substrate coordination to the Rh-catalyst with more internal double bond position.

The developed mechanistic kinetic model (3.18) fits the experimental data very well with only two estimated parameters per isomerization rate equation and one parameter controlling the catalyst pre-equilibrium. This emphasizes the advantage of mechanistic kinetic expressions and supports the assumption that the coordination of n-decenes is determining the rate of double bond isomerization. Using local parameter subset selection explained in section 2.3 proved all kinetic isomerization parameters to be identifiable using the experimental design in Table 3.4 (see Figure D.1a in appendix D). The recalculated apparent activation energies for the isomerization of 1-decene to 2-decene and all other isomerization reactions are 58.2

kJ mol^{-1} and 49.1 kJ mol^{-1} , respectively. These numbers are within the range of quantum chemical calculations for the isomerization of *n*-butenes and *n*-octenes with bulky Rh-diphosphine ligands ($\approx 40 - 80 \text{ kJ mol}^{-1}$ at $125 \text{ }^\circ\text{C}$) [Carvajal et al. 2009].

3.4.3 Hydrogenation subnetwork

Four hydrogenation batch experiments were performed (see Table 3.4) to estimate kinetic parameter values using the generated experimental data. Time resolved concentration profiles of the hydrogenation of 1-decene to decane are presented in Figure 3.15 as well as the corresponding modeling results. The estimated kinetic hydrogenation parameters are summarized in Table 3.5.

Since no CO is present in the hydrogenation experiments, the catalyst is always fully active and causes instant isomerization of 1-decene to internal *n*-decenes (Hyd1). The hydrogenation reaction, however, appears to be slow compared to double bond isomerization. This can be explained by assuming that 1-decene is

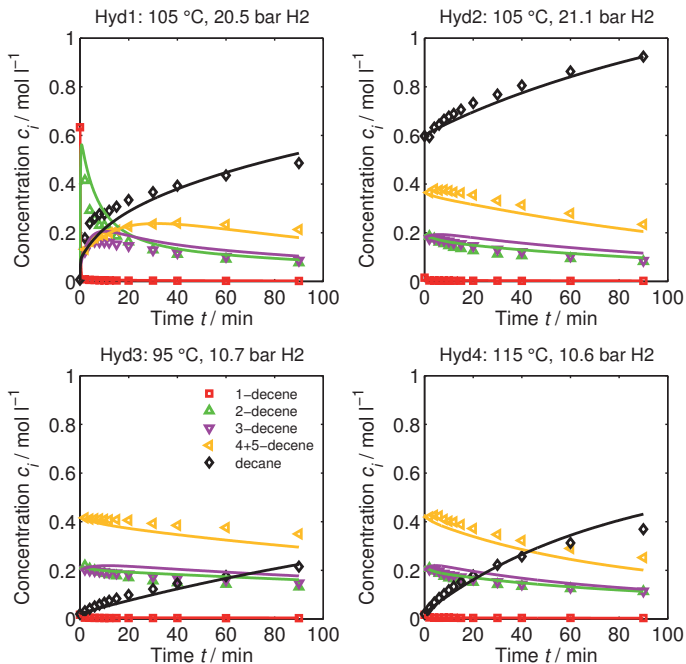


Figure 3.15: Experimental and modeling results of the hydrogenation subnetwork analysis for 1-decene. Symbols: Experimental data, Solid lines: Corresponding simulation using the developed mechanistic kinetic model with estimated parameter values. Experimental conditions: See Table 3.4.

hydrogenated preferably due to low steric hindrances and thus highest reactivity. The low concentration of 1-decene at equilibrium, however, causes a low driving force towards hydrogenation, which explains the low hydrogenation rate. While proceeding, the hydrogenation consumes 1-decene and disturbs the isomerization equilibrium. The double bond isomerization reaction works against this disturbance and restores the equilibrium by converting internal n-decenes to 1-decene (Hyd2). In this sense, the hydrogenation is a tandem reaction as well as the tandem isomerization-hydroformylation discussed in section 3.2.

The mechanistic kinetic model represents the experimental data very well with only three kinetic hydrogenation parameters (see table Table 3.5). Again, the assumption that the olefin coordination is the rate determining step for the hydrogenation as well is supported by the good accordance between model and experimental data. The tandem character of the hydrogenation is achieved by modeling the simultaneously running isomerization reaction as equilibrium limited reaction being able to run back and forth. The coupling element is the concentration of 1-decene, which is consumed by hydrogenation and refilled by the back-isomerization of internal n-decenes. Using local parameter subset selection explained in section 2.3 proved all kinetic hydrogenation parameters to be identifiable using the experimental design in Table 3.4 (see Figure D.1b in appendix D). The recalculated apparent activation energy for the hydrogenation of 1-decene to decane is 64.2 kJ mol^{-1} , which is within a reasonable order of magnitude.

3.4.4 Hydroformylation network

Eight hydroformylation batch experiments were performed (see Table 3.4) to estimate kinetic parameter values using the generated experimental data. Time resolved concentration profiles of the hydroformylation of 1-decene to undecanal are presented in Figure 3.16 and Figure 3.17 as well as the corresponding modeling results. The estimated kinetic hydroformylation parameters are summarized in Table 3.5.

At this stage, all main and side reactions are running in parallel. During hydroformylation of terminal 1-decene (Hyf1-8), the double bond isomerization is the most dominant side reaction. Especially at low synthesis gas pressures, the isomerization is dominating the yield (Hyf1). The hydrogenation to n-decane and the production of branched aldehydes, however, are of minor importance. Increasing the synthesis gas pressure from 6 bar (Hyf1) to 11 bar (Hyf2) and 22 bar (Hyf3) increases the aldehyde yield significantly whereas the yield of undesired internal n-decenes drops because the isomerization is suppressed by CO. The conversion of 1-decene, however, is hardly affected by changing synthesis gas pressure.

Using mixtures of 1-decene and n-decene double bond isomers (Hyf5) allowed to

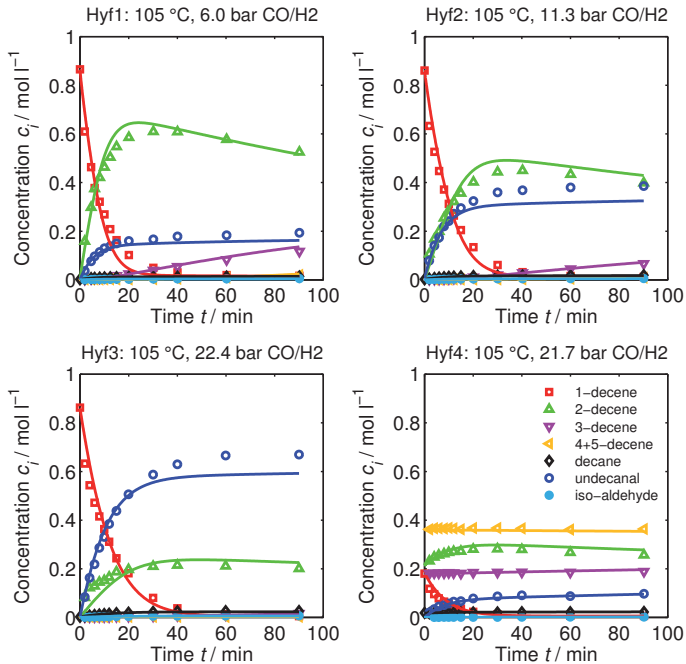


Figure 3.16: Experimental and modeling results of the hydroformylation subnetwork analysis for 1-decene. Symbols: Experimental data, Solid lines: Corresponding simulation using the developed mechanistic kinetic model with estimated parameter values. Experimental conditions: See Table 3.4.

overcome the low aldehyde yield with respect to 1-decene at low synthesis gas pressures. This is possible because the initially present concentration of internal n-decenes reduces the driving force of 1-decene isomerization. As a result, 1-decene undergoes hydroformylation to the desired aldehyde instead of being isomerized to undesired internal n-decenes. This observation suggests recycling produced internal n-olefins in a continuous process to substantially reduce the undesired double bond isomerization, if an isomerization active catalyst is used and isomerization is considered undesired.

The mechanistic kinetic model agrees very well with experimental hydroformylation data using only four kinetic parameters for each of the three hydroformylation rate laws (see Table 3.5). The assumption that the olefin coordination is rate determining for all rates is supported by the good agreement between model and experimental data.

Using local parameter subset selection explained in section 2.3 proved all kinetic

hydroformylation parameters to be identifiable using the experimental design in Table 3.4 (see Figure D.1c in appendix D). The recalculated apparent activation energy for the hydroformylation of 1-decene to undecanal (r_{hyfI}) is 30.3 kJ mol^{-1} , whereas the formation of iso-aldehydes ($r_{\text{hyf2-3}}$) showed an apparent activation energy of 56.7 kJ mol^{-1} , indicating that low reaction temperatures are beneficial for high linear/branched aldehyde selectivity. Similar energy barriers for substrate association controlled hydroformylation ($\approx 25\text{-}30 \text{ kJ mol}^{-1}$) where reported in the literature [Landis and Uddin 2002; Gleich and Hutter 2004; Gellrich et al. 2015].

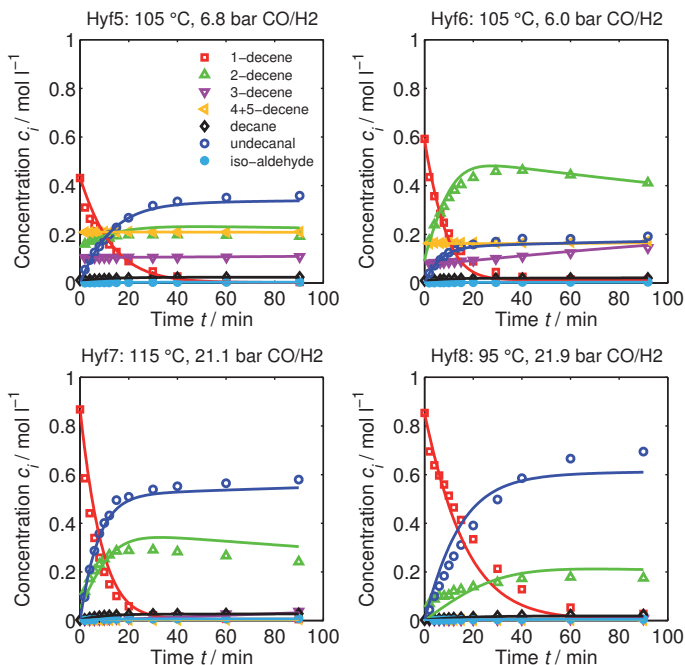


Figure 3.17: Experimental and modeling results of the hydroformylation subnetwork analysis for 1-decene. Symbols: Experimental data, Solid lines: Corresponding simulation using the developed mechanistic kinetic model with estimated parameter values. Experimental conditions: See Table 3.4.

Only one kinetic parameter ($K_{\text{hyf}}^{\text{IV}}$) turned out to be insignificant and was excluded from parameter estimation because the estimated value approached zero. A conceivable mechanistic explanation for the higher apparent activation energy and the insignificant second inhibition parameter $K_{\text{hyf}}^{\text{IV}}$ for the branched aldehyde formation rate is that CO insertion, forming the unsaturated acyl complex, is a slow step as well as the substrate coordination (see branch **IIIb** in Figure 3.11), possibly because of steric

interactions between the ligand and the branched alkyl [Paciello et al. 1999]. This conclusion can be deduced from analyzing the derivation of the hydroformylation rate expression (3.27). The rate constant representing CO insertion k_{45} is a factor of $K_{\text{hyf}}^{\text{IV}}$, but not of $K_{\text{hyf}}^{\text{III}^2}$. Thus, the increased apparent activation energy could be a consequence of two slow steps with significant energy barrier contributing to the branched aldehyde formation rate instead of one step in case of linear aldehyde formation.

3.4.5 Tandem isomerization-hydroformylation network

Five tandem isomerization-hydroformylation semi-batch experiments were performed (see Table 3.4) to estimate kinetic parameter values using the generated experimental data. Time resolved concentration profiles of the tandem isomerization-hydroformylation of n-decene double bond isomers to undecanal are presented in Figure 3.18 as well as the corresponding modeling results. The estimated kinetic hydroformylation parameters are summarized in Table 3.5. It should be noted that the initial composition of internal n-decenes is identical to the equilibrium composition presented in Table 3.3.

In case of the tandem isomerization-hydroformylation, the hydroformylation dependence on synthesis gas pressure was observed to be reversed compared to the hydroformylation of terminal 1-decene (Hyf1-3 vs. iHyf1-3). The explanation for this observation lies within the coupled nature of the tandem isomerization-hydroformylation, where the catalyst pre-equilibrium, the double bond isomerization and the hydroformylation reaction are connected via the concentration of dissolved CO. The equilibrium limited double bond isomerization reaction is the essential coupling element because it converts internal n-decenes to 1-decene, which is consumed by hydroformylation subsequently. However, the CO inhibition of the double bond isomerization is more pronounced compared to the hydroformylation, which is almost hyperbolic with respect to CO. Consequently, the isomerization shows a negative CO reaction order whereas the CO reaction order of the hydroformylation lies between 1 and 0. Therefore, it is optimal for the hydroformylation of 1-decene to be operated at maximum possible CO partial pressure to suppress the undesired isomerization side reaction (see Hyf1-3) whereas the tandem isomerization-hydroformylation requires a low but non-zero CO partial pressure to achieve a fast back-isomerization and hydroformylation rate (see iHyf1-3).

It was found experimentally that temperatures above 135 °C can damage the catalyst after long time of operation [Gaide et al. 2017b]. Hence, the upper reaction temper-

² In principle, the CO coordination could also be responsible because its rate constant k_{34} is a factor of $K_{\text{hyf}}^{\text{IV}}$ as well. However, it is unlikely that the coordination of CO, which is a sterically undemanding ligand with high affinity to Rh, is slow. Therefore, this possibility was rejected.

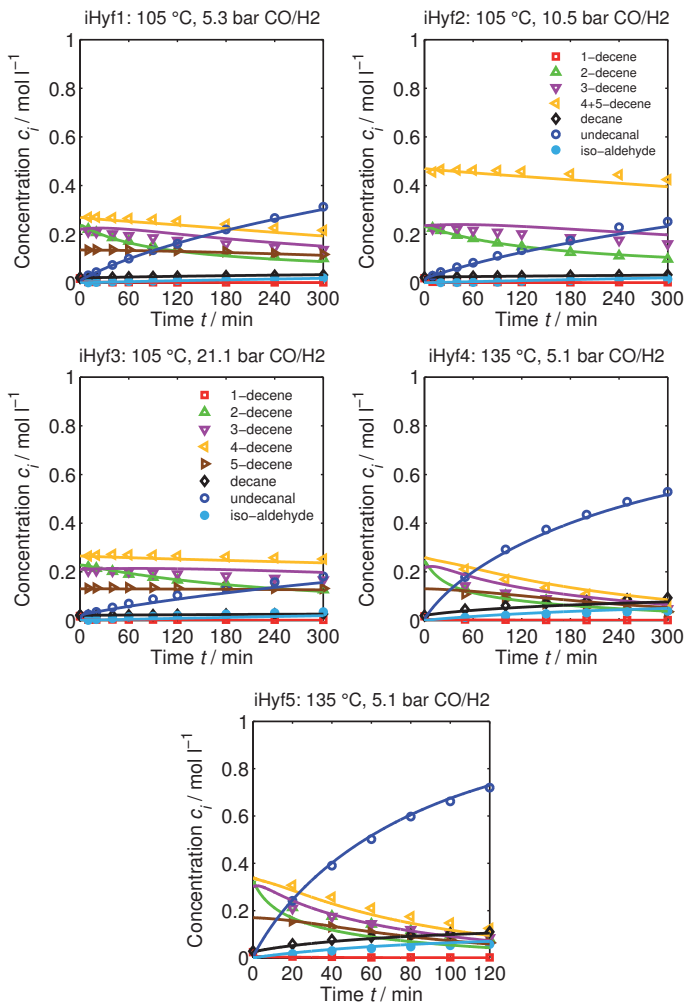


Figure 3.18: Experimental and modeling results of the tandem isomerization-hydroformylation subnetwork analysis for 1-decene. Symbols: Experimental data, Solid lines: Corresponding simulation using the developed mechanistic kinetic model with estimated parameter values. Experimental conditions: See Table 3.4.

ature limit was set to 135 °C (iHyfo4-5) for high productivity without significant catalyst degradation. This measure almost doubled the undecanal yield from 30 % (iHyf1) to 55 % (iHyf4). However, the linear:branched aldehyde ratio dropped at 135 °C to 93:7. In the last experiment (iHyf5), the catalyst loading was doubled

additionally compared to iHyf4. Thus, it was possible to achieve a high product yield and productivity, similar to the hydroformylation of terminal 1-decene. However, twenty-times more catalyst was necessary compared to the hydroformylation of 1-decene, which could be a drawback from an economic point of view, if the catalyst recycling is insufficient. Nevertheless, the presented results encourage to perform tandem isomerization-hydroformylation reactions to produce valuable products with high selectivity and yield from internal n-olefin mixtures.

In summary, the good agreement between model and experimental data (see parity plots in Figure 3.19 and Figure 3.20) speaks again for the benefits of using mechanistic kinetic models and reasonable assumptions regarding rate determining steps. Hence, the developed mechanistic kinetic model is able to reproduce all relevant borderline cases, including double bond isomerization, hydrogenation, hydroformylation of terminal 1-decene as well as the tandem isomerization-hydroformylation of internal n-decenes over a broad range of reaction conditions using a small number of estimated kinetic parameters. The parity plots prove the absence of significant systematic model errors. This holds also for the side products (decane and iso-aldehydes) that

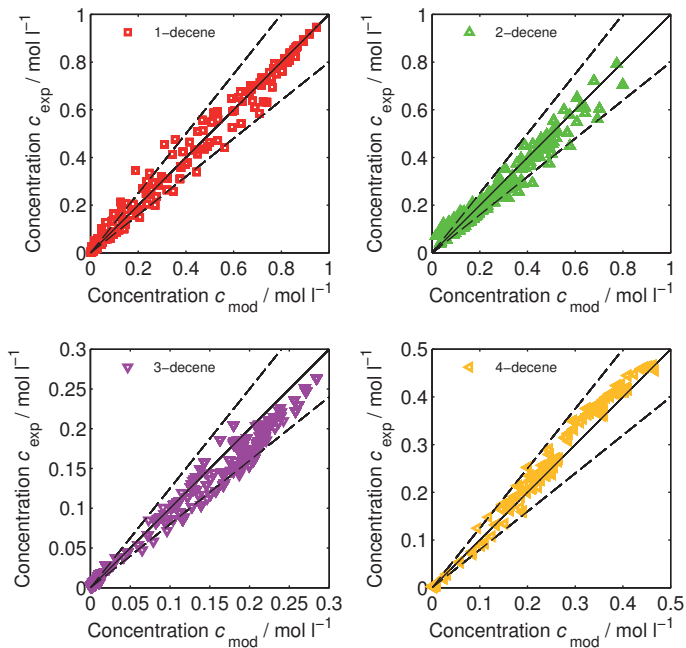


Figure 3.19: Parity plot of all 23 performed kinetic (semi-) batch experiments using 1-decene. Experimental conditions: See table Table 3.4.

appear in low concentrations during hydroformylation.

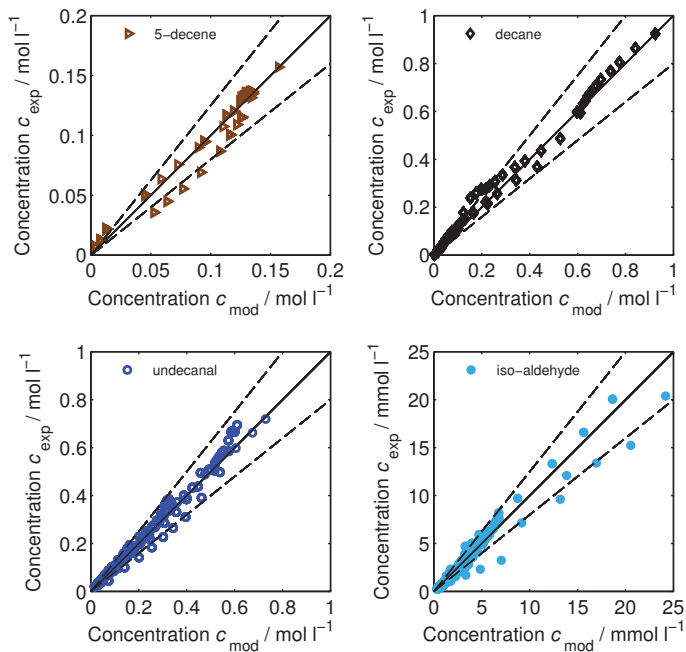


Figure 3.20: Parity plot of all 23 performed kinetic (semi-) batch experiments using 1-decene. Experimental conditions: See table Table 3.4.

Table 3.5: Kinetic parameters for the hydroformylation of n-decenes using a Rh-BiPhePhos catalyst including side reactions. Estimated kinetic parameter values with 95 % confidence interval and recalculated apparent frequency factors and activation energies. Temperature dependence of the rate constant is expressed as $k = \exp(A + B(1 - T_{\text{ref}}/T))$, $T_{\text{ref}} = 378$ K.

Rate equation	Estimated parameters with 95 % CI
Cat. pre-equilibrium: Eq. (3.13)	$K_{\text{cat}}^{\text{I}} = 5.5 \cdot 10^3 \text{ l mol}^{-1} \pm 1.2 \%$
Isomerization 1: Eq. (3.18)	$A_{\text{iso1}} = 11.04 \pm 1.0 \%$ $B_{\text{iso1}} = 18.53 \pm 8.5 \%$ $k_{\infty}^{\text{iso1}} = 7.0 \cdot 10^{12} \text{ l mol}^{-1} \text{ min}^{-1}$ $E_{\text{A}}^{\text{iso1}} = 58.2 \text{ kJ mol}^{-1}$
Isomerization 2: Eq. (3.18)	$A_{\text{iso2}} = 6.94 \pm 1.4 \%$ $B_{\text{iso2}} = 15.63 \pm 10.8 \%$ $k_{\infty}^{\text{iso2}} = 6.3 \cdot 10^9 \text{ l mol}^{-1} \text{ min}^{-1}$ $E_{\text{A}}^{\text{iso2}} = 49.1 \text{ kJ mol}^{-1}$
Isomerization 3: Eq. (3.18)	$A_{\text{iso3}} = 6.96 \pm 2.4 \%$ $B_{\text{iso3}} = 15.63 \pm 10.8 \%$ $k_{\infty}^{\text{iso3}} = 6.5 \cdot 10^9 \text{ l mol}^{-1} \text{ min}^{-1}$ $E_{\text{A}}^{\text{iso3}} = 49.1 \text{ kJ mol}^{-1}$
Isomerization 4: Eq. (3.18)	$A_{\text{iso4}} = 5.96 \pm 3.3 \%$ $B_{\text{iso4}} = 15.63 \pm 10.8 \%$ $k_{\infty}^{\text{iso4}} = 2.4 \cdot 10^9 \text{ l mol}^{-1} \text{ min}^{-1}$ $E_{\text{A}}^{\text{iso4}} = 49.1 \text{ kJ mol}^{-1}$
Hydrogenation: Eq. (3.23)	$A_{\text{hyd}} = 12.73 \pm 1.1 \%$ $B_{\text{hyd}} = 20.44 \pm 7.4 \%$ $k_{\infty}^{\text{hyd}} = 2.5 \cdot 10^{14} \text{ l}^2 \text{ mol}^{-2} \text{ min}^{-1}$ $E_{\text{A}}^{\text{hyd}} = 64.2 \text{ kJ mol}^{-1}$ $K_{\text{hyd}} = 10.20 \text{ l mol}^{-1} \pm 17.4 \%$
Hydroformylation 1: Eq. (3.28)	$A_{\text{hyf1}} = 20.41 \pm 1.0 \%$ $B_{\text{hyf1}} = 9.65 \pm 11.2 \%$ $k_{\infty}^{\text{hyf1}} = 1.1 \cdot 10^{13} \text{ l}^3 \text{ mol}^{-3} \text{ min}^{-1}$ $E_{\text{A}}^{\text{hyf1}} = 30.3 \text{ kJ mol}^{-1}$ $K_{\text{hyf}}^{\text{I}} = 92.10 \text{ l mol}^{-1} \pm 8.2 \%$ $K_{\text{hyf}}^{\text{II}} = 1063.60 \text{ l}^2 \text{ mol}^{-2} \pm 4.0 \%$
Hydroformylation 2: Eq. (3.29)	$A_{\text{hyf2}} = 19.10 \pm 12.2 \%$ $B_{\text{hyf2}} = 18.04 \pm 9.2 \%$ $k_{\infty}^{\text{hyf2}} = 1.3 \cdot 10^{16} \text{ l}^3 \text{ mol}^{-3} \text{ min}^{-1}$ $E_{\text{A}}^{\text{hyf2}} = 56.7 \text{ kJ mol}^{-1}$ $K_{\text{hyf}}^{\text{III}} = 5775.00 \text{ l mol}^{-1} \pm 27.4 \%$ $K_{\text{hyf}}^{\text{IV}} \approx 0 \text{ l}^2 \text{ mol}^{-2} \pm > 10^9 \%$
Hydroformylation 3: Eq. (3.30)	$A_{\text{hyf3}} = 14.90 \pm 15.9 \%$ $B_{\text{hyf3}} = 18.04 \pm 9.2 \%$ $k_{\infty}^{\text{hyf3}} = 2.0 \cdot 10^{14} \text{ l}^3 \text{ mol}^{-3} \text{ min}^{-1}$ $E_{\text{A}}^{\text{hyf3}} = 56.7 \text{ kJ mol}^{-1}$ $K_{\text{hyf}}^{\text{III}} = 5775.00 \text{ l mol}^{-1} \pm 27.4 \%$ $K_{\text{hyf}}^{\text{IV}} \approx 0 \text{ l}^2 \text{ mol}^{-2} \pm > 10^9 \%$

3.5 Optimal reaction control strategies

Finding optimal reaction conditions for the (tandem isomerization-) hydroformylation is not trivial because several reactions are coupled and the dependencies on the dissolved gases are complex. Therefore, the developed and parameterized mechanistic kinetic model presented in the previous section was taken to rigorously optimize n-decene hydroformylation for a maximum yield of undecanal Y at a specified space time yield STY . It should be noted that it is intended with this study to find optimal reaction temperature and pressure control profiles for the (tandem isomerization-)hydroformylation to illustrate how the reaction would have to be controlled in an optimal way over reaction time. However, a realization of these controls is very challenging, especially for a industrially more relevant continuous production process, and the results should be seen more as a comparison between interesting reaction scenarios.

The used batch reactor model, the gas solubilities and mass transfer coefficients are summarized in section 2.2.1 and appendix B, respectively. To compare both, hydroformylation and the tandem reaction, an initial total olefin concentration of 1 mol l^{-1} was fixed for both cases as well as a typical STY for hydroformylation reactors of $100 \text{ kg m}^{-3} \text{ h}^{-1}$ aldehyde product [Beller 2006]. To achieve a reasonable conversion, the required STY for the tandem isomerization-hydroformylation case was set to $50 \text{ kg m}^{-3} \text{ h}^{-1}$ aldehyde product. The degrees of freedom for the optimization are the reaction temperature and the partial pressures of CO and H₂ within the experimentally validated range as time functions.

The resulting optimal control problem (3.31) was solved by transformation into a high dimensional non-linear program (NLP) by discretization of the resulting differential and algebraic equations with orthogonal collocation on finite elements.

$$\begin{aligned} \text{Obj} = & \max_{T(t), p_{\text{CO}}(t), p_{\text{H}_2}(t)} Y_{\text{undecanal}}(t_{\text{end}}) & (3.31) \\ & \text{s.t.} \\ & \text{Balance equations} \\ & \text{Gas solubilities} \\ & \text{Mass transfer coefficients} \\ & \text{Kinetic model} \\ & STY = 100 - 50 \text{ kg m}^{-3} \text{ h}^{-1} \end{aligned}$$

This implicit approach is especially well suited for stiff dynamic systems with steep gradients [Carey and Finlayson 1975]. More details about this method as well as a comprehensive comparison to other methods can be found in [Carey and Finlayson

1975; Biegler 1984; Logsdon and Biegler 1989; Oh and Luus 2007].

The solution of the resulting high-dimensional non-linear optimization problem was carried out using "A Mathematical Programming Language" (AMPL) in combination with the Conopt 3.17A solver using gradient-based sequential quadratic programming [Fourer et al. 2009]. Since AMPL codes are not sequential but equation-oriented and use exact derivatives calculated by automatic differentiation instead of numerical derivatives calculated by finite differences, such problems are solved very fast and efficiently.

The optimization results for the hydroformylation of 1-decene are shown in Figure 3.21. The reaction time is expressed as a normalized reaction time τ to compare the case of 1-decene hydroformylation with the tandem case. This reaction time is normalized to the optimal reaction time of the hydroformylation of 1-decene (87.8 min). As expected, the reaction temperature is at the lower boundary of 80 °C and the partial pressures of CO and H₂ are at the upper boundary of 10 bar (total synthesis

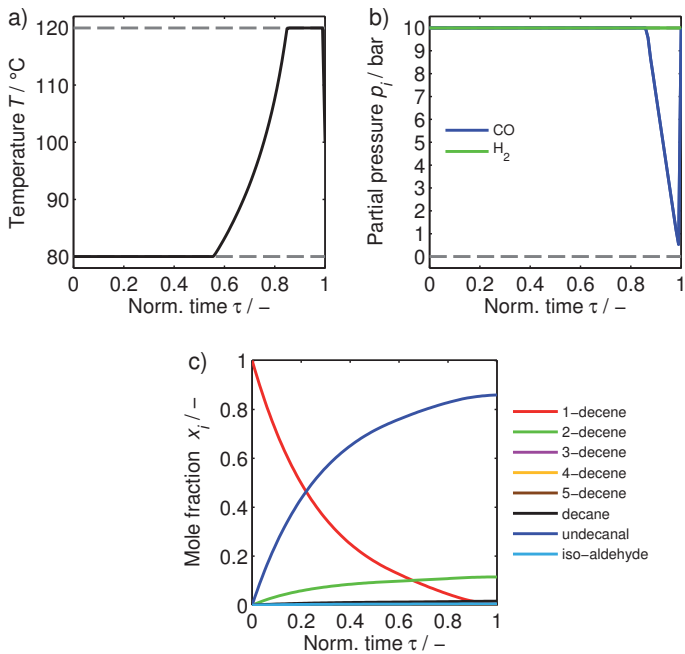


Figure 3.21: Optimization results for the hydroformylation of 1-decene: a) optimal temperature profile. b) optimal partial pressure profiles. c) concentration profiles in molar fractions. ($c_{\text{sub}}^0 = 1 \text{ mol l}^{-1}$, Rh:sub (molar) = 1:10000, $STY = 100 \text{ kg m}^{-3} \text{ h}^{-1}$)

gas pressure = 20 bar), initially. This is a result of the already discussed temperature and pressure dependencies and aims for the suppression of the undesired double bond isomerization. At high conversion of 1-decene, the temperature is increased to the upper limit of 125 °C to increase the low hydroformylation rate because of the low 1-decene concentration. Furthermore, the CO partial pressure is reduced to 1 bar and less to increase the amount of active catalyst while the H₂ partial pressure remains at the upper boundary of 10 bar. This reduction in CO partial pressure aims for increasing the concentration of active catalyst to compensate the decreasing hydroformylation rate caused by the low 1-decene concentration. The maximum achievable yield of undecanal for the hydroformylation of 1-decene at the specified STY is 86 %.

Figure 3.22 summarizes optimization results for the tandem isomerization-hydroformylation of n-decene double bond isomers. The optimal temperature profile is always constant at the upper boundary of 125 °C to keep the hydroformylation rate high as well as the isomerization to reproduce consumed 1-decene from n-decene

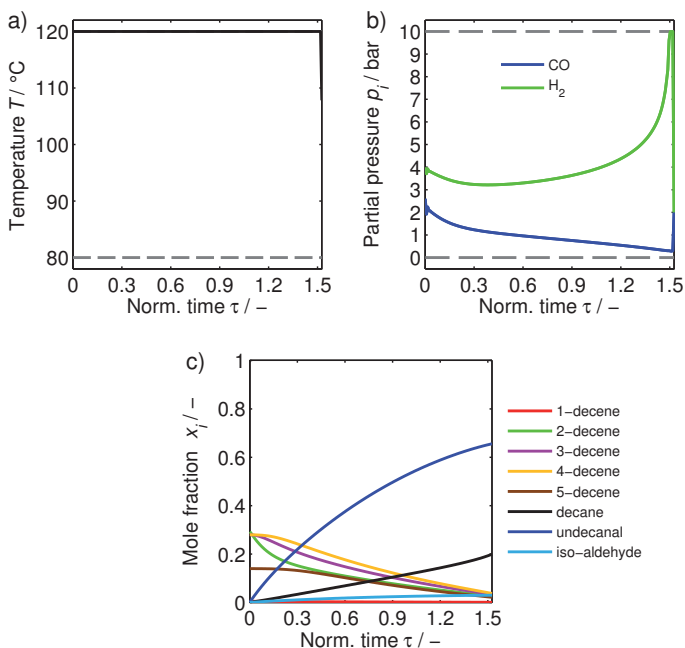


Figure 3.22: Optimization results for the tandem isomerization-hydroformylation of n-decene double bond isomers: a) optimal temperature profile. b) optimal partial pressure profiles. c) concentration profiles in molar fractions. ($c_{\text{sub}}^0 = 1 \text{ mol l}^{-1}$, Rh:sub (molar) = 1:500, STY = 50 kg m⁻³ h⁻¹)

double bond isomers. As expected, the optimal CO pressure profile is always at low values and drops from 2.5 bar to 0.25 bar to compensate the decreasing substrate concentrations by increasing the amount of active catalyst material. The H₂ pressure also follows an optimal trajectory between 4 and 10 bar. Keeping H₂ at the upper limit would result in more hydrogenation and less aldehyde yield whereas a low H₂ pressure would reduce the hydroformylation rate. The increase of the H₂ pressure at the end of the reaction to the upper limit increases the hydroformylation rate and compensates the low substrate concentration to meet the desired *STY*. The maximum yield of undecanal for the tandem isomerization-hydroformylation of n-decene double bond isomers at the specified *STY* is 66 %. In this case, also significant amounts of n-decane are produced by hydrogenation with a yield of 20 %.

3.6 Summary

This chapter was dedicated to the Rh-BiPhePhos catalyzed hydroformylation of 1-decene, a representative long-chain n-olefin. Thereby, side reactions such as hydrogenation and most importantly the double bond isomerization of n-decenes played a crucial key role to understand not only the hydroformylation including side reactions but also the tandem isomerization-hydroformylation. Several issues were addressed theoretically and experimentally:

- Calculation of the thermodynamic reaction equilibrium of the double bond isomerization of n-decenes using Gibbs energy minimization and Benson's groups contribution method
- Detection of catalyst species using FTIR spectroscopy and subsequent reduction of a general hydroformylation reaction mechanism
- Mechanistic kinetic modeling of all relevant main and side reactions based on the reduced reaction mechanism
- Design and conduct of 23 (semi-) batch experiments to analyze the isomerization, hydrogenation, hydroformylation (sub)networks as well as the tandem isomerization-hydroformylation
- Estimation of kinetic parameter values for the developed kinetic model using the observed experimental data
- Optimal reaction control strategies for the hydroformylation of 1-decene as well as the tandem isomerization-hydroformylation of n-decene double bond isomer mixtures

The thermodynamic reaction equilibrium of the double bond isomerization of n-decenes was calculated using a non-stoichiometric Gibbs energy minimization method [White et al. 1958]. The necessary thermodynamic state functions of formation were calculated using Benson's group contribution method [Benson et al. 1969]. The results were validated experimentally and corresponding equilibrium constants were used in kinetic models later on.

A general extended hydroformylation reaction mechanism, including double bond isomerization and hydrogenation as relevant side reactions as well as the formation of several possibly inactive or non-selective catalyst species, was used as basis for mechanistic kinetic modeling. It was possible to show with *operando* FTIR spectroscopy that hydrido-Rh-monocarbonyl complexes $\text{HRh}(\text{BP})(\text{CO})$ are dominating under CO free conditions (isomerization, hydrogenation) whereas the saturated hydrido-Rh-dicarbonyl complex $\text{HRh}(\text{BP})(\text{CO})_2$ was dominant under CO rich conditions (hydroformylation). No other Rh-complexes were detectable and it was concluded additionally that the substrate coordination is rate determining. These conclusions allowed to reduce the general hydroformylation reaction mechanism significantly.

From the reduced hydroformylation mechanism, mechanistic kinetic models were derived using Christiansen's method [Christiansen 1953]. The models include a term for the catalyst pre-equilibrium and the rate-determining-step assumption.

23 isomerization, hydrogenation and hydroformylation (semi-) batch experiments were designed and conducted to generate experimental data for subsequent parameter estimation. Special emphasis was given to the tandem isomerization-hydroformylation reaction of internal n-decenes to undecanal. Interestingly, it was found experimentally that the tandem reaction followed an opposite synthesis gas pressure dependence compared to the conventional hydroformylation of 1-decene.

Fitting the mechanistic kinetic model to experimental data succeeded with low deviation between model and experiment. The estimated kinetic parameters were within reasonable orders of magnitude with low 95 % confidence intervals. Parameter identifiability was verified with local parameter subset selection.

The developed and parameterized mechanistic kinetic model allowed to calculate optimal reaction control profiles in terms of temperature and partial pressures of CO and H_2 to maximize the yield of undecanal semi-batchwise. The results lead to the conclusion that hydroformylation of terminal 1-decene should be operated at high synthesis gas pressure and low temperature to suppress undesired double bond isomerization. The tandem isomerization-hydroformylation, however, should be performed at low synthesis gas pressure and high temperature to accelerate double bond back-isomerization.

The next chapter is dedicated to the hydroformylation of the renewable methyl ester methyl 10-undecenoate with analogous structure compared to 1-decene. It is intended to reveal, if the presence of a methyl ester group has a significant influence on the catalysis and thus the reaction rates compared to 1-decene.

4 Hydroformylation of methyl 10-undecenoate

The hydroformylation of unsaturated oleochemicals is an attractive possibility to generate platform chemicals for the production of e.g. bio-based polymers [Behr and Vorholt 2012; Vanbésien et al. 2016], as already discussed in section 1.2.4. One renewable substrate of interest is the monounsaturated methyl oleate (OME). Using this long-chain C_{18} molecule in hydroformylation implies two major challenges: i) due to the internal double bond, tandem isomerization-hydroformylation is necessary and ii) the weakly nucleophilic carbonyl oxygen of the ester group may interact with the catalyst. Whereas the first issue was clarified in the previous chapter, this chapter is dedicated to investigating interactions between the ester group and the Rh-catalyst. The goal is to derive mechanistic kinetic models, which are not available in the literature up to now, and to deduce optimal hydroformylation reaction conditions for oleochemicals, e.g. the tandem isomerization-hydroformylation of OME. The studies were carried out using methyl 10-undecenoate (UME) with terminal double bond as substrate because the molecule is analogous in structure compared to 1-decene (see Figure 4.1).

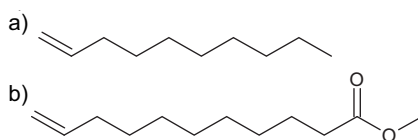


Figure 4.1: Structures of a) 1-decene and b) methyl 10-undecenoate (UME)

Because of the structural similarity, conclusions regarding the influence of the ester group on the catalysis and reaction rates can be drawn by comparison of these substrates under identical reaction conditions. Apart from hydroformylation experiments, special emphasis was given to relevant side reactions, namely hydrogenation and most importantly double bond isomerization. The results were achieved using methods and models presented in chapter 2.

The first part of this chapter compares the isomerization, hydrogenation and hydroformylation (sub)networks using 1-decene and UME. From the observed results,

possible interactions between the ester group, the Rh-catalyst and the dissolved gases can be deduced indirectly. In the second part of this chapter, *operando* FTIR spectroscopy experiments, analogous to those presented in chapter 3, were used to identify relevant Rh-complexes during isomerization, hydrogenation and hydroformylation reactions using UME as substrate. Subsequently, reaction mechanisms as well as the mechanistic kinetic model, presented in chapter 3, were updated based on the experimental observations followed by parameter estimation using (semi-) batch data from carefully designed experiments. The last part of this chapter uses the parameterized mechanistic kinetic model to calculate optimal dynamic reaction control profiles in terms of reaction temperature and synthesis gas pressure to compare and discuss optimal reaction conditions for the (tandem isomerization-) hydroformylation of UME.

4.1 Comparison of UME to 1-decene

In this section, the well understood substrate 1-decene is compared experimentally to the structural analogous oleocompound UME. Kinetic key batch experiments, using the same equipment as in the previous chapter, were performed with both substrates, 1-decene and UME, under identical reaction conditions, respectively. All internal double bond isomers were lumped to "iso-decene" and "iUME" for the following comparison because it was not possible to assign UME double bond isomers analytically using gas chromatography due to non-availability of calibration standards.

The comparison comprises not only the hydroformylation but, very importantly, double bond isomerization as well as hydrogenation of the double bond. Putting emphasis on this side reactions, especially on the double bond isomerization, is essential to understand the tandem isomerization-hydroformylation of internal oleochemicals.

Various reports are available in the literature about interactions between carbonyl groups and transition metals. To be more specific, bonding of carbonyl oxygen to Rh [Matsumoto and Tamura 1982; Lee and Alper 1995; Kuriyama et al. 2002; Walczuk et al. 2003; Kamer et al. 2004; Nishimura et al. 2010; Schreiner and Beck 2010; Behr and Neubert 2012; Yang et al. 2014; Nelsen et al. 2015; Costa et al. 2016], Pd [Roesle et al. 2012, 2014], Co and Zn [Houghton 1979] as well as Sn and Sb [Hein 1950] were presented leading to stable complexes. For instance, it was shown in [Walczuk et al. 2003; Kamer et al. 2004] with *in situ* IR and NMR spectroscopy that adding enones to a Rh-TPP catalyzed hydroformylation of 1-octene leads to a severe hydroformylation rate reduction due to the formation of dormant/inactive η^1 -oxygen bound Rh-enolate species. After the enone was hydrogenated to the saturated ketone, the catalyst

activity was reversibly restored. Thus, it is likely that the ester group of UME interacts with the Rh-BiPhePhos catalyst as well, leading to possibly inactive Rh-complexes [Franke et al. 2012]. Of course, such an effect has to be included into a mechanistic kinetic model in order to correctly reproduce reaction rates of unsaturated esters. However, systematic and quantitative studies or even kinetic models containing these effects are hardly available in the literature, especially not for interactions between methyl esters and the Rh-BiPhePhos hydroformylation catalyst.

Another point of interest is the solvent in which the reactions should be carried out. It is known for the Rh-BiPhePhos catalyzed isomerization of 1-decene that solvent polarity has no effect on reaction rates [Jörke et al. 2015a]. Thus, it is likely that the hydroformylation is, apart from different gas solubilities, also not influenced by solvent polarity. However, no studies are available proving the absence or existence of solvent influences for the hydroformylation of substrates with heteroatomic functional groups, e.g. methyl esters.

The addressed issues need clarification which is intended in this section by comparing experimental isomerization, hydrogenation and hydroformylation batch data of 1-decene and UME. Two solvents with strongly different polarity and coordination ability to metal complexes (toluene: non-polar and low coordination ability, DMF: strongly polar and high coordination ability [Shestakova et al. 2014; Kohls 2017, 2018 - in preparation]) are used to study possible solvent effects. The comparison basis is the turnover frequency TOF_n (4.1), normalized by the initial substrate concentration c_{sub}^0 . This normalization allows to evaluate catalyst activity at different substrate concentrations because the initial rates depend strongly on these concentrations.

$$TOF_n = \frac{TOF}{c_{\text{sub}}^0} = \frac{r(t \rightarrow 0)}{c_{\text{Rh,tot}} \cdot c_{\text{sub}}^0} \quad (4.1)$$

4.1.1 Isomerization subnetwork

In order to understand the tandem isomerization-hydroformylation of long-chain internal oleochemicals, the double bond isomerization of oleochemicals has to be understood well. More specifically, the influence of the ester group on the catalyst and consequently on the isomerization reaction rate was investigated in the following sections as well as the influences of solvent and dissolved CO.

4.1.1.1 Influence of substrate and solvent

The first set of isomerization experiments compares both substrates in toluene and DMF as solvent. The results are shown in Figure 4.2. Comparing the isomerization of 1-decene to UME using toluene as solvent (Figure 4.2a vs. c) reveals a strong influence of the substrate on the catalyst activity, which is reduced by a factor of ≈ 100 when

using UME instead of 1-decene. The same holds for using DMF as solvent (Figure 4.2b vs.d) but with a significant lower catalyst activity reduction for UME (Figure 4.2c vs. d). In contrast to this observation, the catalyst activity for 1-decene is not influenced by the solvent (Figure 4.2a vs. b)¹.

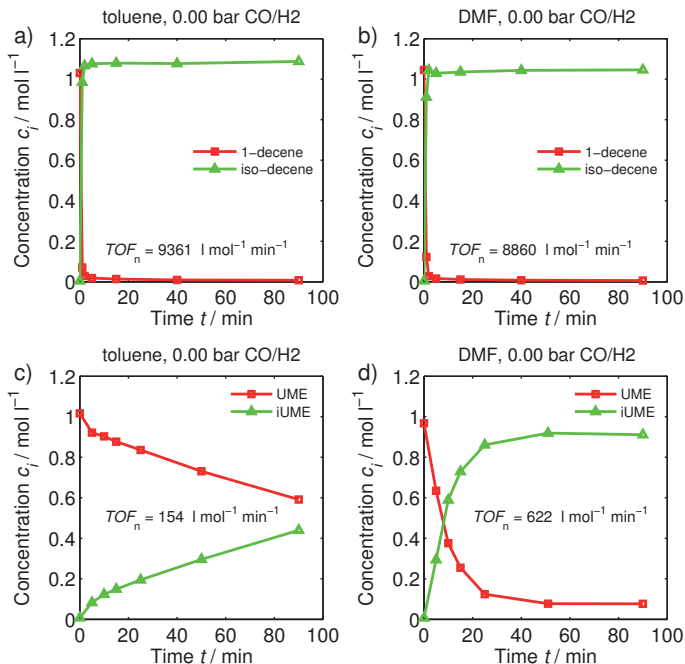


Figure 4.2: Isomerization of 1-decene and UME in toluene or DMF. (100 °C, $c_{\text{sub}}^0 = 1 \text{ mol l}^{-1}$, Rh:sub (molar) = 1:10000, Rh:lig (molar) = 1:3)

An explanation for the reduced isomerization rate in toluene would be a coordination of the carbonyl oxygen of the ester group to the catalyst. Thus, stable inactive Rh-ester complexes are formed, which reduce the amount of active Rh. Similar observations were made using enones with Rh-TPP catalysts [Walczuk et al. 2003] or unsaturated methyl esters [Nelsen et al. 2015; Costa et al. 2016]. Using polar DMF reduces this catalyst deactivation to a certain extent because it stabilizes the ester group in solution, reducing its coordination potential. Another possible explanation is a stronger competitive coordination between the polar solvent and ester carbonyl oxygen to the Rh-catalyst.

¹ It should be noted that only inert N₂ was present in the gas phase to allow sampling. Therefore, the observed substrate and solvent influence is evidently caused by catalyst-substrate-solvent interactions and cannot be explained by differences in gas solubility of both substrate-solvent-systems.

The observed phenomena deserve further investigations to reveal their origin. Hence, a second set of isomerization experiments was designed to compare pure 1-decene and UME to mixtures of both substrates. If the suspected interaction between ester and Rh-catalyst is truly the formation of a stable complex, as described in [Walczuk et al. 2003] or [Nelsen et al. 2015; Costa et al. 2016], the isomerization rate of 1-decene would decrease in case of simultaneously present ester. If the isomerization rate of 1-decene is not affected by the simultaneously present ester, the reason for the low catalyst activity for UME is something else, maybe a different rate determining step in the reaction mechanism.

In principle, two Rh-ester interactions are possible: i) Coordination of the ester carbonyl oxygen as monodentate ligand [Walczuk et al. 2003] and ii) chelation of the unsaturated ester after double bond coordination [Nelsen et al. 2015; Costa et al. 2016]. The decision tree in Figure 4.3 illustrates the logic behind designing isomerization experiments with substrate mixtures. Two methyl esters were used for mixing with 1-decene: i) UME and ii) its saturated counterpart methyl undecanoate (abbreviated with hUME because it is the hydrogenation product of UME). In the first stage, an isomerization of pure 1-decene will be compared to an isomerization of a 1:1 mixture of 1-decene and hUME. The second stage compares the isomerization of a 1:1 mixture of 1-decene and UME with first stage results. A reduced catalyst activity in presence of hUME would prove coordination of the ester to the catalyst as monodentate ligand.

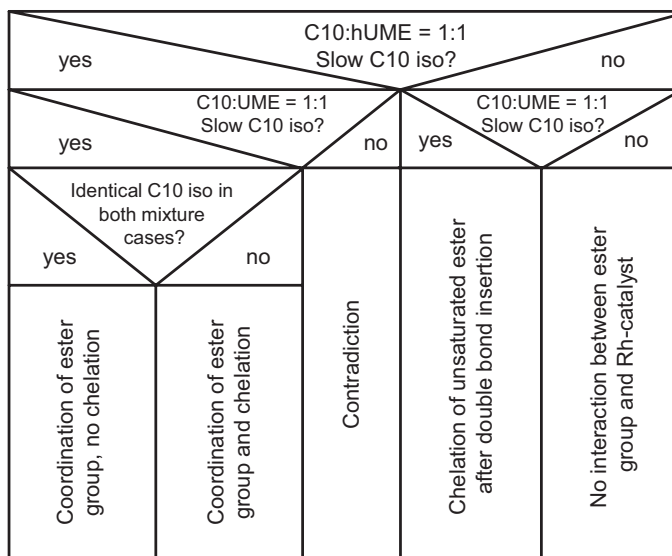


Figure 4.3: Decision tree for clarification of the described Rh-ester interaction.

Therefore, the isomerization of 1-decene can not be faster in presence of UME because both are esters that would both coordinate to Rh. If both mixture experiments show a reduced and identical catalyst activity in terms of TOF_n , the ester group coordinates as a monodentate ligand exclusively. If the catalyst activity in both mixture experiments is different but less compared to pure 1-decene, coordination of the ester group as well as chelation of UME occurs. If the rate is not affected by hUME but reduced by UME, chelation of UME occurs exclusively. No interaction between ester and Rh was already disproven (Figure 4.2a vs. c).

Figure 4.4 compares the isomerization of 1-decene to the isomerization of a 1:1 mixture of 1-decene and hUME. First of all, reducing the initial concentration of 1-decene to 0.5 mol l^{-1} does not change the catalyst activity in terms of TOF_n (Figure 4.2a vs. Figure 4.4a). This is reasonable and was expected because the TOF_n is equal to the isomerization rate constant, if no double bond isomers or dissolved CO is present initially (see equation (3.18)). Secondly, the isomerization rate of 1-decene is evidently not influenced by the presence of hUME. Hence, ester coordination as monodentate ligand is refuted.

The isomerization rate of pure UME is again lower compared to 1-decene (Figure 4.4a vs. Figure 4.4c). However, the catalyst activity in terms of TOF_n is higher for lower initial concentrations of UME (Figure 4.2c vs. Figure 4.4c). In contrast to isomerization results using a 1-decene/hUME mixture, the isomerization rate of 1-decene is drastically reduced in presence of UME (Figure 4.4b vs. d). Interestingly, the TOF_n is almost identical for both substrates and the concentration profiles are shaped equally. The same holds for the isomerization of a 2:1 mixture of 1-decene and UME, respectively (Figure 4.4e). It can be concluded that UME chelates and forms stable and inactive dormant Rh-complexes, similar to complexes reported in [Nelsen et al. 2015; Costa et al. 2016], leading to the observed isomerization rate reduction. The isomerization reaction itself, however, is the same for both substrates with, most probably, identical mechanisms and rate determining steps.

Figure 4.5 summarizes the observed catalyst activities in terms of normalized turnover frequency as a function of initial substrate concentration. In case of 1-decene, the TOF_n is constant for all studied initial substrate concentrations² proving no substrate effects for olefins. However, increasing initial concentrations of UME lead to significantly decreased catalyst activity. The pronounced concentration dependence is most probably a consequence of thermodynamic equilibrium limitations of the Rh-ester complex formation.

² A third isomerization experiment with a 1-decene initial concentration of 0.25 mol l^{-1} was performed analogously to already discussed experiments.

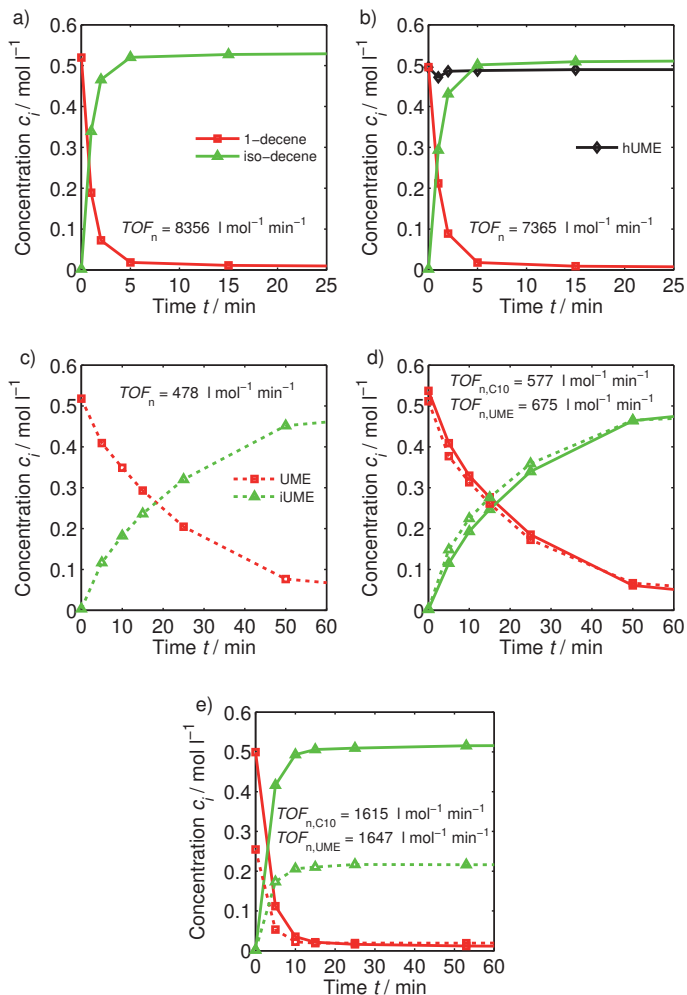


Figure 4.4: Isomerization of a) pure 1-decene compared to b) a 1:1 mixture of 1-decene and hUME, c) pure UME, d) a 1:1 mixture of 1-decene and UME and e) a 2:1 mixture of 1-decene and UME. (toluene, 100 °C, 0.00 bar CO, Rh:sub (molar) = 1:2500-5000, Rh:lig (molar) = 1:3)

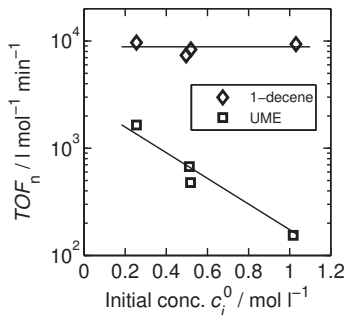


Figure 4.5: Influence of initial substrate concentration on catalyst activity expressed as TOF_n for 1-decene and UME (toluene, 100 °C, 0.00 bar CO, Rh:sub (molar) = 1:2500-10000, Rh:lig (molar) = 1:3).

4.1.1.2 Influence of dissolved CO

It was already proven experimentally in the previous chapter that dissolved CO strongly reduces the isomerization rate of 1-decene (see section 3.4.2). However, it is unknown to this point how dissolved CO influences the isomerization of UME and especially the Rh-ester complexation. Hence, isomerization experiments at different CO pressures (0, 1 and 5 bar) using 1-decene and UME are compared in the following. Figure 4.6 summarizes the respective TOF_n values (see Figure G.1 in appendix G for corresponding concentration profiles). As already shown and discussed in section 3.4.2, the isomerization rate of 1-decene steadily decreases by an increasing amount of

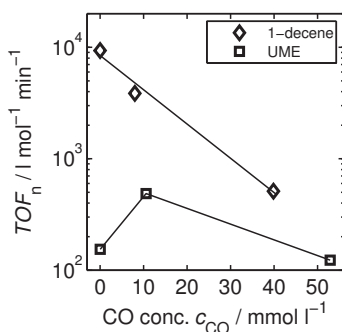


Figure 4.6: Influence of dissolved CO on catalyst activity expressed as TOF_n for 1-decene and UME. Concentrations of dissolved CO (corresponding pressure = 0, 1 and 5 bar from left to right) were calculated using Henry's law (see appendix B). (toluene, 100 °C, $c_{\text{sub}}^0 = 1 \text{ mol l}^{-1}$, Rh:sub (molar) = 1:10000, Rh:lig (molar) = 1:3)

dissolved CO due to the CO dependent catalyst pre-equilibrium.

The dependence of UME isomerization on dissolved CO, however, appears to be more complex. Although the reaction rate is low without CO, it increases at elevated CO partial pressure (1 bar) and decreases again at higher partial pressures (5 bar). Obviously, an optimal CO partial pressure for a maximum UME isomerization reaction rate exists. A possible explanation for this observation would be a competitive coordination between CO and the carbonyl oxygen of the ester group to the Rh-catalyst. In this way, the highly Rh-affine CO occupies free coordination sites, preventing the rather weak interaction between Rh and the ester group. In this way, the isomerization can proceed more rapidly. A more detailed mechanistic discussion is presented later in section 4.2.2 after additional *operando* FTIR spectroscopic studies.

4.1.2 Hydrogenation subnetwork

Since unsaturated oleochemicals undergo undesired hydrogenation to saturated molecules as well as olefins, it is worth to study and understand this side reaction for oleochemicals in order to avoid it. More specifically, the influence of the ester group on the catalyst and consequently on the hydrogenation and isomerization reaction rates was studied by comparison of 1-decene and UME in the following sections as well as the influences of solvent and dissolved H₂.

4.1.2.1 Influence of substrate and solvent

The first set of hydrogenation experiments compares both substrates, 1-decene and UME, in toluene and DMF, analogously to the isomerization experiments discussed above at standard reaction conditions. The results are shown in Figure 4.7 and prove significant influences of the ester group on the catalysis, although the effect is much less pronounced compared to the isomerization case (cf. Figure 4.7a and c and Figure 4.2a and c). Apart from lower rates for UME compared to 1-decene, the observed concentration profiles are qualitatively similar. Furthermore, a significant solvent effect for UME is evident from experimental data (cf. Figure 4.7c and d) which is absent for 1-decene, as expected³ (cf. Figure 4.7a and b). The results have in common that, compared to 1-decene, the isomerization rate of UME is always lower as well as the hydrogenation rate and yield of the hydrogenation product methyl undecanoate (hUME). This can be assigned to the already discussed Rh-ester complexation reducing the catalyst activity. The increased rates in DMF may also result from already discussed competitive coordination of the polar solvent at the catalyst or the stabilization of the ester group in solution by the polar solvent. However, the hydrogenation experiments were conducted under CO free

³ Differences in reaction rate originate from different gas solubility of H₂ in toluene compared to DMF.

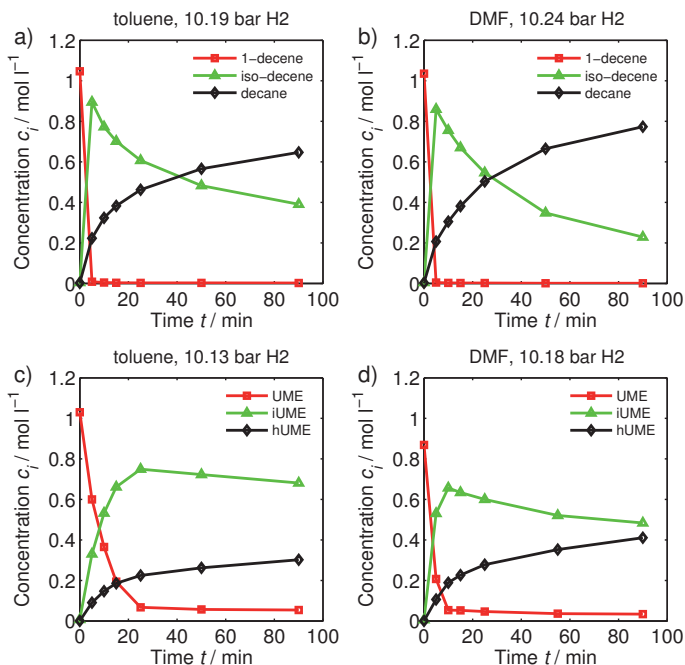


Figure 4.7: Comparison of 1-decene to UME in toluene or DMF - hydrogenation sub-network. (100 °C, 0.00 bar CO, $c_{\text{sub}}^0 = 1 \text{ mol l}^{-1}$, Rh:sub (molar) = 1:10000, Rh:lig (molar) = 1:3)

conditions and therefore the rates for UME should be much lower since the Rh-ester complexation should be stronger. Hence, it is evident from the observations that the presence of H₂ increases the catalyst activity in case of using UME.

4.1.2.2 Influence of dissolved H₂

As second experimental set, a dynamic experiment was performed for further clarification of the H₂ influence. The experiment started as isomerization with addition of H₂ after a certain time (approx. 20 min). The result is shown in Figure 4.8 and proves that it is possible to "switch" from isomerization to hydrogenation and thus from low to high catalyst activity by adding H₂. This can be seen most clearly from the concentration profile of UME double bond isomers (iUME) because H₂ should not directly influence the isomerization reaction. Consequently, the rate increase has to be related to a certain reactivation of deactivated Rh-ester complexes. One possible explanation would be that H₂ oxidizes a certain amount of HRh^I(BP)(CO) under CO free conditions to Rh^{III}-trihydride complexes, which

are active and catalyze double bond isomerization and hydrogenation, as described experimentally and by DFT calculations for a similar Rh-catalyst in [Walter et al. 2017]. In this way, inactive Rh-ester complexes are converted to a certain extent to active Rh^{III}-trihydride complexes, which would explain the observed catalyst activity increase.

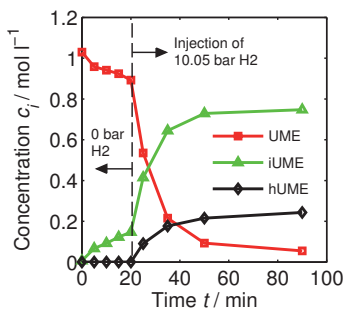


Figure 4.8: Perturbed hydrogenation of UME. (toluene, 100 °C, 0.00 bar CO, $c_{\text{sub}}^0 = 1 \text{ mol l}^{-1}$, Rh:sub (molar) = 1:10000, Rh:lig (molar) = 1:3)

Of course, this oxidation should happen as well in case of using 1-decene but nothing significant in terms of a H₂ influence could be observed experimentally. Additionally, the kinetic model for 1-decene, which does not include the discussed phenomena, fits the data very well (see section 3.4.3). A possible explanation would be that i) all Rh is active under CO free conditions because 1-decene cannot interact deactivatingly with Rh and ii) the rate would probably be the same for both catalytic cycles starting from Rh^I or Rh^{III} since the coordination of the substrate is rate limiting and determined by steric interactions between ligand and substrate [Walter et al. 2017]. If this is true, the total amount of active catalyst (Rh^I + Rh^{III}) is still 100% under olefin hydrogenation conditions, which explains why this effect was not observed for 1-decene.

In conclusion, the activity increase under UME hydrogenation conditions results probably from indirect reactivation of inactive Rh-ester complexes by H₂ induced oxidation of Rh^I to Rh^{III}-complexes. A more detailed mechanistic discussion is presented later in section 4.2.2 after additional *operando* FTIR spectroscopic studies.

4.1.3 Hydroformylation network

After studying the isomerization and hydrogenation subnetworks, UME is compared to 1-decene in toluene or DMF under typical hydroformylation conditions (20 bar synthesis gas) including all relevant side and main reactions. The results in Figure 4.9 prove no significant substrate influences apart from a slightly lower UME

isomerization rate (cf. Figure 4.9a and c) as well as no significant solvent influences apart from a slightly higher UME isomerization rate in DMF compared to toluene (cf. Figure 4.9c and d). The hydroformylation product yields after 90 min reaction time are almost identical in all four cases as well as the regioselectivity in terms of a linear:branched oxo-ester ratio ($\approx 99:1$). The same holds for undesired hydrogenation yields ($\approx 2\%$). Again, the Rh-ester complexation may be responsible for slightly

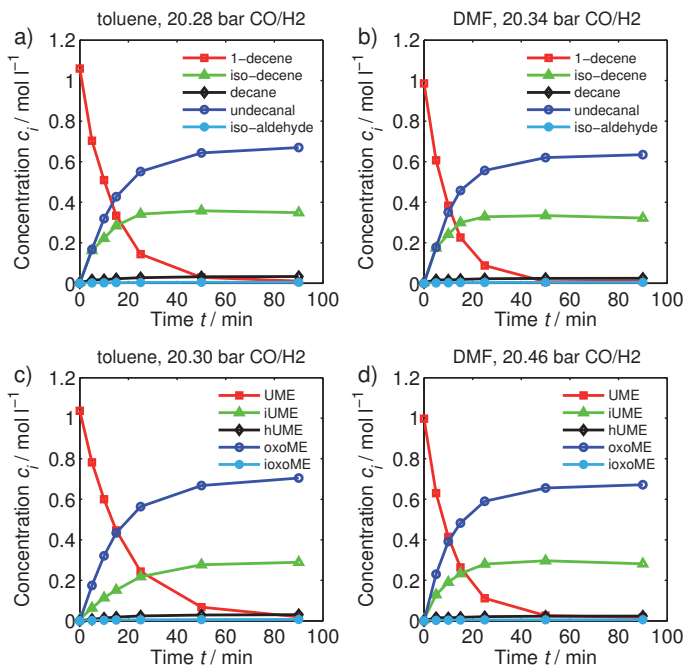


Figure 4.9: Comparison of 1-decene to UME in toluene or DMF - hydroformylation network. ($c_{\text{sub}}^0 = 1 \text{ mol l}^{-1}$, Rh:sub (molar) = 1:10000, Rh:lig (molar) = 1:3)

lower isomerization rates of UME in toluene compared to 1-decene. DMF, as already discussed, reduces this Rh-ester interaction, which leads to higher rates because more active Rh is available.

Apart from that, the solubility of CO and H₂ is different in both solvent/substrate systems, which affects the catalyst pre-equilibria. The experimental data proves that high partial pressures and concentrations of CO and H₂ reduce the deactivating Rh-ester interactions significantly. Therefore, no significant differences between olefin and ester are present under typical hydroformylation reaction conditions.

4.2 Hydroformylation reaction mechanism for UME

In the previous section, kinetic key experiments comparing the isomerization, hydrogenation and hydroformylation (sub)networks of 1-decene and UME were discussed. It was possible to conclude that i) both substrates follow the same reaction mechanisms with the same rate determining steps (see section 3.2.2, Figure 3.11), ii) Rh-ester complexation reduces the amount of active Rh under CO/H₂ free conditions significantly and iii) the dissolved gases strongly influence the ester-catalyst interactions. Hence, the hydroformylation reaction mechanism valid for 1-decene has to be enhanced for UME in terms of catalyst pre-equilibria to include the suspected additional Rh-species. In order to clarify the true nature of the suspected Rh-ester complexes further, *operando* FTIR experiments, analogously to those presented in section 3.2.1, were conducted and will be discussed in the following. Finally, the enhanced hydroformylation reaction mechanism for UME will be presented. The mechanistic kinetic model presented in section 3.3 will be enhanced subsequently in accordance to the respective mechanistic findings.

4.2.1 Mechanistic investigations using *operando* FTIR spectroscopy

This section presents experimental results of *operando* FTIR spectroscopic investigations of the Rh-BiPhePhos catalyzed isomerization, hydrogenation and hydroformylation of UME. It is the goal to find relevant Rh-complexes that contribute to the overall catalyst material mass balance as well as to identify suspected Rh-ester complexes. The experimental equipment and procedures are identical to those being used in section 3.2.1⁴.

Figure 4.10 summarizes series of *operando* FTIR spectra recorded during a) isomerization, b) hydrogenation and c) hydroformylation of UME focusing on reactants and reaction products. Most interesting in this context is the =C–H bending vibration region between 850 - 1050 cm⁻¹ to observe conversion of the double bond as well as isomerization from terminal to internal positions. The C=O stretching vibration region between 1650 - 1800 cm⁻¹ is not well suited to observe oxo-ester production because the ester carbonyl group shows strong IR absorption in this wavenumber region and overlaps with the aldehyde group. Therefore, the overtone of the C=O stretching vibration between 2650 - 2800 cm⁻¹ was used to observe the production of oxoUME.

Compared to the isomerization of 1-decene in Figure 3.7a, the isomerization rate of UME (=C–H bending bands at 913 and 995 cm⁻¹) to double bond isomers iUME (=C–H bending band at 967 cm⁻¹) under the same reaction conditions is much

⁴ 12 mg Rh(acac)(CO)₂ and 60 mg BiPhePhos in 15 ml toluene + 5 ml UME in 5 ml toluene.

lower (see Figure 4.10a, > 90 min for approx. 90 % conversion for UME, 12 min for 100% conversion for 1-decene). As already discussed in the previous section, ester chelation under CO free conditions is most probably responsible for significantly reducing catalyst activity. However, the Rh-ester interaction seems to be weaker in these experiments, probably due to low temperatures (40 °C) and higher Rh-substrate ratios (1:500).

Under hydrogenation conditions, the catalyst activity is drastically increased. This increase can be assigned to reactivation of inactive Rh-ester complexes by oxidation of Rh^I to Rh^{III}-species. This can be seen by the fast isomerization of UME (full conversion of UME to mostly double bond isomers iUME after 18 min, see Figure 4.10b). It is not possible to observe the hydrogenation product directly because it has the same bands as UME and iUME, apart from bands belonging to the double bond. However, the decreasing signal intensity of the band belonging to the internal double bond at 967 cm⁻¹ proves production of hUME indirectly.

Under hydroformylation conditions, almost no double bond isomerization and

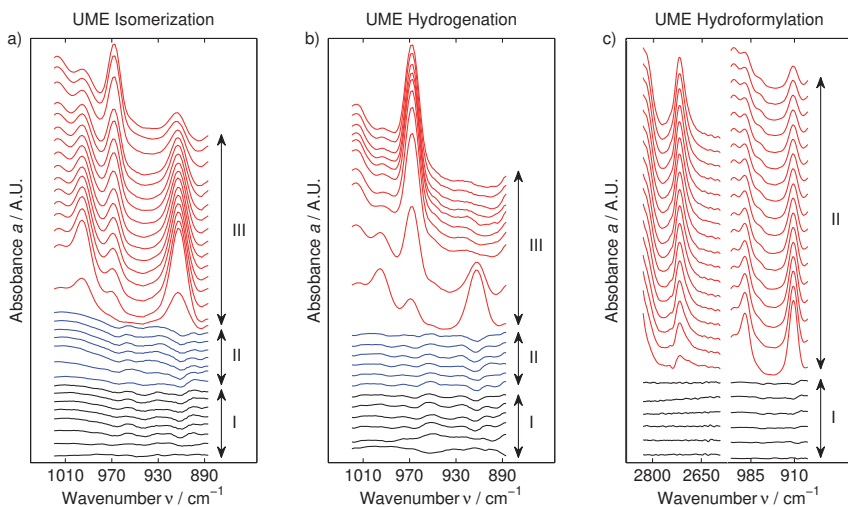


Figure 4.10: *Operando* FTIR spectra (=C–H bending vibration and C=O stretching vibration overtone region) recorded during isomerization, hydrogenation and hydroformylation of UME after solvent background subtraction. a) I: catalyst activation at 10 bar synthesis gas, II: gas phase exchange to 1 bar N₂, III: substrate injection, b) I: catalyst activation at 10 bar synthesis gas, II: gas phase exchange to 10 bar H₂, III: substrate injection and c) I: catalyst activation at 10 bar synthesis gas, II: substrate injection at 20 bar synthesis gas. (toluene, 40 °C, $c_{\text{sub}}^0 = 1 \text{ mol l}^{-1}$, Rh:sub (molar) = 1:500, Rh:lig (molar) = 1:1.5, time interval between spectra = 6 min)

hydrogenation occurs whereas high conversion of UME to oxoUME (C=O carbonyl stretching overtone band at 2717 cm^{-1}) is achieved. The selectivity to the linear oxo-ester, expressed as linear:branched ratio, was confirmed by gas chromatography to be $\approx 99:1$.

Figure 4.11 summarizes series of *operando* FTIR spectra recorded during a) isomerization, b) hydrogenation and c) hydroformylation of UME focusing on the metal carbonyl region to detect catalyst complexes or intermediates. Pre-formation of the Rh-BiPhePhos catalyst was carried out the same way as described in section 3.2.1. Adding 10 bar synthesis gas under stirring initiated catalyst activation to form exclusively hydrido-Rh-dicarbonyl complexes *e,e*-HRh(BP)(CO)₂ with their typical carbonyl bands at 2017 and 2075 cm^{-1} (see spectra set I in Figure 4.11a-c).

Addition of UME into the liquid phase under synthesis gas atmosphere did not change the detected spectra despite a reduction of signal intensity caused by dilution (see Figure 4.11c, spectra set II). This observation is perfectly identical to results using 1-decene in section 3.2.1 proving the same reaction mechanism and rate determining

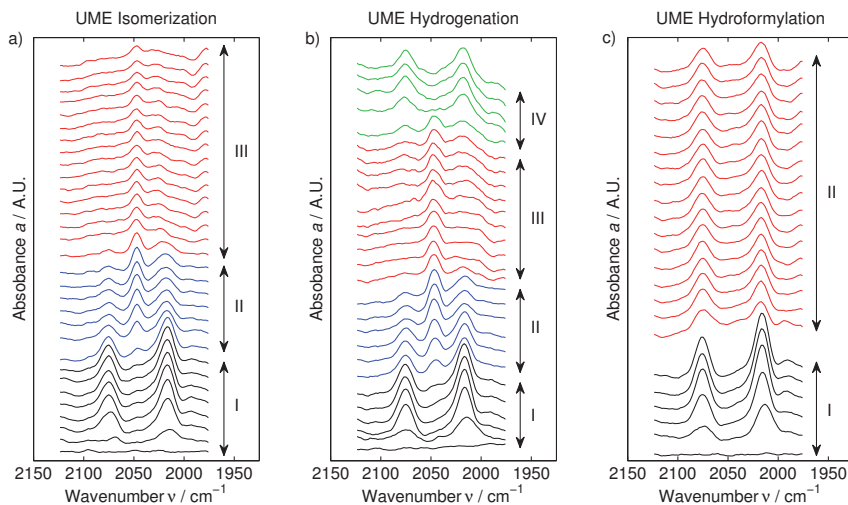


Figure 4.11: *Operando* FTIR spectra (metal carbonyl vibration region) recorded during isomerization, hydrogenation and hydroformylation of UME after solvent background subtraction. a) I: catalyst activation at 10 bar synthesis gas, II: gas phase exchange to 1 bar N₂, III: substrate injection, b) I: catalyst activation at 10 bar synthesis gas, II: gas phase exchange to 10 bar H₂, III: substrate injection, IV: addition of 10 bar CO and c) I: catalyst activation at 10 bar synthesis gas, II: substrate injection at 20 bar synthesis gas. (toluene, $40\text{ }^{\circ}\text{C}$, $c_{\text{sub}}^0 = 1\text{ mol l}^{-1}$, Rh:sub (molar) = 1:500, Rh:lig (molar) = 1:1.5, time interval between spectra = 6 min)

step for both substrates under hydroformylation conditions.

After the synthesis gas atmosphere was exchanged with inert nitrogen or hydrogen (see Figure 4.11a-b, spectra set II) the hydrido-Rh-monocarbonyl complex with its characteristic band 2047 cm^{-1} was formed. This complex remained stable under isomerization and hydrogenation conditions, which is completely analogous to experiments with 1-decene (see Figure 4.11a-b, spectra set III). However, the signal intensity of this band is lower under isomerization conditions compared to the corresponding 1-decene experiment (see Figure 3.8a, spectra set III), supporting the presumption that less Rh is active as a consequence of ester chelation. Since no other bands were detectable, the suspected Rh-ester complex is most probably not containing a carbonyl ligand.

After the hydrogenation experiment, 10 bar CO were injected into the 10 bar H_2 atmosphere (spectra set VI in Figure 4.11b). The results prove the reversibility of the transformation between hydrido-Rh-mono- and dicarbonyl complexes because the corresponding typical carbonyl bands returned immediately.

4.2.2 Extended hydroformylation reaction mechanism for UME

Combining experimental findings discussed in section 4.1 and *operando* FTIR experiments discussed in section 4.2.1 leads to the following conclusions regarding the Rh-BiPhePhos catalyzed hydroformylation reaction mechanism of UME:

- Under typical hydroformylation conditions (high partial pressures of CO and H_2), the reaction rates of 1-decene and UME do not differ. Hence, the mechanisms and rate determining steps of the isomerization, hydrogenation and hydroformylation reactions are identical.
- Without CO and H_2 , UME chelates and forms inactive Rh-ester complexes, reducing the amount of active catalyst. Similar interactions with Rh-catalysts were observed in [Nelsen et al. 2015; Costa et al. 2016].
- Presence of dissolved CO counteracts the Rh-ester complexation.
- The Rh-ester complex does not contain a CO ligand.
- Presence of dissolved H_2 increases the catalyst activity by reactivation of deactivated Rh-ester complexes, probably caused by oxidation of Rh^{I} to Rh^{III} -trihydride, as described in [Walter et al. 2017].

Hence, the catalyst pre-equilibrium was extended for UME (see Figure 4.12), whereas the catalytic cycles for isomerization, hydrogenation and hydroformylation remain the same as in Figure 3.11. Two respective Rh-species were added: i) An inactive

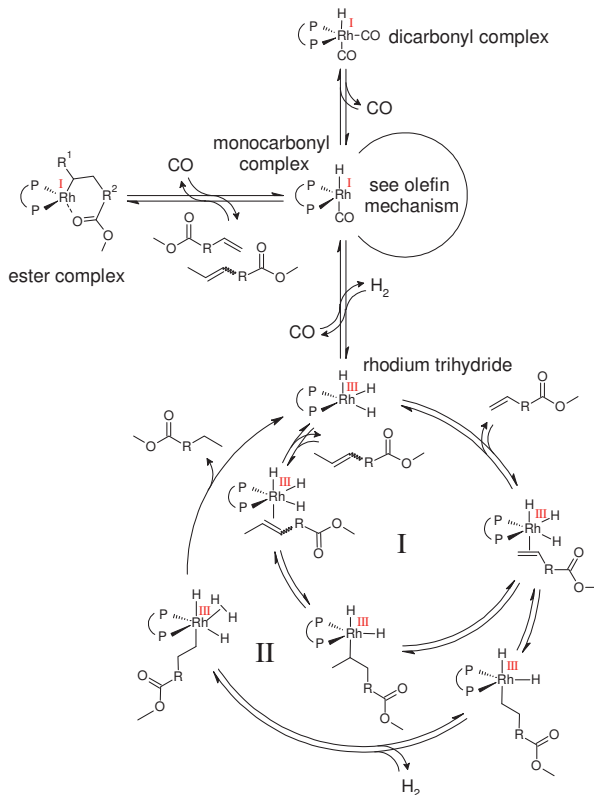


Figure 4.12: Extended hydroformylation reaction mechanism for UME with two new added Rh-species: Rh-ester complex and Rh^{III}-trihydride complex catalyzing I: isomerization and II: hydrogenation of UME. For Rh^I catalyzed reactions see Figure 3.11.

Rh-ester complex, similar to dormant ring-structures⁵ described in [Nelsen et al. 2015; Costa et al. 2016] and ii) a Rh^{III}-trihydride complex, catalyzing double bond isomerization and hydrogenation [Walter et al. 2017].

The reaction mechanisms for the Rh^{III}-trihydride catalyzed isomerization and hydrogenation start with association of the double bond to the unsaturated Rh-trihydride complex. Insertion of the double bond into the Rh-hydride bond followed by β -H elimination yields subsequently the double bond isomer of UME and restores

⁵ The real nature of the inactive Rh-ester complex could not be proven yet, but it is more likely that ring formation occurs. This can be explained by the observed catalyst reactivation after addition of CO (cf. Figure 4.6). CO probably prevents ring formation by occupation of necessary coordination sites. If Rh-carboalkoxy complex formation would occur, as observed in [Walczuk et al. 2003], the catalyst activity would not be increased by CO.

the Rh^{III} -trihydride complex. The hydrogenation pathway requires double bond insertion into a Rh-hydride bond followed by association of an H_2 molecule, similar to complexes reported in [Morris 2008]. Subsequent irreversible product elimination and instant re-oxidation of Rh by the associated H_2 molecule produces the saturated ester hUME and closes the catalytic cycle. DFT calculations presented in [Walter et al. 2017] support the existence of the suspected Rh^{III} -trihydride mechanism.

In the following sections, the mechanistic kinetic model, derived in section 3.3, will be adjusted in accordance to the enhanced hydroformylation reaction mechanism for UME and fitted to carefully designed kinetic (semi-) batch experiments.

4.3 Kinetic modeling

In this section, the mechanistic kinetic model for the hydroformylation of UME including double bond isomerization and hydrogenation side reactions is presented. The reaction network is very similar to the reaction network for 1-decene. However, the hydroformylation of UME double bond isomers to branched hydroformylation products was neglected. Double bond isomers of UME as well as branched hydroformylation products were lumped to the pseudo-components iUME and ioxoUME, respectively, because unique analytical identification was not possible due to non-available calibration standards. Figure 4.13 summarizes the hydroformylation reaction network including isomerization of UME to iUME (r_{iso}), hydrogenation of UME to hUME (r_{hyd}), hydroformylation of UME to oxoUME (r_{hyf1}) and its branched counterpart ioxoUME (r_{hyf2}).

As already discussed in previous sections, the reaction mechanisms are identical for 1-decene and UME. The catalyst pre-equilibrium for UME, however, is different and contains two additional Rh-complexes, an inactive Rh-ester complex [Nelsen et al. 2015; Costa et al. 2016] and an isomerization and hydrogenation active Rh^{III} -trihydride complex [Walter et al. 2017]. Hence, all kinetic equations from section 3.3, apart from the catalyst pre-equilibrium, are also valid for UME (for their derivation: see section 3.3). This holds for the isomerization and hydrogenation catalyzed by Rh^{III} -trihydride complexes as well since the reaction steps are formally the same and lead therefore to the same kinetic rate equation. The respective rate constants are assumed to be identical to those for isomerization and hydrogenation catalyzed by hydrido-Rh-monocarbonyl complexes to reduce the number of unknown kinetic parameters. This assumption is reasonable because the rate determining substrate coordination is mostly hindered by steric interactions between substrate and ligand, which are the same for both active catalyst complexes [Walter et al. 2017].

Apart from the inactive hydrido-Rh-dicarbonyl complex (DC), the catalyst pre-equilibrium contains two additional Rh-species, inactive Rh-ester complexes (EC)

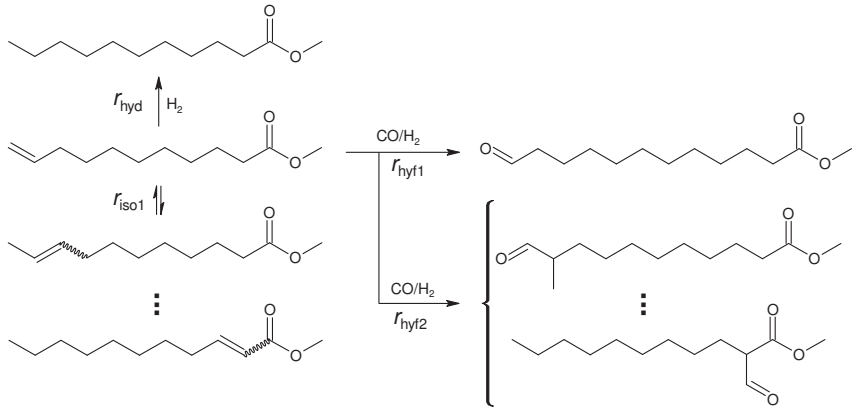


Figure 4.13: Proposed hydroformylation reaction network of UME including main (r_{hyf1}) and side reactions.

and active Rh^{III} -trihydride complexes (TH). It should be noted that all unsaturated esters may form Rh-ester complexes. Therefore, terminal UME as well as internal iUME are assumed to form Rh-ester complexes, denoted as EC1 and EC2. To derive an explicit expression for the concentrations of the two active catalyst complexes, hydrido-Rh-monocarbonyl (MC) and trihydride (TH), a Rh mass balance (4.2) as well as classical mass action law formulations (4.3)-(4.6) were used. The total amount of Rh is equal to the amount of catalyst precursor $\text{Rh}(\text{acac})(\text{CO})_2$.

$$c_{\text{Rh,tot}} = c_{\text{DC}} + c_{\text{MC}} + c_{\text{EC1}} + c_{\text{EC2}} + c_{\text{TH}} \quad (4.2)$$

$$K_{\text{cat}}^{\text{I}} = \frac{c_{\text{DC}}}{c_{\text{MC}}c_{\text{CO}}} \quad (4.3)$$

$$K_{\text{cat}}^{\text{II}} = \frac{c_{\text{EC1}}c_{\text{CO}}}{c_{\text{MC}}c_{\text{UME}}} \quad (4.4)$$

$$K_{\text{cat}}^{\text{III}} = \frac{c_{\text{EC2}}c_{\text{CO}}}{c_{\text{MC}}c_{\text{iUME}}} \quad (4.5)$$

$$K_{\text{cat}}^{\text{IV}} = \frac{c_{\text{TH}}c_{\text{CO}}}{c_{\text{MC}}c_{\text{H}_2}} \quad (4.6)$$

Combining equations (4.2)-(4.6) leads to an explicit expression for the concentration of active MC (4.7) and TH (4.8) as function of the catalyst precursor concentration, unsaturated ester concentration and dissolved CO/H_2 concentrations.

$$c_{MC} = \frac{c_{Rh,tot}}{\left(1 + K_{cat}^I c_{CO} + K_{cat}^{II} \frac{c_{UME}}{c_{CO}} + K_{cat}^{III} \frac{c_{iUME}}{c_{CO}} + K_{cat}^{IV} \frac{c_{H_2}}{c_{CO}}\right)} \quad (4.7)$$

$$c_{TH} = \frac{c_{Rh,tot}}{\left(1 + \frac{K_{cat}^I}{K_{cat}^{IV}} \frac{c_{CO}^2}{c_{H_2}} + \frac{K_{cat}^{II}}{K_{cat}^{IV}} \frac{c_{UME}}{c_{H_2}} + \frac{K_{cat}^{III}}{K_{cat}^{IV}} \frac{c_{iUME}}{c_{H_2}} + \frac{1}{K_{cat}^{IV}} \frac{c_{CO}}{c_{H_2}}\right)} \quad (4.8)$$

In summary, the set of kinetic rate equations for the isomerization, hydrogenation and hydroformylation of UME is shown in (4.9)-(4.12). The equilibrium constant used in (4.9) was assumed to be identical to the equilibrium constant between 1- and 2-decene K_{21}^{eq} , because under typical hydroformylation conditions of 1-decene, no significant amounts of double bond isomers beyond 2-decene were observed and it is assumed that this pattern holds for UME as well.

$$r_{iso} = k_{iso}(T) \left(c_{UME} - \frac{c_{iUME}}{K_{21}^{eq}} \right) \cdot (c_{MC} + c_{TH}) \quad (4.9)$$

$$r_{hyd} = \frac{k_{hyd}(T) c_{UME} c_{H_2}}{\left(1 + K_{hyd}^I c_{H_2}\right)} \cdot (c_{MC} + c_{TH}) \quad (4.10)$$

$$r_{hyf1} = \frac{k_{hyf1}(T) c_{UME} c_{CO} c_{H_2}}{\left(1 + K_{hyf}^I c_{H_2} + K_{hyf}^{II} c_{H_2} c_{CO}\right)} \cdot c_{MC} \quad (4.11)$$

$$r_{hyf2} = \frac{k_{hyf2}(T) c_{UME} c_{CO} c_{H_2}}{\left(1 + K_{hyf}^{III} c_{H_2} + K_{hyf}^{IV} c_{H_2} c_{CO}\right)} \cdot c_{MC} \quad (4.12)$$

4.4 Kinetic experiments and parameter estimation

In this section, kinetic (semi-) batch experiments were designed and conducted in terms of a subnetwork analysis, analogous to section 3.4.1. The experimental equipment and procedures used are described in detail in appendix A. Subsequently, estimation of unknown kinetic parameters of the developed mechanistic kinetic model followed using the observed experimental data. The parameter estimation was performed by minimizing a least-squares objective function, analogously to section 3.4.

4.4.1 Experimental design and subnetwork analysis

The subnetwork analysis strategy for UME is identical to the strategy for 1-decene discussed in section 3.4.1. Table 4.1 summarizes all designed kinetic experiments. Less experiments were designed because the UME system has less components and kinetic parameters compared to the 1-decene system. Additionally, parameter subset

selection was used to support the experimental design for reduction of the amount of necessary kinetic experiments. Interesting key experiments, such as Hyd3 (perturbed hydrogenation experiment, see Figure 4.8), were added because the mechanistic kinetic model should be able to reproduce these data points.

Table 4.1: Experimental design for subnetwork analysis: Isomerization, hydrogenation and hydroformylation. (toluene, $c_{\text{UME}}^0 = 1 \text{ mol l}^{-1}$, Rh:sub (molar) = 1:10000, Rh:lig (molar) = 1:3)

Exp. ID	p / bar	$T / ^\circ\text{C}$	Gas supply
Iso1	0	100	No consumption
Iso2	1	100	No consumption
Iso3	5	100	No consumption
Hyd1	5	100	batch
Hyd2	10	100	batch
Hyd3	10	100	batch
Hyf1	20	100	batch
Hyf2	5	100	semi-batch
Hyf3	20	110	batch
Hyf4	20	90	batch

4.4.2 Isomerization subnetwork

In order to estimate unknown kinetic parameters of the double bond isomerization of UME as well as catalyst pre-equilibrium parameters associated with CO induced (de)activation, three isomerization batch experiments at different partial pressures of CO were conducted (see Table 4.1). These experimental results were already discussed in section 4.1.1.2, see Figure 4.6.

Figure 4.14 presents the corresponding experimental concentration profiles of the isomerization of UME to iUME as well as simulation results using the estimated kinetic parameters, summarized in Table 4.2. As already discussed in section 4.1.1.2, the isomerization of UME shows a complex dependence on the concentration of dissolved CO, which is completely different compared to the CO dependence of the isomerization of 1-decene. Whereas the catalyst activity is low under CO free conditions (Figure 4.14, Iso1), the activity increases with increasing CO pressure (Figure 4.14, Iso2), passes a maximum and decreases at higher CO levels (Figure 4.14, Iso3). It was concluded that the interplay between catalyst deactivation by Rh-ester formation and the equilibrium between hydrido-Rh-mono- and dicarbonyl complexes is responsible for the observations because both equilibria depend on dissolved CO.

It can clearly be seen in Figure 4.14 that the extended mechanistic model is able to reproduce the CO dependence of the double bond isomerization reaction with good

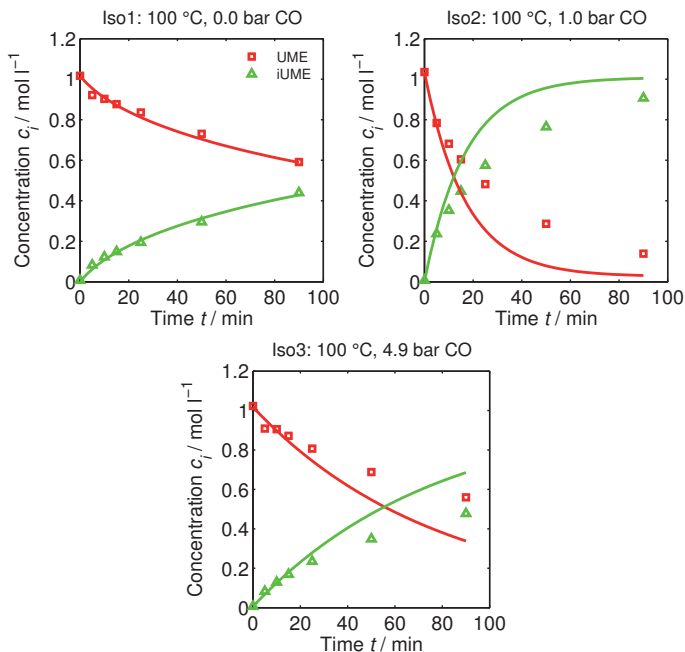


Figure 4.14: Experimental and modeling results of the isomerization subnetwork analysis for UME. Symbols: Experimental data, Solid lines: Corresponding simulation using the developed mechanistic kinetic model with estimated parameter values. Experimental conditions: See Table 4.1.

accuracy. This supports the proposed extension of the catalyst pre-equilibrium for UME presented in Figure 4.12 and the assumption that the reaction follows the same mechanism with the same rate determining step (substrate coordination) as 1-decene. Using local parameter subset selection (see section 2.3) proved all kinetic isomerization and catalyst pre-equilibrium parameters to be identifiable using the experimental design (see Figure D.2a in appendix D).

4.4.3 Hydrogenation subnetwork

In order to estimate unknown kinetic parameters of the double bond hydrogenation of UME as well as catalyst pre-equilibrium parameters associated with H_2 caused Rh^{III} -trihydride complex formation, three hydrogenation batch experiments at different partial pressures of H_2 were conducted (see Table 4.1). These experimental results were already partly discussed in section 4.1.2.2, Figure 4.7c and Figure 4.8. Figure 4.15 presents the corresponding experimental concentration profiles of the

hydrogenation of UME to hUME, including the isomerization to iUME, as well as simulation results using the estimated kinetic parameters, summarized in Table 4.2.

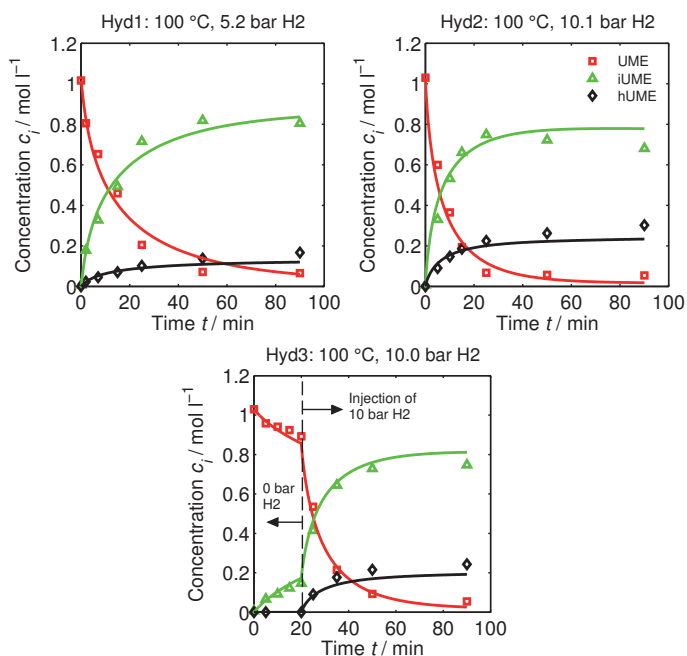


Figure 4.15: Experimental and modeling results of the hydrogenation subnetwork analysis for UME. Symbols: Experimental data, Solid lines: Corresponding simulation using the developed mechanistic kinetic model with estimated parameter values. Experimental conditions: See Table 4.1.

As already discussed in section 4.1.2.2, the catalyst activity under H_2 rich conditions is higher compared to isomerization conditions without H_2 or CO (see Figure 4.14, Iso1 and Figure 4.15, Hyd1-2). Comparing the experimental and modeling results in Figure 4.15, Hyd1-2 reveals that the catalyst activity increases with increasing H_2 pressure/concentration, indicated by the increased isomerization reaction rate. The perturbed experiment that started as isomerization with addition of 10 bar H_2 after 20 minutes (see discussion in section 4.1.2.2) proved that the low catalyst activity under isomerization conditions can be increased drastically and instantly by H_2 addition (see Figure 4.15, Hyd3). It was concluded that significant oxidation of Rh^I to Rh^{III} -trihydride complexes reactivates deactivated Rh-ester complexes and thus increases the overall amount of active catalyst.

The corresponding mechanistic kinetic model, which includes the discussed catalyst

species, reproduces the observed experimental data with very good accuracy. This supports the proposed extension of the catalyst pre-equilibrium for UME presented in Figure 4.12 and the assumption that the reaction follows the same mechanism with the same rate determining step (substrate coordination) as 1-decene.

Using local parameter subset selection (see section 2.3) proved all kinetic hydrogenation and catalyst pre-equilibrium parameters to be identifiable using the experimental design (see Figure D.2b in appendix D).

4.4.4 Hydroformylation network

The missing kinetic parameters associated with hydroformylation of UME were estimated using four (semi-) batch hydroformylation experiments at different partial pressures of synthesis gas and temperatures (see Table 4.1). Parts of the presented experimental results were already discussed in section 4.1.3, Figure 4.9c. The corresponding experimental concentration profiles of the hydroformylation of UME to oxoUME and ioxoUME are presented in Figure 4.16. Additionally, the isomerization of UME to iUME and the hydrogenation of UME to hUME are included as well as simulation results using the estimated kinetic parameters, which are summarized in Table 4.2.

As already discussed in section 4.1.3, no significant difference between reaction rates under hydroformylation conditions between UME and 1-decene were observable. The data in Figure 4.16a and b shows that it is possible to shift the product selectivity from mostly double bond isomers iUME at low synthesis gas pressures to mostly linear hydroformylation product oxoUME at high synthesis gas pressures, which is very similar to hydroformylation results using 1-decene (see 3.4.4, Figure 3.16). Also, a significant temperature dependence of the main and side reactions was observed (see Figure 4.16c and d).

In total, the extended mechanistic kinetic model is able to reproduce the concentration profiles under the studied (semi-) batch conditions and reaction temperatures with high accuracy. This supports the proposed extension of the catalyst pre-equilibrium for UME presented in Figure 4.12 and the assumption that the reaction follows the same mechanism with the same rate determining step (substrate coordination) as 1-decene.

Using local parameter subset selection (see section 2.3) proved that all kinetic hydroformylation parameters are identifiable with the experimental design (see Figure D.2c in appendix D). Their values are summarized in Table 4.2. The apparent activation energies for the hydroformylation rates are in a similar reasonable order of magnitude compared to the olefin case ($\approx 56.0 \text{ kJ mol}^{-1}$). Interestingly, both hydroformylation rates for the formation of linear and branched oxo-esters have

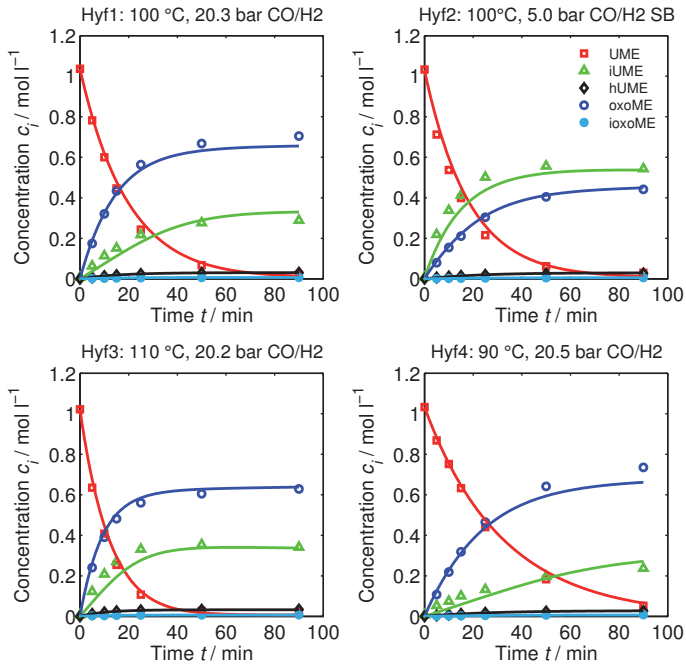


Figure 4.16: Experimental and modeling results of the hydroformylation network analysis for UME. Symbols: Experimental data, Solid lines: Corresponding simulation using the developed mechanistic kinetic model with estimated parameter values. Experimental conditions: See Table 4.1.

the same apparent activation energy, which is almost identical to the apparent activation energy of the formation of branched aldehydes for 1-decene. Furthermore, the second inhibition parameter in both hydroformylation rate equations turned out to be insignificant because they were estimated to be zero, analogously to the branched aldehyde formation rate using 1-decene. Hence, it can be concluded that the CO insertion may also be a slow step for the formation of linear and branched oxo-esters, similar to branched aldehyde formation (see discussion in section 3.4.4). As a consequence, the temperature does not influence the linear:branched ratio to a significant extent.

The presented subnetwork analysis allowed to estimate all catalyst pre-equilibrium parameters for the UME case, which represent the influence of substrate, CO and H₂ concentrations on catalyst activity. Figure 4.17 compares both expressions for the amount of active catalyst (hydrido-Rh-monocarbonyl and Rh-trihydride complexes) for 1-decene (see (3.13)) and UME (see (4.7)-(4.8)) using the respective estimated

parameters. The amount of active catalyst is steadily decreasing with increasing CO partial pressure for the 1-decene system and is not influenced by H₂ at all, as already discussed in section 3.2.2. Using UME as substrate, however, results in more complex dependencies of the active catalyst concentrations on dissolved CO and H₂. It can be seen in Figure 4.17 that an optimal CO partial pressure for a maximum amount of active catalyst (≈ 100 mbar) and a critical CO partial pressure at which both models become identical (≈ 500 mbar) exist. This explains the observed identical reaction rates of UME compared to 1-decene under hydroformylation conditions but strongly different reaction rates in CO/H₂ free cases.

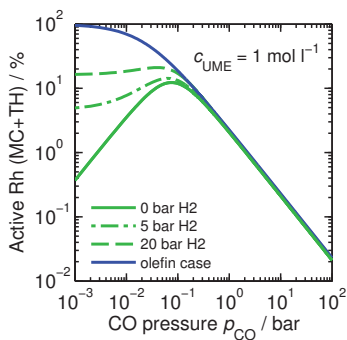


Figure 4.17: Comparison of the relative amount of active catalyst for UME (green) and 1-decene (blue) in % as a function of CO and H₂ partial pressure at 115 °C.

In summary, the good agreement between model and experimental data (see Figure 4.18), especially under borderline or perturbed reaction conditions, speaks again for the benefits of using mechanistic kinetic models. The suspected Rh-ester complexation as well as Rh-trihydride formation under H₂ atmosphere in CO free cases are likely to exist since the corresponding kinetic model perfectly explains all experimental observations. However, it was not possible yet to proof the existence of the suspected complexes e.g. spectroscopically. The good fit of the mechanistic kinetic model to experimental data supports assuming identical reaction mechanisms for UME and 1-decene as well as the substrate coordination being rate determining.

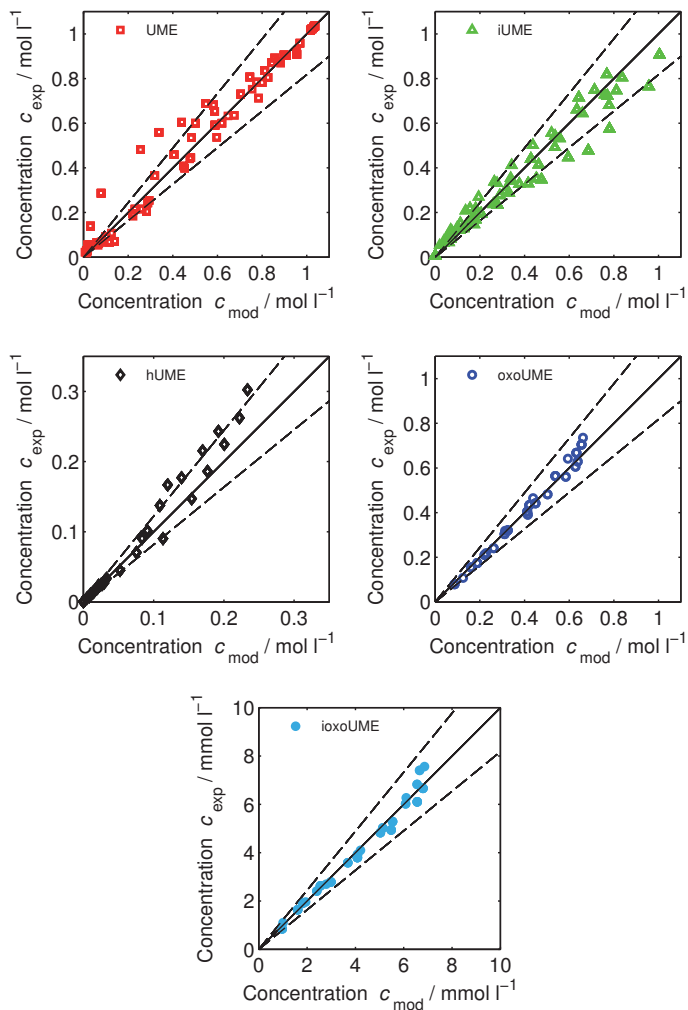


Figure 4.18: Parity plot of all 10 performed kinetic (semi-) batch experiments using UME. Experimental conditions: See table Table 4.1.

Table 4.2: Mechanistic kinetic models for the hydroformylation of UME using a Rh-BiPhePhos catalyst including side reactions. Estimated kinetic parameter values with 95 % confidence interval and recalculated apparent frequency factors and activation energies. Temperature dependence of the rate constant is expressed as $k = \exp(A + B(1 - T_{\text{ref}}/T))$, $T_{\text{ref}} = 373$ K.

Rate equation	Estimated parameters with 95 % CI
Cat. pre-equilibrium: Eq. (4.7) and (4.8)	$K_{\text{cat}}^{\text{I}} = 5.5 \cdot 10^3 \text{ l mol}^{-1} \pm 1.2 \%$ $K_{\text{cat}}^{\text{II}} = 2.3 \cdot 10^{-3} \pm 6.1 \%$ $K_{\text{cat}}^{\text{III}} = 1.7 \cdot 10^{-2} \pm 13.0 \%$ $K_{\text{cat}}^{\text{IV}} = 4.6 \cdot 10^{-3} \pm 7.4 \%$
Isomerization: Eq. (4.9)	$A_{\text{iso}} = 10.46 \pm 1.0 \%$ $B_{\text{iso}} = 22.90 \pm 29.0 \%$ $k_{\infty}^{\text{iso}} = 3.1 \cdot 10^{14} \text{ l mol}^{-1} \text{ min}^{-1}$ $E_{\text{A}}^{\text{iso}} = 71.0 \text{ kJ mol}^{-1}$
Hydrogenation: Eq. (4.10)	$A_{\text{hyd}} = 12.35 \pm 1.0 \%$ $B_{\text{hyd}} = 23.70 \pm 12.9 \%$ $k_{\infty}^{\text{hyd}} = 4.5 \cdot 10^{15} \text{ l}^2 \text{ mol}^{-2} \text{ min}^{-1}$ $E_{\text{A}}^{\text{hyd}} = 73.5 \text{ kJ mol}^{-1}$ $K_{\text{hyd}} \approx 0 \text{ l mol}^{-1} \pm > 10^9 \%$
Hydroformylation 1: Eq. (4.11)	$A_{\text{hyf1}} = 19.68 \pm 1.3 \%$ $B_{\text{hyf1}} = 18.24 \pm 16.8 \%$ $k_{\infty}^{\text{hyf1}} = 7.0 \cdot 10^{12} \text{ l}^3 \text{ mol}^{-3} \text{ min}^{-1}$ $E_{\text{A}}^{\text{hyf1}} = 56.6 \text{ kJ mol}^{-1}$ $K_{\text{hyf}}^{\text{I}} = 1.3 \cdot 10^2 \text{ l mol}^{-1} \pm 7.2 \%$ $K_{\text{hyf}}^{\text{II}} \approx 0 \text{ l}^2 \text{ mol}^{-2} \pm > 10^9 \%$
Hydroformylation 2: Eq. (4.12)	$A_{\text{hyf2}} = 14.79 \pm 2.0 \%$ $B_{\text{hyf2}} = 18.12 \pm 24.4 \%$ $k_{\infty}^{\text{hyf2}} = 7.0 \cdot 10^{12} \text{ l}^3 \text{ mol}^{-3} \text{ min}^{-1}$ $E_{\text{A}}^{\text{hyf2}} = 56.2 \text{ kJ mol}^{-1}$ $K_{\text{hyf}}^{\text{III}} = 1.4 \cdot 10^3 \text{ l mol}^{-1} \pm 7.2 \%$ $K_{\text{hyf}}^{\text{IV}} \approx 0 \text{ l}^2 \text{ mol}^{-2} \pm > 10^9 \%$

4.5 Optimal reaction control strategies

It is very likely that optimal hydroformylation reaction conditions for UME differ to some extent from those found for 1-decene (see section 3.5). Especially the interesting tandem isomerization-hydroformylation case may be controlled differently using long-chain oleocompounds as substrates because the Rh-ester complexation has a significant influence on the essential double bond isomerization reaction. The role of dissolved CO and H₂ is pronounced in this context because both gases are strongly involved in catalyst pre-equilibria controlling the overall catalyst activity. Therefore,

the developed mechanistic kinetic model, presented in the previous section, was taken to rigorously optimize a semi-batch UME hydroformylation for a maximum yield of oxoUME Y at a specified space time yield STY . The optimization problem for UME was defined and solved identically to the olefin case (3.31) but with different equality constraints in terms of kinetic rate equations and corresponding parameters. All other constraints and the objective function are identical (see section 3.5).

The reaction time τ is again normalized to the optimal reaction time of the hydroformylation of 1-decene (87.8 min) to compare both cases. Evidently, UME needs $\approx 30\%$ more reaction time compared to 1-decene to meet the desired STY under optimal temperature and pressure control (see Figure 4.19).

Figure 4.19a shows the optimal temperature profile for the hydroformylation of UME. Qualitatively, the profile does not differ strongly from the optimal temperature profile for 1-decene (see Figure 3.21a). Similar activation energies are responsible for similar temperature dependence of the reactions, which is reasonable because both substrates follow the same reaction mechanism.

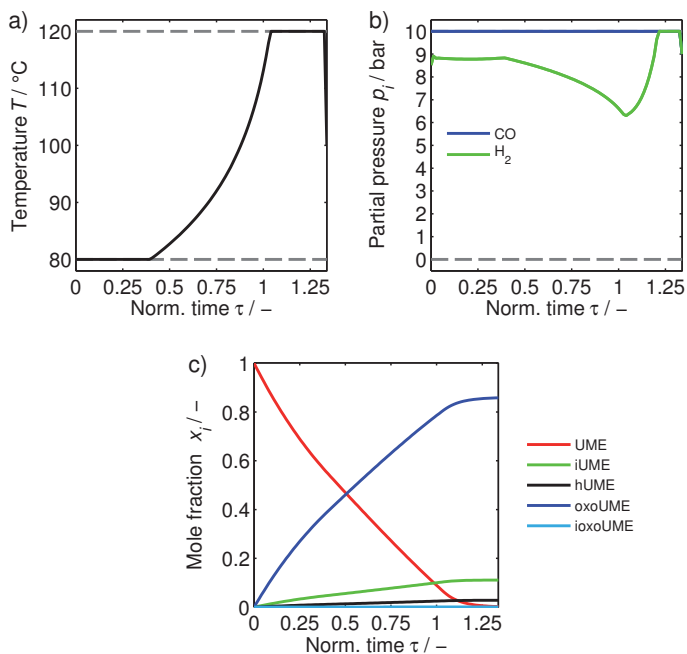


Figure 4.19: Optimization results for the hydroformylation of UME: a) optimal temperature profile. b) optimal partial pressure profiles. c) concentration profiles in molar fractions. ($c_{\text{sub}}^0 = 1 \text{ mol l}^{-1}$, $\text{Rh:sub (molar)} = 1:10000$, $STY = 100 \text{ kg m}^{-3} \text{ h}^{-1}$)

Regarding optimal partial pressures, the optimal profile for H₂ is not at the upper boundary most of the reaction time in contrast to the olefin case. It follows an optimal trajectory as a compromise between high hydroformylation rate and low undesired isomerization and hydrogenation rate. At high UME conversions, the optimal pressure of H₂ meets the upper boundary to accelerate back-isomerization of iUME to UME for fast oxoUME production. The optimal partial pressure of CO, however, is always at the upper boundary to counteract Rh-ester complexation and suppress undesired isomerization and hydrogenation. The maximum achievable yield of oxoUME for the hydroformylation of UME at the specified *STY* is 86 %, which is identical to the undecanal yield in case of using 1-decene.

To study how the tandem isomerization-hydroformylation reaction of renewable long-chain internal oleo-esters compares to a mixture of internal olefins, an optimization calculation was performed using pure iUME initially. Figure 4.20 summarizes the optimization results of this tandem isomerization-hydroformylation study. The optimal temperature profile is always constant at the upper boundary of 125 °C to keep the hydroformylation rate high as well as the back-isomerization for reproduction of consumed UME from iUME. This finding is identical to internal *n*-decene results. Regarding optimal partial pressure profiles, the UME results differ significantly from those calculated for internal *n*-decenes. The optimal CO partial pressure profile decreases with increasing reaction time almost linearly from high values (≈ 7 bar) to low values (≈ 0.3 bar). The reason for this linear trajectory is to counteract Rh-ester complexation at high ester concentrations to maintain high catalyst activity. Furthermore, the hydroformylation rate is kept high whereas undesired hydrogenation is suppressed by the optimal CO partial pressure profile. The optimal H₂ partial pressure profile looks qualitatively similar to the olefin case but the absolute optimal value is lower to balance high hydroformylation and back-isomerization rates against the undesired hydrogenation rate. At high iUME conversion, the optimal partial pressure of H₂ increases to compensate hydroformylation rate reduction due to low substrate concentrations. Theoretically, these measures allow to produce oxoUME with excellent selectivity and yield (≈ 95 %) from iUME with very low yield of undesired hydrogenated ester (≈ 4 %) at the specified *STY*.

In summary, the hydroformylation of UME is controlled optimally in a similar way compared to 1-decene, which is a consequence of almost identical reaction rates under hydroformylation conditions. The tandem isomerization-hydroformylation of iUME, however, has to be operated differently compared to internal *n*-decenes. Especially the partial pressure of CO plays a crucial role for the catalyst activity because it significantly influences catalyst deactivation by Rh-ester complexation.

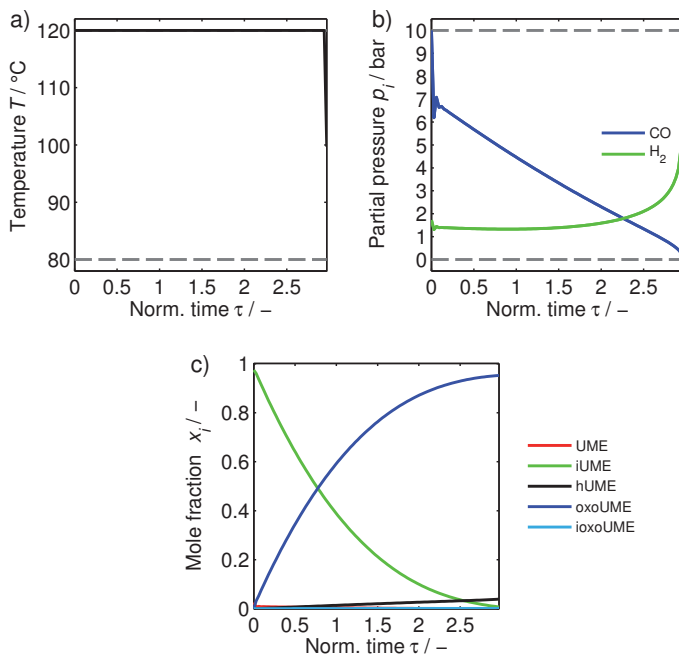


Figure 4.20: Optimization results for the tandem isomerization-hydroformylation of UME: a) optimal temperature profile. b) optimal partial pressure profiles. c) concentration profiles in molar fractions. ($c_{\text{sub}}^0 = 1 \text{ mol l}^{-1}$, $\text{Rh:sub (molar)} = 1:500$, $\text{STY} = 50 \text{ kg m}^{-3} \text{ h}^{-1}$)

4.6 Summary

This chapter was dedicated to the Rh-BiPhePhos catalyzed hydroformylation of UME as representative long-chain oleo-ester from renewable resources (castor oil). The benefit of studying UME as hydroformylation substrate is the possibility to investigate influences of the ester group on the Rh-BiPhePhos catalyst by direct comparison of experimental results to those obtained from the structurally similar olefin 1-decene. Several issues were addressed in this chapter theoretically and experimentally:

- Comparison of key experiments for the isomerization, hydrogenation and hydroformylation (sub)networks using UME and 1-decene in different solvents (toluene, DMF) to reveal substrate and solvent effects
- Detection of catalyst species using FTIR spectroscopy and subsequent extension of the reduced olefin hydroformylation reaction mechanism

- Extension of the mechanistic kinetic model developed in the previous chapter including additional (in)active Rh-complexes that become relevant in case of using UME as substrate
- Design and conduct of 10 (semi-) batch experiments for isomerization, hydrogenation, hydroformylation (sub)networks using UME
- Estimation of kinetic parameter values for the enhanced mechanistic kinetic model using the observed (semi-) batch experimental data
- Optimal reaction control strategies for the hydroformylation of UME as well as the tandem isomerization-hydroformylation of iUME

Comparing UME to 1-decene revealed a significant influence of the ester group on the catalyst activity under H_2 free isomerization conditions. Especially without CO, the catalyst activity was reduced drastically by a factor of ≈ 100 compared to the olefin case. This effect was assigned to the formation of inactive Rh-ester complexes by chelation of the unsaturated ester, which reduces the amount of available active Rh-catalyst.

Furthermore, the comparison study revealed a strong solvent influence on the catalyst activity for UME under isomerization conditions, which was not observable for 1-decene. It was concluded that polar solvents might compete for free coordination sites at the Rh-catalyst or stabilize the ester group in solution reducing its tendency to chelate. Both possibilities would increase the catalyst activity by preventing Rh-ester complexation.

Under CO free hydrogenation conditions, significant catalyst reactivation by H_2 was observable. It is likely that this reactivation is a consequence of an oxidation of Rh^I to isomerization and hydrogenation active Rh^{III} -trihydride complexes, increasing the amount of active Rh.

Since both, the Rh-ester and Rh-trihydride complex formations, are suppressed by CO, no significant difference in reaction rates and catalyst activity between UME and 1-decene was observable under typical hydroformylation conditions using high synthesis gas pressure. The choice of solvent did not significantly affect the reactions rates of UME under hydroformylation conditions because the Rh-ester complex formation was already suppressed by CO.

It was not possible to observe new catalyst complexes using *operando* FTIR spectroscopy, analogously conducted to studies using 1-decene in the previous chapter. It was concluded that the suspected (in)active complexes do not contain carbonyl ligands. Furthermore, it became evident that the reactions themselves follow the same mechanism with identical rate determining steps for both substrates. Thus, the reaction mechanism as well as the mechanistic kinetic model presented in the

previous chapter were extended in terms of catalyst pre-equilibria including the suspected Rh-ester and Rh-trihydride complexes.

Fitting of the model by parameter estimation to 10 carefully designed (semi-) batch isomerization, hydrogenation and hydroformylation experiments was successful with a high quality of fit. Thus, the existence of the suspected additional Rh-complexes is likely because the model including them is able to reproduce all experimental observations, even under borderline conditions. Furthermore, the good fit supports the assumption that the reactions follow the same mechanism with the same rate determining steps for both substrates.

The extended mechanistic kinetic model allowed to calculate optimal control profiles for semi-batch hydroformylation reaction temperature and pressures to maximize the yield of oxoUME. It was revealed that the optimal control profiles for the hydroformylation of UME are similar to those obtained using the n-decene model. The tandem isomerization-hydroformylation of iUME, however, needs different control strategies because of more complex interactions between the Rh-catalyst and the ester carbonyl group.

5 Outlook

The intention of this thesis was to contribute to the understanding of tandem isomerization-hydroformylation reactions, especially those using long-chain unsaturated renewable oleochemicals as feedstocks (e.g. methyl oleate (OME)). These molecules are promising platform chemicals for e.g. renewable polymers production and could substitute petrochemicals in the future [Behr and Vorholt 2012]. The conducted model substance investigations using n-decenes, to understand the tandem isomerization-hydroformylation mechanism of internal substrates, and methyl 10-undecenoate, to evaluate the influence of the ester group on the used Rh-BiPhePhos catalyst, revealed that:

1. An optimal CO partial pressure exists for the tandem isomerization-hydroformylation to achieve a maximum aldehyde production rate.
2. Oleo-esters form inactive Rh-complexes under CO free conditions, which leads to catalyst deactivation.
3. Polar solvents (e.g. DMF) are suited to counteract Rh-ester complexation, which causes catalyst deactivation.

A special role in this context plays the double bond isomerization reaction. If substrates are not a thermodynamic mixture of double bond isomers (e.g. OME), it would be reasonable to perform double bond isomerization prior to tandem isomerization-hydroformylation. This measure ensures the presence of terminal double bonds for hydroformylation to the desired linear oxo-product and facilitates back-isomerization of consumed terminal double bonds from next neighbor positions. To evaluate the potential of the discussed measures, two preliminary tandem isomerization-hydroformylation batch experiments using the Rh-BiPhePhos catalyst and OME were performed in DMF: i) without pre-isomerization of the substrate and ii) with pre-isomerization of the substrate. The chosen experimental conditions are oriented towards those used in the literature [Behr et al. 2005]. A high synthesis gas pressure of 20 bar was chosen to suppress catalyst deactivation by Rh-ester complexation.

Figure 5.1 summarizes the experimental results of both preliminary batch experiments. The quantities of interest in Figure 5.1a are OME conversion X_{OME} ,

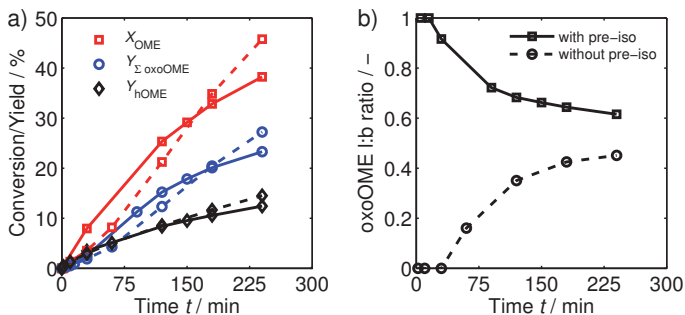


Figure 5.1: Tandem isomerization-hydroformylation of OME: a) OME conversion and product yields, b) regioselectivity expressed as linear:branched ratio. (DMF, 150 °C, 20 bar synthesis gas, $c_{\text{sub}}^0 = 1.35 \text{ mol l}^{-1}$, Rh:sub (molar) = 1:700, Rh:lig (molar) = 1:5)

hydroformylation product yield (sum of all linear and branched oxo-esters) $Y_{\Sigma \text{oxoOME}}$ and hydrogenation product yield Y_{hOME} . The dashed lines in Figure 5.1 represent the case without pre-isomerization, whereby OME was injected into the liquid solvent-catalyst mixture after catalyst activation with 20 bar synthesis gas. The solid lines correspond to the experiment with pre-isomerization of OME after catalyst activation (2 h pre-isomerization at 120 °C and 0 bar CO) before synthesis gas injection. No significant effect of the pre-isomerization on the conversion of OME or the product yields (see Figure 5.1a, solid lines) was observable.

The hydroformylation regioselectivity, expressed as linear:branched oxoOME ratio, however, was significantly improved by pre-isomerization of OME (see Figure 5.1b). After ≈ 20 min reaction time, however, the linear:branched selectivity breaks down, since the hydroformylation of terminal double bonds is faster than the back-isomerization to restore them.

At 150 °C and 20 bar synthesis gas in DMF, the TOF_n of OME was $\approx 30 \text{ l mol}^{-1} \text{ h}^{-1}$ after 4 h reaction time in the preliminary experiments. In the literature, the reported TOF_n of the tandem isomerization-hydroformylation of OME was significantly lower ($\approx 10 \text{ l mol}^{-1} \text{ h}^{-1}$, toluene, 125 °C and 20 bar synthesis gas) after 17 h reaction time [Behr et al. 2005]. Regarding hydrogenation, a similar unfavorably high yield of methyl stearate (hOME) was reported.

These facts underline the great importance of understanding the complex interactions between solvent, catalyst and substrate to improve the hydroformylation productivity for OME. Future work may thus address these issues to overcome poor hydroformylation rates and selectivities of OME by systematic modeling and further optimization based on extending the findings of this thesis.

6 Summary and conclusions

This thesis is part of the collaborative research center SFB/TRR63 "Integrated Chemical Processes in Liquid Multiphase Systems (InPROMPT)" and intends to contribute to the understanding of complex tandem isomerization-hydroformylation reaction networks catalyzed by Rh-BiPhePhos complexes. Substrates of particular interest are mono-unsaturated long-chain renewable oleochemicals, such as methyl oleate (OME) originating from e.g. rapeseed oil. Their hydroformylation products are bi-functional (aldehyde- or oxo-esters) and can be used elegantly in e.g. subsequent renewable polymers production. In contrast to established hydroformylation processes converting n-olefins with terminal double bond, two major issues arise from using OME as substrate:

1. The double bond of OME is located at position 9 of the carbon chain, which makes double bond isomerization essential for desired linear oxo-ester production.
2. The mildly polar ester group contains oxygen and may thus interact with the hydroformylation catalyst, altering its activity.

These issues are hardly discussed in the literature up to now. To be more specific, no systematic strategy and no kinetic models are available for tandem isomerization-hydroformylation reactions using n-olefins or oleo-esters. In fact, no kinetic models are available for the hydroformylation of oleo-esters at all. The lack of this information makes it difficult to rigorously design and optimize hydroformylation processes using renewable feeds. Hence, it was decided to contribute to this field by developing mechanistic kinetic models for the (tandem isomerization-) hydroformylation of mono-unsaturated long-chain substrates in this thesis, including all relevant main and side reactions with subsequent generation of optimal reaction control strategies.

However, studying OME as substrate is difficult because it contains both, an internal double bond and an ester group. Consequently, the influence of the ester group will overlap the double bond isomerization, hydroformylation and the tandem isomerization-hydroformylation reaction, which complicates a correct assignment of observations to causes. Hence, a decoupling strategy of using two model compounds, 1-decene as representative long-chain n-olefin and methyl 10-undecenoate (UME) as oleo-ester with analogous structure compared to 1-decene, was used to study the mentioned issues separately. The long-chain n-decenes can be characterized

well in terms of analytical resolution of double bond isomers. Hence, they were used to develop and parameterize a mechanistic kinetic model for the double bond isomerization, hydrogenation and hydroformylation as well as the tandem isomerization-hydroformylation. The oleo-ester UME was used to reveal influences of the ester group on the Rh-catalyst and its activity under various reaction conditions by comparison to 1-decene results because UME is structurally analogous to 1-decene. The observed ester-catalyst interactions were subsequently included in the mechanistic kinetic model for UME. These mechanistic kinetic models for both substrates are the ultimate objectives of this thesis, from which conclusions regarding improved hydroformylation reaction conditions for OME were drawn.

In the following, major findings and results of the thesis are summarized.

Parameter identifiability

Model parameter estimation for both substrates using experimental (semi-) batch data requires determination of parameter identifiability depending on model structure and experimental design beforehand. In case of dynamic (semi-) batch experiments, the parameter identifiability is also time-dependent, which leads to time domains in the experimental data with different information density. Knowing these time domains is essential to adapt sampling frequencies. Hence, a model based method, which exploits rigorously calculated parameter sensitivities, was used and extended in this thesis to a local analysis to account for dynamic (semi-) batch systems [Jörke et al. 2015b]. This local parameter subset selection method is able to determine the identifiability of model parameters and time domains with high informational density. A set of unknown model parameters can thus be divided into a sensitive (identifiable) and insensitive (non-identifiable) subset depending on the experimental design, which can be adjusted iteratively to increase the sensitive parameter subset. Generally, the presented method is not limited to reaction systems but applicable to any dynamic system.

Hydroformylation of n-decene

Double bond isomerization equilibrium The double bond isomerization reaction equilibrium for all internal n-decenes was calculated using Gibbs energy minimization [White et al. 1958]. This method requires provision of thermodynamic state functions only, which were calculated using Benson's group contribution method [Benson et al. 1969]. Assuming a distinct stoichiometry of the reaction equilibrium network is not necessary. The method allowed to calculate the weakly temperature dependent n-decene isomer distribution at thermodynamic equilibrium efficiently,

which served for determining equilibrium constants [Jörke et al. 2015a]. Thus, the number of unknown kinetic model parameters was reduced. It was found that most n-decene isomers have an internal double bond at equilibrium ($\approx 99\%$). The symmetric 5-decenes are half as stable than the other non-symmetric internal n-decenes, which are all almost equally stable. Comparing the results to quantum chemical calculations as well as experimental data confirmed their reliability [Jörke et al. 2016].

Hydroformylation reaction mechanism for n-decene A general extended Wilkinson-type hydroformylation reaction mechanism [Evans et al. 1968], including a detailed catalyst pre-equilibrium as well as double bond isomerization and hydrogenation side reactions, was presented and used as basis for further mechanistic kinetic modeling. Significant reduction of the detailed catalyst pre-equilibrium was possible using *operando* FTIR spectroscopy by detection of Rh-catalyst species during catalyst pre-formation as well as under various reaction conditions. It was possible to prove that hydrido-Rh-mono- $\text{HRh}(\text{BP})(\text{CO})$ and dicarbonyl $\text{HRh}(\text{BP})(\text{CO})_2$ complexes are the dominating observable Rh-species during isomerization, hydrogenation and hydroformylation of n-decenes. Furthermore, the coordination of the substrate double bond to the Rh-BiPhePhos catalyst was found to be the rate determining step for the hydroformylation, hydrogenation and isomerization of n-decenes [Jörke et al. 2017b]. Upon these findings, the general reaction mechanism was reduced.

Mechanistic kinetic modeling and parameter estimation Based on the reduced reaction mechanism, a set of mechanistic kinetic rate equations was derived for 1-decene using Christiansen's method [Christiansen 1953] for all main (hydroformylation) and side reactions (double bond isomerization and hydrogenation). The design of kinetic experiments for subsequent parameter estimation was supported by local parameter subset selection, as mentioned above. It was possible to estimate all significant kinetic parameters with low 95 % confidence intervals using (semi-) batch data from only 23 carefully designed n-decene isomerization, hydrogenation, hydroformylation and tandem isomerization-hydroformylation experiments [Jörke et al. 2017a]. The experiments revealed that the yield of the desired hydroformylation product undecanal increased with increasing synthesis gas pressure. This observation is explained by suppression of the undesired isomerization side reaction, which shows a negative partial reaction order with respect to CO caused by the CO dependent catalyst pre-equilibrium. This indirect CO influence was included in the kinetic model by separate modeling of the catalyst pre-equilibrium. The tandem isomerization-hydroformylation of internal n-decenes, however, showed a reversed dependence on synthesis gas pressure because high synthesis gas pressure (and

therefore CO concentration) inhibits the essential reproduction of consumed 1-decene by back-isomerization of internal *n*-decenes. The mechanistic kinetic model was able to reproduce all experimental observations with very good accordance to experimental data, even borderline cases and tandem isomerization-hydroformylation experiments [Jörke et al. 2017a].

Hydroformylation of methyl 10-undecenoate

Comparison of UME to 1-decene The influence of the ester group on the Rh-BiPhePhos catalyst was investigated by comparing kinetic key isomerization, hydrogenation and hydroformylation experiments of 1-decene to the structurally similar oleo-ester UME. It turned out that the catalyst activity was reduced significantly by the presence of UME under CO/H₂ free isomerization conditions, which could be reversed by small amounts of dissolved CO. Presence of saturated esters, however, had no influence on the catalyst activity. The findings suggested that the unsaturated ester chelates and forms inactive Rh-ester complexes, reducing the overall available amount of active Rh-BiPhePhos catalyst. The choice of solvent also influenced the catalyst activity significantly in case of converting UME depending on the gas phase composition. A five-fold activity increase was observed by using a polar solvent (DMF) compared to a non-polar solvent (toluene) for the isomerization of UME under CO free conditions. The catalyst activity during the same experiment conducted with 1-decene, however, was independent from the solvent choice. Competitive coordination of DMF or stabilization of the ester group in solution might be responsible but could not be proven yet.

Under CO free hydrogenation conditions (10 bar H₂), the catalyst activity was significantly higher compared to isomerization results. This observation was traced to reactivation of deactivated Rh-catalyst by H₂ induced oxidation of Rh^I to double bond isomerization and hydrogenation active Rh^{III}-trihydride complexes, as described in [Walter et al. 2017]. Using DMF instead of toluene increased the hydrogenation and isomerization reaction rates of UME, but not as much as under isomerization conditions. Additionally, the different solubility of H₂ in both solvents influences the observations as well.

Under typical hydroformylation conditions (20 bar CO/H₂), no significant differences in reaction rates between UME and 1-decene were experimentally detectable in DMF or toluene. Thus, it can be concluded that the presence of highly Rh affine CO suppresses the formation of inactive Rh-ester and Rh^{III}-trihydride complexes because it occupies necessary coordination sites.

Hydroformylation reaction mechanism for UME Unfortunately, *operando* FTIR spectroscopy was incapable to prove directly the existence of the presumed Rh-ester and Rh^{III}-trihydride complexes under isomerization, hydrogenation and hydroformylation conditions. Only the hydrido-Rh-mono- HRh(BP)(CO) and dicarbonyl HRh(BP)(CO)₂ complexes were observable while converting UME. However, the catalyst activity during UME isomerization was significantly reduced in the FTIR experiments compared to 1-decene. Also, the H₂ induced catalyst reactivation was experimentally evident in FTIR experiments. It was concluded that the suspected complexes are lacking CO ligands, which makes them difficult to observe in the IR spectrum. All findings were included in an extended reaction hydroformylation reaction mechanism for UME, which contains catalyst deactivation by Rh-ester complexation as well as its reactivation by H₂. Based on the comparison to 1-decene results, it was evident that the catalytic cycles and rate determining steps for double bond isomerization, hydrogenation and hydroformylation are the same for UME.

Mechanistic kinetic modeling and parameter estimation The mechanistic kinetic model derived from the extended hydroformylation reaction mechanism for UME contains the extended catalyst pre-equilibrium but identical rate expressions compared to the n-decene model, which is equivalent with assuming the same rate determining steps and catalytic cycles for UME and n-decenes. Parameters were estimated using data from only 10 carefully designed UME isomerization, hydrogenation and hydroformylation (semi-) batch experiments. Parameter identifiability was verified by local parameter subset selection and very good accordance of simulations to experimental data was achieved.

Optimal reaction control strategies

Dynamic optimization was used to calculate optimal reaction control strategies for semi-batch (tandem isomerization-) hydroformylation reactions of both substrates using the developed mechanistic kinetic models. The objective was to maximize the yield of linear hydroformylation product, subject to an industrially relevant space-time-yield under variation of dynamic process variable trajectories (reaction temperature and partial pressures of CO/H₂). The optimal control problem was transformed into a high dimensional non-linear program by discretization of the resulting differential and algebraic equations with orthogonal collocation on finite elements. AMPL in combination with the Conopt 3.17A solver was used to obtain the solution efficiently. The optimization results suggested that substrates with terminal double bond (n-olefins and esters) should be converted preferably using low reaction temperature and high synthesis gas pressures to suppress undesired double

bond isomerization, which has a higher apparent activation energy. The tandem isomerization-hydroformylation, however, should be conducted for both substrates at the highest reaction temperature possible to increase the back-isomerization rate from internal to terminal double bond isomers. In terms of gas phase composition, different optimal partial pressure trajectories for internal n-olefins and esters were obtained. Internal n-olefins should be converted preferably at low synthesis gas (especially CO) pressure to keep reproduction of consumed 1-decene by back-isomerization of internal n-decenes at a high rate. For internal oleo-esters, a high CO partial pressure is beneficial to counteract catalyst deactivation by Rh-ester complexation at low conversion. With increasing conversion, the optimal CO partial pressure should be reduced to counteract catalyst deactivation by formation of inactive hydrido-Rh-dicarbonyl complexes. The H₂ partial pressure should be kept low for both substrates to reduce undesired hydrogenation.

Outlook

Preliminary experiments showed that it is possible to improve the tandem isomerization-hydroformylation of OME significantly based on combined findings of n-decene and UME. The selectivity towards the desired linear oxo-ester was increased drastically from $\approx 0\%$ to $\approx 100\%$ initially by pre-isomerization. Conducting the reactions in a polar solvent (DMF) caused a threefold productivity increase compared to literature results, which used non-polar toluene as solvent. Therefore, further systematic investigations of renewable oleo-compound hydroformylation seem to be promising for future work.

Conclusion

This interdisciplinary thesis contributed to several research areas. The parameter identifiability results are generally applicable and may help to further improve experimental design methods. Regarding the studied chemistry, significant contributions to the understanding of thermodynamics, catalysis and systematic kinetic modeling of hydroformylation systems were made. It was possible to derive and present comprehensive mechanistic kinetic models for the double bond isomerization, hydrogenation, hydroformylation and most importantly the tandem isomerization-hydroformylation of long-chain n-olefins and renewable oleo-esters. These models were not available in the literature so far but are desirable for rigorous development and optimization of "Green Hydroformylation" processes.

References

- M. Baerns. *Technische Chemie*. Wiley-VCH GmbH & Co. KGaA, Weinheim, 2012.
- H. Bahrman, H. W. Bach, and G. D. Frey. Oxo synthesis. In *Ullmann's Encyclopedia of Industrial Chemistry*. Wiley-VCH GmbH & Co. KGaA, Weinheim, 2013.
- T. Barz and G. Wozny. Kalibrierung dynamischer Modelle durch adaptive, optimale Versuchspläne. *Chem. Ing. Tech.*, 86(7):953–965, 2014.
- T. Barz, D. C. López C., H. Arellano-Garcia, and G. Wozny. Experimental evaluation of an approach to online redesign of experiments for parameter determination. *AIChE J.*, 59(6):1981–1995, 2013.
- A. D. Becke. Density-functional exchange-energy approximation with correct asymptotic behavior. *Phys. Rev. A*, 38(6):3098–3100, 1988.
- A. Behr. Technische Konzepte zum Recycling von Homogenkatalysatoren. *Chem. Ing. Tech.*, 70(6):685–695, 1998.
- A. Behr and C. Fängewisch. Temperatur-gesteuerte Lösungsmittelsysteme - Ein alternatives Konzept zum Recycling homogener Übergangsmetallkatalysatoren. *Chem. Ing. Tech.*, 73(7):874–878, 2001.
- A. Behr and P. Neubert. *Applied Homogeneous Catalysis*. Wiley-VCH GmbH & Co. KGaA, Weinheim, 2012.
- A. Behr and A. Vorholt. Hydroformylation and related reactions of renewable resources. In *Organometallics and Renewables*, pages 103–127. Springer, Berlin-Heidelberg, 2012.
- A. Behr, D. Obst, C. Schulte, and T. Schosser. Highly selective tandem isomerization-hydroformylation reaction of trans-4-octene to n-nonanal with rhodium-BIPHEPHOS catalysis. *J. Mol. Catal. A: Chem.*, 206(1-2):179–184, 2003.
- A. Behr, D. Obst, and C. Schulte. Kinetik der isomerisierenden Hydroformylierung von trans-4-Octen. *Chem. Ing. Tech.*, 76(7):904–910, 2004.
- A. Behr, D. Obst, and A. Westfechtel. Isomerizing hydroformylation of fatty acid esters: Formation of ω -aldehydes. *Eur. J. Lipid. Sci. Technol.*, 107(4):213–219, 2005.
- A. Behr, A. Westfechtel, and J. Pérez Gomes. Catalytic processes for the technical use of natural fats and oils. *Chem. Eng. Tech.*, 31(5):700–714, 2008.
- M. Beller. *Catalytic carbonylation reactions*. Springer, Berlin, 2006.
- M. Beller, B. Cornils, C. D. Frohning, and C. W. Kohlpaintner. Progress in hydroformylation and carbonylation. *J. Mol. Catal. A: Chem.*, 104(1):17–85, 1995.

- M. Beller, B. Zimmermann, and H. Geissler. Dual catalytic systems for consecutive isomerization-hydroformylation reactions. *Chem. Eur. J.*, 5(4):1301–1305, 1999.
- S. W. Benson, F. R. Cruickshank, D. M. Golden, G. R. Haugen, H. E. O'Neal, A. S. Rodgers, R. Shaw, and R. Walsh. Additivity rules for the estimation of thermochemical properties. *Chem. Rev.*, 69(3):279–324, 1969.
- B. M. Bhanage, S. S. Divekar, R. M. Deshpande, and R. V. Chaudhari. Kinetics of hydroformylation of 1-dodecene using homogeneous HRh(CO)(PPh₃)₃ catalyst. *J. Mol. Catal. A: Chem.*, 115(2):247–257, 1997.
- L. T. Biegler. Solution of dynamic optimization problems by successive quadratic programming and orthogonal collocation. *Comput. Chem. Eng.*, 8(3-4):243–247, 1984.
- E. Billig, A. G. Abatjoglou, and D. R. Bryant. US Patent 4668651 A: Polyphosphite complex hydroformylation catalyst (1985), 1987.
- E. Billig, A. G. Abatjoglou, and D. R. Bryant. US Patent 4769498 A: Transition metal complex catalyzed processes (1985), 1988.
- A. Börner and R. Franke. *Hydroformylation: Fundamentals, Processes, and Applications in Organic Synthesis*. Wiley-VCH GmbH & Co. KGaA, Weinheim, 2016.
- A. Börner, D. Hess, D. Röttger, and D. Selent. EP 1099678 A1: Verfahren zur katalytischen Herstellung von Aldehyden aus Olefinen unter Einsatz von Ligandenmischungen (1999), 2001.
- P. S. Braterman. *Metal carbonyl spectra*. Academic Press, London-New York, 1975.
- C. Breschi, L. Piparo, P. Pertici, A. Maria Caporusso, and G. Vitulli. (η^6 -cyclohepta-1,3,5-triene)(η^4 -cycloocta-1,5-diene)iron(0) complex as attractive precursor in catalysis. *J. Organomet. Chem.*, 607(1-2):57–63, 2000.
- R.P.J. Bronger, J. P. Bermon, J. Herwig, P.C.J. Kamer, and P.W.N.M. vanLeeuwen. Phenoxaphosphino-modified Xantphos-type ligands in the rhodium-catalysed hydroformylation of internal and terminal alkenes. *Adv. Synth. Catal.*, 346(7):789–799, 2004.
- M. Burth, G. C. Verghese, and M. Velez-Reyes. Subset selection for improved parameter estimation in on-line identification of a synchronous generator. *IEEE Trans. Power Syst.*, 14(1):218–225, 1999.
- P. Čapek and A. Seidel-Morgenstern. Multicomponent mass transport in porous solids and estimation of transport parameters. *Appl. Catal., A*, 211(2):227–237, 2001.
- M. Caporali, P. Frediani, A. Salvini, and G. Laurency. In situ high pressure FT-IR spectroscopy on alkene hydroformylation catalysed by RhH(CO)(PPh₃)₃ and Co₂(CO)₈. *Inorg. Chim. Acta*, 357(15):4537–4543, 2004.
- M. Caracotsios and W. E. Stewart. Sensitivity analysis of initial value problems with mixed odes and algebraic equations. *Comput. Chem. Eng.*, 9(4):359–365, 1985.
- G. F. Carey and B. A. Finlayson. Orthogonal collocation on finite elements. *Chem. Eng. Sci.*, 30(5-6):587–596, 1975.

- M. À. Carvajal, S. Kozuch, and S. Shaik. Factors controlling the selective hydroformylation of internal alkenes to linear aldehydes. 1. The isomerization step. *Organometallics*, 28(13):3656–3665, 2009.
- W. Chew, E. Widjaja, and M. Garland. Band-target entropy minimization (BTEM): An advanced method for recovering unknown pure component spectra. Application to the FTIR spectra of unstable organometallic mixtures. *Organometallics*, 21(9):1982–1990, 2002.
- J. A. Christiansen. The elucidation of reaction mechanisms by the method of intermediates in quasi-stationary concentrations. pages 311–353. Elsevier, 1953.
- A. Cintrón-Arias, H. T. Banks, A. Capaldi, and A. L. Lloyd. A sensitivity matrix based methodology for inverse problem formulation. *J. Inv. Ill-Posed Problems*, 17(6), 2009.
- C. Cobelli and J. J. DiStefano. Parameter and structural identifiability concepts and ambiguities: A critical review and analysis. *Am. J. Physiol.*, 239(1):R7–R24, 1980.
- G. N. Costa, R. M. B. Carrilho, L. D. Dias, J. C. Viana, G. L. B. Aquino, M. Pineiro, and M. M. Pereira. Highly efficient Rh(I)/tris-binaphthyl monophosphite catalysts for hydroformylation of sterically hindered alkyl olefins. *J. Mol. Catal. A: Chem.*, 416: 73–80, 2016.
- A. A. Dabbawala, H. C. Bajaj, and R. V. Jasra. Rhodium complex of monodentate phosphite as a catalyst for olefins hydroformylation. *J. Mol. Catal. A: Chem.*, 302(1-2):97–106, 2009.
- D. B. Dahl, C. Davies, R. Hyden, M. L. Kirova, and W. G. Lloyd. The Pd(II)-catalyzed homogeneous isomerization of hexenes. *J. Mol. Catal. A: Chem.*, 123(2-3):91–101, 1997.
- R. M. Deshpande, A. A. Kelkar, A. Sharma, C. Julcour-Lebigue, and H. Delmas. Kinetics of hydroformylation of 1-octene in ionic liquid-organic biphasic media using rhodium sulfoxantphos catalyst. *Chem. Eng. Sci.*, 66(8):1631–1639, 2011.
- O. Diebolt, P. W. N. M. van Leeuwen, and P. C. J. Kamer. Operando spectroscopy in catalytic carbonylation reactions. *ACS Catal.*, 2(11):2357–2370, 2012.
- J. Dodonow and H. Medox. Zur Kenntnis der Grignardschen Reaktion: Über die Darstellung von Tetraphenyl-phosphoniumsalzen. *Ber. Dtsch. Chem. Ges.*, 61(5):907–911, 1928.
- E. S. Domalski and E. D. Hearing. Estimation of the thermodynamic properties of hydrocarbons at 298 K. *J. Phys. Chem. Ref. Data*, 17(4):1637–1678, 1988.
- V. G. Doví, A. P. Reverberi, and L. Maga. Optimal design of sequential experiments for error-in-variables models. *Comput. Chem. Eng.*, 17(1):111–115, 1993.
- J. Dreimann, H. Warmeling, J. Weimann, K. Künnemann, A. Behr, and A. Vorholt. Increasing selectivity of the hydroformylation in a miniplant: Catalyst, solvent, and olefin recycle in two loops. *AIChE J.*, 62(12):4377–4383, 2016.
- J. Dreimann, F. Hoffmann, M. Skiborowski, A. Behr, and A. Vorholt. Merging thermomorphic solvent systems and organic solvent nanofiltration for hybrid catalyst recovery in a hydroformylation process. *Ind. Eng. Chem. Res.*, 56(5):1354–1359, 2017a.

- J. M. Dreimann, T. A. Faßbach, S. Fuchs, M. R. L. Fürst, T. Gaide, R. Kuhlmann, K. A. Ostrowski, A. Stadler, T. Seidensticker, D. Vogelsang, H. W. F. Warmeling, and A. J. Vorholt. Vom Laborkuriosum zum kontinuierlichen Prozess: Die Entwicklung thermomorpher Lösungsmittelsysteme. *Chem. Ing. Tech.*, 89(3):252–262, 2017b.
- E. Drent and P.H.M. Budzelaar. The oxo-synthesis catalyzed by cationic palladium complexes, selectivity control by neutral ligand and anion. *J. Organomet. Chem.*, 593-594:211–225, 2000.
- V. Dubois, S. Breton, M. Linder, J. Fanni, and M. Parmentier. Proposition de classement des sources végétales d'acides gras en fonction de leur profil nutritionnel. *Ol. Corps Gras, Lipides*, 15(1):56–75, 2008.
- D. Evans, J. A. Osborn, and G. Wilkinson. Hydroformylation of alkenes by use of rhodium complex catalysts. *J. Chem. Soc. A*, 0:3133–3142, 1968.
- J. Falbe. The Hydroformylation Reaction Oxo Reaction/Roelen Reaction. In *Carbon Monoxide in Organic Synthesis*, pages 3–77. Springer, Berlin-Heidelberg, 1970.
- B. Fell, D. Leckel, and C. Schobben. Mizellare Zweiphasen-Hydroformylierung von ungesättigten Fettstoffen mit wasserlöslichen Rhodiumcarbonyl/tert. Phosphan-Komplekxkatalysatorsystemen. *Fett Wiss. Technol.*, 97(6):219–228, 1995.
- M. Fink, A. Attarian, and H. Tran. Subset selection for parameter estimation in an HIV model. *Proc. Appl. Math. Mech.*, 7(1):1121501–1121502, 2007.
- I. Ford and S. D. Silvey. A sequentially constructed design for estimating a nonlinear parametric function. *Biometrika*, 67(2):381–388, 1980.
- R. Fourer, D. M. Gay, and B. W. Kernighan. *AMPL: A modeling language for mathematical programming*. Brooks/Cole, Belmont, 2nd edition, 2009.
- R. Franke, D. Selent, and A. Börner. Applied hydroformylation. *Chem. Rev.*, 112(11):5675–5732, 2012.
- E. N. Frankel. Selective hydroformylation of unsaturated fatty acid esters. *Ann. N. Y. Acad. Sci.*, 214:79–93, 1973.
- C. Fyhr and M. Garland. Phenomenological aspects of homogeneous catalysis. The case of equilibrium-controlled precursor conversion. *Organometallics*, 12(5):1753–1764, 1993.
- T. Gaide, J. Bianga, K. Schlipköter, A. Behr, and A. Vorholt. Linear selective isomerization/hydroformylation of unsaturated fatty acid methyl esters: A bimetallic approach. *ACS Catal.*, 7(6):4163–4171, 2017a.
- T. Gaide, A. Jörke, K. E. Schlipköter, C. Hamel, A. Seidel-Morgenstern, A. Behr, and A. J. Vorholt. Isomerization/hydroformylation tandem reaction of a decene isomeric mixture with subsequent catalyst recycling in thermomorphic solvent systems. *Appl. Catal., A*, 532:50–56, 2017b.
- M. Garland and P. Pino. Kinetics of the formation and hydrogenolysis of acylrhodium tetracarbonyl. *Organometallics*, 10(6):1693–1704, 1991.

- U. Gellrich, T. Koslowski, and B. Breit. Full kinetic analysis of a rhodium-catalyzed hydroformylation: beyond the rate-limiting step picture. *Catal. Sci. Technol.*, 5(1): 129–133, 2015.
- D. Gleich and J. Hutter. Computational approaches to activity in rhodium-catalysed hydroformylation. *Chem. Eur. J.*, 10(10):2435–2444, 2004.
- G. Golub. Numerical methods for solving linear least squares problems. *Numer. Math.*, 7(3):206–216, 1965.
- S. Grimme, J. Antony, S. Ehrlich, and H. Krieg. A consistent and accurate ab initio parametrization of density functional dispersion correction (DFT-D) for the 94 elements H-Pu. *J. Chem. Phys.*, 132(15):154104, 2010.
- S. Güven, B. Hamers, R. Franke, M. Priske, M. Becker, and D. Vogt. Kinetics of cyclooctene hydroformylation for continuous homogeneous catalysis. *Catal. Sci. Technol.*, 4(2):524–530, 2014.
- T. Hamerla, A. Rost, Y. Kasaka, and R. Schomäcker. Hydroformylation of 1-dodecene with water-soluble rhodium catalysts with bidentate ligands in multiphase systems. *Chem. Cat. Chem.*, 5(7):1854–1862, 2013.
- M. Haumann, H. Koch, P. Hugo, and R. Schomäcker. Hydroformylation of 1-dodecene using Rh-TPPTS in a microemulsion. *Appl. Catal., A*, 225(1-2):239–249, 2002.
- R. F. Heck and D. S. Breslow. The reaction of cobalt hydrotetracarbonyl with olefins. *J. Am. Chem. Soc.*, 83(19):4023–4027, 1961.
- F. Hein. *Chemische Koordinationslehre*. S. Hirzel, Leipzig, 1st edition, 1950.
- F. G. Helfferich. *Kinetics of multistep reactions*. Elsevier, Amsterdam-Boston, 2nd edition, 2004.
- J. Hibbel, E. Wiebus, and B. Cornils. 75 Jahre Hydroformylierung - Oxoreaktoren und Oxoanlagen der Ruhrchemie AG und der Oxea GmbH von 1938 bis 2013. *Chem. Ing. Tech.*, 85(12):1853–1871, 2013.
- L. Hohl, N. Paul, and M. Kraume. Dispersion conditions and drop size distributions in stirred micellar multiphase systems. *Chem. Eng. Process.*, 99:149–154, 2016.
- R. P. Houghton. *Metal complexes in organic chemistry*. Cambridge Univ. Press., Cambridge, 1979.
- C. Y. Hsu and M. Orchin. Hydridotrichlorostannatocarbonylbis(triphenylphosphine)-platinum(II), $\text{PtH}(\text{SnCl}_3)(\text{CO})(\text{PPh}_3)_2$, as a selective hydroformylation catalyst. *J. Am. Chem. Soc.*, 97(12):3553, 1975.
- M. Illner, D. Müller, E. Esche, T. Pogrzeba, M. Schmidt, R. Schomäcker, G. Wozny, and J. U. Repke. Hydroformylation in microemulsions: Proof of concept in a miniplant. *Ind. Eng. Chem. Res.*, 55(31):8616–8626, 2016.
- M. Janssen, J. Wilting, C. Müller, and D. Vogt. Continuous rhodium-catalyzed hydroformylation of 1-octene with polyhedral oligomeric silsesquioxanes (poss) enlarged triphenylphosphine. *Angew. Chem. Int. Ed.*, 49(42):7738–7741, 2010.

- R. Jennerjahn, I. Piras, R. Jackstell, R. Franke, K. D. Wiese, and M. Beller. Palladium-catalyzed isomerization and hydroformylation of olefins. *Chemistry*, 15(26):6383–6388, 2009.
- A. Jess and P. Wasserscheid. *Chemical Technology: An Integral Textbook*. Wiley-VCH GmbH & Co. KGaA, Weinheim, 2013.
- A. Jörke, A. Seidel-Morgenstern, and C. Hamel. Isomerization of 1-decene: Estimation of thermodynamic properties, equilibrium composition calculation and experimental validation using a Rh-BIPHEPHOS catalyst. *Chem. Eng. J.*, 260:513–523, 2015a.
- A. Jörke, S. Triemer, A. Seidel-Morgenstern, and C. Hamel. Kinetic investigation exploiting local parameter subset selection: Isomerization of 1-decene using a Rh-Biphephos catalyst. *Chem. Ing. Tech.*, 87(6):713–725, 2015b.
- A. Jörke, E. Kohls, S. Triemer, A. Seidel-Morgenstern, C. Hamel, and M. Stein. Resolution of structural isomers of complex reaction mixtures in homogeneous catalysis. *Chem. Eng. Process.*, 102:229–237, 2016.
- A. Jörke, T. Gaide, A. Behr, A. Vorholt, A. Seidel-Morgenstern, and C. Hamel. Hydroformylation and tandem isomerization-hydroformylation of n-decenes using a rhodium-BiPhePhos catalyst: Kinetic modeling, reaction network analysis and optimal reaction control. *Chem. Eng. J.*, 313:382–397, 2017a.
- A. Jörke, A. Seidel-Morgenstern, and C. Hamel. Rhodium-BiPhePhos catalyzed hydroformylation studied by operando FTIR spectroscopy: Catalyst activation and rate determining step. *J. Mol. Catal. A: Chem.*, 426:10–14, 2017b.
- P. C. J. Kamer, A. van Rooy, G. C. Schoemaker, and P. W. N. M. van Leeuwen. In situ mechanistic studies in rhodium catalyzed hydroformylation of alkenes. *Coord. Chem. Rev.*, 248(21-24):2409–2424, 2004.
- P. Kandanarachchi, A. Guo, and Z. Petrovic. The hydroformylation of vegetable oils and model compounds by ligand modified rhodium catalysis. *J. Mol. Catal. A: Chem.*, 184(1-2):65–71, 2002.
- G. Kiedorf, D. M. Hoang, A. Müller, A. Jörke, J. Markert, H. Arellano-Garcia, A. Seidel-Morgenstern, and C. Hamel. Kinetics of 1-dodecene hydroformylation in a thermomorphic solvent system using a rhodium-biphephos catalyst. *Chem. Eng. Sci.*, 115: 31–48, 2014.
- L. Kirch and M. Orchin. The intermediate cobalt hydrocarbonyl-olefin complex in the oxo reaction. *J. Am. Chem. Soc.*, 80(16):4428–4429, 1958.
- L. Kirch and M. Orchin. On the mechanism for the oxo reaction. *J. Am. Chem. Soc.*, 81(14):3597–3599, 1959.
- M. Klähn and M. Garland. On the mechanism of the catalytic binuclear elimination reaction in hydroformylation systems. *ACS Catal.*, 5(4):2301–2316, 2015.
- H. Klein, R. Jackstell, K. D. Wiese, C. Borgmann, and M. Beller. Highly selective catalyst systems for the hydroformylation of internal olefins to linear aldehydes. *Angew. Chem. Int. Ed.*, 40(18):3408–3411, 2001.

- E. Kohls. *Personal communications*, Magdeburg, 2017.
- E. Kohls. *Quantum Mechanical Modeling of Carbonylation Reactions in Industrial Catalysis*. Dissertation, Otto-von-Guericke-Univ. Magdeburg, 2018 - in preparation.
- D. Konya, K. Q. Almeida Leñero, and E. Drent. Highly selective halide anion-promoted palladium-catalyzed hydroformylation of internal alkenes to linear alcohols. *Organometallics*, 25(13):3166–3174, 2006.
- M. Kranenburg, van der Burgt, Y. E. M., Kamer, P. C. J., van Leeuwen, P. W. N. M., K. Goubitz, and J. Fraanje. New diphosphine ligands based on heterocyclic aromatics inducing very high regioselectivity in rhodium-catalyzed hydroformylation: Effect of the bite angle. *Organometallics*, 14(6):3081–3089, 1995.
- C. Kubis. *Untersuchungen zur Kinetik der Hydroformylierung mit Phosphit-modifizierten Rhodiumkatalysatoren unter Einsatz der in situ IR-Spektroskopie*. Dissertation, Univ. Rostock, 2012.
- C. Kubis, D. Selent, M. Sawall, R. Ludwig, K. Neymeyr, W. Baumann, R. Franke, and A. Börner. Exploring between the extremes: Conversion-dependent kinetics of phosphite-modified hydroformylation catalysis. *Chemistry*, 18(28):8780–8794, 2012.
- C. Kubis, W. Baumann, E. Barsch, D. Selent, M. Sawall, R. Ludwig, K. Neymeyr, D. Hess, R. Franke, and A. Börner. Investigation into the equilibrium of iridium catalysts for the hydroformylation of olefins by combining in situ high-pressure FTIR and NMR spectroscopy. *ACS Catal.*, 4(7):2097–2108, 2014.
- C. Kubis, I. Profir, I. Fleischer, W. Baumann, D. Selent, C. Fischer, A. Spannenberg, R. Ludwig, D. Hess, R. Franke, and A. Börner. In situ FTIR and NMR spectroscopic investigations on ruthenium-based catalysts for alkene hydroformylation. *Chemistry*, 22(8):2746–2757, 2016.
- M. Kuriyama, K. Nagai, K. Yamada, Y. Miwa, T. Taga, and K. Tomioka. Hemilabile amidomonophosphine ligand-rhodium(I) complex-catalyzed asymmetric 1,4-addition of arylboronic acids to cycloalkenones. *J. Am. Chem. Soc.*, 124(30):8932–8939, 2002.
- C. R. Landis and J. Uddin. Quantum mechanical modelling of alkene hydroformylation as catalyzed by xantphos-Rh complexes. *Dalton Trans.*, (5):729–742, 2002.
- C. Lee, W. Yang, and R. G. Parr. Development of the Colle-Salvetti correlation-energy formula into a functional of the electron density. *Phys. Rev. B*, 37(2):785–789, 1988.
- C. W. Lee and H. Alper. Influence of 1,4-bis(diphenylphosphino)butane on the hydroformylation of α,β -unsaturated esters catalyzed by zwitterionic, cationic, and neutral rhodium(I) complexes. The asymmetric hydroformylation of α -methylene- γ -butyrolactone. *J. Org. Chem.*, 60(3):499–503, 1995.
- M. Lemberg, G. Sadowski, M. Gerlach, E. Kohls, M. Stein, C. Hamel, and A. Seidel-Morgenstern. Predicting solvent effects on the 1-dodecene hydroformylation reaction equilibrium. *AIChE J.*, 63(10):4576–4585, 2017.
- O. Levenspiel. *Chemical reaction engineering*. Wiley, New York, 3rd edition, 1999.

- C. Li, E. Widjaja, W. Chew, and M. Garland. Rhodium tetracarbonyl hydride: The elusive metal carbonyl hydride. *Angew. Chem. Int. Ed.*, 41(20):3785–3789, 2002.
- J. S. Logsdon and L. T. Biegler. Accurate solution of differential-algebraic optimization problems. *Ind. Eng. Chem. Res.*, 28(11):1628–1639, 1989.
- D. C. López C., T. Barz, M. Peñuela, A. Villegas, S. Ochoa, and G. Wozny. Model-based identifiable parameter determination applied to a simultaneous saccharification and fermentation process model for bio-ethanol production. *Biotechnol. Progr.*, 29(4):1064–1082, 2013.
- D. C. López C., T. Barz, S. Körkel, and G. Wozny. Nonlinear ill-posed problem analysis in model-based parameter estimation and experimental design. *Comput. Chem. Eng.*, 77:24–42, 2015.
- J. Markert, Y. Brunsch, T. Munkelt, G. Kiedorf, A. Behr, C. Hamel, and A. Seidel-Morgenstern. Analysis of the reaction network for the Rh-catalyzed hydroformylation of 1-dodecene in a thermomorphic multicomponent solvent system. *Appl. Catal., A*, 462-463:287–295, 2013.
- Matlab R2014a. Documentation: “rank” function (accessed December 1, 2017). URL <https://de.mathworks.com/help/matlab/ref/rank.html>.
- M. Matsumoto and M. Tamura. Rhodium-catalyzed low pressure hydroformylation of substituted terminal olefins. Role of α,ω -bis(diphenylphosphino)alkane in combination with excess triphenylphosphine. *J. Mol. Catal.*, 16(2):195–207, 1982.
- K. A. P. McLean and K. B. McAuley. Mathematical modelling of chemical processes - Obtaining the best model predictions and parameter estimates using identifiability and estimability procedures. *Can. J. Chem. Eng.*, 90(2):351–366, 2012.
- K. A. P. McLean, S. Wu, and K. B. McAuley. Mean-squared-error methods for selecting optimal parameter subsets for estimation. *Ind. Eng. Chem. Res.*, 51(17):6105–6115, 2012.
- B. Moasser, W. L. Gladfelter, and D. C. Roe. Mechanistic aspects of a highly regioselective catalytic alkene hydroformylation using a rhodium chelating bis(phosphite) complex. *Organometallics*, 14(8):3832–3838, 1995.
- M. Moreno. Promoted iridium complexes as catalysts in hydroformylation of 1-hexene. *J. Catal.*, 215(2):326–331, 2003.
- T. C. Morrill and C. A. D’Souza. Efficient hydride-assisted isomerization of alkenes via rhodium catalysis. *Organometallics*, 22(8):1626–1629, 2003.
- R. H. Morris. Dihydrogen, dihydride and in between: NMR and structural properties of iron group complexes. *Coord. Chem. Rev.*, 252(21-22):2381–2394, 2008.
- K. F. Muilwijk, P. C. J. Kamer, and P. W. N. M. van Leeuwen. A bulky phosphite-modified rhodium catalyst for the hydroformylation of unsaturated fatty acid esters. *J. Am. Oil Chem. Soc.*, 74(3):223–228, 1997.
- D. Murzin and T. Salmi. *Catalytic kinetics*. Elsevier, Amsterdam, 2005.

- V. S. Nair, S. P. Mathew, and R. V. Chaudhari. Kinetics of hydroformylation of styrene using homogeneous rhodium complex catalyst. *J. Mol. Catal. A: Chem.*, 143(1-3):99–110, 1999.
- E. R. Nelsen, A. C. Brezny, and C. R. Landis. Interception and characterization of catalyst species in rhodium bis(diazaphospholane)-catalyzed hydroformylation of octene, vinyl acetate, allyl cyanide, and 1-phenyl-1,3-butadiene. *J. Am. Chem. Soc.*, 137(44):14208–14219, 2015.
- T. Nishimura, Y. Maeda, and T. Hayashi. Asymmetric cyclopropanation of alkenes with dimethyl diazomalonate catalyzed by chiral diene-rhodium complexes. *Angew. Chem. Int. Ed.*, 49(40):7324–7327, 2010.
- J. Nocedal and S. J. Wright. *Numerical Optimization*. Springer, New York, 2nd edition, 2006.
- H. Nowothnick, A. Rost, T. Hamerla, R. Schomäcker, C. Müller, and D. Vogt. Comparison of phase transfer agents in the aqueous biphasic hydroformylation of higher alkenes. *Catal. Sci. Technol.*, 3(3):600–605, 2013.
- S. H. Oh and R. Luus. Use of orthogonal collocation method in optimal control problems. *Int. J. Control*, 26(5):657–673, 2007.
- M. Orchin, L. Kirch, and I. Goldfarb. Evidence for the presence of cobalt hydrocarbonyl under conditions of the oxo reaction. *J. Am. Chem. Soc.*, 78(20):5450–5451, 1956.
- R. Paciello, L. Siggel, H. J. Kneuper, N. Walker, and M. Röper. Structure-activity relationship for chelating phosphite ligands used in rhodium-catalyzed hydroformylations. *J. Mol. Catal. A: Chem.*, 143(1-3):85–97, 1999.
- I. Piras, R. Jennerjahn, R. Jackstell, A. Spannenberg, R. Franke, and M. Beller. A general and efficient iridium-catalyzed hydroformylation of olefins. *Angew. Chem.*, 123(1):294–298, 2011.
- E. Platone and L. Tinucci. EP 0380154 A3: Process for the catalytic hydroformylation of olefins (1989), 1991.
- T. Pogrzeba, D. Müller, M. Illner, M. Schmidt, Y. Kasaka, A. Weber, G. Wozny, R. Schomäcker, and M. Schwarze. Superior catalyst recycling in surfactant based multiphase systems - Quo vadis catalyst complex? *Chem. Eng. Process.*, 99:155–166, 2016.
- B. E. Pohling, J. M. Prausnitz, and J. P. O'Connell. *The Properties of Gases and Liquids*. McGraw-Hill Professional, New York, 2000.
- J. Pospech, I. Fleischer, R. Franke, S. Buchholz, and M. Beller. Alternative metals for homogeneous catalyzed hydroformylation reactions. *Angew. Chem. Int. Ed.*, 52(10):2852–2872, 2013.
- H. F. Ramalho, K. M. C. Di Ferreira, P. M.A. Machado, R. S. Oliveira, L. P. Silva, M. J. Prauchner, and P. A. Z. Suarez. Biphasic hydroformylation of soybean biodiesel using a rhodium complex dissolved in ionic liquid. *Ind. Crops Prod.*, 52:211–218, 2014.

- S. K. Rao, R. Imam, K. Ramanathan, and S. Pushpavanam. Sensitivity analysis and kinetic parameter estimation in a three way catalytic converter. *Ind. Eng. Chem. Res.*, 48(8):3779–3790, 2009.
- J. Reid. Structural identifiability in linear time invariant systems. In *1976 IEEE Conference on Decision and Control including the 15th Symposium on Adaptive Processes*, pages 437–442, 1976.
- O. Roelen. US Patent 2327066 A: Production of oxygenated carbon compounds (1938), 1943.
- O. Roelen. DE Patent 849548 C: Verfahren zur Herstellung von sauerstoffhaltigen Verbindungen (1938), 1952.
- P. Roesle, C. J. Durr, H. M. Möller, L. Cavallo, L. Caporaso, and S. Mecking. Mechanistic features of isomerizing alkoxyacylation of methyl oleate. *J. Am. Chem. Soc.*, 134(42):17696–17703, 2012.
- P. Roesle, L. Caporaso, M. Schütte, V. Goldbach, L. Cavallo, and S. Mecking. A comprehensive mechanistic picture of the isomerizing alkoxyacylation of plant oils. *J. Am. Chem. Soc.*, 136(48):16871–16881, 2014.
- S. N. Rush, Yu. G. Noskov, T. E. Kron, and G. A. Korneeva. Kinetics and mechanism of propene hydroformylation catalyzed by rhodium complexes with a diphosphite ligand. *Kinet. Catal.*, 50(4):557–566, 2009.
- M. K. Sabbe, M. Saeys, M. F. Reyniers, G. B. Marin, V. van Speybroeck, and M. Waroquier. Group additive values for the gas phase standard enthalpy of formation of hydrocarbons and hydrocarbon radicals. *J. Phys. Chem. A*, 109(33):7466–7480, 2005.
- M. K. Sabbe, F. de Vleeschouwer, M. F. Reyniers, M. Waroquier, and G. B. Marin. First principles based group additive values for the gas phase standard entropy and heat capacity of hydrocarbons and hydrocarbon radicals. *J. Phys. Chem. A*, 112(47):12235–12251, 2008.
- R. C. Saxena, D. Seal, S. Kumar, and H. B. Goyal. Thermo-chemical routes for hydrogen rich gas from biomass: A review. *Renew. Sust. Energ. Rev.*, 12(7):1909–1927, 2008.
- E. Schäfer, Y. Brunsch, G. Sadowski, and A. Behr. Hydroformylation of 1-dodecene in the thermomorphic solvent system dimethylformamide/decane. Phase behavior-Reaction performance-Catalyst recycling. *Ind. Eng. Chem. Res.*, 51(31):10296–10306, 2012.
- G. Schiller. DE Patent 953605 C: Verfahren zur Herstellung sauerstoffhaltiger Verbindungen (1952), 1956.
- B. Schreiner and W. Beck. Coordination of the ester group - hydrido-rhodium(III) and iridium(III) complexes of orthometallated diphenylmethylene glycine esters. *Z. anorg. allg. Chem.*, 636(3-4):499–505, 2010.
- M. Schwaab and J. C. Pinto. Optimum reference temperature for reparameterization of the Arrhenius equation. Part I: Problems involving one kinetic constant. *Chem. Eng. Sci.*, 62(10):2750–2764, 2007.

- M. Schwaab, L. P. Lemos, and J. C. Pinto. Optimum reference temperature for reparameterization of the Arrhenius equation. Part 2: Problems involving multiple reparameterizations. *Chem. Eng. Sci.*, 63(11):2895–2906, 2008.
- D. Selent, R. Franke, C. Kubis, A. Spannenberg, W. Baumann, B. Kroidler, and A. Börner. A new diphosphite promoting highly regioselective rhodium-catalyzed hydroformylation. *Organometallics*, 30(17):4509–4514, 2011.
- M. S. Shaharun, B. K. Dutta, and H. Mukhtar. Ab initio energy calculations and macroscopic rate modeling of hydroformylation of higher alkenes by Rh-based catalyst. *AIChE J.*, 55(12):3221–3233, 2009.
- M. S. Shaharun, B. K. Dutta, H. Mukhtar, and S. Maitra. Hydroformylation of 1-octene using rhodium-phosphite catalyst in a thermomorphic solvent system. *Chem. Eng. Sci.*, 65(1):273–281, 2010.
- E. P. Shestakova, Y. S. Varshavsky, V. N. Khrustalev, G. L. Starova, and S. N. Smirnov. Rhodium(III) cationic methyl complexes containing dimethylformamide ligand, cis-[Rh(β -diket)(PPh₃)₂(CH₃)(DMF)][BPh₄] (β -diket = acetylacetonate or benzoylacetonate), in comparison with their acetonitrile analogs. *J. Organomet. Chem.*, 774: 1–5, 2014.
- G. P. Startseva, P. E. Matkovskii, V. Y. Churkina, G. N. Boiko, E. I. Knerel'man, G. I. Davydova, V. N. Troitskii, S. M. Aldoshin, M. A. Demidov, V. G. Shamsutdinov, and G. L. Il'yasov. Isomerization of 1-decene by the nickel stearate-ethylaluminum chloride catalytic system. *Petrol. Chem.*, 44(1):28–37, 2004.
- J. Ternel, J. L. Couturier, J. L. Dubois, and J. F. Carpentier. Rhodium versus iridium catalysts in the controlled tandem hydroformylation-isomerization of functionalized unsaturated fatty substrates. *Chem. Cat. Chem.*, 7(3):513–520, 2015.
- L. A. van der Veen, P. C. J. Kamer, and P. W. N. M. van Leeuwen. Hydroformylation of internal olefins to linear aldehydes with novel rhodium catalysts. *Angew. Chem. Int. Ed.*, 38(3):336–338, 1999.
- J. I. van der Vlugt, R. van Duren, G. D. Batema, R. den Heeten, A. Meetsma, J. Fraanje, K. Goubitz, P. C. J. Kamer, P. W. N. M. van Leeuwen, and D. Vogt. Platinum complexes of rigid bidentate phosphine ligands in the hydroformylation of 1-octene. *Organometallics*, 24(22):5377–5382, 2005.
- R. van Duren, J. I. van der Vlugt, H. Kooijman, A. L. Spek, and D. Vogt. Platinum-catalyzed hydroformylation of terminal and internal octenes. *Dalton Trans.*, (10): 1053–1059, 2007.
- P. W. N. M. van Leeuwen and C. Claver. *Rhodium catalyzed hydroformylation*. Kluwer Academic Publishers, Dordrecht-Boston, 2000.
- P. W. N. M. van Leeuwen and C. F. Roobeek. Hydroformylation of less reactive olefins with modified rhodium catalysts. *J. Organomet. Chem.*, 258(3):343–350, 1983.
- P. W. N. M. van Leeuwen, C. F. Roobeek, R. L. Wife, and J. H. G. Frijns. Platinum hydroformylation catalysts containing diphenylphosphine oxide ligands. *J. Chem. Soc., Chem. Commun.*, (1):31, 1986.

- P. W. N. M. van Leeuwen, C. F. Roobeek, J. H. G. Frijns, and A. G. Orpen. Characterization of the intermediates in the hydroformylation reaction catalyzed by platinum diphenylphosphinous acid complexes. *Organometallics*, 9(4):1211–1222, 1990.
- P. W. N. M. van Leeuwen, P. C. J. Kamer, J. N. H. Reek, and P. Dierkes. Ligand bite angle effects in metal-catalyzed C-C bond formation. *Chem. Rev.*, 100(8):2741–2770, 2000.
- A. van Rooy, E. N. Orij, P. C. J. Kamer, F. van den Aardweg, and P. W. N. M. van Leeuwen. Hydroformylation of oct-1-ene with extremely high rates using rhodium catalysts containing bulky phosphites. *J. Chem. Soc., Chem. Commun.*, (16):1096–1097, 1991.
- A. van Rooy, E. N. Orij, P. C. J. Kamer, and P. W. N. M. van Leeuwen. Hydroformylation with a rhodium/bulky phosphite modified catalyst. A comparison of the catalyst behavior for oct-1-ene, cyclohexene, and styrene. *Organometallics*, 14(1):34–43, 1995.
- A. van Rooy, P. C. J. Kamer, P. W. N. M. van Leeuwen, K. Goubitz, J. Fraanje, N. Veldman, and A. L. Spek. Bulky diphosphite-modified rhodium catalysts: Hydroformylation and characterization. *Organometallics*, 15(2):835–847, 1996a.
- A. van Rooy, J. N. H. de Bruijn, K. F. Roobeek, P. C. J. Kamer, and P. W. N. M. van Leeuwen. Rhodium-catalysed hydroformylation of branched 1-alkenes; bulky phosphite vs. triphenylphosphine as modifying ligand. *J. Organomet. Chem.*, 507(1-2):69–73, 1996b.
- F. van Vyve and A. Renken. Hydroformylation in reverse micellar systems. *Catal. Today*, 48(1-4):237–243, 1999.
- T. Vanbésien, E. Monflier, and F. Hapiot. Hydroformylation of vegetable oils: More than 50 years of technical innovation, successful research, and development. *Eur. J. Lipid. Sci. Technol.*, 118(1):26–35, 2016.
- M. Vilches-Herrera, L. Domke, and A. Börner. Isomerization-hydroformylation tandem reactions. *ACS Catal.*, 4(6):1706–1724, 2014.
- C. Vogelpohl, C. Brandenbusch, and G. Sadowski. High-pressure gas solubility in multicomponent solvent systems for hydroformylation. Part I: Carbon monoxide solubility. *J. Supercrit. Fluids*, 81:23–32, 2013.
- C. Vogelpohl, C. Brandenbusch, and G. Sadowski. High-pressure gas solubility in multicomponent solvent systems for hydroformylation. Part II: Syngas solubility. *J. Supercrit. Fluids*, 88:74–84, 2014.
- C. Vogl, E. Paetzold, C. Fischer, and U. Kragl. Highly selective hydroformylation of internal and terminal olefins to terminal aldehydes using a rhodium-BIPHEPHOS-catalyst system. *J. Mol. Catal. A: Chem.*, 232(1-2):41–44, 2005.
- E. B. Walczuk, P. C. J. Kamer, and P. W. N. M. van Leeuwen. Dormant states of rhodium hydroformylation catalysts: Carboalkoxyrhodium complex formed from enones in the alkene feed. *Angew. Chem. Int. Ed.*, 42(38):4665–4669, 2003.

- S. Walter, M. Haumann, P. Wasserscheid, H. Hahn, and R. Franke. n-butane carbonylation to n-pentanal using a cascade reaction of dehydrogenation and SILP-catalyzed hydroformylation. *AIChE J.*, 61(3):893–897, 2015.
- S. Walter, H. Spohr, R. Franke, W. Hieringer, P. Wasserscheid, and M. Haumann. Detailed investigation of the mechanism of rh-diphosphite supported ionic liquid phase (SILP)-catalyzed 1-butene hydroformylation in the gas phase via combined kinetic and density functional theory (DFT) modeling studies. *ACS Catal.*, 7(2):1035–1044, 2017.
- I. Wender, H. W. Sternberg, and M. Orchin. Evidence for cobalt hydrocarbonyl as the hydroformylation catalyst. *J. Am. Chem. Soc.*, 75(12):3041–3042, 1953.
- W. B. White, S. M. Johnson, and G. B. Dantzig. Chemical equilibrium in complex mixtures. *J. Chem. Phys.*, 28(5):751, 1958.
- Z. Yang, R. Pal, G. L. Hoang, X. C. Zeng, and J. M. Takacs. Mechanistic insights into carbonyl-directed rhodium-catalyzed hydroboration: Ab initio study of a cyclic γ,δ -unsaturated amide. *ACS Catal.*, 4(3):763–773, 2014.
- C. Zhang, Z. Shao, X. Chen, Z. Yao, X. Gu, and L. T. Biegler. Kinetic parameter estimation of HDPE slurry process from molecular weight distribution: Estimability analysis and multistep methodology. *AIChE J.*, 60(10):3442–3459, 2014.
- J. Zhang, M. Poliakoff, and M. W. George. Rhodium-catalyzed Hydroformylation of alkenes using in situ high-pressure IR and polymer matrix techniques. *Organometallics*, 22(8):1612–1618, 2003.
- Y. Zhao and D. G. Truhlar. The M06 suite of density functionals for main group thermochemistry, thermochemical kinetics, noncovalent interactions, excited states, and transition elements: Two new functionals and systematic testing of four M06-class functionals and 12 other functionals. *Theor. Chem. Acc.*, 120(1-3):215–241, 2008.
- E. Zuidema, L. Escorihuela, T. Eichelsheim, J. J. Carbó, C. Bo, P. C. J. Kamer, and P. W. N. M. van Leeuwen. The rate-determining step in the rhodium-Xantphos-catalysed hydroformylation of 1-octene. *Chemistry*, 14(6):1843–1853, 2008.

Appendices

A Experimental details

A.1 Setup

All experiments presented in this thesis were conducted in 75 ml high pressure (semi-) batch autoclaves (Parr Instrument Co., see Figure A.1). These reactors are equipped with a magnetic stirrer, a pressure lock for substrate injection and can be inertized using a vacuum pump and inert N_2 . Additionally, the reactors are temperature controlled with total pressure recording by the process control system.

Two different reactor head setups were used: i) a kinetic reactor and ii) an *operando* FTIR reactor (see Figure A.2 for photographs). For the kinetic reactor, sampling of the liquid phase was possible by opening a valve connected to a sampling tube. Excess pressure inside the reactor allowed drawing a liquid sample (≈ 0.25 ml). Analysis of the sample was made offline using gas chromatography, which is explained later on.

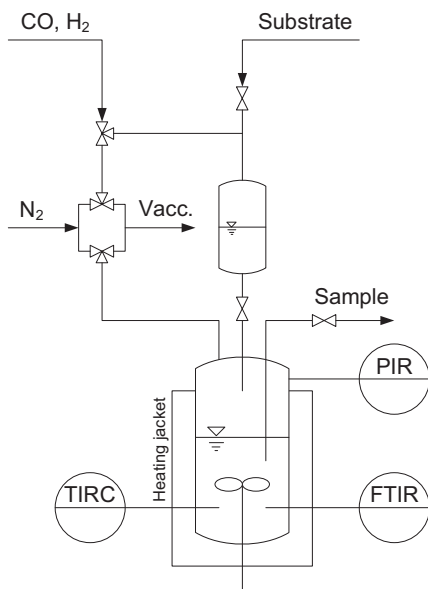


Figure A.1: Scheme of the used 75 ml high pressure (semi-) batch autoclaves.

The FTIR reactor was equipped with a Si-ATR-FTIR probe for *operando* spectroscopic measurements, connected to a FTIR spectrometer (Mettler Toledo, ReactIR 10) with liquid N₂ cooled MCT detector and a resolution of 4 cm⁻¹. Offline sampling was also possible for the FTIR reactor. The reactor head setup for the 3/4" FTIR probe was not available by standard and had to be redesigned and manufactured (see Figure A.3).



Figure A.2: Photographies of the used (semi-) batch reactors: left) reactor for kinetic experiments, right) reactor for *operando* FTIR spectroscopic experiments.

A.2 Procedures, solvents and materials

If not stated otherwise, experiments with n-decene were conducted in a thermomorphic multicomponent solvent (TMS) system (see section 1.2.3) [Behr and Fängewisch 2001; Schäfer et al. 2012]. The TMS consisted of polar DMF (> 99.5 %, used as received, Roth), non-polar n-dodecane (> 99 %, used as received, Alfa Aesar) and the substrate n-decene (1-decene: 94 %, used as received, Sigma Aldrich; equilibrium mixture of internal n-decenes: 95 %, used as received, Sasol) in a molar ratio of 4:3:1, respectively. The TMS becomes homogeneous at $T \geq 85$ °C. Experiments with UME (purified by distillation prior to use, Sigma Aldrich) were always conducted in pure DMF or toluene (> 99.9 %, used as received, Merck).

All experiments (except preliminary gas solubility measurements) started with catalyst pre-formation. For the catalyst pre-formation, catalyst precursor $\text{Rh}(\text{acac})(\text{CO})_2$ (99.9 %, used as received, Umicore) and ligand BiPhePhos (99.9 %, used as received, Molisa) were dissolved in the solvent used followed by inertization with standard Schlenk technique. After inert transfer of the solvent-catalyst mixture into the reactor, addition of synthesis gas (2 bar below desired reaction pressure, $\text{CO}:\text{H}_2 = 1:1$, used as received and stored in aluminum bottle, Linde) while heating to reaction temperature under constant stirring (1200 rpm) initiated catalyst pre-formation. It should be noted that during catalyst pre-formation no substrate was present in the reactor. The substrate was injected after catalyst pre-formation to start the reactions.

All experiments were prepared by transfer of substrate into the pressure lock with Schlenk technique parallel to catalyst pre-formation. For hydroformylation experiments, substrate injection with the desired synthesis gas pressure via the pressure lock started the experiment after reaching reaction temperature. For isomerization or hydrogenation experiments, the activated solvent-catalyst mixture was cooled down to room temperature after reaching reaction temperature with subsequent gas phase exchange to inert N_2 (1 bar) or H_2 (2 bar below desired reaction pressure), respectively. Cooling to room temperature was necessary to prevent significant solvent evaporation during evacuation for gas phase exchange. Injection of the substrate with 3 bar N_2 (isomerization) or H_2 (hydrogenation) started the respective experiments after reaching reaction temperature again. The stirring rate was always at the maximum possible rate (1200 rpm) for all experiments to minimize gas-liquid mass transfer limitations.

A.3 Gas chromatographic analysis

Offline sample analysis was done using a gas chromatograph (Agilent 6890 Series), equipped with a flame ionization detector. Two column setups were used: i) A HP-INNOWax column (120 m length, 0.25 mm inner diameter, 0.50 μm film thickness) for complete resolution of n-decenes (see Figure A.4a) and ii) a HP-5 column (30 m length, 0.25 mm inner diameter, 0.25 μm film thickness) for short analysis time (see Figure A.4b) [Jörke et al. 2015a, 2016]. The method of internal standard was used for quantification, using n-dodecane (TMS experiments) or toluene (all other experiments) as internal standard (ISTD). All used calibration standards and response factors are summarized in Table A.1. Response factors of compounds with non-available calibration standards were estimated by closing atom balances.

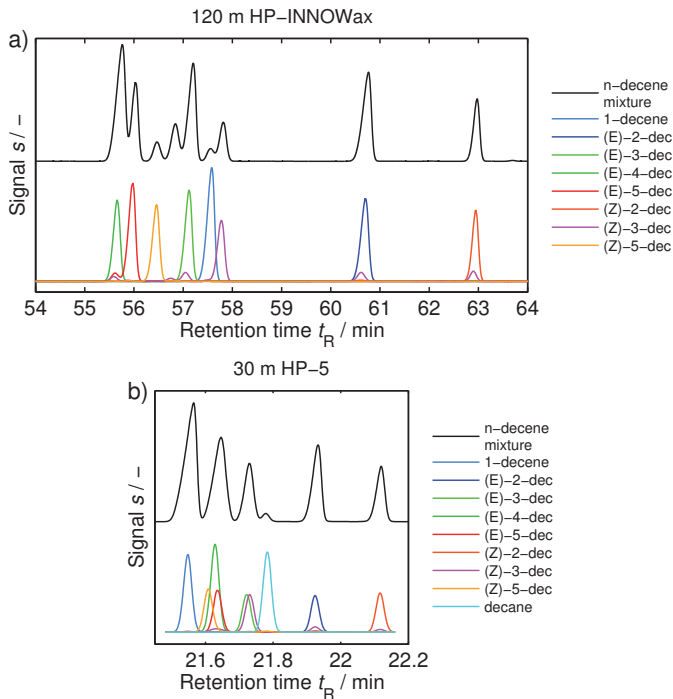


Figure A.4: Resolution of n-decenes using a) 120 m HP-INNOWax column and b) 30 m HP-5 column.

Table A.1: Calibration standards and respective response factors RF for quantification

Component	Supplier	Purity	ISTD	RF	R^2	Median
1-decene	Fluka	99%	n-dodecane	1.03	0.99	-
(E)-2-dec	ChemSampCo	95%	n-dodecane	0.99	0.99	1.07
(E)-3-dec	ChemSampCo	95%	n-dodecane	1.07	0.99	
(E)-4-dec	ChemSampCo	89%	n-dodecane	1.17	0.99	
(E)-5-dec	ABCR	95%	n-dodecane	1.07	0.99	
(Z)-2-dec	TCI	86%	n-dodecane	1.19	0.99	1.19
(Z)-3-dec	ChemSampCo	62%	n-dodecane	1.04	0.99	
(Z)-5-dec	ChemSampCo	72%	n-dodecane	1.47	0.99	
decane	Alfa Aesar	99%	n-dodecane	1.02	0.99	-
undecanal	Alfa Aesar	99%	n-dodecane	1.49	0.99	-
UME	TCI	99%	toluene	1.34	0.99	-
iUME	-	-	toluene	1.34	= UME	-
hUME	TCI	99%	toluene	1.35	0.99	-
oxoUME	-	-	toluene	1.70	C-balance	-
OME	TCI	96%	n-dodecane	1.10	0.99	-
iOME	-	-	n-dodecane	1.10	= OME	-
hOME	TCI	95%	n-dodecane	1.10	0.99	-
oxoOME	-	-	n-dodecane	1.05	C-balance	-

B Gas solubility and mass transfer coefficient

Modeling multiphase hydroformylation systems requires knowledge about the solubility of the gaseous reactants CO and H₂ in the complex liquid reaction mixtures as well as the effective mass transfer coefficient k_{eff} . Data from preliminary gas solubility experiments at different temperatures was used to determine these parameters. In these experiments, the pressure drop of CO or H₂ was measured after injecting the gases into 45 ml liquid reaction mixture with standard initial composition ($c_{\text{sub}}^0 = 1 \text{ mol l}^{-1}$) but without catalyst to avoid conversion of the dissolved gases. From the recorded pressure drop curves followed the amount of dissolved substance and thus the Henry coefficient as well as its temperature dependence. Additionally, the effective mass transfer coefficient k_{eff} followed from the dynamics of the pressure curves. The results are presented in Figure B.1 and Table B.1.

Parameter estimation was done by fitting the solution of a dynamic differential equation describing the pressure curve to experimental data. Starting point of the derivation of this equation is (2.27). Since no reaction takes place, the reaction mixture will dissolve gas molecules until the equilibrium between gas and liquid is reached (see (B.1)).

$$\frac{dp_i}{dt} = k_{\text{eff}} \left(c_i - \frac{p_i^*}{H_i} \right) \frac{V_{\text{liq}}}{V_{\text{gas}}} RT = k_{\text{eff}} (n_{i,\text{liq}} - n_{i,\text{liq}}^*) \frac{RT}{V_{\text{gas}}} \quad (\text{B.1})$$

The amount of dissolved substance $\Delta n_{i,\text{liq}}$ is directly proportional to the pressure drop in the gas phase (see (B.2)).

$$(n_{i,\text{liq}} - n_{i,\text{liq}}^*) = \Delta n_{i,\text{liq}} = -\Delta n_{i,\text{gas}} = \frac{\Delta p_i V_{\text{gas}}}{RT} = \frac{(p_i^* - p_i) V_{\text{gas}}}{RT} \quad (\text{B.2})$$

From combining (B.1) and (B.2) follows the differential equation for the pressure curve (B.3). However, the equilibrium pressure p_i^* is unknown and has to be substituted.

$$\frac{dp_i}{dt} = k_{\text{eff}} (p_i^* - p_i) \quad (\text{B.3})$$

At equilibrium, the amount of dissolved substance $n_{i,\text{liq}}^*$ (B.4) follows from the final pressure difference between initial pressure p_i^0 and final equilibrium pressure p_i^* .

$$n_{i,\text{liq}}^* = -n_{i,\text{gas}}^* = \frac{(p_i^0 - p_i^*) V_{\text{gas}}}{RT} \quad (\text{B.4})$$

To calculate the equilibrium pressure with (B.5), (B.4) is inserted into Henry's Law 2.24.

$$\begin{aligned} p_i^* &= H_i(T) c_i^* = H_i(T) \frac{n_i^*}{V_{\text{liq}}} = \frac{H_i(T) V_{\text{gas}}}{RT} (p_i^0 - p_i^*) = \hat{K} (p_i^0 - p_i^*) \\ &= \frac{\hat{K}}{1 + \hat{K}} p_i^0 \end{aligned} \quad (\text{B.5})$$

From substituting the equilibrium pressure in (B.3) with (B.5) follows the final differential equation for the pressure curve (B.7) after normalizing by the corresponding initial partial pressure p_i^0 (B.6). The advantage of using the normalized pressure $p_{n,i}$ instead of the real pressure p_i lies within the well defined initial condition $p_{n,i}(t = 0) = 1$.

$$\frac{dp_i}{dt} = k_{\text{eff}} \left(\frac{\hat{K}}{1 + \hat{K}} p_i^0 - p_i \right) \quad /: p_i^0 \quad (\text{B.6})$$

$$\frac{dp_{n,i}}{dt} = k_{\text{eff}} \left(\frac{\hat{K}}{1 + \hat{K}} - p_{n,i} \right) \quad (\text{B.7})$$

with

$$\hat{K} = \frac{H_i(T) V_{\text{gas}}}{RT} \quad i = \text{CO}, \text{H}_2$$

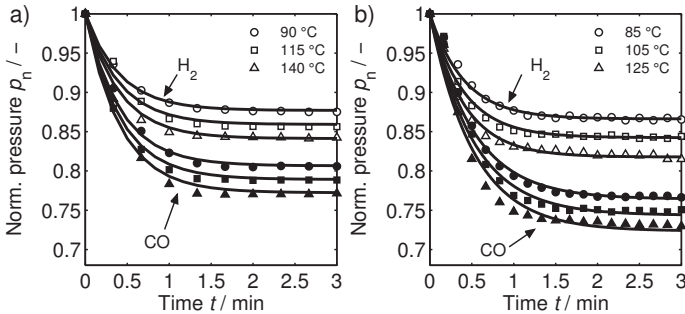


Figure B.1: Experimental (symbols) and modeling (solid lines) results of the solubility of CO (closed symbols) and H₂ (open symbols) at different temperatures: a) n-decene-TMS system and b) UME-toluene system.

Table B.1: Gas solubility and effective mass transfer parameters with 95 % confidence interval for the n-decene-TMS and the UME-toluene system. Reference temperatures for Henry's Law (2.24): 388 K (n-decene) and 378 K (UME).

Parameter	n-decene-TMS system	UME-toluene system
k_{eff}	$2.4122 \text{ min}^{-1} \pm 8.0 \%$	$2.1938 \text{ min}^{-1} \pm 4.8 \%$
$H_{\text{CO,ref}}$	$1.2352\text{e}+04 \text{ Pa m}^3 \text{ mol}^{-1} \pm 0.4 \%$	$9.3246\text{e}+03 \text{ Pa m}^3 \text{ mol}^{-1} \pm 0.8 \%$
B_{CO}	$0.5977 \pm 12.9 \%$	$1.0202 \pm 12.8 \%$
$H_{\text{H}_2,\text{ref}}$	$2.0136\text{e}+04 \text{ Pa m}^3 \text{ mol}^{-1} \pm 0.5 \%$	$1.7190\text{e}+04 \text{ Pa m}^3 \text{ mol}^{-1} \pm 0.5 \%$
B_{H_2}	$1.3006 \pm 6.9 \%$	$2.4609 \pm 3.5 \%$

C Characterization of gas-liquid mass transfer limitations

Multiphase reaction systems have to be characterized in terms of possible mass transfer limitations. For fluid-fluid systems, a common characterization quantity is the dimensionless Hatta number Ha [Baerns 2012]. The Hatta number is defined as the ratio of reaction rate in the liquid bulk phase to the mass transfer rate of a gaseous reactant from the phase boundary into the liquid bulk phase. It is analogous to the Thiele-modulus known in heterogeneous catalysis. Four typical Hatta regimes are distinguished:

I: Slow reaction ($Ha < 0.3$): Bulk reaction

II: Transition regime ($0.3 \leq Ha \leq 3$): Bulk reaction

III: Fast reaction ($Ha > 3$): Film reaction

IV: Instantaneous reaction ($Ha \gg 3$): Reaction in the phase boundary

In case of a slow reaction, the mass transfer is not limiting, the concentration of dissolved reactant is constant in the whole liquid volume with the reaction taking place in the bulk. In the transition regime, mass transfer and reaction rate are in the same order of magnitude with a linear concentration drop of the dissolved reactant in the film and bulk reaction. Fast reactions are characterized by a non-linear concentration profile of the dissolved reactant, which is completely consumed in the film. In this case, the enhancement factor E (C.7) has to be considered. Instantaneous reactions are so fast, the reaction takes place in the phase boundary and depends only on the mass transfer rate and the interfacial area (see Figure C.1).

In case of 1-decene hydroformylation, starting point of the Hatta number calculation is the mass balance of a gaseous reactant (C.1). In the following calculation, the Hatta number is calculated with respect to H_2 because it has a lower solubility than CO and could become limiting in cases of low synthesis gas pressure (1 bar in this calculation). However, the discussion could be conducted with CO in an analogous fashion.

$$\frac{dc_{H_2}}{dt} = k_{\text{eff}} \left(\frac{p_{H_2}}{H_{H_2}} - c_{H_2} \right) - \frac{k_{\text{hyfl}}(T) c_{1D} c_{CO} c_{H_2}}{\left(1 + K_{\text{hyf}}^I c_{H_2} + K_{\text{hyf}}^{II} c_{H_2} c_{CO} \right)} \cdot \frac{c_{R_{h,tot}}}{(1 + K_{\text{cat}} c_{CO})} \quad (\text{C.1})$$

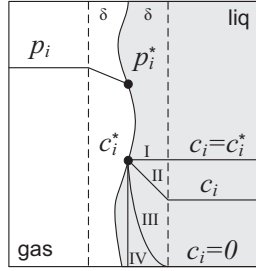


Figure C.1: Hatta regimes. I: Slow reaction ($Ha < 0.3$), II: Transition regime ($0.3 \leq Ha \leq 3$), III: Fast reaction ($Ha > 3$) and IV: Instantaneous reaction ($Ha \gg 3$).

Assuming a steady state situation ($d/dt = 0$) and low H_2 concentration, the reaction rate becomes a first order reaction with respect to H_2 and (C.1) simplifies to (C.2).

$$k_{\text{eff}} \left(\frac{p_{H_2}}{H_{H_2}} - c_{H_2} \right) = \frac{k_{\text{hyfl}}(T) c_{1D} c_{CO} c_{H_2} c_{Rh,\text{tot}}}{(1 + K_{\text{cat}} c_{CO})} \quad (\text{C.2})$$

Assuming constant concentrations of CO, 1-decene and catalyst precursor (differential conversion), (C.2) simplifies to (C.3).

$$k_{\text{eff}} \left(\frac{p_{H_2}}{H_{H_2}} - c_{H_2} \right) = \hat{K} c_{H_2} \quad (\text{C.3})$$

with

$$\hat{K} = \frac{k_{\text{hyfl}}(T) c_{1D} c_{CO} c_{Rh,\text{tot}}}{(1 + K_{\text{cat}} c_{CO})}$$

An explicit expression for the H_2 concentration (C.4) follows from (C.3) and is needed for insertion into the effective reaction rate (C.5) which is influenced by mass transfer.

$$c_{H_2} = \frac{k_{\text{eff}} \frac{p_{H_2}}{H_{H_2}}}{(\hat{K} + k_{\text{eff}})} \quad (\text{C.4})$$

The effective reaction rate is then

$$r_{\text{eff}} = \hat{k} c_{H_2} = \left(\frac{1}{1/k_{\text{eff}} + 1/\hat{K}} \right) \frac{p_{H_2}}{H_{H_2}}. \quad (\text{C.5})$$

It is obvious from (C.5) that two limiting cases exist, namely fast mass transfer compared to reaction rate and vice versa. The first case represents a situation with intense gas-liquid mixing, low catalyst or substrate concentrations or low temperature ($k_{\text{eff}} \gg \hat{K}$). The concentration of the gaseous reactants in the liquid phase in this case is equal to the equilibrium concentration at the phase boundary c_i^* and can be calculated

with Henry's law. Hence, the effective reaction rate shows a first order dependence with respect to the concentrations of (gaseous and liquid) reactants and catalyst. The temperature dependence is dominated by the reaction rate constant k_{hyfl} .

The second case represents a situation with insufficient gas-liquid mixing, very high catalyst or substrate concentrations or high temperature ($k_{\text{eff}} \ll \hat{K}$). In this case, the effective reaction rate is limited by mass transfer and shows a zero order dependence with respect to liquid substrate and catalyst concentrations but a first order dependence with respect to gaseous reactants. The temperature dependence is much less pronounced compared to the first case and dominated by mildly temperature dependent Henry constants because the effective mass transfer coefficient is considered to be almost temperature independent [Baerns 2012].

The Hatta number Ha can be calculated as the square root of the ratio of the characteristic reaction time $t_R = 1/\hat{K}$ divided by characteristic diffusion time $t_D = 1/k_{\text{eff}}$ (C.6) [Baerns 2012]. Using the estimated parameter values for the 1-decene system, standard initial concentration of 1-decene (0.9 mol l^{-1}), standard rhodium to substrate ratio (1:10000), and 1 bar synthesis gas pressure, the calculated Hatta number at standard reaction temperature ($105 \text{ }^\circ\text{C}$) is ≈ 2 . For this extreme borderline case, the value is in the transition regime $0.3 \leq Ha \leq 3$ where mass transport and reaction rate are in a similar order of magnitude [Baerns 2012].

$$Ha = \sqrt{\frac{t_R}{t_D}} = \sqrt{\frac{\hat{K}}{k_{\text{eff}}}} \approx 2 < 3 \quad (\text{C.6})$$

The enhancement factor E , describing the mass transfer increase due to reaction in the liquid film near the phase boundary (C.7), is also ≈ 2 in this case.

$$E = \frac{Ha}{\tanh(Ha)} \approx 2 \quad (\text{C.7})$$

More generally, the characteristic reaction time t_R is the reaction rate divided by the concentration of the gaseous reactant of interest (in this case: H_2). Figure C.2 shows the Hatta number as well as the enhancement factor as a function of the synthesis gas pressure using standard substrate and catalyst concentrations without simplifying (C.1). At standard hydroformylation conditions (1-decene system, 5-20 bar synthesis gas pressure), the Hatta number is between 0.7 - 1.4 with an enhancement factor between 1.1 - 1.5 for the equipment and conditions used in this thesis.

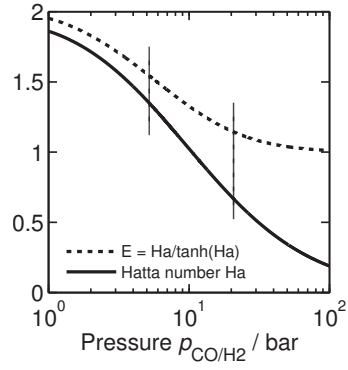


Figure C.2: Hatta number Ha and enhancement factor E for the 1-decene system as function of synthesis gas pressure at standard substrate and catalyst concentrations. $T = 105$ °C.

D Local parameter subset selection results

Local parameter subset selection results are presented for the isomerization, hydrogenation and (tandem isomerization-) hydroformylation (sub)network analysis for n-decenes in Figure D.1 and UME in Figure D.2. Evidently, the experimental designs, presented in Table 3.4 and Table 4.1 allowed to maintain identifiability of all kinetic parameters of the developed mechanistic kinetic models, discernable by the condition

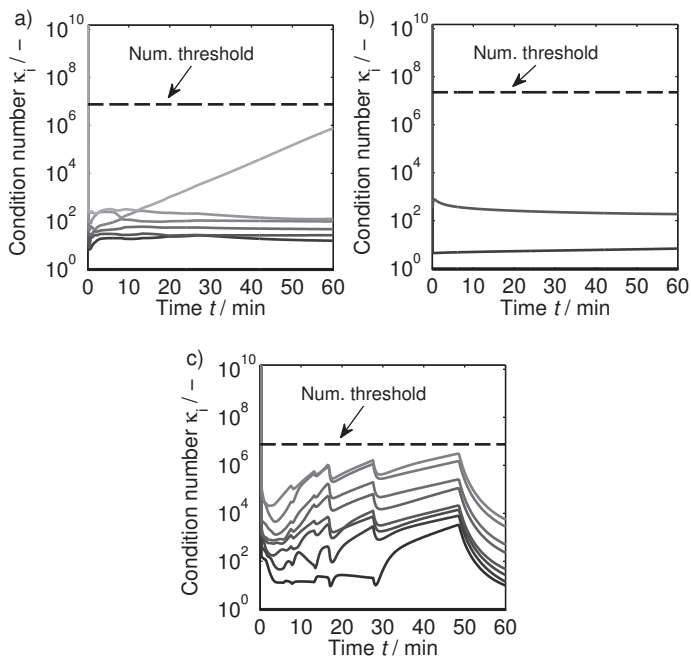


Figure D.1: Time-resolved $\overline{\overline{\kappa_i}}$ condition numbers for reaction subnetwork analysis for n-decene: a) isomerization, b) hydrogenation and c) (tandem isomerization-) hydroformylation (see Table 3.4).

numbers $\bar{\kappa}$ of the $\overline{\overline{FIM}}$ (mostly) not exceeding the numerical threshold (see discussion in section 2.3).

The parameter estimation problem for n-decenes is conditioned best in the first 10-20 min of reaction time, indicated by low condition numbers in this time domain. Hence, a high sampling rate was realized in this time domain to exploit the high informational content.

The condition of the parameter estimation problem for UME looks different as a result of the extended kinetic model and less experiments in the design. Less experiments were designed to increase the efficiency in terms of resources consumption. However, all kinetic parameters were identifiable using this reduced experimental design and could be determined with high accuracy (see section 4.4).

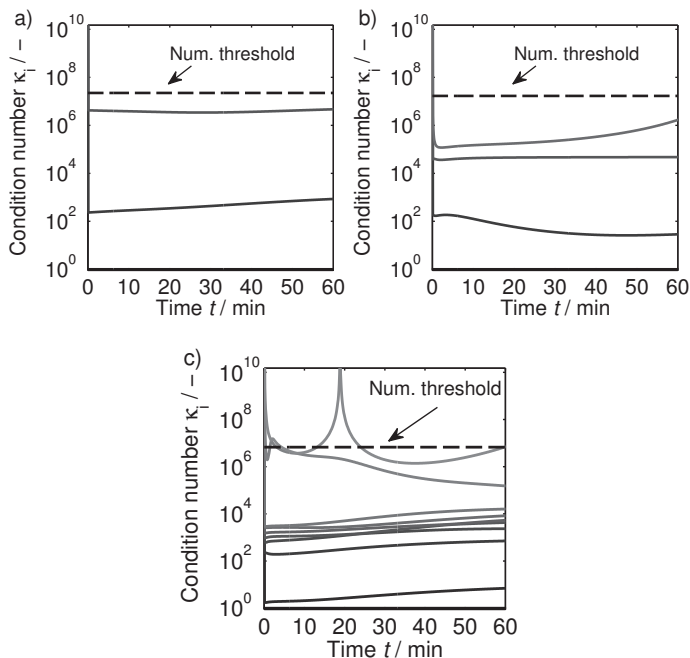


Figure D.2: Time-resolved $\overline{\overline{FIM}}$ condition numbers for reaction subnetwork analysis for UME: a) isomerization, b) hydrogenation and c) hydroformylation (see Table 4.1).

E Derivation of the non-stoichiometric equilibrium formulation

The non-stoichiometric equilibrium formulation (2.3)-(2.4) is derived by transformation of the Gibbs energy minimization (E.1) of a reaction system, subject to atom balances (E.2) of N_{el} chemical elements present in N_s species at equilibrium.

$$G_{\text{eq}} = \min_{\bar{n}} G = \sum_{i=1}^{N_s} \Delta g_i n_i \quad (\text{E.1})$$

s.t.

$$0 = b_j - \sum_{i=1}^{N_s} \beta_{ij} n_i \quad \text{for } j = 1 : N_{\text{el}} \quad (\text{E.2})$$

The optimization problem includes the element-species-matrix $\bar{\beta}$, the amount of substance \bar{n} and the total amount of chemical elements \bar{b} . Since this optimization problem is equality constrained, it can be reformulated into an unconstrained optimization problem by introduction of Lagrange multipliers $\bar{\lambda}$ [Nocedal and Wright 2006]. From the transformation follows the modified Gibbs energy G_{mod} (E.3).

$$G_{\text{eq}} = \min G_{\text{mod}} = \sum_{i=1}^{N_s} \Delta g_i n_i + \sum_{j=1}^{N_{\text{el}}} \lambda_j \left(b_j - \sum_{i=1}^{N_s} \beta_{ij} n_i \right). \quad (\text{E.3})$$

The molar standard potential Δg_i of species i is defined as

$$\Delta g_i = \Delta_f g_i^\circ(T) + RT \ln(a_i) \quad (\text{E.4})$$

with the temperature dependent molar standard potential of formation $\Delta_f g_i^\circ(T)$ of species i . Inserting the definitions of activity $a_i = x_i \cdot \gamma_i$, with the activity coefficient γ_i and molar fraction $x_i = n_i/n_{\text{tot}}$ in (E.4), generates

$$\Delta g_i = \Delta_f g_i^\circ(T) + RT \ln(x_i) + RT \ln(\gamma_i). \quad (\text{E.5})$$

In case of n-decene isomerization, ideal behavior of n-olefins in a solvent is assumed since the molecules are similar, non-polar and diluted, which corresponds to $\gamma_i = 1$. The third term in (E.5) becomes zero in this case. Combining (E.5) with (E.3) leads to a simplified expression for G_{mod}

$$G_{\text{eq}} = \min G_{\text{mod}} = \sum_{i=1}^{N_s} \left[\Delta_f g_i^\circ(T) n_i + RT n_i \ln \left(\frac{n_i}{n_{\text{tot}}} \right) \right] + \sum_{j=1}^{N_{\text{el}}} \lambda_j \left(b_j - \sum_{i=1}^{N_s} \beta_{ij} n_i \right). \quad (\text{E.6})$$

The minimum of G_{mod} has to satisfy the necessary first order optimality conditions

$$\frac{\partial G_{\text{eq}}}{\partial n_i} = 0 \quad \text{and} \quad \frac{\partial G_{\text{eq}}}{\partial \lambda_j} = 0. \quad (\text{E.7})$$

Calculating the first derivative of G_{eq} with respect to the amount of substance n_i of species i leads to

$$\frac{\partial G_{\text{eq}}}{\partial n_i} = \Delta_f g_i^\circ(T) + RT \left(\ln \left(\frac{n_i}{n_{\text{tot}}} \right) + 1 \right) - \sum_{j=1}^{N_{\text{el}}} \lambda_j \beta_{ij} = 0. \quad (\text{E.8})$$

An explicit expression for the molar fraction x_i at equilibrium (E.9) can be obtained by rearranging (E.8).

$$x_i = \exp \left[\frac{1}{RT} \left(\sum_{j=1}^{N_{\text{el}}} \lambda_j \beta_{ij} - \Delta_f g_i^\circ(T) \right) - 1 \right] \quad (\text{E.9})$$

The second optimality condition and the bootstrap condition that the sum of all molar fractions x_i is equal to 1 leads to

$$\frac{\partial G_{\text{eq}}}{\partial \lambda_j} = b_j - \sum_{i=1}^{N_s} \beta_{ij} n_i = 0 \quad (\text{E.10})$$

and

$$\sum_{i=1}^{N_s} x_i - 1 = 0. \quad (\text{E.11})$$

Dividing (E.10) by the total amount of substance n_{tot} and inserting (E.9) generates the final algebraic equation system (2.3)-(2.4) that has to be solved in order to calculate the reaction equilibrium composition.

F Quantum chemical calculations

It should be noted that the author of this thesis published significant parts of this chapter as first author in [Jörke et al. 2016]. Further details and results can be found in the cited article. All QM calculations that are presented in this chapter were done by Emilija Kohls. More details and results can be found in her thesis [Kohls 2018 - in preparation].

F.1 Comparison of BGCM to quantum chemical calculations

Benson's group contribution method (BGCM) is a well-established and easy to implement method to calculate thermodynamic state functions of organic compounds. However, the degree of structural molecular complexity that can be distinguished by BGCM is limited. In case of n-decenes, it is not possible to distinguish all n-decene isomers (cis-3-decene = cis-4-decene, trans-3-decene = trans-4-decene). Conformers of the same isomer are generally not considered in BGCM. Additionally, BGCM is depending on the experimental database to which the increment values were fitted. Because of these drawbacks, BGCM was compared to results from *ab initio* quantum chemistry calculations (QM) presented in [Jörke et al. 2016; Kohls 2018 - in preparation] and experimental data to evaluate the quality of BGCM.

Starting point of calculating thermodynamic state functions with QM methods are molecule structures that represent potential energy minima (see Figure F.1) [Kohls 2017, 2018 - in preparation]. Two representative DFT exchange-correlation functionals (B3LYP-D3 [Becke 1988; Lee et al. 1988; Grimme et al. 2010], M06-2X [Zhao and Truhlar 2008]) as well as the post-Hartree-Fock second order Møller-Plesser MP2 correlated wavefunction method were used for the calculations.

The calculated enthalpies, entropies and heat capacities relative to 1-decene at 298 K are summarized in Table F.1. BGCM data was used as a reference point to calculate root mean squared errors *RMSE*'s due to the lack of experimental data. Generally, the enthalpies are in good agreement with BGCM and follow the same trend in enthalpy difference from cis to trans isomers (see Figure F.2a). At 298 K, the calculations yield that the cis isomers are less stable than the trans isomers by 5.2, 5.8 and 5.0 kJ mol⁻¹

on average, at B3LYP-D3, M06-2X and MP2 levels, respectively. In BGCM at 298 K, the enthalpy difference between cis and the respective trans isomer is always 4.9 kJ mol⁻¹.

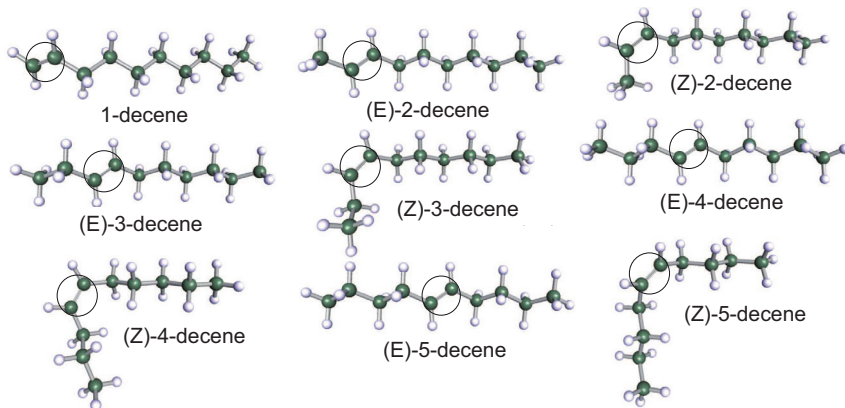


Figure F.1: Structures corresponding to global energy minima of n-decenes used for QM calculations after thorough exploration of conformer energy landscape. The double-bonds in all molecules are highlighted with circles [Jörke et al. 2016; Kohls 2017, 2018 - in preparation].

Experimental Gibbs energy differences were calculated from experimentally observed molar fractions of n-decene isomers at equilibrium (see Table 3.3 in section 3.1.3) using a standard mass action law formulation (F.1). The resulting experimental Gibbs energy differences are presented in Figure F.2b and Table F.1.

$$K_{i-1D}^{\text{eq}} = \exp\left(-\frac{\Delta\Delta_{iD}^{\circ}(T)}{RT}\right) = \frac{a_i^{\text{eq}}}{a_{1D}^{\text{eq}}} = \frac{\gamma_i x_i^{\text{eq}}}{\gamma_{1D} x_{1D}^{\text{eq}}} \approx \frac{x_i^{\text{eq}}}{x_{1D}^{\text{eq}}} \quad (\text{F.1})$$

The calculated relative Gibbs energy differences at process conditions (378 K, 1 bar) were compared to experimental values directly (Figure F.2b and Table F.1). B3LYP-D3, M06-2X and MP2 show small mean deviation relative to experimental data ($RMSE = 3.4, 4.3$ and 3.0 kJ mol⁻¹, respectively) but do not follow the trend in isomer energy ranking. Although the deviation between QM and experiment is not huge, BGCM is much closer to experimental data. If it is of interest to study the reaction equilibrium of energetically similar components using calculated Gibbs energy differences, it is questionable, if the accuracy of thermodynamic data generated with QM methods is sufficient for this task.

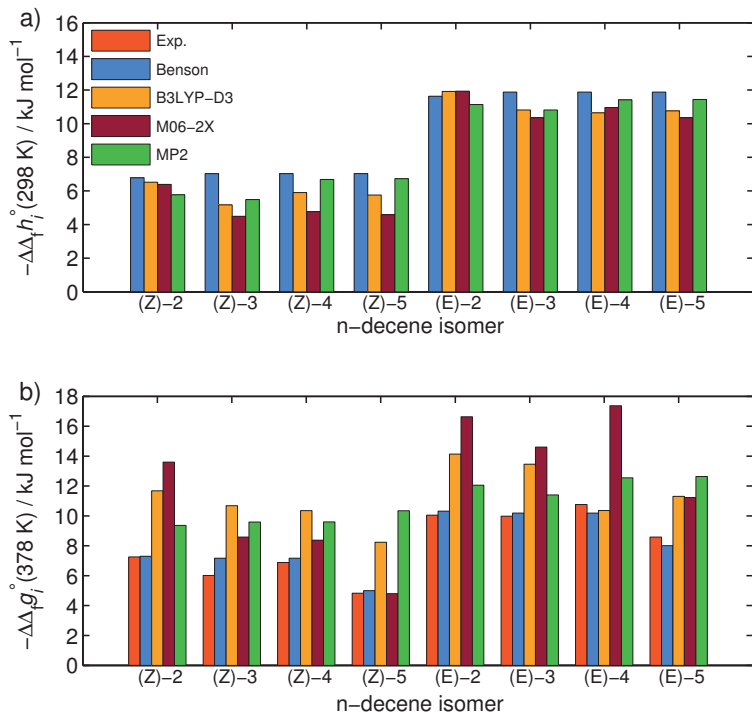


Figure F.2: Comparison of selected QM calculation results: a) Calculated enthalpy differences $-\Delta\Delta_f h^{\circ}(298\text{ K})$ at B3LYP-D3, M06-2X and MP2 levels of theory compared to results obtained with BGCMB; b) Calculated Gibbs energy differences $-\Delta\Delta_f g^{\circ}(378\text{ K})$ at B3LYP-D3, M06-2X and MP2 levels of theory compared to results obtained with BGCMB and experimental data at process conditions (378 K). QM data taken from [Jörke et al. 2016; Kohls 2018 - in preparation].

Although the enthalpy differences calculated with QM methods give a consistent trend in the ranking of the n-decene isomers at every level of theory (Figure F.2a), this trend is not preserved for the calculated relative Gibbs energy differences (Figure F.2b). In the following paragraph, linear error propagation analysis is used to emphasize the origin of these deviations.

The Gibbs energy differences between internal n-decenes and 1-decene at process conditions (378 K, 1bar) were calculated using the Legendre transformation of the Gibbs-Helmholtz-equation (F.2) and Kirchhoff's law.

$$\begin{aligned} \Delta\Delta_{fg}^{\circ}(T) &= \Delta\Delta_{fh}^{\circ}(T) - T\Delta s^{\circ}(T) \\ &= \Delta\Delta_{fh}^{\circ} + \int_{T^{\circ}}^T \Delta c_p(T) dT - T \left(\Delta s^{\circ} + \int_{T^{\circ}}^T \frac{\Delta c_p(T)}{T} dT \right) \end{aligned} \quad (F.2)$$

The required values for enthalpies, entropies and heat capacities from QM results are summarized in Table F.1. Assuming a constant mean heat capacity as first rough estimate, (F.2) becomes (F.3).

$$\Delta\Delta_{fg}^{\circ}(T) = \Delta\Delta_{fh}^{\circ} + \Delta c_p (T - T^{\circ}) - T \left(\Delta s^{\circ} + \Delta c_p \ln\left(\frac{T}{T^{\circ}}\right) \right) \quad (F.3)$$

Form the total differential of $\Delta\Delta_{fg}^{\circ}(T)$ follows the expression for linear error propagation (F.4), which depends only on temperature and error values of the thermodynamic state functions.

$$\begin{aligned} \delta\Delta\Delta_{fg}^{\circ}(T) &= \left| \frac{\partial\Delta\Delta_{fg}^{\circ}(T)}{\partial\Delta\Delta_{fh}^{\circ}} \right| \delta\Delta\Delta_{fh}^{\circ} + \left| \frac{\partial\Delta\Delta_{fg}^{\circ}(T)}{\partial\Delta s^{\circ}} \right| \delta\Delta s^{\circ} + \left| \frac{\partial\Delta\Delta_{fg}^{\circ}(T)}{\partial\Delta c_p} \right| \delta\Delta c_p \\ &= |\delta\Delta\Delta_{fh}^{\circ}| + |-T| \delta\Delta s^{\circ} + \left| (T - T^{\circ}) - T \ln\left(\frac{T}{T^{\circ}}\right) \right| \delta\Delta c_p \end{aligned} \quad (F.4)$$

To estimate the error of Gibbs energy differences at 378 K, the *RMSE*'s as errors for relative enthalpy, entropy and heat capacity were taken from Table F.1 as a first approximation. For MP2, the best performing QM method, the single contributions to the mean error of Gibbs energy differences $\delta\Delta\Delta_{fg}^{\circ}(378 \text{ K})$ are shown in (F.5).

$$\begin{aligned} \delta\Delta\Delta_{fg}^{\circ}(378 \text{ K}) &= \pm 4.27 \text{ kJ mol}^{-1} \approx 1 \text{ kcal} \\ &= \underbrace{|1| 0.8 \text{ kJ mol}^{-1}}_{0.8 \text{ kJ mol}^{-1}} + \underbrace{|-378 \text{ K}| 9.0 \text{ J mol}^{-1} \text{ K}^{-1}}_{3.4 \text{ kJ mol}^{-1}} + \underbrace{|-9.89 \text{ K}| 7.4 \text{ J mol}^{-1} \text{ K}^{-1}}_{0.07 \text{ kJ mol}^{-1}} \end{aligned} \quad (F.5)$$

It is obvious that the uncertainty of entropy is responsible for 80 % of the $\Delta\Delta_{fg}$ error at 378 K. The contribution of the heat capacity, however, is negligible compared to the contribution of entropy, although the uncertainty of both thermodynamic state functions is in the same range. A strong reduction of entropy uncertainty by one order of magnitude would be necessary to achieve a similar error contribution compared to enthalpies. Hence, a precise prediction of $\Delta\Delta_{fg}$ requires further improvement of QM based calculation of entropy values.

It can be concluded that thermodynamic state function values generated with QM

methods are useful as far as enthalpies are concerned. If Gibbs energy at elevated temperatures is of interest, errors become relevant that originate from entropy uncertainties. Therefore, thermodynamic state function values calculated with BGCM were preferred in this thesis because of their accordance to experimental data.

Table F.1: Calculated enthalpy, entropy, heat capacity and Gibbs energy differences relative to 1-decene at B3LYP-D3 (II), M06-2X (III) and MP2 (IV) level of theory [Jörke et al. 2016; Kohls 2018 - in preparation] versus results from BGCM (I). Thermodynamic corrections at 298 K and 1 bar. *RMSE*'s are relative to BGCM results, except for $\Delta\Delta_i\bar{g}^\circ$ (378 K) (relative to experimental data).

	I	II	III	IV	I	II	III	IV	Exp.
	$-\Delta\Delta_i\bar{h}^\circ / \text{kJ mol}^{-1}$				$\Delta\bar{c}_p(298 \text{ K}) / \text{J mol}^{-1} \text{K}^{-1}$				
1-decene	0.0	0.0	0.0	0.0	0.0	0.0	0.0	0.0	-
(E)-2-dec	11.6	11.9	11.9	11.1	0.2	2.6	3.9	2.2	-
(E)-3-dec	11.9	10.8	10.4	10.8	-2.1	2.2	3.0	1.7	-
(E)-4-dec	11.9	10.6	11.0	11.4	-2.1	1.6	3.4	1.8	-
(E)-5-dec	11.9	10.8	10.3	11.4	-2.1	1.8	2.1	1.8	-
(Z)-2-dec	6.8	6.5	6.4	5.8	-7.8	1.9	3.1	1.5	-
(Z)-3-dec	7.0	5.2	4.5	5.5	-10.1	1.3	1.9	0.9	-
(Z)-4-dec	7.0	5.9	4.8	6.7	-10.1	1.3	2.0	0.9	-
(Z)-5-dec	7.0	5.8	4.6	6.7	-10.1	1.1	1.3	0.8	-
<i>RMSE</i>	-	1.1	1.6	0.8	-	7.7	8.3	7.4	-
	$\Delta\bar{s}^\circ / \text{J mol}^{-1} \text{K}^{-1}$				$\Delta\Delta_i\bar{g}^\circ(378 \text{ K}) / \text{kJ mol}^{-1}$				
1-decene	0.0	0.0	0.0	0.0	0.0	0.0	0.0	0.0	0.0
(E)-2-dec	-3.4	5.8	12.3	2.4	10.3	14.1	16.6	12.1	10.0
(E)-3-dec	-4.4	6.9	11.2	1.5	10.2	13.5	14.6	11.4	10.0
(E)-4-dec	-4.4	-0.8	16.9	2.9	10.2	10.4	17.4	12.5	10.8
(E)-5-dec	-10.2	1.4	2.3	3.1	8.0	11.3	11.2	12.6	8.6
(Z)-2-dec	1.6	13.6	19.0	9.5	7.3	11.7	13.6	9.4	7.3
(Z)-3-dec	0.7	14.5	10.8	10.8	7.2	10.7	8.6	9.6	6.0
(Z)-4-dec	0.7	11.7	9.5	7.7	7.2	10.4	8.4	9.6	6.9
(Z)-5-dec	-5.1	6.5	0.5	9.5	5.0	8.2	4.8	10.3	4.8
<i>RMSE</i>	-	10.3	13.4	9.0	0.5	3.4	4.3	3.0	-

F.2 Rh-BiPhePhos catalyst structures

The calculated IR spectra for the comparison to experimental data, shown in Figure 3.9, based on DFT calculations [Kohls 2017, 2018 - in preparation]. Figure F.3 summarizes the optimized geometries of the corresponding Rh-BiPhePhos complexes.

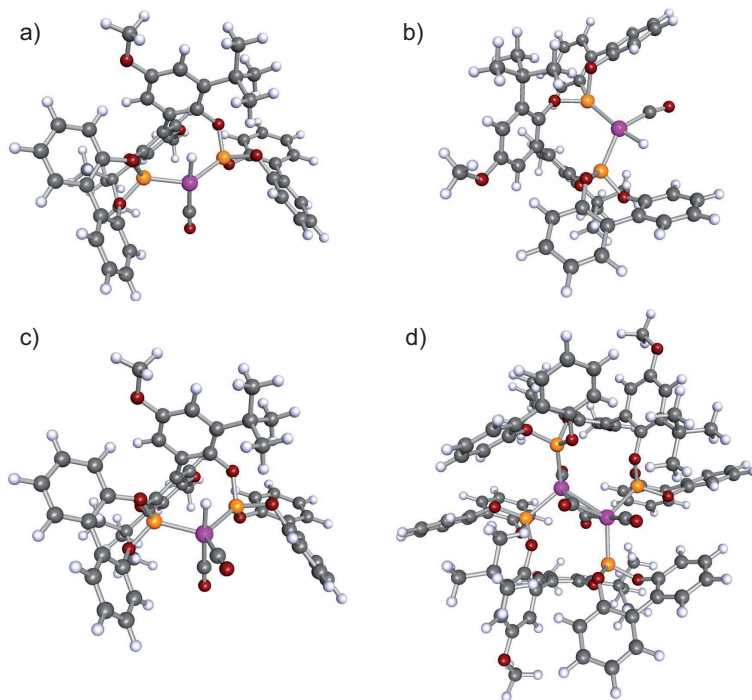


Figure F.3: Rh-BiPhePhos structures that correspond to calculated DFT IR spectra shown in Figure 3.9 (BP86/def2-TZVP) [Kohls 2017, 2018 - in preparation]: a) hydrido-Rh-monocarbonyl with hydride and carbonyl ligand in the same vertical axis, b) hydrido-Rh-monocarbonyl with hydride and carbonyl ligand in cis position, c) hydrido-Rh-dicarbonyl complex with *e,e*-coordination of the ligand and d) Rh-dimer with simultaneously bridging μ -CO and ligand.

G Additional experimental results

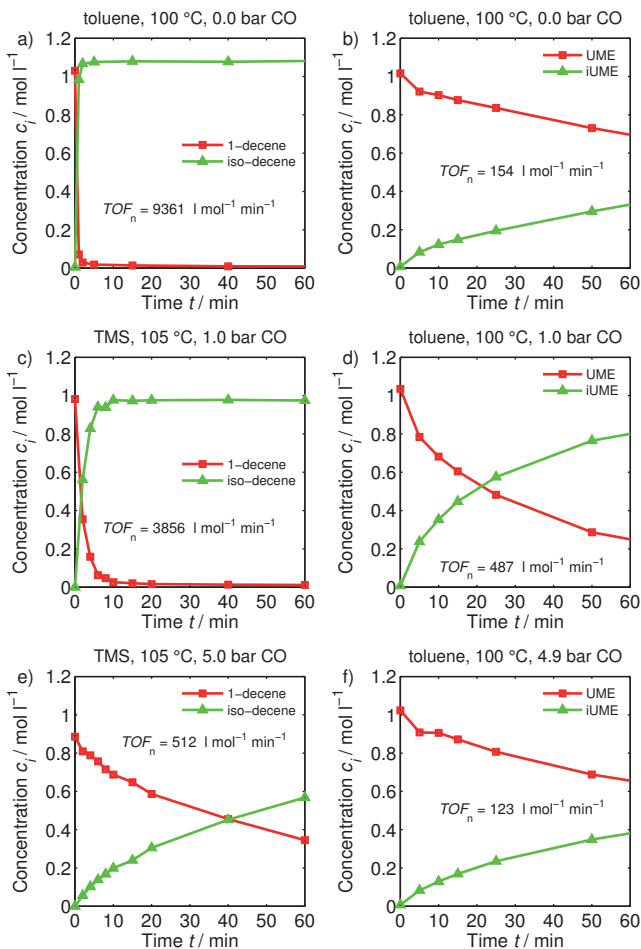


Figure G.1: Isomerization of 1-decene (left column) compared to UME (right column) at 0 (a-b), 1 (c-d) and 5 (e-f) bar CO. ($c_{\text{sub}}^0 = 1 \text{ mol l}^{-1}$, $Rh:\text{sub (molar)} = 1:10000$, $Rh:\text{lig (molar)} = 1:3$)

Lebenslauf

Persönliche Daten

Name: Andreas Jörke
Geburtsdatum und -ort: 30.04.1986 in Magdeburg
Anschrift: Gneisenaustraße 10
67061 Ludwigshafen am Rhein
Staatsangehörigkeit: deutsch
Familienstand: ledig

Berufliche Tätigkeit

seit 02/18 Ingenieur, BASF SE, Ludwigshafen am Rhein
10/12 – 12/17 Wiss. Mitarbeiter, Institut für Verfahrenstechnik,
Otto-von-Guericke-Universität Magdeburg

Studium

10/06 – 07/12 Studiengang: Verfahrenstechnik, Otto-von-
Guericke-Universität Magdeburg
Abschluss: Diplom-Ingenieur (Dipl.-Ing.)

Wehrdienst

07/05 – 03/06 Grundwehrdienst: ABC-Abwehr Bataillon 7,
Höxter

Schulbildung

08/98 – 06/05 Humboldt Gymnasium, Magdeburg
Abschluss: Allgemeine Hochschulreife

Ludwigshafen am Rhein, 21.05.2018